UNIVERSITY OF SOUTHAMPTON

Magnetic flux instabilities in high temperature superconductors

John William Burgoyne

Doctor of Philosophy

The Institute of Cryogenics
Faculty of Engineering and Applied Science

April 1993

UNIVERSITY OF SOUTHAMPTON

ABSTRACT

FACULTY OF ENGINEERING & APPLIED SCIENCE
INSTITUTE OF CRYOGENICS

Doctor of Philosophy

MAGNETIC FLUX INSTABILITIES IN HIGH TEMPERATURE SUPERCONDUCTORS

by John William Burgoyne

The occurrence of magnetic flux instabilities, or flux jumping, has been studied in macroscopic tubes of the $YBa_2Cu_3O_{7-x}$ and $Bi_2Sr_2CaCu_2O_{8+x}$ high temperature superconductors between 2.2 and 4.5K, up to $\pm$3T. The first flux jump field B_{fj} has been determined for $Bi_2Sr_2CaCu_2O_{8+x}$ from shielding measurements and the derivation of magnetisation loops, and the variation of B_{fj} with applied field sweep rate and temperature examined. Values of B_{fj} up to 3.18T at 4.5K, 0.124Tmin^{-1} were found and are compared to the theoretical predictions for high temperature superconductors based on adiabatic theory. The sweep rate and temperature dependencies are found to be in qualitative agreement with some of those empirically established for conventional low temperature superconductors. The sharp rises in temperature which accompany flux jumps have been observed, and from these the specific heat of the material estimated, showing good agreement with the value obtained from the adiabatic theory for the measured B_{fj}, $\gamma C = 0.027 JK^{-1}cm^{-3}$, and indicating that flux jumps occur over the whole tube volume. Some novel flux jumping features were observed in the shielding region which may be due to the microstructure of the material. No flux jumps appeared to be present in $YBa_2Cu_3O_{7-x}$ measurements at continuous sweep rates up to 0.31Tmin^{-1} at 2.2 or 4.5K in fields up to 3T.

Some aspects of the critical current density and flux creep characteristics of the tubes are discussed in the 2.2 to 4.5K and 67 to 77K ranges, and are found to be dominated by the intergranular region. Field sweep rate-dependent magnetisation loops were found for $Bi_2Sr_2CaCu_2O_{8+x}$ tubes at 77K, and for $YBa_2Cu_3O_{7-x}$ at 4.5K.

An investigation into glass-ceramic processing of $Bi_2Sr_2Ca_2Cu_3O_{10}$ is described.

Contents.

List of Figures.

Acknowledgements.

I would like to thank Prof. J.H.P. Watson for supervision of this project, Iain Mears and Mike Webb for seemingly endless practical help in the lab, Erik Roszkowiak for instruction and patience in the workshop, Colin Miles and Tom Perkins for liquid nitrogen and helium supplies, Adrian Richards for three years of good humour and office-sharing, and all the other members of the Institute of Cryogenics for both their help and friendship.

Thanks also to the various people at Pilkington who helped during my visits there, particularly Brian Tilley for general guidance, Dave Taylor for XRD measurements and Christine Grayson for help with DTA. Financial assistance from Pilkington plc is greatly appreciated.

I am grateful to ICI and Hoechst AG for supply of HTS tubes, British Aerospace (Space Systems) Ltd. for loan of the superconducting magnet and SERC for financial support.

Finally, thank-you to the too-many-to-mention friends I have made in Southampton and in Above Bar Church. Most of all, much love and thanks to Caroline for her constant love, support and encouragement;

> *"A wife of noble character who can find? She is worth far more than rubies... Charm is deceptive, and beauty is fleeting; but a woman who fears the LORD is to be praised." (Proverbs 31)*

Nomenclature.

Where appropriate, the dimensions of quantities are given for clarity. SI units are used throughout. Quantities which are only quoted locally in the review sections are not included.

a	width or thickness
a_{fj}	adiabatically stable thickness
a_i	coefficient of flux line velocity in Wipf's theory
B	magnetic flux density, [T]
$\bar{B}$	average magnetic flux density across tube wall, $= (B_i+B_a)/2$
B_a	applied magnetic flux density
B_{c2}	upper critical field, [T]
B_{fj}	first flux jump field
b_i	coefficient of flux line velocity in Wipf's theory
B_i	magnetic flux density in enclosed volume of tube
B_M	magnetising applied flux density
B_o	expansion coefficient of $J(B)$ in critical state model
B_{sh}	maximum shielded flux density of tube
B_{tr}	trapped magnetic flux density
c	heat capacity, [JK^{-1}]
C	specific heat, [$Jkg^{-1}K^{-1}$]
C_{eff}	effective specific heat, [$Jkg^{-1}K^{-1}$]
d	thickness of shielding layer
D_M	magnetic diffusivity
D_{TH}	thermal diffusivity
E	electric field
f	function measuring steadiness of temperature distribution

F	force (density)
F_L	Lorentz force
F_P	flux pinning force
H	magnetic field strength, [Am^{-1}]
$\tilde{H}$	average magnetic field strength across tube wall, $= (H_i+H)/2$
H^*	magnetic field at which a slab is penetrated to centre
H_{c1}	lower critical field
$H_{c1}{}^G$	lower critical field of grains
H_{c2}	upper critical field
H_{fi}	magnetic field limit for full stability (Wipf's theory)
H_i	magnetic field in enclosed volume of tube
H_{sh}	shielded magnetic field of tube
I	electric current
J	current density
J_c	critical current density
k_B	Boltzmann constant, $\simeq 1.38\times10^{-23}$ JK^{-1}
M	magnetisation, [Am^{-1}]
M^+	magnetisation in positive region of loop
M^-	magnetisation in negative region of loop
M_o	initial remanent magnetisation
p	penetration depth
q	heat energy
Q_s	heat applied to slab (adiabatic theory)
r	radial variable
r_p	range of pinning potential
R	mean radius of tube
s	displacement
t	time variable
t_o	initial time
T	temperature
T_c	critical temperature
T_F	final temperature reached in flux jump

T_o operating temperature

u_B magnetic energy density

U_B magnetic energy

U_o ideal flux pinning energy

v flux line velocity

v_{dr} flux line drift velocity

V volume

w tube wall thickness

x distance variable

x_o magnetic flux penetration distance prior to flux jump

α expansion coefficient of $J(B)$ in critical state model, [ATm^{-1}]

β coefficient of T^3 in specific heat temperature dependence

γ density

δ indicates incremental quantity

Δ indicates change in quantity

η "viscosity" of flux movement

θ opening angle of tube

κ thermal conductivity

μ_o permeability of free space, $= 4\pi \times 10^{-7}$ Hm^{-1}

ν flux line hopping frequency

ν_o attempt frequency

ξ_o coherence length

ρ_f flux flow resistivity

ρ_N normal state resistivity

Φ magnetic flux

T_g glass transition temperature (Appendix 1)

T_m melting temperature (Appendix 1)

T_x crystallisation temperature (Appendix 1)

1 Introduction.

1.1 High temperature superconductors: discovery and possibility.

Following the discovery of superconductivity above 77K in 1987[1][2], there was an almost unprecedented rush of interest and expectancy, both scientific and popular. It was soon found however that these high temperature superconductors (HTS) were severely limited in their performance, and optimism was replaced by a degree of pessimism. Recent advances have redressed the balance so that goals and possible applications are viewed with an optimistic realism. Other ceramic HTS have been found in addition to the original $YBa_2Cu_3O_{7-x}$ ("YBCO 123", where the numbers refer to the cation ratios, $T_c \simeq 93K$), most importantly those of the Bi-Sr-Ca-Cu-O[3] (BSCCO 2201, $T_c = 10K$; 2212, 80K; 2223, 110K) and Tl-Ba-Ca-Cu-O[4] (with similar phases to BSCCO, $T_c = 110\text{-}125K$) families, each with their own particular potential areas of applicability. Many of the problems with HTS materials arise in the fabrication process because they are ceramics, and hence have a brittle, granular structure. Nevertheless, many small-scale applications have been realised, and HTS microwave components and antennae are already available off the shelf. Medium-scale prototypes have been built to demonstrate the use of HTS in energy storage, magnets and large current-carrying capacities, with relative success.

1.2 Limiting factors in HTS materials.

Two issues quickly became obvious in the development of HTS, those of critical current density and flux creep[5]. As already noted, early results were disappointing for the applications of HTS where high critical current is important. To be

comparable at 77K to "conventional" low temperature superconductors (LTS) such as Nb-Ti and Nb_3Sn operating around 4.2K, HTS require a critical current density $J_c \geq 10^6 Acm^{-2}$. Critical transport currents of early sintered samples of YBCO were around $10^3 Acm^{-2}$, and $10^4 Acm^{-2}$ for melt-grown samples, despite an intrinsic critical current on the order of 10^5 to $10^6 Acm^{-2}$ within the superconducting grains[6]. Thus the control of granularity is seen to be fundamental to bulk HTS development; much higher critical currents are observed in thin films.

In the granular system of a polycrystalline HTS the transport current must flow across weak-link Josephson-type junctions between the grains, limiting the intergranular (transport) J_c, despite the high intragranular J_c. This is accentuated by the very short coherence length of HTS ($\xi_o < 100Å$), so that even small grain boundaries have a deleterious effect on transport current. The weak-link grain boundaries lead to a highly magnetic field-dependent critical current, decreasing around an order of magnitude in 10mT at 77K[6]. Much effort has concentrated on improving and controlling HTS microstructure with grain orientation (the grain properties are highly anisotropic), melt-texturing and grain growth.

Flux creep strictly occurs at all temperatures in a superconductor (the detailed theory will be described in 3.2), but in HTS at elevated temperatures does so in a massive way. Unless the flux lines can be effectively pinned, the Lorentz force between the transport current and the flux lines causes the latter to move, generating a voltage and dissipating energy. Flux lines are pinned by inhomogeneities in the superconductor: inclusions, voids, dislocations, *etc.* However, because of the small coherence length, such inclusions must be very small to act as effective pinning centres. Twin boundaries within grains are known to act as pinning sites, and finely-dispersed inclusions such as the non-superconducting phase Y_2BaCuO_5 (YBCO 211) in YBCO have shown great improvements. Flux creep is particularly a problem in BSCCO, where it is very fast above 30K; below this both flux pinning and $J_c(B)$ are much enhanced.

1.3 Prospects for HTS: magnets and large-scale applications.

The possibility of HTS magnets and conductors operating at 77K is undoubtedly attractive, with the associated economies of scale and refrigeration. It is clear, given the conditions described above, that much more effort is required to realise such devices, and goals have changed to accommodate the strictures of working with these materials. Not only the electrical and magnetic, but also the mechanical properties of the material in question are of importance: the superconductor has to be made into wires or tapes and wound in a suitable form, and must be able to withstand the stresses generated by the magnet's field. Since ceramic HTS are so brittle, the majority of wires produced have been of the "wind-and-react" variety. Because of the weak-link nature, the wire is only as good as the weakest link along its length, making the production of long lengths very difficult.

The greatest success so far has been with Ag/BSCCO wires and tapes using the "powder-in-tube" method, in which BSCCO (2212 or 2223) powder is compacted into a silver tube, which is then successively drawn to small diameters (1-2mm) and rolled or pressed into ribbons ($\sim$0.1mm thick by 3mm wide) to make tapes. Multifilamentary tapes can also be produced by such a method. The composite HTS-metallic conductor structure serves a number of purposes: the conductor provides a parallel current path in case of failure in the HTS; Ag is chosen for its low reactivity with the HTS. The metallic sheath also conducts heat, which will be seen to be important when designing for stability in magnets, and gives mechanical and atmospheric protection.

The rolling process may be repeated several times, with intermediate sintering, to align the grains with the preferential superconducting plane parallel to the conduction path, with low-angle grain boundaries, significantly improving J_c. Various partial melting and directional solidification techniques are also used. Critical currents for such wires at 77K have been achieved in the range of 30 000 to 47 000Acm^{-2} in 0T,

and 6 000 to 11 000Acm^{-2} for 1T parallel to the tape. However, for magnetic fields applied perpendicular to the tape, practically no current is found above 1T[7]. The high field-dependence of J_c is well-known around 77K, but is very much reduced at low temperatures, close to 4.2K, even for fields over 20T. This behaviour suggests the high level of thermally-activated flux creep to be the reason for the $J_c(B)$ deterioration rather than the weak-link structure. Thus unless flux pinning can be improved, BSCCO materials are likely to be limited to operation below 30K. The major flux-pinning advances have been made in YBCO which has a higher J_c than BSCCO at 77K, but lower at 4.2K, and is much more difficult to make into wires. The continued development of HTS wires is essential, not only for magnets, but also motors, generators, energy storage and a range of large-scale applications.

A possible alternative to the powder-in-tube methods is the glass-ceramic approach for BSCCO[8], in which the precursors are quenched to a glass, from which fibres may be drawn in a similar process to that for optic fibres. The wound fibres can then be heat treated to grow the appropriate superconducting phase[9]. This has many advantages, although only moderate success has been achieved so far. An investigation into glass-ceramic BSCCO superconductors is described in Appendix 1.

A number of small HTS magnets have been constructed using Ag/BSCCO wire and tape[10][11][12][13], operating mainly below 30K. These have used liquid helium (LHe) or neon (LNe) as refrigerants, although Ne is expensive and cannot currently be obtained in liquid form in the UK at least, requiring it to be condensed from gas; pressurised LHe may be an alternative for LNe temperatures. A second possibility for cooling is the use of closed-cycle refrigerators, eliminating the need for liquid cryogens and increasing efficiency and reliability. Recent advances make such systems a viable and attractive option[14], especially for the 20-30K range in which BSCCO properties might be optimised. Based on recent design studies, HTS magnets may be used to generate fields up to around 5T, or as inserts to LTS magnets to generate very high fields of 20T and above[11].

A useful comparison of some relevant issues may be made between LTS at 4.2K and HTS operating in the 20 to 80K range[11]:

	LTS *vs.* HTS
Achievable field	approximately same
Mechanical requirements	approximately same
Stability	much easier in HTS
Coil protection	much more difficult in HTS

1.4 Flux tubes: an alternative magnet design.

A suggested alternative to the use of wire-wound HTS magnets to generate high magnetic fields is that of the "flux tube": a macroscopic HTS component in a tubular geometry. This circumvents the fabrication difficulties of HTS wires, and high magnetic fields could be produced by flux pumping[15]. Such methods have previously been studied for LTS[16], although flux jumping limited the fields which could be generated[17]. As will be seen, the limits on HTS, particularly at higher temperatures, are much less strict. It has been shown that higher fields can be trapped in a solid tube than a solenoid configuration[18].

Other uses of superconducting tubes include magnetic shields, which are less reliant on high critical currents. A number of studies of magnetic shielding have been made[19][20][21][22][23], and the particular properties of tubes have also been used to extract magnetisation and critical current information for HTS[24][25][26].

1.5 Research aims and method.

Among the parameters to be considered in designing superconducting magnets is that of magnetic stability or flux jumping, and it is upon this issue that the following work concentrates. In the flux jump process large amounts of magnetic flux move through the superconductor in a short time, dissipating large amounts of energy which may lead to the whole superconducting magnet undergoing a transition to the normal state. A fuller qualitative description of flux jumping is given in Chapter 2, with the detailed theory and mechanism being outlined in Chapter 3.

Flux jumping is a well known phenomenon in high field type II superconductors, and as such has been extensively characterised for conventional LTS materials. Adiabatic theories such as will be described in Chapter 3 allow predictions of flux jumping, and hence stabilisation against it, and empirical dependencies for applied field sweep rate and temperature have been found. The usual stabilising solution of finely-divided filamentary superconducting wire is not a desirable one, and may not even be practicable with HTS; it is therefore important to know the limitations placed upon such bulk materials by flux jumping. It has been predicted that HTS are immune up to quite high fields at 77K; at 4.2K instabilities may begin to appear around 0.4T (see 2.4.1) and flux jumping must be considered in light of the possible high-field applications of Bi-based HTS at low temperatures.

Flux jumps have previously been observed in single crystal and melt-textured cuprate oxides in small samples, and these results are reviewed in 2.4.2. In the present study both $YBa_2Cu_3O_{7-x}$ and $Bi_2Sr_2CaCu_2O_x$ flux tubes (4.1) have been used to investigate flux jumping and other superconducting properties in these materials. The use of such a geometry allows the straightforward observation of these features in a bulk sample, as opposed to the small-sample measurements made to date.

Shielding and flux creep measurements were made on the HTS flux tubes by measuring the field inside the tube and the applied magnetic field. Magnetisation

curves can be derived from the field difference across the tube wall (see 3.1.2), and critical current values calculated from these and the shielding curves. By examining the occurrence of flux jumping in the magnetisation and shielding curves, the relationships with respect to field sweep rate and temperature can be established for HTS, and the theoretical predictions checked. In addition, measuring the temperature rises due to flux jumps will allow the estimation of specific heat data which may be further used in confirming adiabatic predictions.

2 Flux jumping: qualitative description and review.

In this chapter the phenomenon of flux jumping is qualitatively discussed, and the literature for both LTS and HTS is reviewed. The detailed theories of magnetic flux movement and flux jumping in particular will be outlined in Chapter 3.

2.1 The flux jump process.

The magnetisation of type II superconductors is described by the concept of "critical states". While this theory will be described in detail in 3.1, it may be stated briefly as being the state in which every macroscopic region of a superconducting sample carries the maximum current density, or critical current, determined only by the local magnetic field in that region. In an increasing applied magnetic field the superconductor moves from one critical state to another. As will be shown later, critical states are inherently unstable, and flux jump instabilities may occur when this movement between critical states becomes fast. This was quickly observed in the development of the critical state models considered in 3.1[27].

The flux jump process occurs when part or all of the superconductor sample experiences a temperature rise, allowing the rapid re-distribution of large amounts of magnetic flux. Such a rise in temperature may result from a fast change in magnetic field (or other change in the Lorentz force) which requires the dissipation of energy, from mechanical shock, or directly from other outside influences. In extreme cases all of the sample may undergo a transition to the normal state.

To initiate a flux jump, enough thermal energy must be dissipated to depin the flux lines from their pinning centres (explained more fully in 3.2). Since this heat is usually generated by the viscous movement of flux lines, one can see that a positive

feedback situation can occur. Whether the thermal energy goes into depinning flux lines or is simply conducted away depends on the thermal conductivity and heat capacity of the superconductor. Materials with low thermal conductivity, low heat capacity and low density are the most vulnerable, showing flux jumping to be an intrinsic materials property. For high rates of magnetic field change there are correspondingly high rates of heat generation which may be greater than the energy loss via conduction, *etc.* in a given region.

In addition to viscous flux motion, heat may also be generated by the annihilation of flux lines of opposite signs[28]. This happens when magnetic flux of the opposite sign to that trapped in the superconductor begins to penetrate the sample. The energy released in annihilation is enough to depin some of the neighbouring flux lines, generating further heat through viscous movement. This type of flux jump initiation has been observed experimentally in LTS[29].

Flux jumps may be observed as sharp drops in the shielding or magnetisation curves of a sample. Following a complete jump, the magnetic field inside the superconductor is equal to the applied field, the sample temperature having exceeded T_c and all the stored magnetic energy being lost. For the case of a partial flux jump, stability is recovered by thermal conduction, *etc.* before all the flux in the sample is lost. The shielding curve shows a sharp drop in trapped or excluded field over a very short time, followed by a plateau at which the flux remains constant until the equilibrium curve is reached (Figure 2.1). In a magnetisation curve, the jump is followed by an increasing magnetisation, parallel to the virgin penetration curve; the heating produced in a flux jump may be observed as a sharp increasing spike in the sample temperature. In brittle LTS materials a large-scale flux jump can in fact cause severe mechanical damage, or even disintegration of the sample, due to the large amounts of energy moving on a short timescale (Figure 2.2). HTS are also very brittle and mechanical support is more difficult, so flux jumping must be carefully considered in the mechanical as well as superconducting design of a magnet, *etc.*

The most common parameter by which a material's stability is characterised is the flux jump field, B_{fj}, at which instabilities first occur. This will be derived fully in 3.4, but is stated here to make the following discussion of various materials clear. Two equivalent forms of the equation can be obtained[30][31]:

$$B_{fj} = [3\mu_o \gamma C(T_c - T_o)]^{\frac{1}{2}}$$

$$B_{fj} = [3\mu_o \gamma C \frac{J_c}{\partial J_c / \partial T}]^{\frac{1}{2}}$$

where γ is the density and C the specific heat. Adiabatic conditions are assumed in the analysis, usually a good approximation.

2.2 Review of flux jumping in LTS.

Flux jumping was quickly recognised as a problem following the discovery of high-field type-II superconductors[32]. Prior to the discovery of such materials (alloys such as Nb_3Sn, Nb-Zr, Nb-Ti), superconductivity had remained an esoteric curiosity of low temperature physics for almost half a century since its discovery in 1911 by Kamerlingh Onnes. The poor prospects for application were due to the low critical fields of the then available materials. The advent of high-field superconducting alloys led to a much greater interest, both experimental and theoretical.

Following Bean's phenomenological theory of flux penetration[33], the highly influential work of Kim *et al.* (1962, 1963) also brought to light the existence of what they called "flux jumping"[34][27]. This was done with Nb_3Sn and Nb-Zr hollow tubes in which the field inside the tube and the applied field were measured to obtain shielding curves. The tubular geometry provided a simple measurement method, and was also of practical interest at the time, following the suggestion of flux compression in such geometries by Swartz & Rosner[17].

Subsequent studies quickly derived empirical dependencies for a number of quantities. Goldsmid & Corsan (1964)[35] found flux jumping to be absent in Nb_3Sn tubes with applied field sweep rates up to $4kGmin^{-1}$ and noted the importance of this and thermal effects. Corsan (1964)[36] made systematic measurements of the effect of sweep rate in Nb_3Sn solid cylinders, also observing large amounts of heating due to flux jumps. Later measurements of sweep rate dependence were made by Lange (1965)[37] in Nb_3Sn tubes, Wipf & Lubell (1965)[38] in Nb-Zr cylinders and Watson (1966, 1967)[39][40] in In impregnated glass, the latter two being the most complete. These results are treated fully in 3.6. Lange also considered the effects of temperature, finding that there existed a boundary temperature for a given sweep rate above which flux jumping did not occur, and of current density. It was observed that there was an increased tendency to jumping with increasing current density (*i.e.* lower temperature and improved sample quality), and that improved thermal conductivity also reduced the tendency.

A number of other authors studied various aspects of flux jumping. Evetts *et al.* (1964)[29] in Pb-Bi cylinders, found the two mechanisms responsible as described in 2.1. While most studies reported jumps in shielding curves, Carden (1965)[41] observed the resulting discontinuities in the magnetisation loops of Nb-Zr and Nb_3Sn wires and cylinders. Incomplete, or partial, flux jumps were observed by Smith *et al.* (1965)[42], those previously reported having been complete jumps. They found that the effect of sweep rate was smaller for the sample in He gas than in liquid, and that the jumps were more closely spaced in gas. Since flux jumping prevented establishment of the full critical state in their Nb_3Sn tubes, Smith *et al.* suggested the use of concentric cylinders such that the current would flow across the whole width of each cylinder, also improving cooling. Such suggestions of sub-division of the superconductor may be considered to precee later solutions to flux jumping based on a complete theory, and the need for such a theory based on thermal qualities is indeed noted. The fact that flux jumping is determined by macroscopic parameters rather than individual pinning configurations is noted by such authors as Morton (1968)[43] investigating Nb-Zr and Nb_3Sn tubes. The speed with which flux jumps proceed

through Nb discs was measured by Goodman & Wertheimer (1965)[44] using a high-speed camera technique to observe the flux fronts.

A simple criterion for stability against flux jumping was derived by Hancox (1965)[45] in analysing a Nb_3Sn cylinder. Following an early theory proposed by Swartz & Bean (1965)[46], Neuringer & Shapira (1966)[47] discussed their results for Nb-Zr cylinders, particularly noting the reproducibility of flux jump positions and a decreasing jump spacing with decreasing temperature. They derived an equation for instabilities to occur, based on an adiabatic assumption, and noted that a comparison of the thermal and magnetic diffusivities could determine the validity of such an assumption. For high fields, the flux line diffusion time was short compared to thermal diffusion and long compared to magnetic relaxation, justifying adiabaticity.

Major progress towards a complete theory over the various stages of instability was made by Wipf (1967)[48] using a force-balance approach which will be discussed in detail in 3.3. Yamafuji *et al.* (1969)[49] developed Wipf's theory further to include a number of external variables explicitly, also taking in the annihilation instability region. These were largely superseded by the adiabatic theory of Swartz & Bean (1968)[31], which has been used almost universally since as the main basis for predicting and analysing flux jump instabilities. A derivation of the Swartz & Bean result is detailed in 3.4.

Subsequent to these theoretical developments very little was published on flux jumping, now much more regarded as a solvable engineering problem than a physics research interest. The nature of the solution will be outlined below, centring mainly on the use of filamentary superconducting wires to achieve stability. A very complete study of these was published by Wilson *et al.* (1970)[50]. Later studies of the field are those of Akachi *et al.* (1981)[51] in which a diffusion theory for instabilities in Nb-Ti cylinders was developed, and of Mints & Rakhmanov (1981)[52], a broad review of flux jumping in superconducting composites under varying conditions.

2.3 Methods of stabilisation.

2.3.1 Cryostability and quench protection.

Although a small normal zone may contract and disappear if heat is conducted away faster than it is generated, this is not likely to be sufficient for large disturbances, and improved heat conduction and transfer must be arranged. The solution of cryostability is to have a parallel normal conductor, in good contact with the superconductor, which will provide a parallel current path, sharing the current with the normal zone. The heat generated in the stabiliser, which will have a higher thermal conductivity than the superconductor, is transferred to the cryogen. For a given heat generation rate, heat transfer coefficient and operating and critical temperatures, a cryostable geometry can be deduced.

The improved overall thermal conductivity gives protection in a quench, when the whole magnet goes normal. To avoid damage to the coil, heat should be removed as quickly as possible to minimise local temperature rises due to ohmic heating, which otherwise could burn out the winding. This ability to remove heat and have a normal zone spread quickly is quantified as the quench propagation velocity. In addition to the above passive protection method, other active techniques are sometimes used.

2.3.2 Adiabatic stability.

A parallel solution to cryostability is that of adiabatic stabilisation. This deals directly with the prevention of flux jumping and is derived from the adiabatic theory of Swartz & Bean[31]. If the superconductor is fully penetrated before the first flux jump field, then flux jumping is eliminated. In high-J_c LTS materials this is achieved by fine sub-division of the superconductor into filaments of around 100μm. The critical size is called the adiabatically stable thickness, a_{fj}, the half-width below which a slab

is self-stable against flux-jumping. Since single 100μm wires are not practical, and would need too many windings for high fields, a large number of such strands are embedded in a copper matrix (providing cryostability) to produce a multifilamentary composite conductor.

2.4 Flux jumping in HTS.

In this section the predicted and experimental flux jumping properties of HTS are reviewed. Numerical values are widely quoted to facilitate comparison with those obtained in this work.

2.4.1 Stability predictions for HTS.

The possibility of using HTS materials in magnets was one of the very obvious ideas widely discussed following their discovery. As a direct replacement for LTS considerable economies in scale and cost could be achieved. Thus the criteria for HTS magnet stability came to be examined, even before HTS wires or suitable current densities were available. Since the fabrication difficulties posed by such brittle material were quickly recognised, the limits placed on magnet conductor geometries by stability criteria were of great interest in establishing what form of conductor would be necessary.

Iwasa (1988)[53] found that HTS tapes up to about 10mm wide should be stable for a magnet operated adiabatically, but also noted that some form of active quench protection would be necessary since the propagation velocity of a normal zone in HTS is extremely slow, rendering self-protection impossible. Wipf (1988)[54] also discusses a number of stability issues. The first flux jump field at 77K is predicted to be an order of magnitude higher that for LTS at 4.2K, allowing non-filamentary conductors to be stable; for a conceptual 123 HTS with $10^7 < J_c < 10^9 \mathrm{Am}^{-2}$ the

adiabatically stable thickness is $600 > a_{fj} > 6$mm. This is attributed to the high specific heat at high operating temperatures T_o, and the higher operating margin T_c-T_o. Figure 2.3 shows Wipf's plot of $B_{fj}(T)$. The data suggests that tape conductors 5 to 10mm wide would be adiabatically self-stable. The idea of using HTS solid cylinders as "permanent" magnets which would perform better than the best present ferromagnets may be feasible. Wipf also discusses cryostability which, being the more conservative stability criterion, demands the use of stabilising material. Here again HTS is more stable and requires less stabiliser than LTS. Quench protection is again noted to be poor compared to LTS.

A thorough study of various factors affecting stability is given by Laquer *et al.* (1989)[55], finding that B_{fj} peaks at 60K and 7 ± 2T for $T_c \sim 90$K, and at 75K and around 12T for $T_c \sim 120$K. The adiabatically stable thickness is plotted as a function of temperature, increasing two orders of magnitude from ~ 5 to 85K. The quench propagation velocity is predicted to drop 4 or 5 orders of magnitude from 5 to 80K, being very low at high temperatures. It is suggested that the whole area of quench protection may need re-thinking for HTS. Although more stable against quenching, if such a quench should occur then propagation is so slow as to make burn-out of the winding highly likely. The high stability is attributed to the same causes as above. In a companion paper, Wipf & Laquer (1989)[56] reconsider the possibilities for superconducting "permanent" magnets using flux trapped in cylinders or tubes. As was seen in 2.2, such methods using LTS were frustrated by the low flux jump fields of bulk samples. It is proposed that a 90K superconductor with $B_{fj}=6$T should be able to trap 3T, five times better than the best permanent magnet materials. Replacing wound electromagnets with bulk flux-trapping structures would bypass fabrication difficulties and avoid current-carrying normal-superconductor contacts.

Collings (1988, 1989, 1990)[57][58][59] considers a wide range of flux jump and cryostability influences. For a 90K superconductor operating at 80K, $B_{fj}=5.24$T is derived; the adiabatically stable diameter of an isolated filament is found as 8.68cm, compared to 4.65×10^{-2}cm for Nb-Ti[57][58]. For a fully cryostable HTS operating around in liquid nitrogen 30% more copper stabiliser is needed compared to

Cu/Nb-Ti at a given current load[57][58]. A later paper[59] obtains values at 4, 20 and 80K which may be summarised as:

	4K	20K	80K
B_{ff} (T)	0.4	4.2	5.5
Quench field (T)	10.0	9.9	5.1
Adiabatically stable filament diameter (mm)	0.7	6.8	83.0
Adiab. self-field stable dia. (mm)	1.9	19.0	255.6

The self-field stability is considered as that relating to an isolated current-carrying conductor with no additional external field.

In a series of papers concerned with design issues for HTS conductors, Ogasawara (1989)[60] found values for a_{ff}: $a_{ff}(77K)=4.95mm$ ($J_c=10^9 Am^{-2}$), $a_{ff}(20K)=0.40mm$ ($J_c=10^{10} Am^{-2}$), contrasting these with Nb-Ti and Nb_3Sn, $a_{ff}(4.2K) \sim 100\mu m$. Dynamic stability (which has the same basis as adiabatic but also takes in thermal and magnetic diffusion and heat transfer to the cryogen) is discussed in light of the low thermal conductivity, noting that in LTS the approximate equality of dynamically and adiabatically stable dimensions is fortuitous, and that elevated temperature operation makes dynamic stability the much more stringent condition. It is concluded that a stable conductor would be a composite YBCO/Cu tape or a multifilamentary composite with a Cu matrix.

A recent study by Iwasa (1992)[11] examines these issues based on properties of recent Bi(Pb)SrCaCuO short samples. Stability is discussed in terms of the "stability margin", e_m, the energy required to raise the conductor from the operating temperature T_o to the current-sharing temperature T_{cs} at which current begins to flow in the stabilising material, generating heat. The stability margin is given by

$$e_m = \int_{T_o}^{T_\alpha} C_{wd}(T)\,dT$$

where C_{wd} is the winding heat capacity. For a notional 4.5T HTS magnet at 20K, e_m=4500kJm^{-3}; for 22T at 4.2K (*e.g.* as a high-field insert to a 17T LTS magnet), e_m=105kJm^{-3}. These are very favourably compared to e_m=1.5kJm^{-3} for a Nb_3Sn 4.5T magnet at 4.2K, although the need for active coil protection is reiterated. Since HTS tapes and wires have become more widely available, such stability projections based on real material parameters will provide greater insight and guidance as HTS magnets move from being a possibility to a reality. Some of the predictions above are included in a review of flux jumping in HTS by Wipf (1991)[61], which also includes a number of experimental studies which are among those reviewed in the next section.

2.4.2 Review of HTS experimental data.

Flux jumping has been observed in a number of HTS compounds, for both single crystal and polycrystalline samples. The first observation was that of Levet *et al.* (1988)[62] in large YBCO single crystals, with flux jumps present in magnetisation measurements up to 18T, below 15K. The jumps were found to be periodic, between two magnetisation "envelope" curves. Measurements were performed in both liquid helium (LHe) and a helium exchange gas, showing that the amplitude of the jumps depended on both the sample size and cooling efficiency (jumps in LHe were smaller), and to a lesser extent on applied field variation rate. Since the jumps lowered the attainable J_c by a factor of two, the need for stabilisation is pointed out.

A subsequent paper by the same group, Tholence *et al.* (1988a)[63], reports similar measurements at 1.2, 4.2, 7.0K and higher with the field parallel to the crystallographic *c*-axis ($B_a \parallel c$) and perpendicular ($B_a \perp c$). The number of jumps increased with decreasing temperature T, and no jumps were present above 15K for $B_a \parallel c$. In the case of $B_a \perp c$ the jumps were greater in number and more closely

spaced, disappearing above 7K. Similar conclusions to Levet *et al.* are reached, and the limiting influence of flux jumping on J_c is suggested as a possible reason for the large differences between single crystals and the better thermalised thin films. Guillot *et al.* (1988)[64], again of the same group, report like results, also finding that jumps were slightly larger and more widely spaced for field variations of $0.0015 Ts^{-1}$ than for $0.03 Ts^{-1}$ at 4.2K. Smaller jumps were observed in a small $HoBa_2Cu_3O_7$ single crystal, further suggesting that the amplitude of jumps increases with crystal size and decreases with improved thermal contact (in LHe), depending also on the field rate and waiting time between measurements.

Melt-processed YBCO samples were examined by Chen *et al.* (1990)[65] in fields up to ± 5.4T. With $B_a \parallel c$ jumps were observed all around the magnetisation loop at 5K; at 7.5K the jumps were wider spaced, and only one jump was observed in either half of the loop at 10K, none being present at 20K. The number of jumps at 5K decreased when the measuring time was lengthened, and hardly any jumps were observed for $B_a \perp c$. Hsu *et al.* (1990)[66] found reproducible jumps in magnetisation curves at 5, 7.5 and 10K in the same material, with closer spaced jumps at lower T. The effect of field sweep rate was also considered, finding fewer jumps at 5K for $0.17 Tmin^{-1}$ than for $0.34 Tmin^{-1}$, $B_a \parallel c$. Only one jump was found at 5K, $0.34 Tmin^{-1}$ for $B_a \perp c$; the number increased at $0.68 Tmin^{-1}$, predominantly in the field-increasing region. These results are also summarised in a related paper by Wang *et al.* (1991)[67].

The effect of field sweep rate and relaxation time between measurements was investigated by Chen *et al.* (1991)[68]. Jumps were observed around the magnetisation loop to ± 5.4T at 5K for a sweep rate $S = 1.5 Tmin^{-1}$ and relaxation time $R = 30$s; the jump separation increased for $S = 1.2 Tmin^{-1}$, $R = 30$s. Only one jump was observed for $S = 1.2 Tmin^{-1}$, $R = 52$s and none for $R = 72$s. B_{ff} for various values of S and R are given as:

S (Tmin^{-1})	R (s)	No. of jumps in complete loop	B_{fj} (T)
1.8	30	12	3.3
1.5	30	10	3.4
1.2	19	8	4.2
1.2	30	6	5.2
1.2	40	4	6.1
1.2	52	2	7.1
1.2	72	0	-

The flux jump field is found as the field from maximum or minimum applied field at which flux jumping first occurs. At fixed S, B_{fj} was found to be linear with R. The temperature rise in the sample due to flux jumping was calculated as 32K. The sweep rate and relaxation time data suggests that instabilities may be avoided by increasing the magnetic relaxation or decreasing field variation rates such that the thermal diffusivity exceeds the magnetic diffusivity, conducting away heat impulses which would otherwise create flux jumps.

The high field magnetisation of melt-grown YBCO, up to 23T at 4.2K, was measured by Watanabe *et al.* (1991, 1992a)[69][70]. Flux jumps were found in increasing fields of 0.5Tmin^{-1} for both $B_a \parallel c$ and $B_a \perp c$, and the properties relating to adiabatic stabilisation at 4.2K are listed for a number of superconductors[68]:

	YBCO	BSCCO 2212	BSCCO 2223	Nb-Ti
Electronic specific heat, C_e ($mJcm^{-3}K^{-1}$)	1.41	0.193	0.091	1.95
γ_e ($mJmol^{-1}K^{-2}$)	35	24	14	10
T_c-T_o (K)	88	81	108	7
B_{ff} (T)	0.68	0.24	0.19	0.22

The results here suggest that fine filaments are needed for stable high-field YBCO applications at 4.2K: adiabatically stable filament diameters are given as $\sim 10\mu m$, $B_a \perp c$ and $\sim 80\mu m$, $B_a \parallel c$. Watanabe *et al.* (1992b)[71] also found that different magnetisation measurement methods, which led to differing flux conditions in the sample, gave different flux jumping results. Jumps were again observed in the 4.5-5K region, but none at 77K, up to 23T.

A ring-shaped melt-grown YBCO single crystal was examined by Takizawa *et al.* (1991)[72] in a pulsed magnetic field. The induced voltage in a search coil inside the ring showed a sharp spike during flux penetration, indicative of flux jumping. At 30K the spike appeared when the field was pulsed to a maximum of 0.6T in 15ms. At a maximum pulsed field of 0.69T the sharp spike disappeared above 40K. A stability condition for the ring geometry is derived using specific heat data, but shows poor agreement with the experimental values. Localised flux jumping is suggested as the reason for this, and the data is satisfactorily explained as such.

A number of studies have observed flux jumping in the BSCCO 2212 material: Guillot *et al.* (1989)[73] found jumps in preferentially oriented polycrystalline 2212 in magnetisation curves up to 20T at 4.2K and 10K. The large electromechanical strains produced by flux jumping are noted, these often being large enough to break the crystal. Kadowaki & Mochiku (1992)[74] observed a single, very large, jump in the decreasing field part of a single crystal 2212 magnetisation up to ± 5.5T at 5K.

The magnetisation of single crystal 2212 under very high field sweep rates was considered by Gerber *et al.* (1992)[75]. Flux jumping is regarded as a rapid process, on the order of milliseconds; here, however, it was found that jumps had a time duration of tens of milliseconds at $1Ts^{-1}$ up to hundreds of milliseconds for $5Ts^{-1}$. Gerber *et al.* also performed measurements on a $LaSr_2CuO_4$ single crystal at 4.2K. Jumps were present at 5 and $10Ts^{-1}$, but a strongly suppressed magnetisation with no jumps was found at $42Ts^{-1}$. Calculated values of B_{fj} are 0.86T at 25K and 0.11T at 4.2K. The periodicity of flux jumping was found to be well-defined by the field sweep rate, which also affected the flux jump size.

McHenry *et al.* (1992)[76] have studied a similar compound in a $La_{1.86}Sr_{0.14}CuO_4$ single crystal, and, in common with Chen *et al.*[68], have shown that flux creep may have a stabilising effect in HTS. The magnetisation at 2, 3, 4, 5, 6, and 7K shows jumps in the virgin curves up to 7K in applied fields up to 5T. At 2K the jumps are all incomplete, while at 3-5K the first jumps are nearly complete, with almost all the stored magnetic energy being lost. The jumps are regularly spaced, the number decreasing and spacing increasing with increasing T. No jumps were observed at 7K. A calculation of the temperature rise due to flux jumps confirms that nearly complete jumps raise T to $\sim T_c$, while for incomplete jumps $T < T_c$. The above measurements were taken at an average field rate of $0.24Tmin^{-1}$; since the field is in fact raised stepwise, with a pause for measurement, the inequivalence of such an average to a true sweep rate is emphasised. The pause between steps allowed relaxation through flux creep, and this appeared to aid stability. B_{fj} was significantly affected by the time between steps, the number of jumps decreasing with field rate, with no jumps at the slowest of $0.06Tmin^{-1}$. Adiabatic calculations indicated $B_{fj} \sim 0.075T$ at 5K, around 15 times smaller than that observed. This suggests that adiabatic theory is inadequate here, although consideration of the magnetic and thermal diffusivities suggested that adiabatic conditions did indeed prevail. Thus it is concluded that flux creep between field steps leads to a sub-critical state prior to the next step, stabilising fully or partially against flux jumping.

Other HTS compounds investigated include $HoBa_2Cu_3O_7$, by Tholence *et al.* (1988b)[77], in which jumps were observed at 4.2K in magnetisation curves up to 18T, in a similar way to Guillot *et al.*[64]. Durmeyer *et al.* (1990)[78] found that no jumps occur in the initial magnetisation region (1st quadrant) of $LiTi_2O_4$ up to 1, but that jumps occurred in field decreasing regions (2nd and 4th quadrants) and were closely spaced in the 3rd quadrant reversed field region. The pattern was highly reproducible around subsequent loops, with equal numbers of jumps in the 1st and 3rd quadrants on the second and following cycles. More small instabilities appeared in the 1st and 2nd quadrants at 2K, between an outer unstable envelope and an inner stable envelope in the magnetisation. The jumps disappeared at 7K, and were found to depend strongly on sweep rate and waiting time between measurements. Flux jumping has even been observed in the organic superconductor κ-(BEDT-TTF)$_2$-Cu(NCS)$_2$ (T_c=10.4K) by Swanson *et al.* (1990)[79]. The jumps were found at 40mK in the magnetisation to 4T at $0.4Ts^{-1}$ and $0.13Ts^{-1}$. They were no longer visible at 0.9K, and the amplitude and spacing of the jumps decreased with faster field sweep rate. Although large flux creep steps in a BSCCO 2223 superconductor were attributed to flux jumping by Cao Xiaowen & Huang Sunli (1989)[80], these are not in fact flux jumps as conventionally defined[61] or described here.

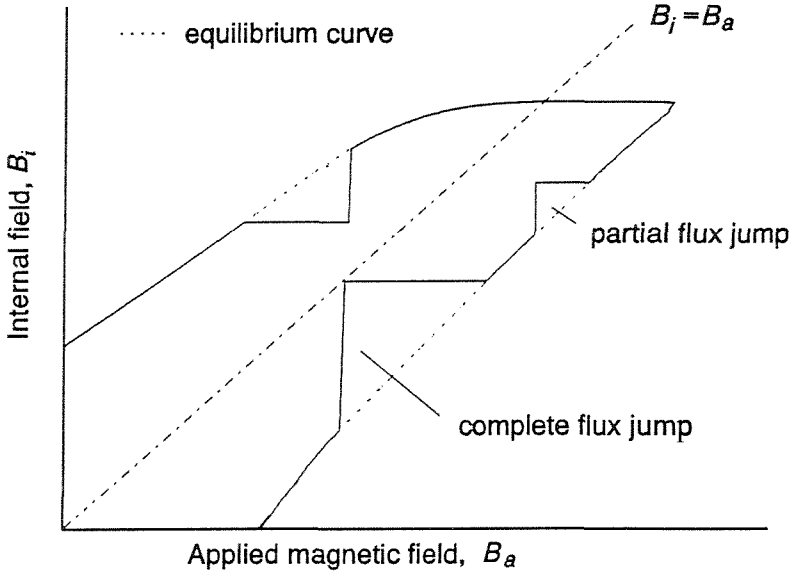

Figure 2.1 Flux jumps in a shielding curve.

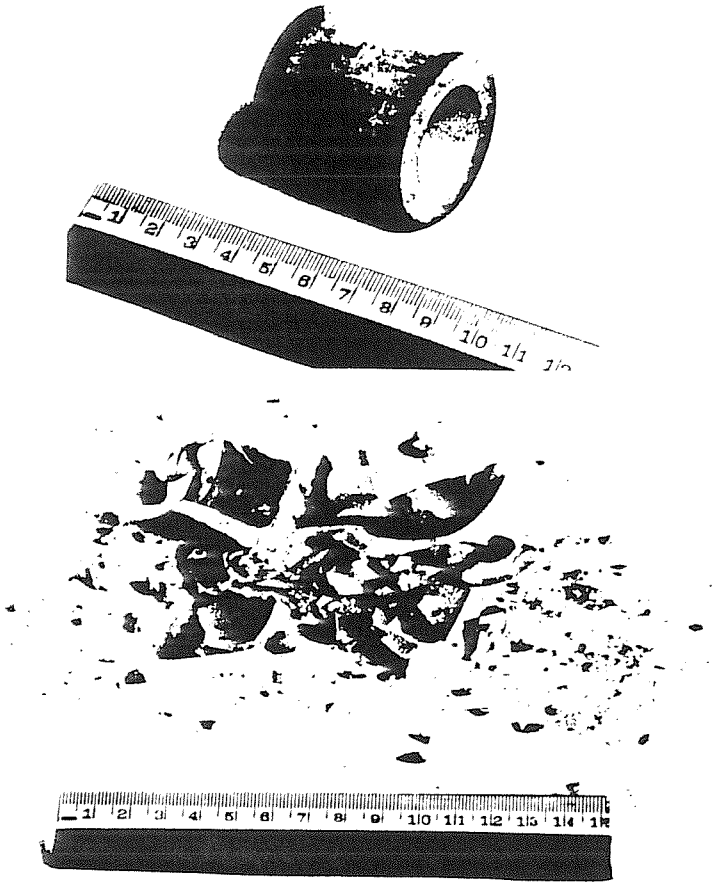

Figure 2.2 Nb_3Sn tube before (top) and after (bottom) catastrophic flux jump. Taken from Ref. 56 (©1989 IEEE, used by permission).

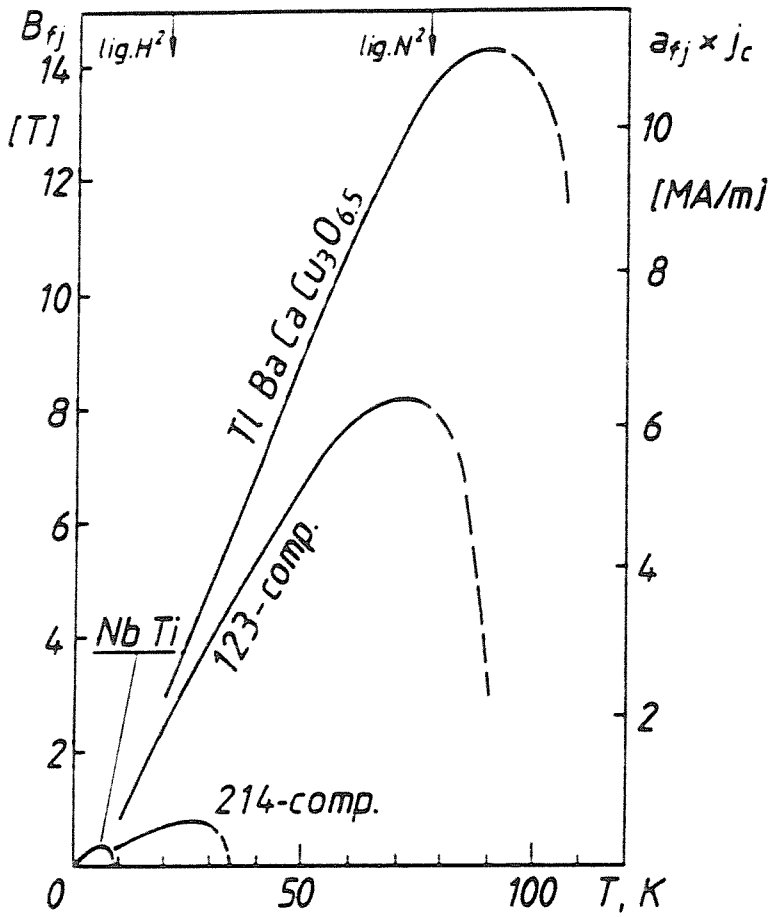

Figure 2.3 Plot of first flux jump field B_{fj} against temperature for HTS materials and Nb-Ti by Wipf[54] (by permission of the publishers, Butterworth Heinemann Ltd. ©1988).

3 Theory.

3.1 Critical state models.

The macroscopic magnetic behaviour of type II superconductors may be characterised by phenomenological "critical state" models. These are extremely useful for HTS since a satisfactory microscopic theory does not yet exist. There are a number of variants of the critical state model, those of Bean[33][81], Kim *et al.*[27][34], and new models developed specifically for HTS. From their simple nature they provide a clear conceptual framework in which to describe magnetic flux in superconductors.

The quasi-microscopic theory of flux penetration shows that magnetic flux enters the superconductor in quantised flux lines, or vortices; the penetration begins at the lower critical field H_{c1} and is completed at the upper, H_{c2}. The magnetic flux and electric currents in the superconductor between these two fields - the mixed state - are described by the aforesaid models.

3.1.1 The Bean model.

The starting assumption of the Bean model[33][81] is that there exists a macroscopic current density J_c, an upper limit to the current which may flow losslessly in the superconductor, and that an induced electric field of any magnitude will cause a current equal to J_c to flow in that locality. This critical current density is assumed independent of local field B; this is equivalent to assuming the external field H is not close to H_{c1} or H_{c2}.

When a magnetic field H is applied parallel to a semi-infinite superconducting slab, an electric field is induced, and thus currents flow in the surface of the slab which

try to screen H from the interior. For the first increment of field ΔH, a screening current greater than J_c is induced. Since a lossless current greater than J_c cannot be sustained, the screening current decays resistively to J_c, whereupon decay ceases. The resistive decay allows the external field to penetrate to a depth p. A further identical increment ΔH allows penetration to a depth $2p$. From Maxwell's equation $\nabla \times \boldsymbol{B} = \mu_o \boldsymbol{J}$ and $\boldsymbol{B}=\{0,B_y,0\}$, we find a linear field profile in the superconductor as shown in Figure 3.1, where $dB_y/dx = \mu_o J_c = \mu_o \Delta H/p$. In equilibrium, oppositely directed current sheets flow at J_c to a depth $p(H)$ on either face of the slab. (The field exclusion up to H_{c1} is not shown in the Figure for simplicity, and the model assumes $H \gg H_{c1}$.)

At $H=H^*$ the field profile reaches the centre of the slab (Figure 3.2a), and the current flows at $\pm J_c$ across either half of the slab (Figure 3.2b). Above $H=H^*$ the field profile does not change while H is not close to H_{c2}. Although J_c is independent of local field B, it is nevertheless a function of external field H. Thus for increasing H the gradient of the internal field profile will decrease, eventually becoming zero at H_{c2} (Figure 3.3). In summary, Bean's model states that, in equilibrium, currents flow at either J_c or zero across the slab with a linear field profile dB/dx.

An identical mechanism operates in the flux trapping regime, and the model gives the maximum trapped field $B_{tr}=\mu_o H^*$. The consequences of complete and incomplete penetration for flux trapping are illustrated in Figure 3.4a,b. B_{tr} is maximised when the slab has been penetrated such that $H \geq 2H^*$, the trapped field for H decreasing from $H=H^*$ being much less (the trapped field is proportional to the area under the field profile). In granular HTS the above applies not only to the bulk material, but also to the individual grains, and therefore care must be taken to obtain the maximum B_{tr}; this is usually attained by field-cooling the sample since HTS are known to have a high intrinsic (granular) H_{c2}.

The preceding description of flux penetration and trapping is similarly applied to a tubular geometry, where the field profile in the non-superconducting enclosed volume will always be flat, and the field in that volume, H_i, will be equal to that at the inner

radius of the tube wall. The enclosed volume is totally screened from the external field up to a value $H=H_{sh}$, the maximum shielded field (Figure 3.5). At H_{sh} the critical current density J_c flows across the entire width of the tube wall. Above H_{sh}, H_i increases until complete penetration gives $H_i=H$. Flux may be trapped in the enclosed volume of the tube, in which case, for $H=0$, J_c flows in the opposite sense to the shielding region. For an ideal tube in the Bean model, the maximum trapped field is $H_{tr}=H_{sh}$.

3.1.2 Kim *et al.*: the critical state.

The model of Kim *et al.*[27][34] is a generalisation of the Bean model in which the "critical state" is defined as that wherein a critical current density $J_c(B)$ flows in every macroscopic region of the superconductor, dependent only on the local field B in that region. In general J_c is a decreasing function of B, so that once a critical state is reached further increases of H tend to reduce J_c since the mean field in the sample increases.

This model is based on experiments with hollow superconducting tubes, where $H_i(H)$ is measured. Reproducible and predictable curves of $H_i(H)$ are found for H and H_i close to their equilibrium values (*i.e.* low $\dot{H}$). A magnetisation M due to the induced currents in the tube is defined as $M = H_i-H$, which may be written as

$$H_i = H + \int_0^w J[B(r)]\,dr \qquad (3.1)$$

where r is the radial variable and w the wall thickness. Thus M is a direct measure of current density J in the tube. For given H, the shielding current corresponding to negative M ($M^-=H-H_i$) is greater than the trapping current for positive M ($M^+=H_i-H$) since the tube experiences a larger average field at M^+ than M^-. This difference is made negligible by considering the average field $\bar{H}$:

$$\bar{H} = \frac{H_i + H}{2} = H + \frac{M}{2} = H \pm \frac{M^{\pm}}{2} \tag{3.2}$$

Eliminating r in (3.1) gives an integral equation

$$w = \int_{\mu_o H}^{\mu_o H_i} \frac{dB}{J(B)} = \int_{\mu_o(\bar{H}-\frac{M}{2})}^{\mu_o(\bar{H}+\frac{M}{2})} \frac{dB}{J(B)} \tag{3.3}$$

The average current density in the tube may be found as

$$J = \frac{M}{w\cos\theta} \tag{3.4}$$

where θ is the opening angle of the tube. For $\cos\theta \simeq 1$ this is simply $\bar{J}=M/w$. For $H=H_{sh}$, where H_i is just equal to zero, the critical current density J_c may be found since J_c flows in one direction across the whole wall thickness at that point:

$$J_c = \frac{H_{sh}}{w\cos\theta} \tag{3.5}$$

which is again usually simplified by taking $\cos\theta=1$. $J(B)$ may be expanded as

$$\frac{\alpha}{J} = B_o + B + a_2 B^2 + a_3 B^3 + \ldots \tag{3.6}$$

and for small a_n

$$\frac{\alpha}{J} = B_o + B \tag{3.7}$$

Substituting into (3.3) gives

$$\frac{w\alpha}{\mu_o M} = \mu_o \bar{H} + B_o \tag{3.8}$$

which implies a straight-line relationship between $1/M$ and $\bar{H}$, and may be used to test the validity of the critical state model. From this and the current relationship of (1.7) the critical state curve $H_i(H)$ may be derived to give two hyperbolas in the first quadrant:

$$(\mu_o H_i + B_o)^2 - (\mu_o H + B_o)^2 = \pm 2\alpha w \qquad (3.9)$$

and a circle in the second quadrant:

$$(\mu_o H_i + B_o)^2 + (\mu_o H - B_o)^2 = 2(\alpha w + B_o^2) \qquad (3.10)$$

The curves thus derived are found to be in agreement with experimental data.

For $B \gg B_o$, $JB = \alpha$ = constant, which implies that the flux line movement is dominated by the Lorentz force F_L. It is found that α is temperature dependent (with the form $(1 - T/T_c)^2$ for $T/T_c > 0.4$) implying a thermally-activated process for flux line motion (this will be discussed further in 3.2). The critical state, therefore, is actually only a quasi-equilibrium and is inherently unstable; $\dot{H}$ must be slow in moving from one critical state to another otherwise the rapid change in magnetic field distribution may dissipate heat, initiating a flux jump as will be described in 3.3 and 3.4. In the critical state, pinning and Lorentz forces are balanced, $\boldsymbol{F_P} = \boldsymbol{F_L} = \boldsymbol{J} \times \boldsymbol{B}$, and α is seen as the pinning force density. The physical role of B_o is not fully clear.

For the field-independent current density of Bean's model a linear internal field profile *dB/dx* was obtained. The critical state model of Kim *et al.* with $J(B)$ given by (3.7) has a parabolic field profile.

3.1.3 Variants of the critical state model for HTS.

Other critical state models have been derived specifically for HTS. These result from other $J(B)$ relationships than (3.7), mostly taking the form of exponential or power-law dependencies. The HTS situation is complicated by the granular nature of the materials, as will be seen, and by the extreme anisotropy of the electrical and magnetic properties. Some models have regarded the material as an array of Josephson junction weak links between strongly superconducting grains, and have used the appropriate equations to obtain a macroscopic description. A detailed

analysis of HTS is complicated by the exact nature of the superconducting weak links which form the intergranular network. The properties of the grains have also been widely considered where microstructural features such as twinning planes are present.

3.2 Flux creep.

3.2.1 Basic flux creep theory.

The basic model used to describe flux creep in all superconductors is that of Anderson[82] which was developed at the same time as the critical state model. This showed that the critical state is in fact only a quasi-equilibrium, and that a thermally-activated process leads to flux movement at constant applied fields for $T \neq 0$. Anderson introduced the concept of "flux bundles", localised groups of flux lines, which could be "pinned" by free energy barriers in the material. Such flux pinning centres occur in voids, inhomogeneities, *etc.* - at any strain centre. Since the flux creep theory is well-documented it will be summarised here.

Flux bundles are trapped in potential wells of height U_o, the pinning potential. The thermally-activated "hopping" of flux bundles between pinning sites is described by a hopping frequency,

$$\nu = \nu_o \exp(-\frac{U}{k_b T}) \tag{3.11}$$

where ν_o is an attempt frequency, and the activation energy U is

$$U = U_o - V\int_0^a F(s)\,ds \tag{3.12}$$

where V is the mean flux bundle volume, F is a driving force density, s is the flux bundle displacement, and a is the half-size of the pinning potential. In the presence of a Lorentz force with energy

$$U_L = JBVr_p \tag{3.13}$$

where r_p is the range of the pinning force, the forward (in the direction of the Lorentz force) hopping rate is

$$\nu_{fwd} = \nu_o \exp(-\frac{U_o - U_L}{k_B T}) \tag{3.14}$$

and the reverse hopping rate is

$$\nu_{rev} = \nu_o \exp(-\frac{U_o + U_L}{k_B T}) \tag{3.15}$$

The resulting net effective hopping rate is then

$$\nu_{eff} = \nu_o \exp(-\frac{U}{k_b T}) \sinh(\frac{U_L}{k_b T}) \tag{3.16}$$

The Lorentz force "tilts" the pinning potential as shown in Figure 3.6[83]. For $U_L = U_o$ the barrier height is zero, and complete depinning occurs leading to diffusion of the flux lines and a transition to the flux flow regime. In LTS this is characterised by a flux flow resistivity $\rho_f = \rho_N(B/B_{c2})$, and flux line movement is no longer governed by a barrier-hopping probability but by a viscosity due to vortex interactions.

The main result of the Anderson flux creep theory is that it predicts a logarithmic relaxation of magnetisation,

$$\frac{dM}{d(\ln t)} = M_o(\frac{k_b T}{U_o}) \tag{3.17}$$

where M_o is the initial magnetisation. Flux creep can be shown to occur at all values of B and J and there is thus no precise "critical state"; the critical state is usually defined as one at which flux creep has dropped to an unobservably small level.

3.2.2 Flux creep in HTS.

The mechanisms of flux creep and pinning have been one of the most controversial topics in HTS research, due to the much higher levels of creep found in these materials than in LTS. Two main theories have been proposed. The superconducting glass model of Ebner & Stroud[84] treats the superconductor as a disordered array of weak links between grains, which are coupled as Josephson junctions. Although this interpretation explains a number of features in ceramics well, it does not seem to be satisfactory for single crystals. A more conventional approach is that of the giant flux creep model of Yeshurun & Malozemoff[85] which explains the high rates of flux creep in HTS in terms of the Anderson theory, in which the combination of high T_c and low pinning barriers leads to the "giant" creep. While this is much more compatible with general theories of superconductivity than the superconducting glass model, there remain some aspects which are still better explained by the latter.

The precise nature of flux pinning sites in HTS is still not completely clear, particularly on a granular scale. Recent observations have shown that the flux lines in HTS can form either a vortex lattice in a triangular array, as classically expected, or a "vortex glass" in a disordered pattern[86], depending on whether the material is clean, with few defects (lattice) or dirty (glass). At high fields and temperatures there is a "vortex liquid" region where thermal fluctuations melt the solid. The discovery of such novel states makes the investigation of flux pinning fundamental to a full understanding of the macroscopic magnetic properties of HTS.

3.3 Flux jumping theory (1): a force-balance approach.

The starting point of one conventional theory of flux jumping, based on that of Wipf[48], is a force-balance equation for flux motion in the shielding layer in equilibrium:

$$F_L = F_P + \eta v \tag{3.18}$$

The stability of this equation against disturbances is to be found.

To solve the above force-balance equation two approximations are introduced:

1. The viscous force ηv is neglected since v is small. This is equivalent to assuming isothermal conditions throughout the sample such that $J=J(B)$ only. In HTS, where flux pinning is known to be weak at elevated temperatures, the validity of this approximation must be carefully considered. The continuity of B and H at the superconductor surface implies a drift velocity:

$$v_{dr} = \frac{\partial H/\partial t}{\partial B/\partial x}\Big|_{x=0} = \frac{\partial H/\partial t}{4\pi J(B=H)} \tag{3.19}$$

   A disturbance leads to an increment of flux $\Delta\Phi$ into the interior of the sample, which may be pictured as a flux density wave propagating much faster than v_{dr}. This leads to the second approximation:

2. Assume H constant over the timescale of $\Delta\Phi$.

These simplify the force-balance equation in equilibrium to

$$F_L = F_P \tag{3.20}$$

i.e. the sample is in the critical state.

A disturbance changes F_L and F_P such that F_L is reduced since $\partial B/\partial x$ is smaller for the same value of B (see Figure 3.7); F_P changes due to ΔT from the energy dissipated in $\Delta\Phi$, and is reduced since $\partial F_P/\partial T < 0$. Thus the limit for full stability is given by

$$-|\Delta F_L| = -|\Delta F_P| \tag{3.21}$$

which is approached with increasing H since the reduction of F_L with $\Delta\Phi$ is greater for small H than for large (Figure 3.8a). This has two important applicational results. For a slab or cylinder of superconductor, once the field has penetrated to the centre a given change in F_L requires a smaller $\Delta\Phi$ than before, since flux enters from both

sides (Figure 3.8b). Thus the risk of flux jumping is reduced if the superconductor is penetrated to the centre without a flux jump occurring (see also 3.4). If the superconductor is in the form of a hollow tube, as will be specifically considered in this work, the likelihood of flux jumping increases once the field has penetrated to the inner wall, since an increased $\Delta\Phi$ is then needed to fill the non-superconducting volume (Figure 3.8c).

Above the stability limit, $F_L > F_P$ and the flux lines accelerate under a disturbance; it is then necessary to include the viscous force since v is no longer negligible and the original force-balance equation $F_L = F_P + \eta v$ must be solved. Under a disturbance, the thermal conductivity leads to a decreasing temperature difference ΔT which restores F_P and reduces the flux line acceleration, limiting the instability to a local, although large, disturbance. The process is short enough that the shielding layer does not grow significantly compared to the original x_o. If $\int v dt$ becomes comparable to x_o during acceleration, heat conduction becomes progressively less effective and the shielding region may grow at such a rate that heat conduction becomes negligible and the process is effectively adiabatic. This process is a "runaway" instability, producing a flux jump.

3.3.1 Full stability.

As stated at the outset, the purpose of this theory is to find the stability limit in terms of H. This is obtained by considering the conditions of full stability under an incremental change in B:

$$\begin{aligned} B(x) &\rightarrow B(x) + \Delta B(x) \\ \Rightarrow F_L &\rightarrow F_L + \Delta F_L \\ F_P &\rightarrow F_P + \Delta F_P \end{aligned} \tag{3.22}$$

Since this is a fast process, the stability limit for all x is given by

$$\Delta F_L = \Delta F_P \tag{3.23}$$

The Lorentz and pinning force increments are considered as follows. F_L is mainly dependent on $B(x)$:

$$\begin{aligned} \Delta F_L &= F_L(B+\Delta B) - F_L(B) \\ &= -\frac{1}{\mu_o}\left(B\frac{\partial \Delta B}{\partial x} + \Delta B\frac{\partial B}{\partial x}\right) \end{aligned} \tag{3.24}$$

the second-order term in $\Delta B\ \partial \Delta B/\partial x$ being negligible. ΔF_P is primarily dependent on ΔT and to a lesser extent on ΔB; thus

$$\Delta F_P = \frac{\partial F_P}{\partial T}\Delta T + \frac{\partial F_P}{\partial B}\Delta B \tag{3.25}$$

The energy dissipated in an ingression of flux $\Delta\Phi$ is

$$\Delta q = J\Delta\Phi = -\frac{1}{\mu_o}\frac{\partial B}{\partial x}\int_x^{x_o}\Delta B\,dx \tag{3.26}$$

The initial temperature rise is

$$\Delta T = \frac{\Delta q}{c} \tag{3.27}$$

where c is the specific heat (this assumes that the magnetic diffusivity, D_M, is much greater than the thermal diffusivity, D_{TH}), and thus

$$\Delta F_P = -\frac{\partial F_P}{\partial T}\frac{1}{\mu_o c}\frac{\partial B}{\partial x}\int_x^{x_o}\Delta B\,dx + \frac{\partial F_P}{\partial B}\Delta B \tag{3.28}$$

Hence, with the stability limit $\Delta F_L = \Delta F_P$,

$$B\frac{\partial B}{\partial x} + \left(\frac{\partial B}{\partial x} + \mu_o\frac{\partial F_P}{\partial B}\right)\Delta B - \frac{1}{c}\frac{\partial B}{\partial x}\frac{\partial F_P}{\partial T}\int_x^{x_o}\Delta B\,dx = 0 \tag{3.29}$$

The boundary conditions $\Delta B(x=0) = 0$ and $\Delta B(x_o) =$ constant give the limit for full stability in terms of external field, H_{fi}. This requires the explicit dependencies of $F_P(B,T)$. Wipf's theory takes the usual empirical approximations

$$F_P = \alpha\left(\frac{B}{B+B_o}\right) \tag{3.30}$$

$$\frac{\partial F_P}{\partial T} = \frac{\partial \alpha}{\partial T}\left(\frac{B}{B+B_o}\right) \tag{3.31}$$

where $\partial\alpha/\partial B = \partial B_o/\partial T = 0$. Since $F_P = F_L$,

$$\frac{\alpha}{B+B_o} + \frac{1}{\mu_o}\frac{\partial B}{\partial x} = 0 \tag{3.32}$$

Continuity requires that $B = \mu_o H$ at $x=0$, thus

$$(\mu_o H + B_o)^2 - (B+B_o)^2 = 2\mu_o \alpha x \tag{3.33}$$

Substituting into (3.29) gives a differential equation

$$(R-2x)\Delta B'' - 3\Delta B' - S\Delta B = 0 \tag{3.34}$$

where $S = (1/c)(\partial\alpha/\partial T)$ and $R = (B_o + \mu_o H)^2/\mu o\alpha$. This may be solved to give

$$H_{fi} = \frac{\pi}{2}\left(\frac{-\mu_o c\alpha}{\partial\alpha/\partial T}\right)^{\frac{1}{2}} \tag{3.35}$$

The empirical temperature dependence of F_P is given by

$$F_{P(T)} = F_{P(0)}[1-(T/T_c)^2]^2 \tag{3.36}$$

(The free energy difference between normal and superconducting states is proportional to H_c^2 which has a temperature dependence like (3.36), therefore it is reasonable to take that for F_P as the same.) From (3.30), (3.31) and (3.36) the temperature dependence of α is found to be

$$\frac{\partial\alpha}{\partial T} = \frac{-\alpha(T)4T}{(T_c^2 - T^2)} \tag{3.37}$$

Substituting into (3.35) gives an explicit equation for H_{fi}:

$$H_{fi} = \frac{\pi}{2}\left[\frac{\mu_o c}{4}\frac{(T_c^2 - T^2)}{T}\right]^{\frac{1}{2}} \tag{3.38}$$

It is notable that H_{fi} is not dependent on J_c, dH/dt, α, F_P, *etc.*, but only on material parameters: the heat capacity c and critical temperature T_c, and on sample temperature T. Wipf asserts that H_{fi} in (3.38), the full stability limit, is not synonymous with H_{fj}, the flux jump field, since the viscous force ηv has not been taken into account. The process initiated by an instability above H_{fi} is examined in a "limited instability" region, taking the full equilibrium equation (3.18).

3.3.2 Limited instability.

The full force-balance equation (3.18) may be written as an equation of motion for the flux lines:

$$\frac{\partial F_L}{\partial t} - \frac{\partial F_P}{\partial t} = \eta \frac{\partial v}{\partial t} + v \frac{\partial \eta}{\partial t} \tag{3.39}$$

This must be valid for all x and t. Conservation of flux across the superconductor surface must also be fulfilled:

$$Bv = \int_{B=0}^{B} \frac{\partial B}{\partial t} dx \tag{3.40}$$

$$\Rightarrow -\frac{\partial B}{\partial t} = \frac{\partial Bv}{\partial x} = B\frac{\partial v}{\partial x} + v\frac{\partial B}{\partial x} \tag{3.41}$$

where the negative sign appears from $x(B) < x(B=0)$. Expressions for $\partial F_L/\partial t$ and $\partial F_P/\partial t$ then have to be derived. From (3.41) and $F_L = -B/\mu_o \, \partial B/\partial x$,

$$\frac{\partial F_L}{\partial t} = \frac{1}{\mu_o}\left[B\frac{\partial^2 B}{\partial x \partial t} - v\left(\frac{\partial B}{\partial x}\right)^2 - B\frac{\partial v}{\partial x}\frac{\partial B}{\partial x}\right] \tag{3.42}$$

This is simplified by the following approximations:

1. For $\int v(x_o)dt \ll x_o$, neglect $\partial v/\partial x$, giving

$$\frac{\partial F_L}{\partial t} = -\frac{\nu}{\mu_o}\left[\left(\frac{\partial B}{\partial x}\right)^2 + B\frac{\partial^2 B}{\partial x^2}\right] \tag{3.43}$$

2. For $\int v dt \simeq x_o$ approximate as

(i) $\int v(0)dt = \frac{1}{2}\int v(x_o)dt$, from which one obtains

$$\frac{\partial v}{\partial t} = \frac{v}{x_o + x} \tag{3.44}$$

(ii) $\partial B/\partial x \propto H/x_o$, from which it may be shown that

$$\frac{\partial}{\partial t}\frac{\partial B}{\partial x} = -\frac{\partial B}{\partial x}\frac{2v}{x_o + x} \tag{3.45}$$

$$\Rightarrow \frac{\partial F_L}{\partial t} = -\frac{\nu}{\mu_o}\left[\left(\frac{\partial B}{\partial x}\right)^2 + B\frac{\partial B}{\partial x}\frac{3}{x_o + x}\right] \tag{3.46}$$

The difference between (3.42), (3.43) and (3.46) is usually negligible since $(\partial B/\partial x)^2$ dominates.

The term for F_P may be written as:

$$\frac{\partial F_P}{\partial t} = \frac{\partial F_P}{\partial T}\frac{\partial T}{\partial t} + \frac{\partial F_P}{\partial B}\frac{\partial B}{\partial t} \tag{3.47}$$

in which the temperature is given by a heat equation

$$\int \frac{\partial T}{\partial t} dt = \frac{f}{c}\int \frac{\partial q}{\partial t} dt \tag{3.48}$$

where $f = f(x,t,\partial q/\partial t)$ measures the steadiness of the temperature distribution with f(adiabatic) = 1, f(isothermal) = 0. Leaving aside any change in the shielding current,

$$\frac{\partial q}{\partial t} = J\frac{\partial \Phi}{\partial t} = J\nu B = \frac{\nu B}{\mu_o}\frac{\partial B}{\partial x} \tag{3.49}$$

and one can write

$$\frac{\partial F_P}{\partial t} = \frac{\partial F_P}{\partial T}\frac{JvB}{c}f - \frac{\partial F_P}{\partial B}\left(B\frac{\partial v}{\partial x} + v\frac{\partial B}{\partial x}\right) \tag{3.50}$$

Substituting the above terms in F_L, F_P into the equation of motion (3.39), the form of the acceleration of flux lines may be found as

$$\frac{\partial v}{\partial t} = a_i v + b_i v^2 \tag{3.51}$$

where a_i, b_i are terms which may be derived depending on the magnitude of v. For small t (since the process is assumed to be fast in relation to other timescales) this may be solved as

$$v = v_o \exp(at) \tag{3.52}$$

which is valid for the majority of the instability range, where $\int v dt \simeq x_o$. It can be seen that for $a<0$, v decreases, and $v=v_o$=constant for $a=0$; in other words the instability will stop by itself and stable equilibrium will be re-established for $a \leq 0$. Although a is not given here explicitly, the mechanism of the process may be clearly seen. An exact solution of the equation of motion would give $v(x,t)$ to describe the limited instability process completely; this however would be an unjustifiably difficult exercise.

The quantity f was introduced in (3.48), and comes into a. Prior to a disturbance, $f=1$ over the shielding layer (the adiabatic case), except at the surface where $f \simeq 0$ for good heat transfer conditions, *e.g.* in liquid helium. For short timescales, the adiabatic case is a good approximation.

3.3.3 Runaway instability: flux jumping.

Above the stability limit, flux lines are accelerated by F_L due to the weakening of F_P. For a limited instability, the maximum velocity attained is low, allowing thermal conduction to recover the bulk of the shielding layer. The pinning forces recover and decelerate the flux lines, stopping the instability. If the thickness of the shielding layer, $d = x_o + \int v dt$, increases significantly during acceleration, the situation may be different. If d grows faster than $t^{1/2}$, heat conduction is too slow and the process becomes, and remains, adiabatic (f=1). The acceleration continues up to a final runaway speed, the flux movement eventually terminating due to the boundaries of the superconductor. This is the full flux jump process. The field for runaway instability, H_{fj}, may be found through a consideration of d as given above, where H_{fj} comes out in a similar way to H_{fi} in (3.38) from the coefficients associated with v. This is not reproduced here however, since another derivation of H_{fj} will be described.

Although the preceding theory does not give H_{fj} explicitly, it does give a clear picture of the mechanism of flux jumping: the balance-of-forces approach is a conceptually simple one and thus a good starting point. Isothermal conditions were assumed throughout the above as a simplifying approximation; for much of the regime of interest the process is in fact adiabatic, as is the case for large dH/dt. A fully adiabatic theory will therefore be outlined.

3.4 Flux jumping theory (2): adiabatic theory.

The most commonly used theory of flux jumping is the adiabatic theory of Swartz & Bean[31][87]. Wilson[30] outlines a similar theory starting from a heat increase ΔQ_s, which is simpler than the detailed approach of Swartz & Bean who start from an adiabatic increment in the local field. Since both arrive at essentially the same result,

and the mechanism of flux jumping has been shown in 3.3, Wilson's version is followed here.

A thermally isolated slab of width a has an amount of heat ΔQ_s applied, and experiences a temperature rise ΔT. J_c is thus reduced, allowing flux movement and hence energy dissipation δq. The resistive current component decays leaving a new flux profile as shown in Figure 3.9. In a width δx there is a flux change $\delta\Phi(x)$ and thus a resistive voltage. For small ΔJ_c the current in δx may be taken as constant, $I(x) = J_c\delta x$. The heat generated in δx is thus

$$\delta q(x) = \int I(x)E(x)\,dt = J_c\delta x\,\delta\Phi(x) \tag{3.53}$$

The flux change $\delta\Phi(x)$ is found from the change in local field between x and x=0:

$$\delta\Phi(x) = \int_0^x \Delta B(x)\,dx = \mu_o\int_0^x \Delta J_c(a-x)\,dx = \mu_o\Delta J_c(ax - \frac{x^2}{2}) \tag{3.54}$$

The average heat per unit volume across the slab is

$$\Delta Q = \frac{1}{a}\int_0^a \delta q(x)\,dx = \frac{1}{a}\int_0^a \mu_o J_c\Delta J_c(ax - \frac{x^2}{2})\,dx = \mu_o J_c\Delta J_c\frac{a^3}{3} \tag{3.55}$$

Assuming a linear $J_c(T)$ dependence,

$$\Delta J_c = -J_c\frac{\Delta T}{T_c - T_o} \tag{3.56}$$

where T_o is the nominal operating temperature. The heat-balance equation for the complete slab is

$$\Delta Q_s + \frac{\mu_o J_c^2 a^2}{3(T_c - T_o)}\Delta T = \gamma C\Delta T \tag{3.57}$$

where γ is the sample density and C the specific heat. An effective specific heat per unit volume for the whole slab may be defined as

$$\gamma C_{eff} = \frac{\Delta Q_s}{\Delta T} = \gamma C - \frac{\mu_o J_c^2 a^2}{3(T_c - T_o)} \tag{3.58}$$

The temperature rise due to ΔQ_s is increased by the energy stored in the screening current. A flux jump will occur under the smallest disturbance when the temperature is caused to rise without limit, *i.e.* the effective heat capacity is zero; the scenario may be thought of in terms of the positive feedback loop of Figure 3.10. The condition for this to be avoided is

$$\frac{\mu_o J_c^2 a^2}{\gamma C(T_c - T_o)} < 3 \tag{3.59}$$

In practical conductors, this is limited by making $a < a_{fj}$ such that the superconductor is fully penetrated before there is any danger of flux jumping (a_{fj} corresponds to equality in (3.59)). This is the basis of the widely used method of adiabatic stabilisation in which superconducting wires are finely sub-divided to a filament diameter less than a_{fj}. To find the field at which flux jumping will first occur (which is the aim of the quantitative theory), one considers a slab of thickness $a \gg a_{fj}$ in which the shielding layer penetrates to a depth p. For $D_M \gg D_{TH}$, the shielding layer may be taken to be thermally isolated from the rest of the sample during a flux jump, and the above theory may be applied to this layer. In an increasing applied field, flux jumping will first occur at

$$B_{fj} = \mu_o J_c p = [3\mu_o \gamma C(T_c - T_o)]^{\frac{1}{2}} \tag{3.60}$$

from equality in (3.59). The exact theory of Swartz & Bean gives $\pi/4$ instead of 3 in (3.59), and H_{fj} is derived as

$$H_{fj} = [-\pi^3 \gamma C \frac{J_c}{\partial J_c / \partial T}]^{\frac{1}{2}} \tag{3.61}$$

or[61]

$$B_{fj} = [3\mu_o \gamma C \frac{J_c}{\partial J_c / \partial T}]^{\frac{1}{2}} \qquad (3.62)$$

This is the same as the instability limit of Wipf, (3.38), in the adiabatic limit[31]. (It may be noted that since the original Swartz & Bean derivation uses the volume specific heat the density γ does not appear in the references).

In deriving (3.60) *etc.*, the case of a full flux jump, where the temperature rise is unbounded, was considered. Partial flux jumps may occur when C increases rapidly with temperature, thus recovering stability before reaching T_c.

3.5 Diffusion theory of flux jumping.

In the previous section time was ignored as a quantity, and the movement of heat, *etc.* was not considered. This is a good approximation in most superconductors, but not in composites, as will be seen. Theories which take into account the time variable are called "dynamic" stability theories, and are based on the thermal and magnetic diffusion equations:

$$D_{TH} \nabla^2 T = \frac{\partial T}{\partial t} \qquad (3.63)$$

$$D_M \nabla^2 B = \frac{\partial B}{\partial t} \qquad (3.64)$$

where the thermal and magnetic diffusivities are, respectively,

$$D_{TH} = \frac{\kappa}{\gamma C} \qquad (3.65)$$

$$D_M = \frac{\rho_N}{\mu_o} \tag{3.66}$$

where κ is the thermal conductivity, and ρ_N is the normal state resistivity, more accurately replaced by the flux flow resistivity, $\rho_f=\rho_N(B/B_{c2})$. A solution of the diffusion equations is very difficult, and as the adiabatic approximation is sufficient for the superconducting material only, the theory of 3.4 will be that used here. Wilson[30] quotes values of D_{TH} and D_M for Nb-Ti and copper at 4.2K:

	D_{TH} (m^2s^{-1})	D_M (m^2s^{-1})
Nb-Ti	2×10^{-5}	0.5
Cu	1.1	8×10^{-5}

These show clearly that while the adiabatic approximation, valid for $D_M \gg D_{TH}$, is good for the superconductor, it is not applicable to a composite. The Cu stabiliser slows down magnetic movement considerably, allowing even heat dissipation and thermal recovery. Estimates for the diffusion constants in the LaSrCuO HTS give $D_M \simeq 1.3 m^2s^{-1}$ (reduced by a factor of 50 to 250 when the flux flow resistivity is taken) and $D_{TH} \simeq 10^{-3} m^2s^{-1}$, which confirm the validity of the adiabatic assumptions.

3.6 Empirical dependencies for flux jumping.

It is important to know the effects of experimentally variable parameters such as $dH/dt=\dot{H}$ and T on flux jumping. A number of studies have examined these, in particular those of Wipf & Lubell[38] and Watson[39][40]. Although the flux jumping criteria (3.61) and (3.62) give the necessary conditions for a flux jump to occur, this may not be a sufficient condition, and the influence of $\dot{H}$ must be taken into account.

Wipf & Lubell identify three regions for $\dot{H}$: (1) large $\dot{H}$ where $H_{fj} \simeq$ constant; (2) intermediate $\dot{H}$, $H_{fj} \propto 1/\dot{H}$; (3) small $\dot{H}$, where no flux jumping occurs and flux creeps

smoothly. As previously stated, the first case approximates well to adiabatic conditions; the second may be taken to be isothermal.

Watson also gives $\dot{H}$ dependencies: H_{fj} decreases with $\dot{H}$ at constant temperature, and $H_{fj} \propto \log\dot{H}$ over most of the range. At low $\dot{H}$, $\log H_{fj} \propto 1/\dot{H}$. It is noted that for each external field sweep rate there is a temperature above which flux jumping does not occur. Up to H_{fj}, the magnetisation is independent of $\dot{H}$.

Examining the temperature dependence, Watson finds that the value of $\dot{H}$ at which behaviour deviates from $\log H_{fj} \propto 1/\dot{H}$ increases with temperature. H_{fj} increases initially as T is lowered from T_c, reaches a maximum, and then decreases. The maximum is more pronounced for small $\dot{H}$. In general, the number of flux jumps around a magnetisation loop increases as T decreases. The number of jumps per unit of magnetic field decreases with T before increasing at low temperatures, and increases with increasing $\dot{H}$, possibly approaching a constant value at high rates. For given T, $\dot{H}$ the position of jumps around a magnetisation loop is reproducible for subsequent loops.

There seems to be a consistent pattern to the number of flux jumps in each quadrant of the magnetisation loop. Taking the first quadrant Q1 as that in which the virgin magnetisation curve occurs, then for the first cycle the number of jumps in Q1=Q3-1; in the second and subsequent cycles Q1=Q3. For all cycles, Q1=Q2+1 and Q4=Q2.

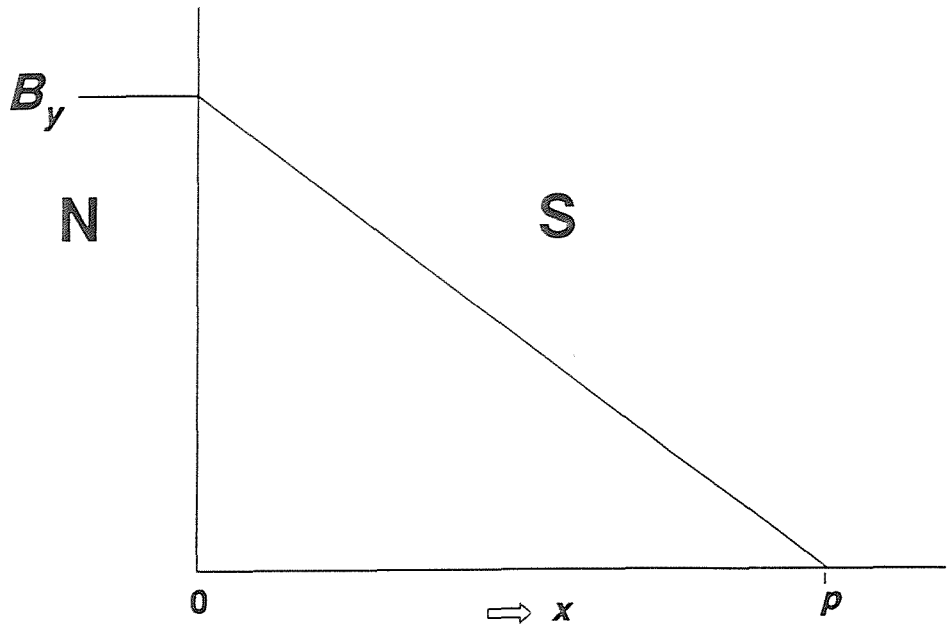

Figure 3.1 Flux penetration profile in the Bean model.

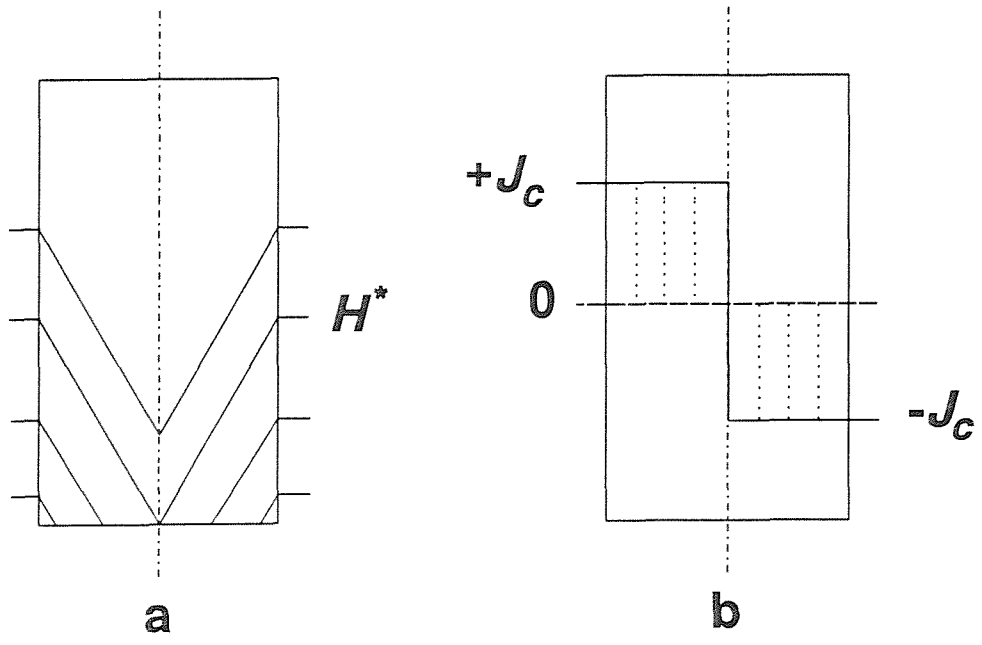

Figure 3.2 Bean's model in a slab: (a) flux penetration in increasing field, (b) critical current flow.

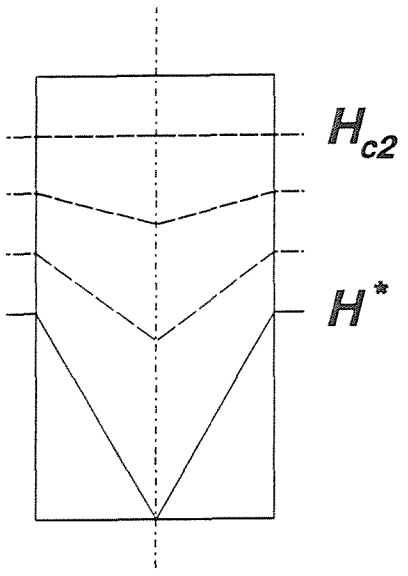

Figure 3.3 Flux profiles in a slab in increasing applied field at high values.

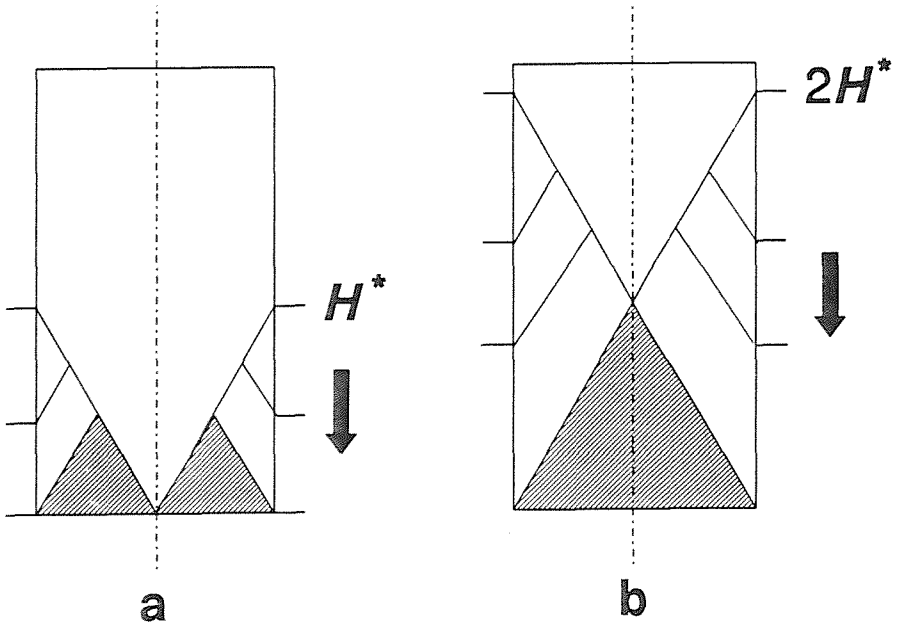

Figure 3.4 Consequences of flux trapping in a slab in applied field decreasing from (a) H^*, (b) $2H^*$.

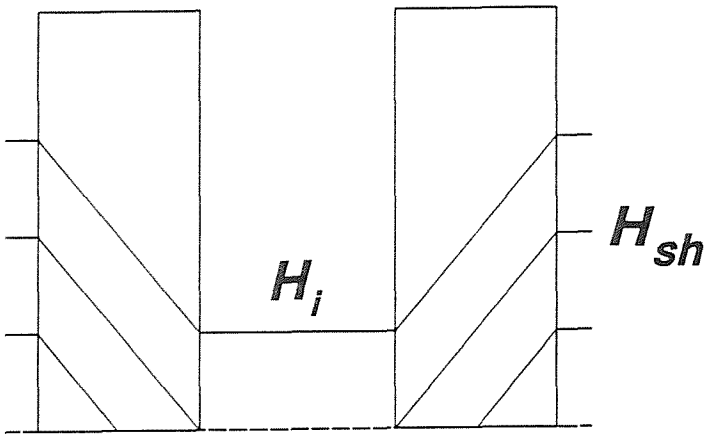

Figure 3.5 Flux penetration in a tube in increasing field.

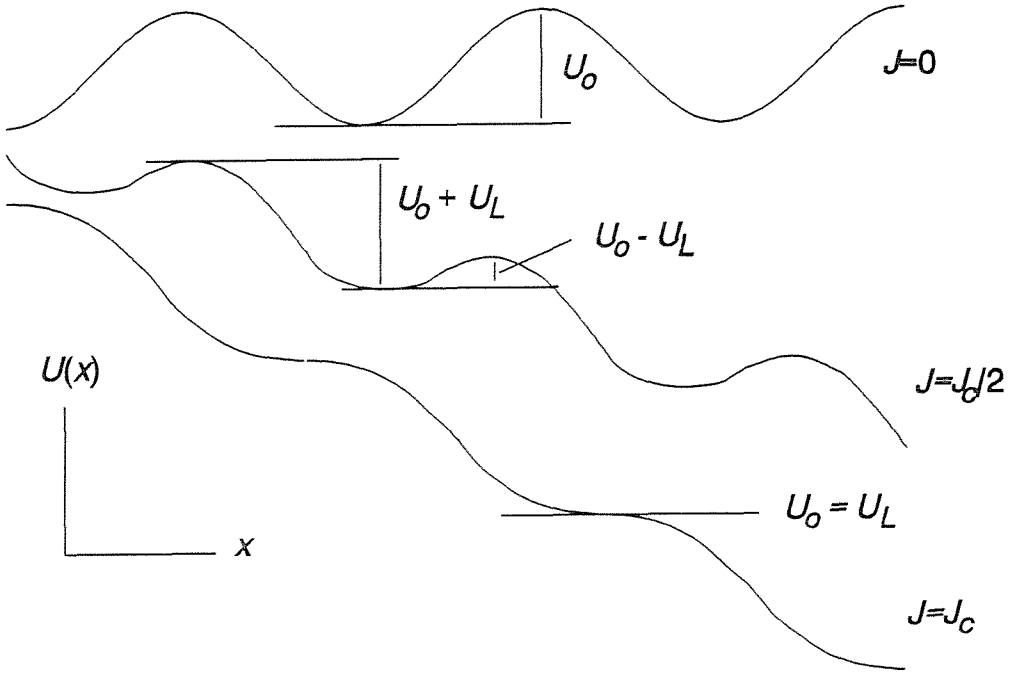

Figure 3.6 Effect of Lorentz force on flux pinning potential[83].

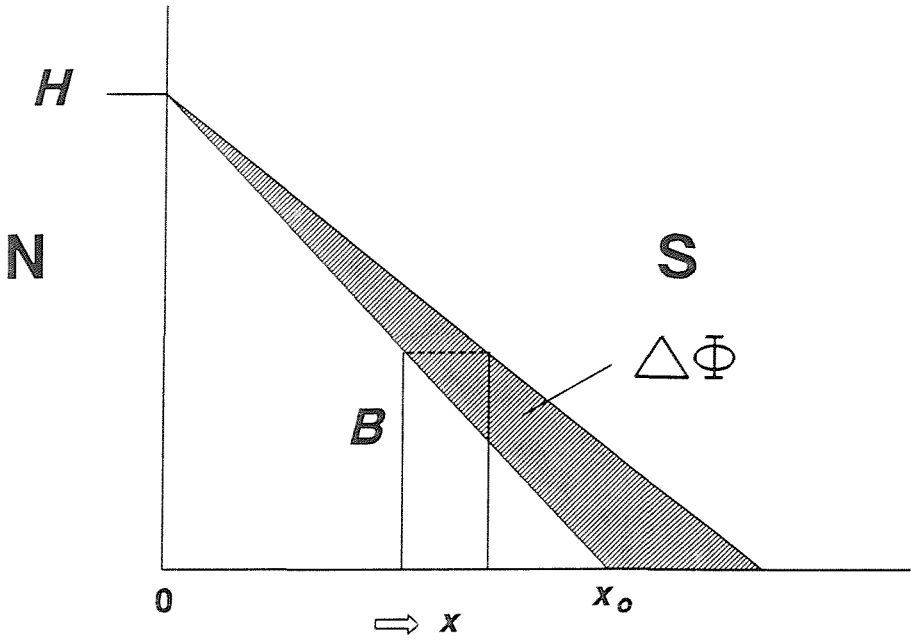

Figure 3.7 Change of flux profile and $\partial B/\partial x$ in flux jump.

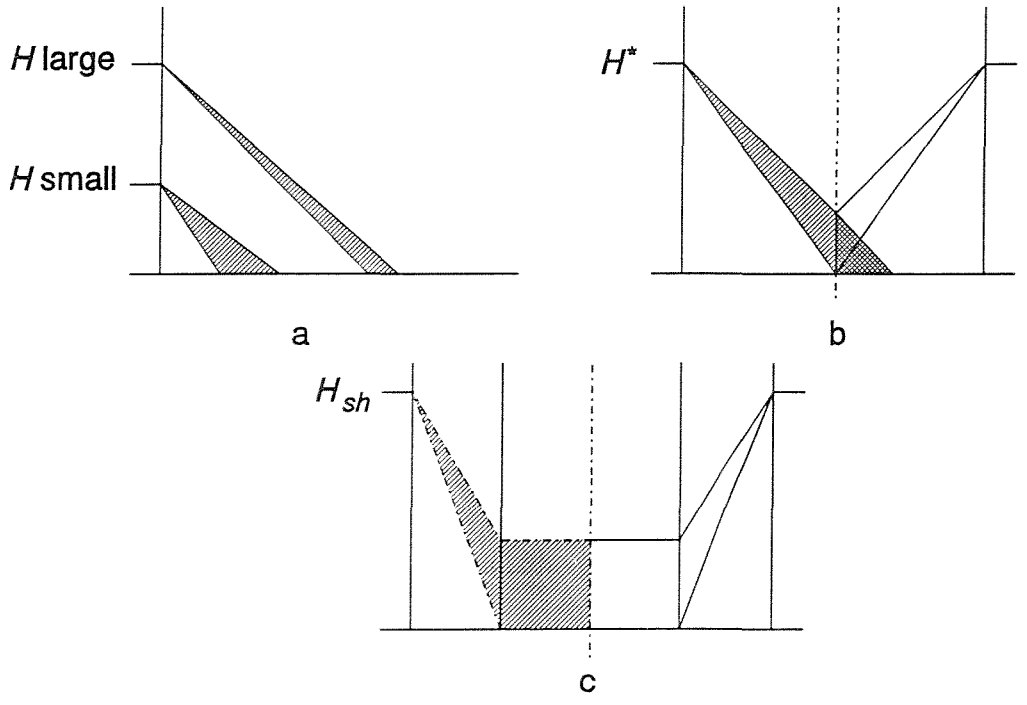

Figure 3.8 (a) Reduction of F_L with $\Delta\Phi$ for H small and large; change of flux $\Delta\Phi$ for given change of F_L: (b) in a slab, (c) in a tube.

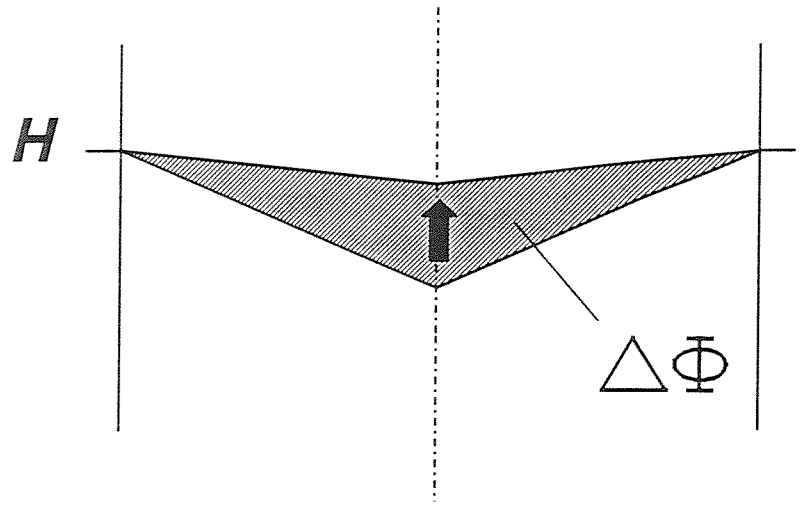

Figure 3.9 Change of flux profile produced by flux jump in a slab.

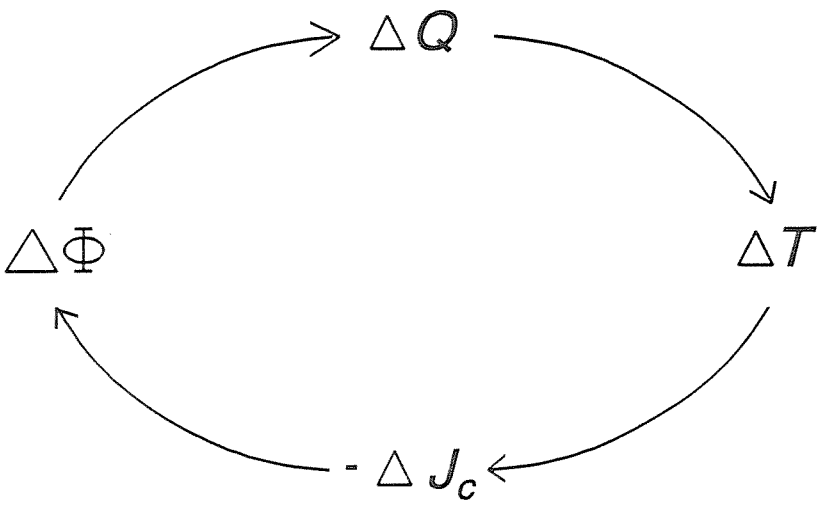

Figure 3.10 Positive feedback loop of quantities controlling flux jump.

4 Experimental setup and apparatus.

4.1 Flux tubes.

Three different flux tubes were used in the work reported here: $YBa_2Cu_3O_{7-x}$, 11.8mm o.d. × 8.3mm i.d. × 52mm; $Bi_2Sr_2CaCu_2O_{8+x}$, 25mm o.d. × 15mm i.d. × 50mm (hereafter denoted by BSCCO #1); $Bi_2Sr_2CaCu_2O_{8+x}$, 48mm o.d. × 42mm i.d. × 50mm (BSCCO #2). These are shown in Figure 4.1.

The YBCO tube was supplied by ICI Advanced Ceramics, and was prepared by mixing polymers and non-aqueous solvents with YBCO powder to form a plastic mass. The mixture was extruded and fired at ~900-930°C in an oxygen atmosphere. The final density of the tube was estimated at 85%, giving an interconnected porous structure to allow O_2 permeation[88]. Both BSCCO tubes were supplied by Hoechst AG. The material is quoted as being phase pure by X-ray diffraction, with $T_c(R=0)$ = 89-91K. The density is estimated as 6.0gcm^{-3}. The tubes were formed by Hoechst's proprietary melt-processing method[89].

4.2 Instrumentation.

4.2.1 Magnetic field measurement.

Magnetic fields inside the HTS tubes were measured by cryogenic Hall probes (BHA-921, F W Bell Inc.) which give a highly linear voltage output for field (±1% max. to ±3T, ±2% max. to ±15T), operating over a wide temperature range from 1.5K to 370K. The mean temperature coefficient is quoted as ±100ppmK^{-1} maximum; it was found that temperature effects on the probes were negligible. The sensing

elements are 6.35mm (0.25") overall diameter, with an active area approximately 0.508mm (0.020") diameter, located ~0.635mm (0.025") behind the front face. The probes are very susceptible to mechanical shock, particularly when cold, and therefore require careful handling; thermal cycling must be $< 100 K min^{-1}$ to prevent damage.

The Hall probe supply current and output voltage were connected to a Redcliffe 102D magnetometer, which gives a calibrated reading in Tesla and a linear voltage output. The Hall probe supply current is set on the magnetometer using a calibrated permanent magnet, and with probe and magnetometer calibrated together an accuracy of ± 0.5mT and maximum resolution of 0.1mT in 0.4T can be obtained; the full-scale reading is 3.9999T. The output of the probes has to be multiplied by ten on the front panel reading of the magnetometer, *i.e.* it reads in the 0.4T range for up to 3.9999T, and provides a rear-panel voltage output of $1 VT^{-1}$.

Applied magnetic fields generated by the magnets were obtained by measuring the voltage across 0.1Ω or 1Ω standard resistors in series with the magnet to find the magnet current. A magnetic field-current calibration could then be applied (see 4.3).

4.2.2 Temperature measurement.

At temperatures around 77K measurement was made by T-type thermocouples. In the low-temperature region (close to 4.2K) a diode thermometer was used (Southampton Miniature Diode Thermometer (SMDT), Cryogenics Advisory Unit, Institute of Cryogenics). The SMDT operates over a range from 1K to 435K, with an output voltage 1.8-0.5V, eliminating the need for further signal amplification. The mean calibration curve is shown in Figure 4.2. An equation was fitted to the low-temperature (< 10K) end of the calibration, and the result offset to fit the measured voltage at 4.2K of the diode used. The SMDT is supplied by a 10μA constant current source. There is known to be a significant magnetic field effect on the diode which depends on supply current and diode orientation[90]. Because of this the diode was

fixed to the magnet for most of the measurements since the trapped flux in the HTS tube would otherwise affect the temperature reading, making subsequent temperature adjustment difficult.

The SMDT was fixed to the desired surface using GE varnish which could be easily dissolved by a 50/50 methanol-toluene solution. The semiconductor chip is mounted on a sapphire substrate ($2 \times 2 \times 0.15$mm) with two gold plated pads to provide electrical contact. Because the chip is connected to one of these pads by a 25μm gold wire, considerable care must be taken in handling the diode.

4.2.3 Data logging.

The various measuring elements are connected to the inputs of a Keithley 199 System DMM/Scanner. The scanner module has eight input channels which can be selected independently or scanned. The DMM is computer controlled by the Asystant GPIB software package (Asyst Software Technologies Inc.) via an IEEE-488 interface. The software allows IEEE devices to be configured and talked to interactively, or by programs. Data can be stored in memory as the Asystant's variable arrays, or written to disk as ASCII files. The Asystant environment also provides a wide range of analysis and manipulation options for the data arrays. The instrumentation setup is illustrated schematically in Figure 4.3.

Programs were written in the Asystant GPIB to scan the appropriate channels for a measurement, store the data and apply calibration equations. Scanning is performed very quickly, giving near-simultaneous measurements on the selected channels. For shielding measurements on the HTS tubes data could be displayed graphically in real time. Waveforms from data could be edited to eliminate erroneous readings due to noise, *etc.*

4.3 Magnets.

4.3.1 Copper-wound solenoid.

For low-field measurements a copper-wound solenoid was fabricated, generating a field of up to 0.085T at 10A. The coil consists of two concentric halves bolted together and connected in parallel. In this configuration a bore of 75mm was available; the magnet length is 270mm. The outer coil could be used alone at lower fields if a larger bore was required (102mm).

In measurements on the HTS tubes, the tube was held in a Tufnel former in a glass cryostat and positioned axially at the point of maximum field using the Hall probe mounted centrally in the tube. A field-current calibration could then be obtained prior to cooling, typically around $8.5mTA^{-1}$. The maximum supply current being 10A, a peak central field of 85mT could be generated.

4.3.2 3T superconducting magnet.

Low-temperature and high-field measurements were performed in a 3T superconducting magnet and cryostat (Oxford Instruments Ltd.). The coil is wound from Nb-Ti and gives a central field of 3T at 4.2K for 4.98A, in a bore of 27mm. Field homogeneity is quoted as 1% in a 10mm diameter spherical volume. The magnet is conduction cooled by the LHe volume, and sits in an exchange gas space, including the magnet bore. The sample temperature is therefore restricted to that of the magnet via the exchange gas. While it should be possible to heat the sample independently of the magnet, sufficient thermal isolation could not be obtained in such a small bore. A schematic diagram of the cryostat is shown in Figure 4.4, and photographs of the magnet and cryostat in Figures 4.5 and 4.6. The tubes were held centrally in the magnet bore by nylon line.

The magnet specification allows a maximum current ramp rate of $0.5Amin^{-1}$ (10 minutes to field) for both increasing and decreasing field, *i.e.* a maximum field sweep rate of $\sim 0.3Tmin^{-1}$.

The LHe cryostat is equipped with a lambda point fridge (LPF) which, by pumping on a port controlled by a needle valve, allowed the magnet and sample temperature to be reduced from 4.2K to 2.2K and points in between.

4.3.3 Applied field sweep controllers.

Both the above magnets were supplied by a Kingshill 10A/100V power supply, which was modified such that the current could be swept by an external control unit. Two of these units were used, the first being an Oxford Instruments sweep unit. This operates by driving a multi-turn potentiometer from an electric motor via a series of gears; the potentiometer is connected in place of the current control on the power supply. The gears can be selected to give fixed and highly reproducible sweep rates. Since the rates were fixed at the intervals determined by the gears, a second sweep unit was designed and constructed using an electronic motor controller (RS components) to give a continuous range. In both cases the sweep direction was switched for up or down, and the polarity of the applied field reversed by a crossover switch.

Figure 4.1 HTS flux tubes, left to right: YBCO, BSCCO #1, BSCCO #2.

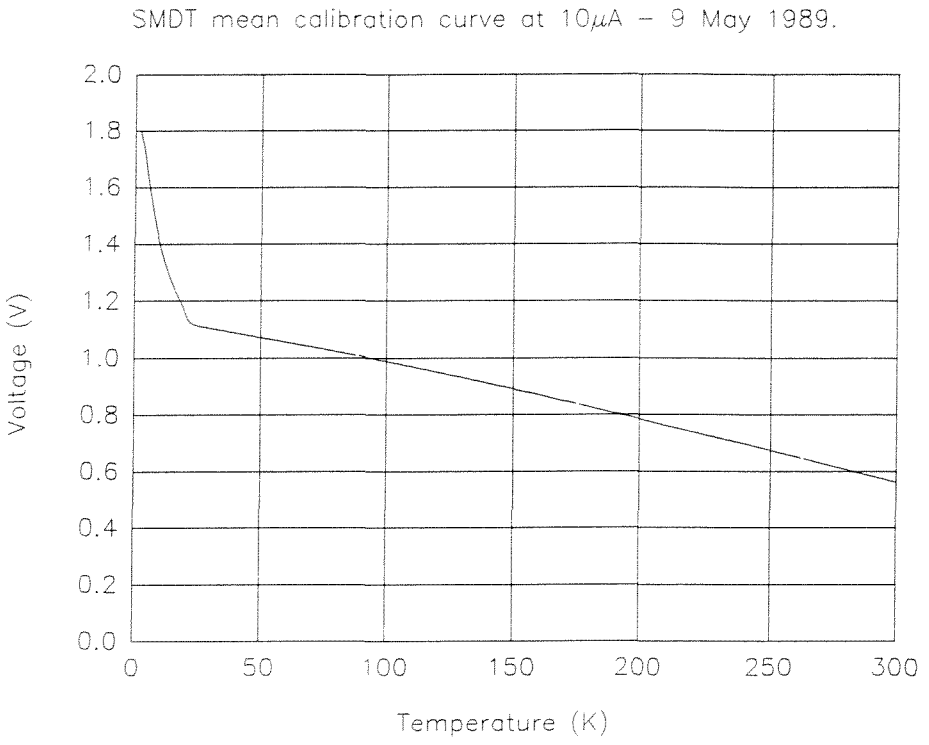

Figure 4.2 Standard calibration for SMDT diode thermometer.

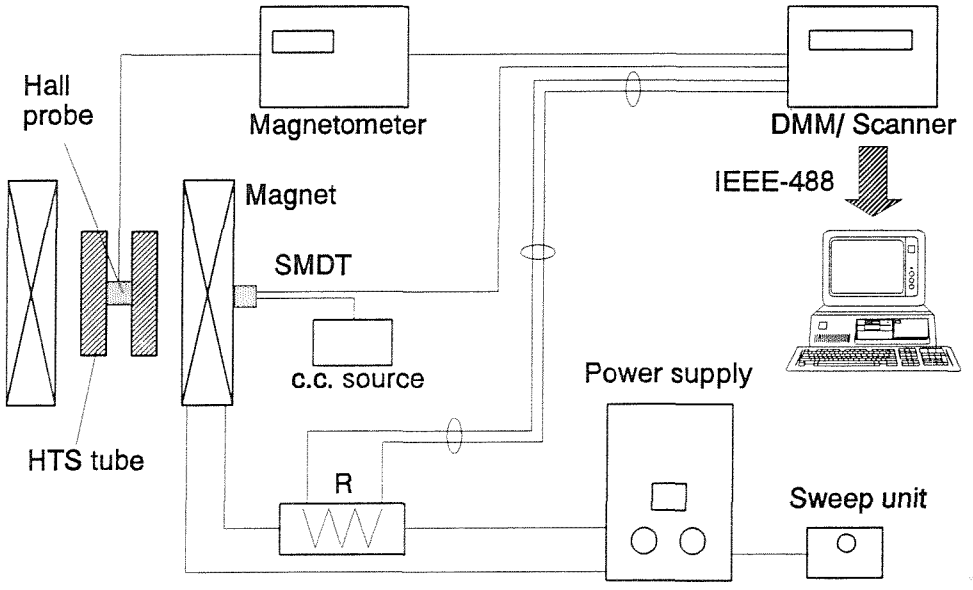

Figure 4.3 Instrumentation setup for shieiding measurements.

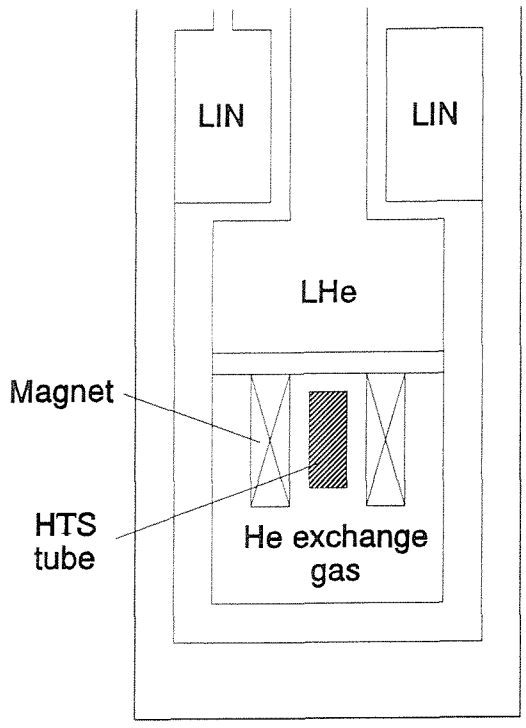

Figure 4.4 Schematic diagram of Oxford Instruments 3T superconducting magnet and cryostat.

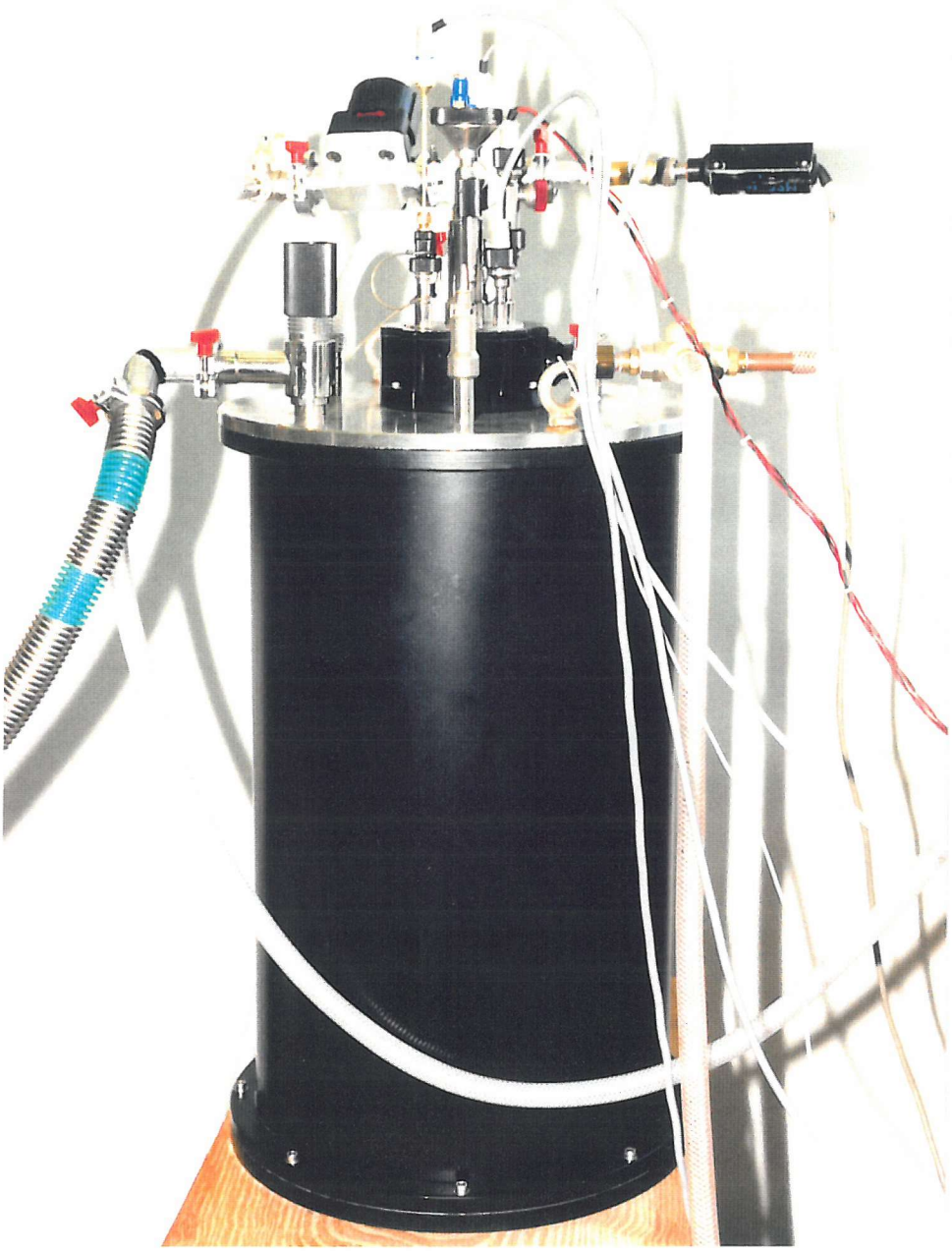

Figure 4.5 Cryostat for 3T superconducting magnet.

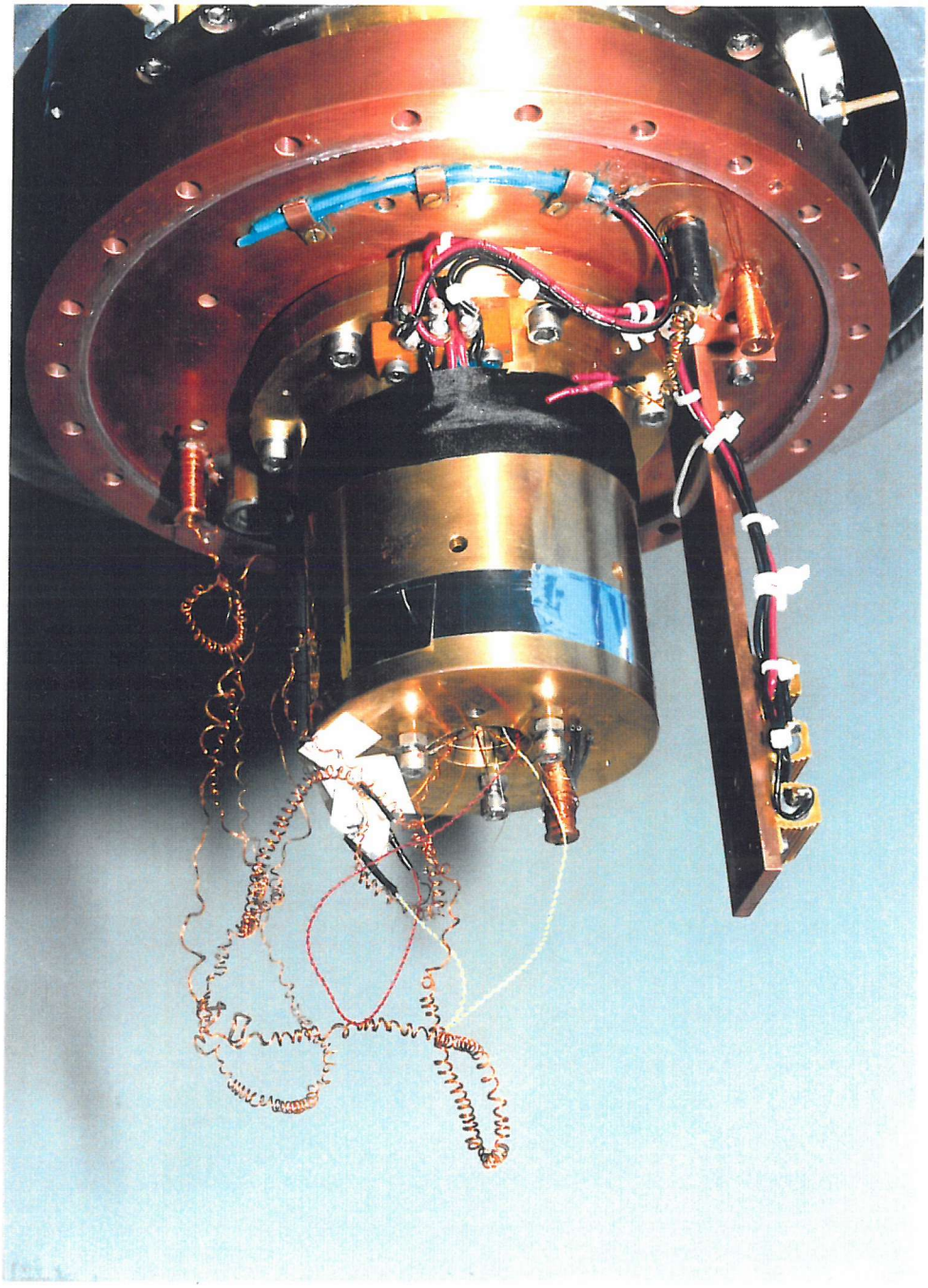

Figure 4.6 3T superconducting magnet.

5 Experimental results, 67-77K.

A number of measurements were performed on the HTS flux tubes at and around 77K to provide general characterisation of the materials. The main purpose of the research being the investigation of flux jumping at low temperatures, these were not exhaustive. Although not a full treatment, useful data relating to the flux shielding, trapping and creep properties could quickly be obtained. From the high predicted flux jump fields at 77K given in 2.4 flux jumping was not expected to be observed at this temperature.

5.1 Magnetic properties of granular HTS tubes.

A number of studies have previously been made on the shielding properties of YBCO tubes[19][20][21][22][23], much of the interest arising from the possible use of HTS tubes as magnetic shields in SQUID systems, *etc.* at high temperatures. As discussed in 3.1, the tube geometry provides a simple method of measuring a number of superconducting properties, and as such was used in the original derivation of the critical state model outlined there. HTS tubes have similarly been used to extract critical current and magnetisation information[18][24][25]. However, care must be taken in interpreting such data because of the granular nature of the material.

In a granular HTS, two systems may operate separately or together, depending on the magnetic field range: the inter- and intra-granular regions. The superconductor is considered to be a network of weakly-linked superconducting grains, with an intergranular current flowing across these weak links. It is well-known that this intergranular transport J_c is orders of magnitude lower than that in the grains for sintered HTS, and thus there is a quite clear difference between the lower critical

fields at which flux first penetrates the superconductor for the intergranular network (very low) and the individual grains (much higher). Furthermore, when measuring the magnetic field enclosed by an HTS tube, the two systems contribute magnetisations of opposite sign[18][24] in the centre of the tube. Up to B_{sh} the tube behaves as a bulk superconducting material and screens the external magnetic field completely from the inside of the tube. Surface screening currents flow in the grains to exclude the field, up to the lower critical field of the grains, $H_{c1}{}^{G}$, after which flux also enters the granular regions. Because the direction of these intragranular currents is the same as the transport current on the outer tube wall, and opposite on the inner tube wall, the grains contribute a magnetisation in the same direction as the intergranular M outside the tube, and opposite to it in the enclosed volume. Thus at intermediate fields the magnetisation due to the grains lowers total magnetisation observed inside the tube. At high fields all of the weak links are broken and only the granular magnetisation will be observed.

Considering the flux trapped by a superconducting ring, Figure 5.1a shows the magnetic field and flux distribution of an ideal sample in which the flux is trapped in the enclosed volume only by a circulating persistent current. With flux trapped inside the granular material only, the magnetisation inside the tube is in the opposite direction to that due to a persistent current, as shown in Figure 5.1b (after Leidener & Feile[91]). Moving between the two situations, as outlined above, the granular contribution will make an increasing negative contribution to the flux profile at the centre of the tube. As the Figure shows, the intragranular contribution in the enclosed volume has a much smaller magnitude than the intergranular part over much of the range where the two act together. Intergranular effects will therefore dominate in observations in which a large bulk persistent current flows.

5.2 YBCO tube.

5.2.1 Shielding and magnetisation.

The shielding curve of the YBCO tube was obtained at 77K in liquid nitrogen by simultaneously measuring the internal and applied magnetic fields as described in Chapter 4, up to $B_a = \pm 20$mT. The curve is given in Figure 5.2, and shows B_{sh}=3.5mT and B_{tr}=4.5mT, with the tube being fully penetrated ($B_i = B_a$) by 15mT. Using the critical state model for a tube at B_{sh} gives the critical current density as

$$J_c = \frac{B_{sh}}{\mu_o w \cos\theta} \qquad (5.1)$$

where θ is the opening angle of the tube; here θ=9.1°, *i.e.* cosθ=0.987. A bulk J_c(77K)=161Acm^{-2} is calculated, typical of critical current values for sintered YBCO. Other measurements at lower temperatures (produced by reducing the pressure above the liquid nitrogen) gave values at 67.5K: B_{sh}=5.8mT, B_{tr}=6.4mT, J_c=267Acm^{-2} and 63K: B_{sh}=6mT, B_{tr}=7.3mT, J_c=276Acm^{-2}. The magnetisation of the tube is found as

$$\mu_o M = B_i - B_a \qquad (5.2)$$

and is shown in Figure 5.3. No variation in the size of the magnetisation loop was observed for field sweep rates between 0.075 and 1.5mTs^{-1}.

There is a significant enhancement of B_{tr} over B_{sh}, as has been previously observed in such tubes[20]. This has been interpreted to be indicative of granular effects where the grains are totally screened in the shielding region, but begin to be penetrated at higher fields, thus trapping an "extra" amount of flux over the intergranular region. It must be borne in mind that the critical state model was developed for a homogeneous superconductor, in which a specific outcome is that $B_{sh}=B_{tr}$. If additional flux was trapped in the grains following a complete field excursion, it would be expected that the point at which B_i crosses zero thereafter would be larger

than B_{sh} for the virgin curve. In fact, both the positive and negative B_a points at which B_i=0 appear to be at $\pm B_{sh}$. It may be that the extra pinning is occurring in the intergranular network itself.

A close examination of the magnetisation loop shows a "tilt" of the higher-field ends approaching the maximum $\pm B_a$, where the magnetisation crosses zero and increases with field, in the opposite direction to that for the intergranular system. This may suggest the onset of magnetisation due to isolated grains. Much higher field measurements are really needed to clarify the situation - excursions to the maximum available field of the copper-wound solenoid used here (4.3.1) did not yield any more useful information. A comparison of the magnetisation loop here with those found for the intergranular region only (*e.g.* Puig *et al.*[92]) suggests that the intergranular magnetisation does indeed dominate, and that the tube is behaving as a superconducting bulk for the greater part. One can then use the concept of an "intergranular critical state". Without attempting to separate the inter- and intra-granular components, the critical current density was derived from the magnetisation curve as[24]

$$J_c = \frac{(M^+ - M^-)}{2\mu_o w \cos\theta} \tag{5.3}$$

where M^+, M^- are the magnetisations in the positive (upper) and negative (lower) parts of the loop respectively at the same B_a value. The applied field dependence of the magnetisation J_c is shown in Figure 5.4, and a J_c of 210Acm^{-2} at zero field is obtained, somewhat higher than that from B_{sh}. This is analogous to the common difference observed between transport and magnetisation J_c's since in this case the shielding current is simply a bulk intergranular transport current. The usual order of magnitude drop in 10mT is observed[6]. The standard critical state model $J(B)$ dependence of

$$\frac{\alpha}{J} = B_o + B \qquad (5.4)$$

does not appear to be followed here at low fields (Figure 5.4). This is similar to the dependence found by Cimberle *et al.*[24], also in an YBCO tube at low field, although they observed no disparity between B_{sh} and B_{tr}, and by Gyorgy *et al.*[93] for a tube in which intragranular effects were shown to be negligible. The behaviour at high and low fields near 4.2K will be considered in Chapter 6.

One way by which it is possible to separate out the inter- and intra-granular effects in a tube or ring is to cut the sample such that the intergranular current path is broken, and the granular magnetisation in the tube can be observed. This was clearly not a viable option with only one sample available. An alternative which time could not permit would be to use an a.c. magnetisation method to find the total bulk magnetisation, and then separate the predominantly intergranular magnetisation obtained above from that obtained. Doing this in a range of applied fields could show the granular influence on the internal field B_i.

5.2.2 Flux creep and pinning.

In any practical use of a flux tube to contain magnetic field, the rate at which the flux creeps out of the enclosed volume is of immediate interest. The decay of trapped flux in the YBCO tube was measured over time up to 10^3s at 77K for both zero-field-cooled (ZFC) and field-cooled (FC) conditions. The initial applied field was 52mT, which was switched off to give a step change to zero field, or an applied field up to 8mT. The magnetisation decay for ZFC and FC is shown in Figure 5.5 and 5.6 respectively. The logarithmic decay can be characterised by

$$\frac{dM}{d(\ln t)} = M_o\left(\frac{k_b T}{U}\right) \qquad (5.5)$$

where $M_o = M(t_o)$ is the remanent magnetisation at an initial time t_o. Obviously $t_o = 0$, the time at which B_M goes to zero cannot be used, so an arbitrary choice is usually made such that the very fast relaxation at the beginning has passed; here $t_o = 2$s was used. U is the "ideal" pinning energy (there may actually be a distribution of pinning energies). Figure 5.7 plots $-U(B_a)$, and shows that as expected the ZFC conditions show greater relaxation than FC[94]. Again, the fact that $M(\mathrm{FC}) > M(\mathrm{ZFC})$ would not seem to suggest granular effects, although one would expect flux to be pinned within the grains in an FC situation. M(FC) may indeed be reduced compared to the same case if granular pinning was not present - the measurement does not make this clear. The zero-field values of U_o are in reasonable agreement with the 0.76eV found in similar tubes by Wang *et al.*[23] (the sign is a matter of convention). It should be noted that this derivation of U is not always valid, especially for fast-relaxing systems, and is only really true if $M(0)$ is equal to the true maximum magnetisation at that point, *i.e.* $J(0) = J_c$[95]. The numerical results are summarised below:

B_a (mT)	ZFC $dM/d(\ln t) \times 10^{-2}$	ZFC $-U$ (eV)	FC $dM/d(\ln t) \times 10^{-2}$	FC $-U$ (eV)
0	-7.11	0.52	-5.92	0.65
1	-5.90	0.57	-4.08	0.83
2	-7.38	0.39	-6.92	0.45
3	-8.84	0.29	-7.55	0.37
4	-7.34	0.31	-6.73	0.33
5	-6.03	0.32	-6.83	0.34
6	-8.74	0.20	-7.51	0.26
7	-10.87	0.12	-7.17	0.21
8	-6.32	0.22	-7.81	0.19

Some deviation from linearity is clear in the 7mT ZFC plot, and possibly in others. This may be due to non-logarithmic relaxation, although it would be expected that consistent results should be obtained for a given tube; a more likely explanation is that it is due to a cross-over in pinning energy at long times[23]. This has been attributed[23] to a change from pinning by both the granular and intergranular regions to that of the intergranular network only: since the local field gradient at the surface of the grains is quite high, flux creep there may dominate initially. Longer time scales (up to at least 10^4s) are needed to investigate this further. Figure 5.8 confirms that the FC initial remanent magnetisation is consistently enhanced over the ZFC. Obviously when $M_o < 0$ the external field exceeds the enclosed field, and flux creeps into the tube.

Leidener & Feile[91] found that rings cooled in small applied fields showed flux trapped only by a persistent current (Figure 5.1a), and that order of magnitude larger cooling fields were needed before any reduction in the enclosed volume field distribution due to flux in the material could be observed (all the fields in question were low here because of poor sample quality). Considering that intergranular effects are dominant, two mechanisms may contribute to the decay of trapped flux in a tube such as this: decay of the persistent current due to an apparent resistance, and thermally-activated creep of the trapped flux. Measurements by Yeh *et al.*[96] and Mohamed *et al.*[97] suggest that the latter is the responsible effect. Persistent currents have been measured to decay at much slower rates than trapped flux, and comparing the results for a disk, ring and cut ring seem to indicate that the observed trapped field decay is due to flux trapped in the intergranular regions. Comparing these results of others to the observations reported here, it appears that the decay of trapped field in the tube is predominantly due to flux creep through the intergranular network.

5.3 BSCCO tubes.

The shielding curves of BSCCO tubes #1 and #2 (4.1) were measured in a similar way to YBCO, and the corresponding magnetisation loops derived as above. Those of BSCCO #1 are shown in Figures 5.9 and 5.10 respectively, for temperatures of 77, 73 and 67K and an applied field sweep rate $\dot{B}_a = 1.5\text{mTs}^{-1}$. The resultant parameters may be summarised as:

	77K	73K	67K
B_{sh} (mT)	11.4	24.2	30.3
B_{tr} (mT)	10.7	23.8	29.4
J_c (Acm^{-2})	189	401	503

The opening angle of this tube is $\theta = 16.6°$, *i.e.* $\cos\theta = 0.958$. In this tube it is apparent that $B_{tr} \simeq B_{sh}$ at all the measured temperatures, and no enhancement of trapping is observed. In fact, the values given show B_{tr} slightly lower; this is because of the discrete field steps at which data was taken, so B_{sh} is probably slightly overestimated in the above since the precise point at which flux first penetrated the tube centre is not clear. B_{tr} data points could be taken more or less exactly at zero field. This is manifestly not the origin of the $B_{tr} > B_{sh}$ in the YBCO tube, since from the foregoing it is obvious that B_{sh} will always tend to be over- and never under-estimated.

The field dependence of J_c calculated from the magnetisation loop by equation (5.3) is shown in Figure 5.11. The zero-field values are equal to those found from the shielding curve within experimental error (77K: 173Acm^{-2}, 73K: 397Acm^{-2}, 67K: 494Acm^{-2}). Although the field at which the very fast fall-off of $J_c(B)$ begins increases with decreasing T, the strong J_c field-dependence is still clearly seen at these temperatures. There is insufficient data to try to find the temperature dependence of the critical current here; this will be returned to in Chapter 6. Surprisingly, J_c is slightly larger than for the YBCO tube. This is most likely to be due to improved

sample quality and density gained through the melt-process production, compared to the extruded and sintered YBCO tube (4.1).

The shielding and magnetisation of both BSCCO tubes were measured at 77K with various applied field sweep rates, $\dot{B}_a$, between 0.075 and 1.5mTs^{-1}. The lower rate was determined by the amount of heating that seemed reasonable to allow in the power supply, and the upper rate by the sweep unit used and the data collection rate to give a useful interval in B_a. These are shown in Figures 5.12 to 5.15, and a significant reduction in the width of the magnetisation loop with decreasing $\dot{B}_a$ is seen. The parameters obtained for tube #2 at 1.5mTs^{-1} are B_{sh}=3.7mT, B_{tr}=3.2mT and J_c=125Acm^{-2}; the opening angle of tube #2 is 40°, cosθ=0.766. The critical current is lower than that of tube #1, presumably reflecting sample quality. The field dependence of J_c of the two BSCCO tubes is compared in Figure 5.16; although tube #2 has a lower $J_c(0)$=110Acm^{-2}, the fall-off with applied field is rather less than tube #1, showing higher current densities at the higher fields. Both the magnetisation and current density plots of BSCCO #2 show a sharp dip at zero field. This is due to a high rate of flux creep which occurs in the field reversal time (data was collected continuously at set time intervals, including this "dead time").

The field dependence of the critical current found from (5.3) at the various sweep rates for tube #1 is shown in Figure 5.17. The curves show very similar shapes. Both the field at which the fast decline of $J_c(B)$ begins and that at which J_c=0 decrease with $\dot{B}_a$. In figure 5.18, the current density at 0, 5, 10 and 20mT for tube #1, and 0mT for tube #2, are plotted against $\dot{B}_a$ on a logarithmic scale, all showing linear relationships. The two tubes have practically the same gradient for 0mT as might be expected. Had a wider sweep rate range been available, we would expect to find that $J_c \propto \dot{B}_a$, up to an undecayed value J_{co} above a certain limit of $\dot{B}_a$. This dependence of "critical" current density on sweep rate is analogous to the voltage criteria used in four-point resistance measurements of J_c[95], and $\dot{B}_a$ defines the dissipative electric field. From the induction law,

$$E = \frac{d\Phi/dt}{2\pi R} = \frac{R}{2}\frac{dB_a}{dt} \qquad (5.6)$$

where R is the mean sample radius (*i.e.* taken here as the radius of the centre of the tube wall). Translating the sweep rates here accordingly, we find E between $37.5\mu Vcm^{-1}$ and $1.69mVcm^{-1}$. Obviously these are not particularly useful criteria for comparison to the usual $1\mu Vcm^{-1}$, but Polák *et al.*[98] have shown that identical measurements on a small YBCO thin-film ring can give much greater sensitivities than those possible with contact methods.

The field sweep rate dependence of magnetisation loop width has previously been observed in solid HTS samples[99][100], and it has been shown theoretically[101] that the conventional relaxation model of Anderson[6] relates the behaviour seen here directly to that of "conventional" flux creep at $B_a=0$. The relaxation rates can be equated:

$$\frac{dM}{d(\ln\dot{B}_a)} = -\frac{dM}{d(\ln t)} \qquad (5.7)$$

Because magnetisation hysteresis measurements are often easier to perform than those of flux decay, the method described above may in many cases provide a more convenient and more sensitive route to discovering flux creep characteristics.

Figure 5.18 indicates that, as expected, the relaxation is more pronounced as the applied field increases: the gradient of $dJ_c/d(\ln\dot{B}_a)$ increases rapidly from 0 to 10mT. At very low J_c, for $B_a=20mT$, the gradient is much less. This is where the curves of $J_c(B)$ in Figure 5.17 begin to converge. One of the restrictions of the critical state model is to fields well below H_{c2}; considering the weak-linked intergranular network, this field is clearly being approached at 20mT.

Applying equation (5.7) to the magnetisation values $M(0)$, corresponding to the ZFC case, of BSCCO #1 for $0.075<\dot{B}_a<1.5mTs^{-1}$ gives $dM/d(\ln\dot{B}_a)\simeq 1$. This may be compared to the directly measured ZFC relaxation up to 3200s shown in Figure 5.19

for the tube with B_M=80mT. The trapped flux decay shows a crossover between two ln$t$ regions around 150s, from dM/d(ln$t$)≃-0.6 to dM/d(ln$t$)≃-0.4. The initial magnetisation $\mu_o M_o$≃9mT, giving U_o≃-0.1eV and -0.15eV for the two regions respectively. As would be expected, these are rather lower than U_o measured for the YBCO tube. The slopes |dM/d(ln$t$)| are of the same order of magnitude as dM/d(ln$\dot{B}_a$); given the limited $\dot{B}_a$ range this seems reasonable agreement.

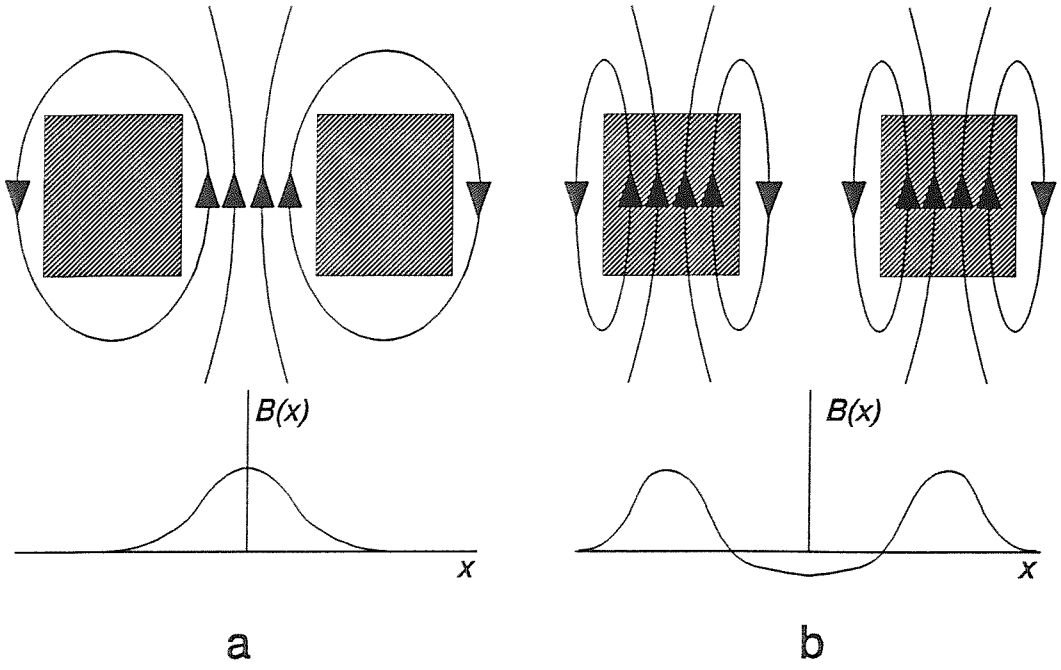

Figure 5.1 Magnetic field pattern and flux distribution of (a) ideal superconducting ring with persistent current enclosing trapped flux in centre only, (b) ring with flux trapped in bulk material only.

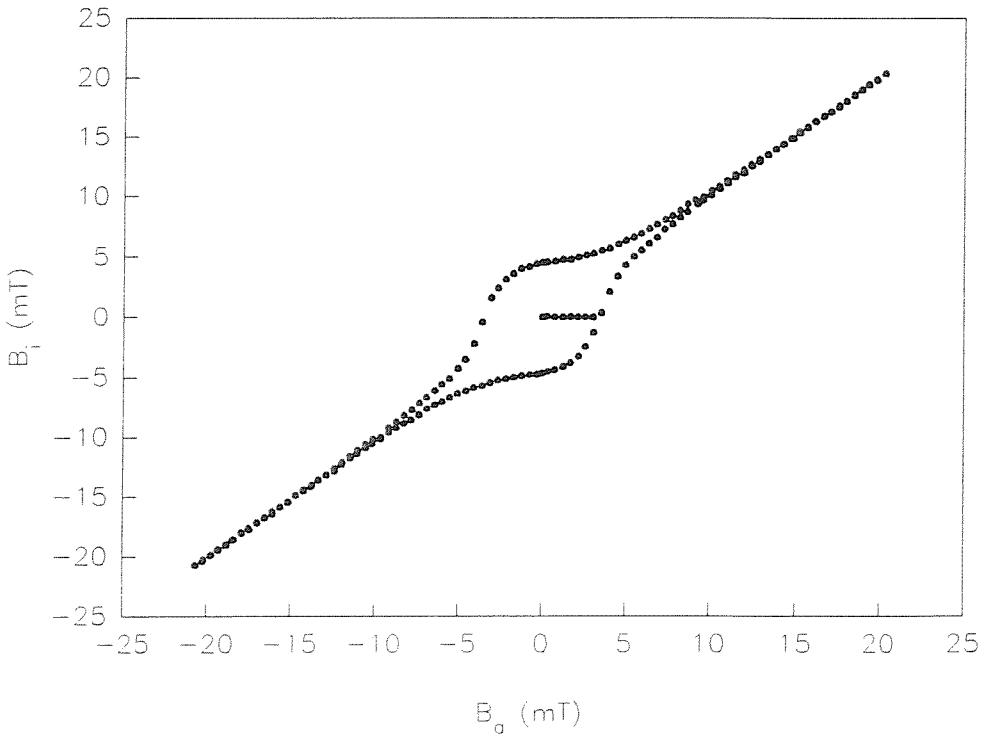

Figure 5.2 Shielding curve of YBCO tube at 77K.

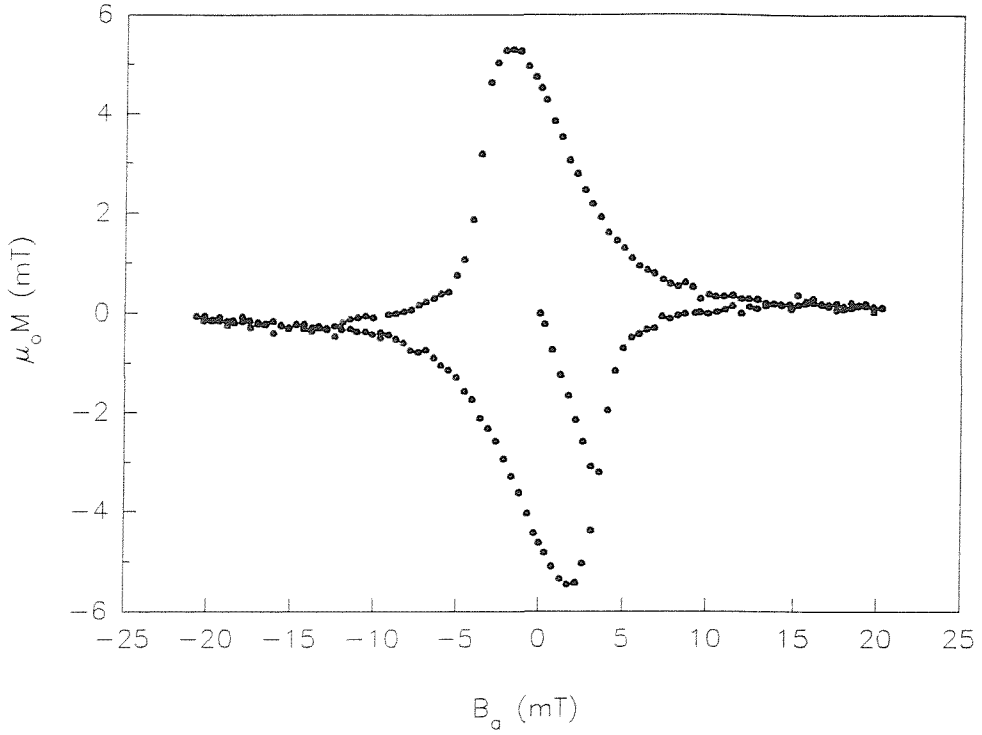

Figure 5.3 Magnetisation loop of YBCO tube at 77K.

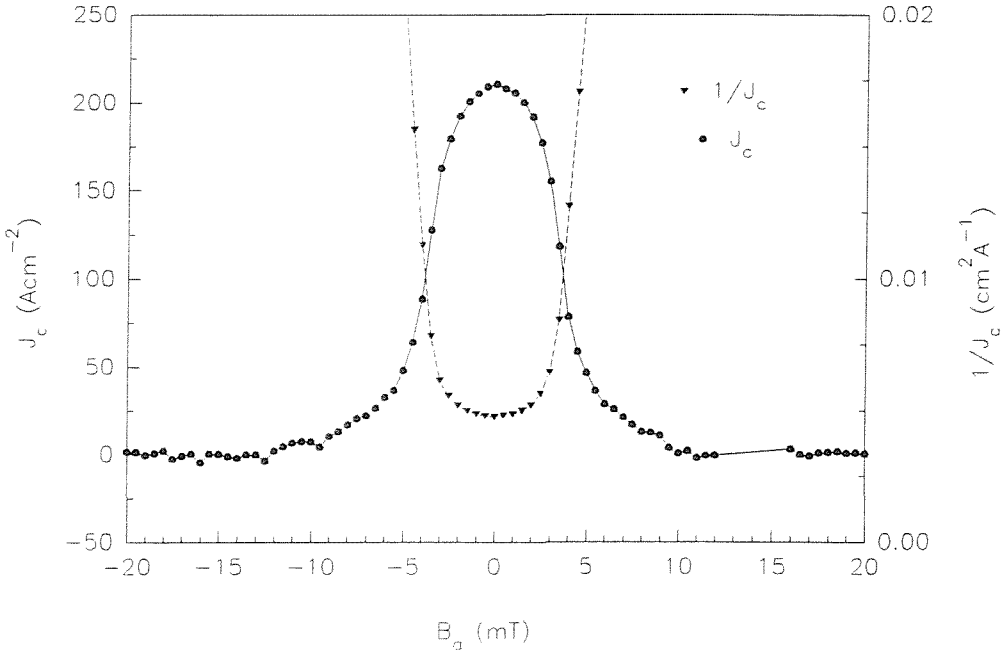

Figure 5.4 Critical current density variation with applied field derived from magnetisation.

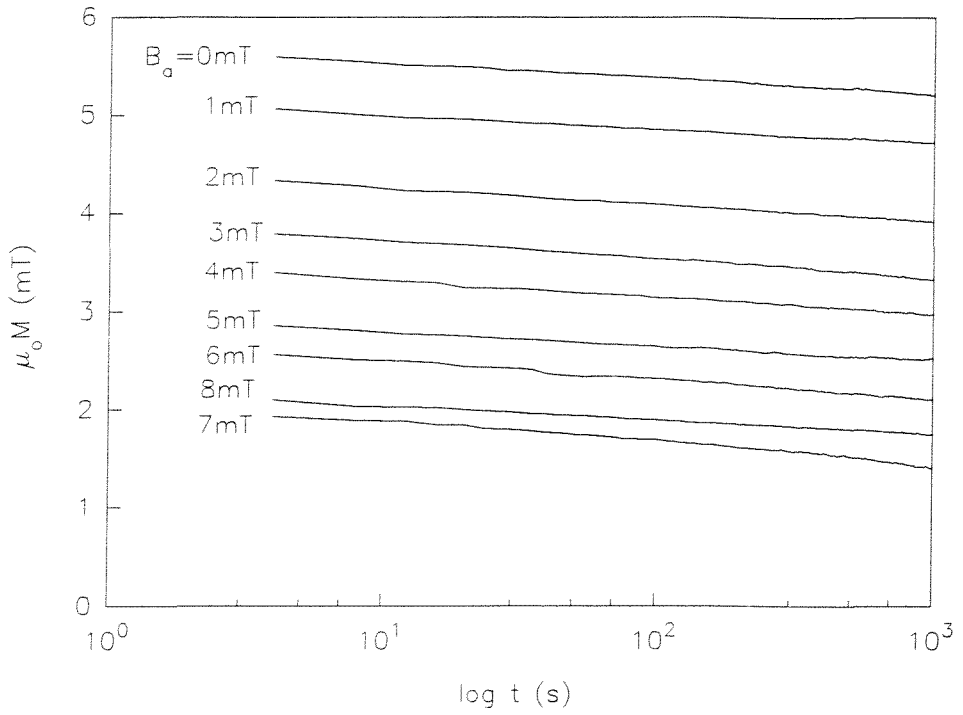

Figure 5.5 Decay of magnetisation in zero-field-cooled YBCO tube.

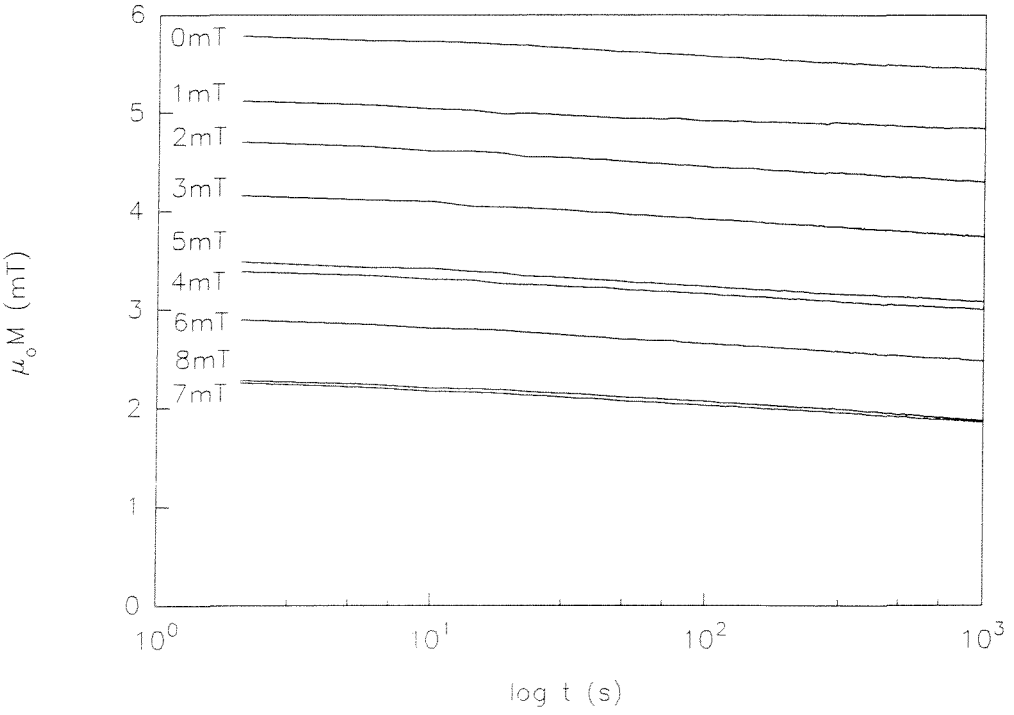

Figure 5.6 Decay of magnetisation in field-cooled YBCO tube

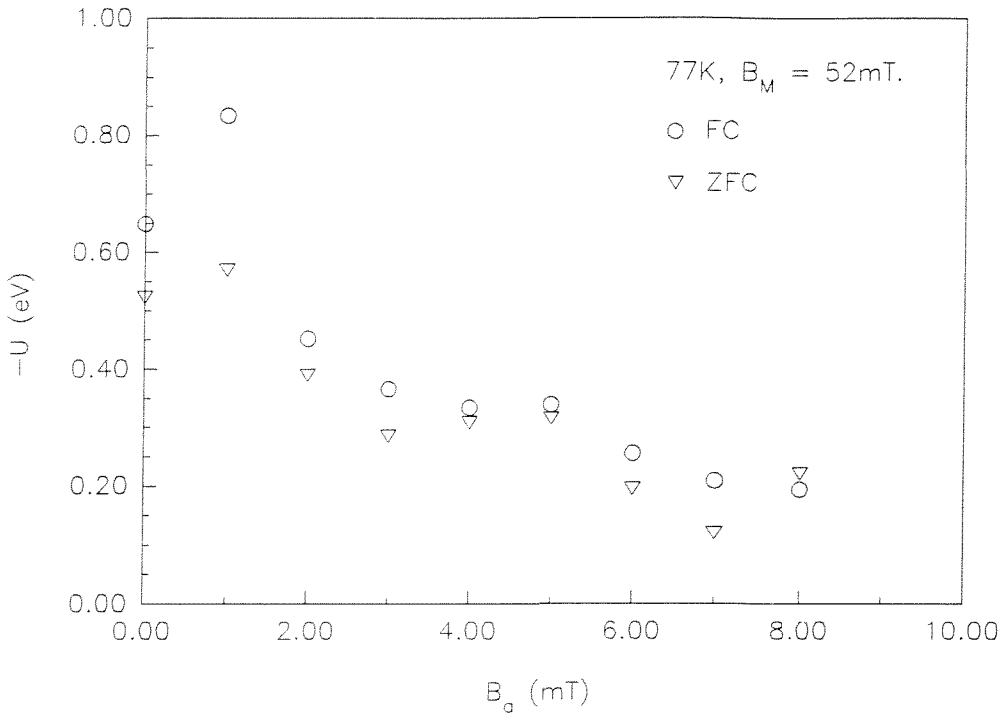

Figure 5.7 Variation of pinning energy with applied field for ZFC and FC YBCO tube.

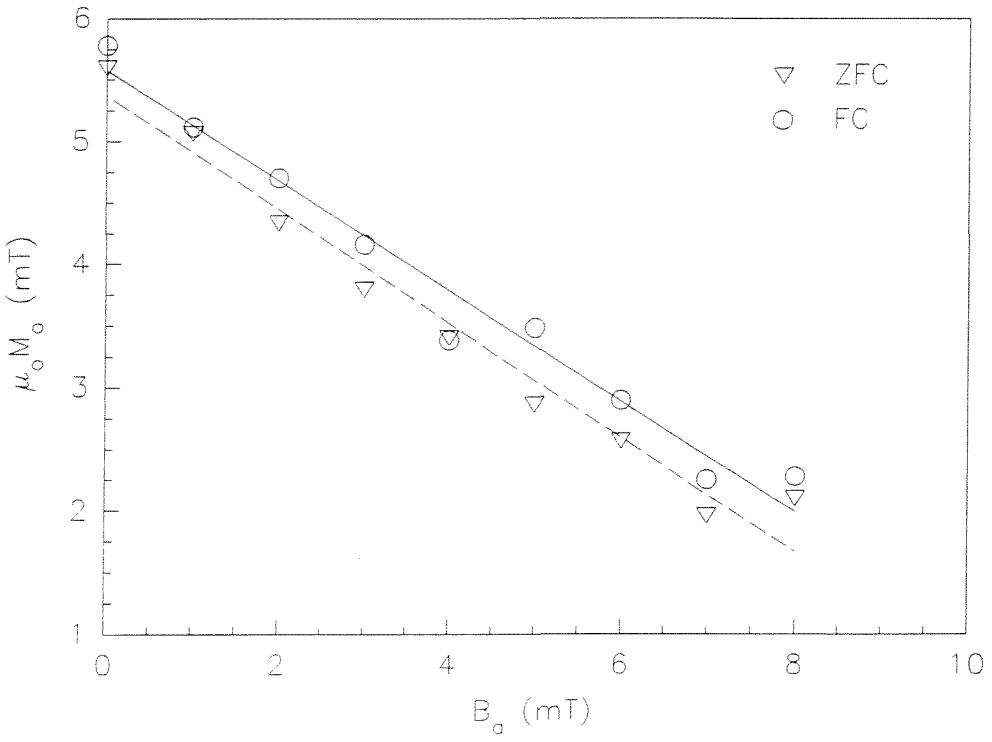

Figure 5.8 Variation of initial remanent magnetisation with applied field for ZFC and FC YBCO tube.

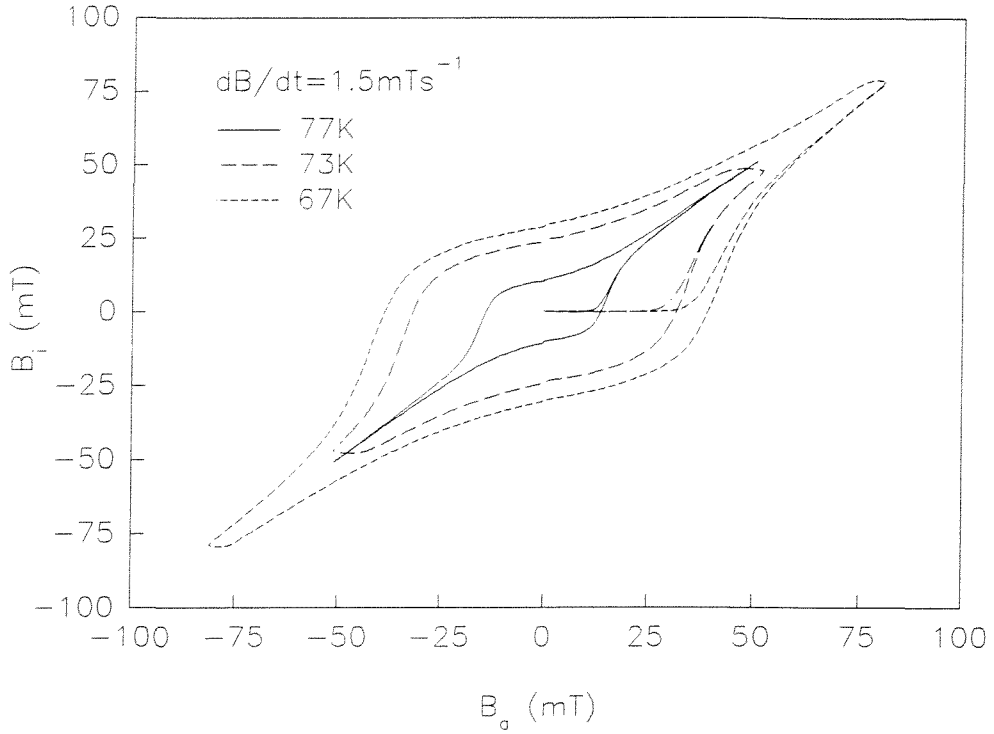

Figure 5.9 Shielding curve of BSCCO #1 at 77, 73 and 67K.

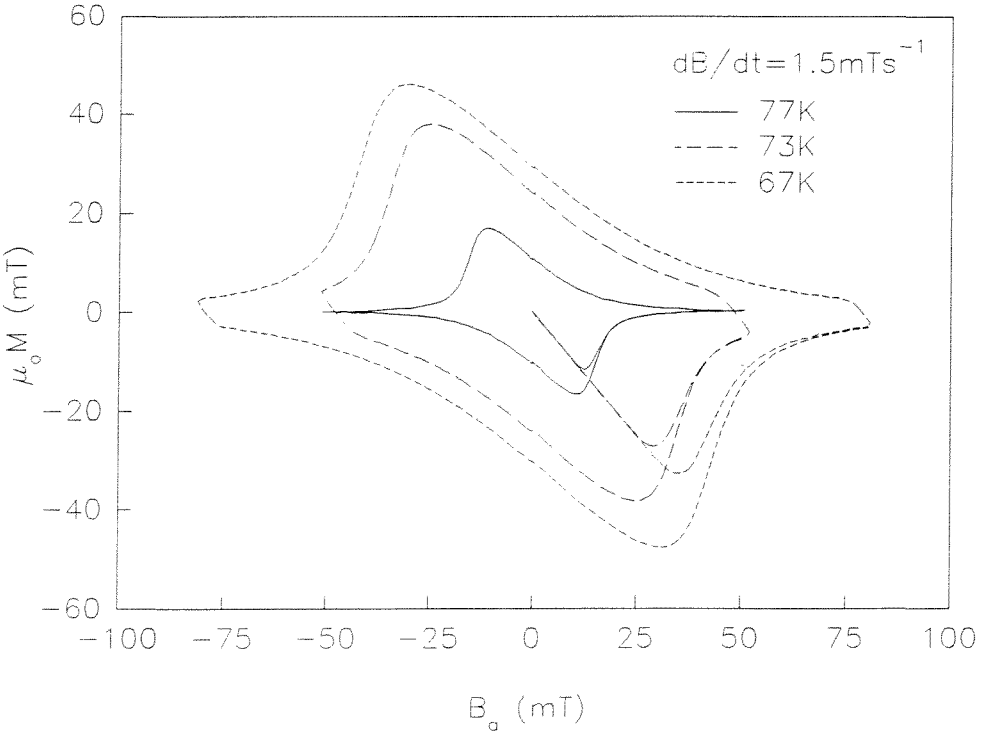

Figure 5.10 Magnetisation loop of BSCCO #1 at 77, 73 and 67K.

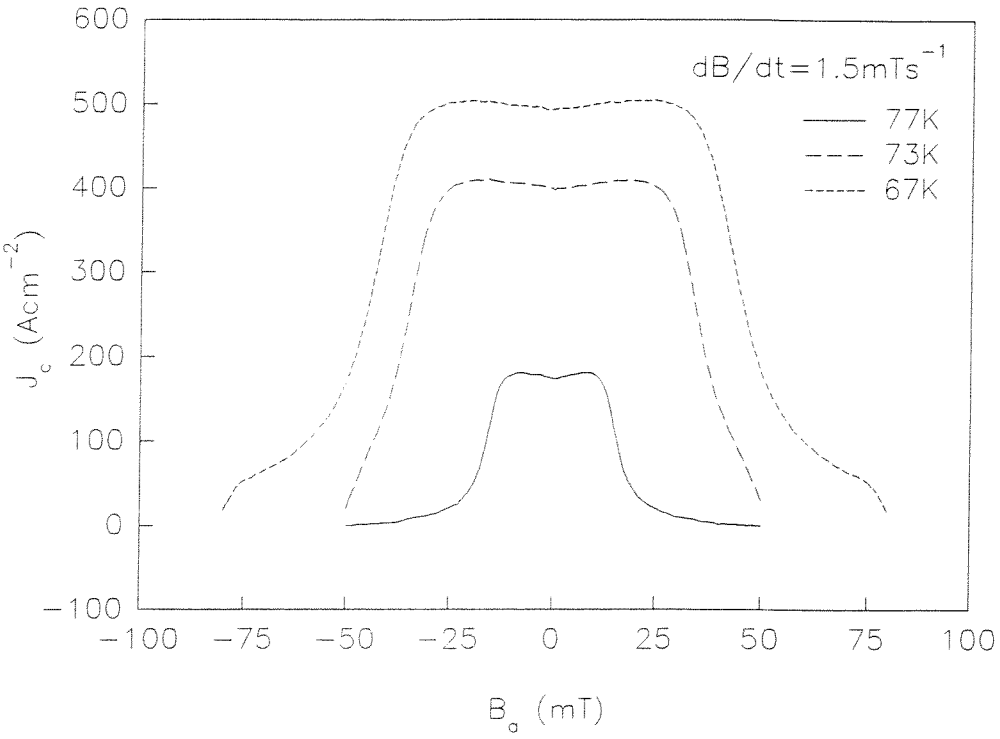

Figure 5.11 Field dependence of critical current for BSCCO #1 at 67, 73 and 77K, 1.5mTs^{-1}.

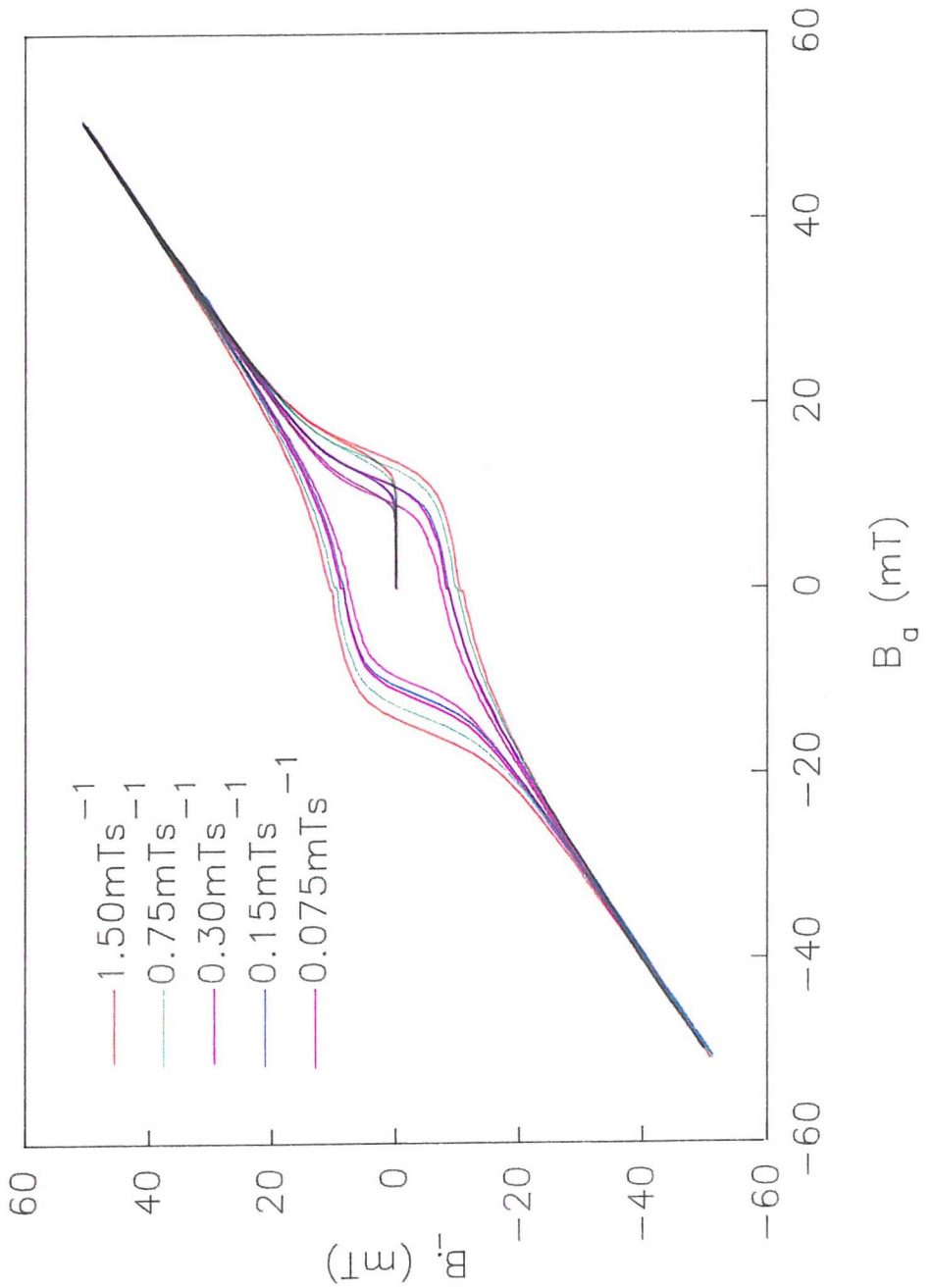

Figure 5.12 Shielding curve of BSCCO #1 at 77K for various applied field sweep rates.

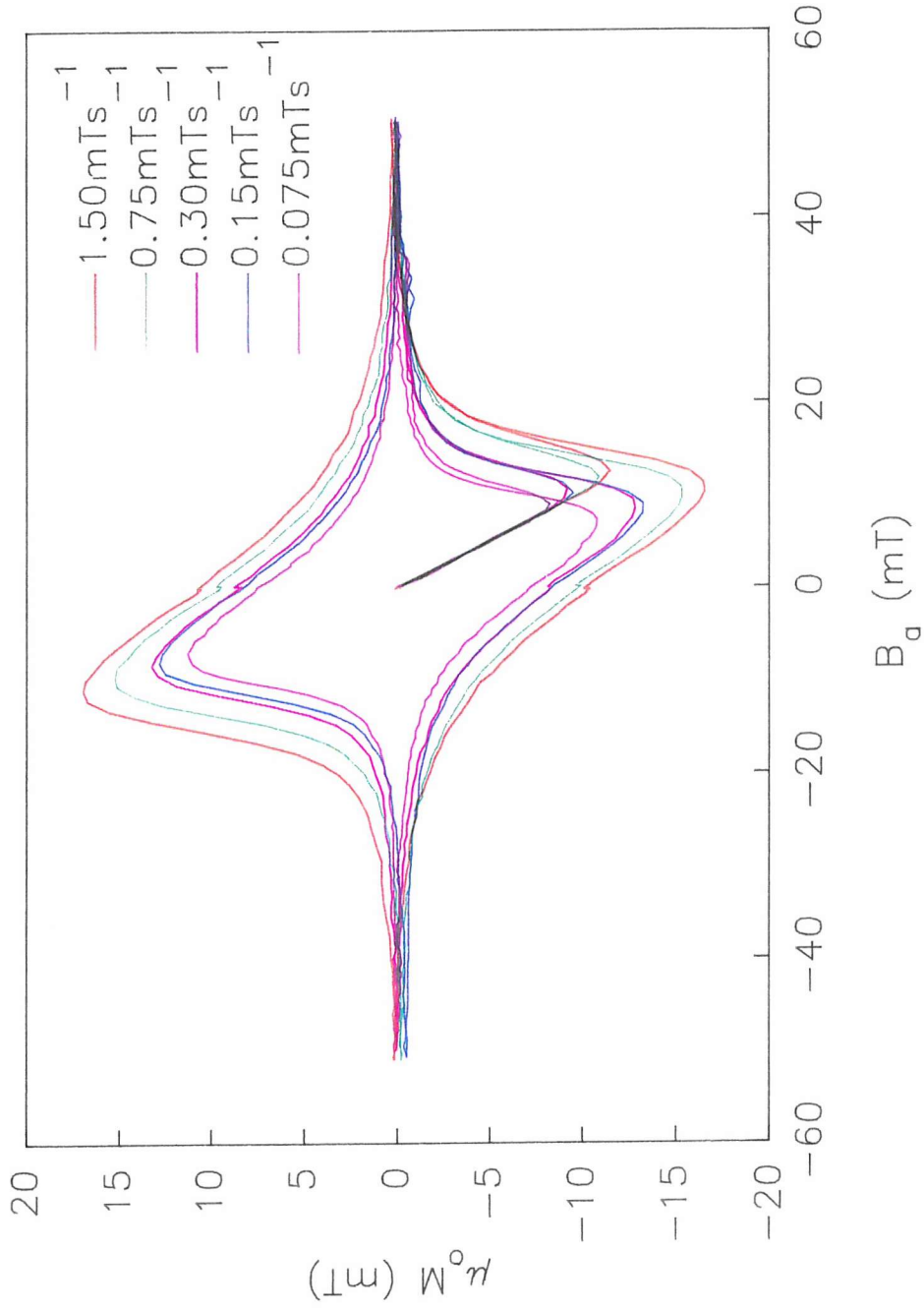

Figure 5.13 Magnetisation loops for BSCCO #1 at 77K and various applied field sweep rates.

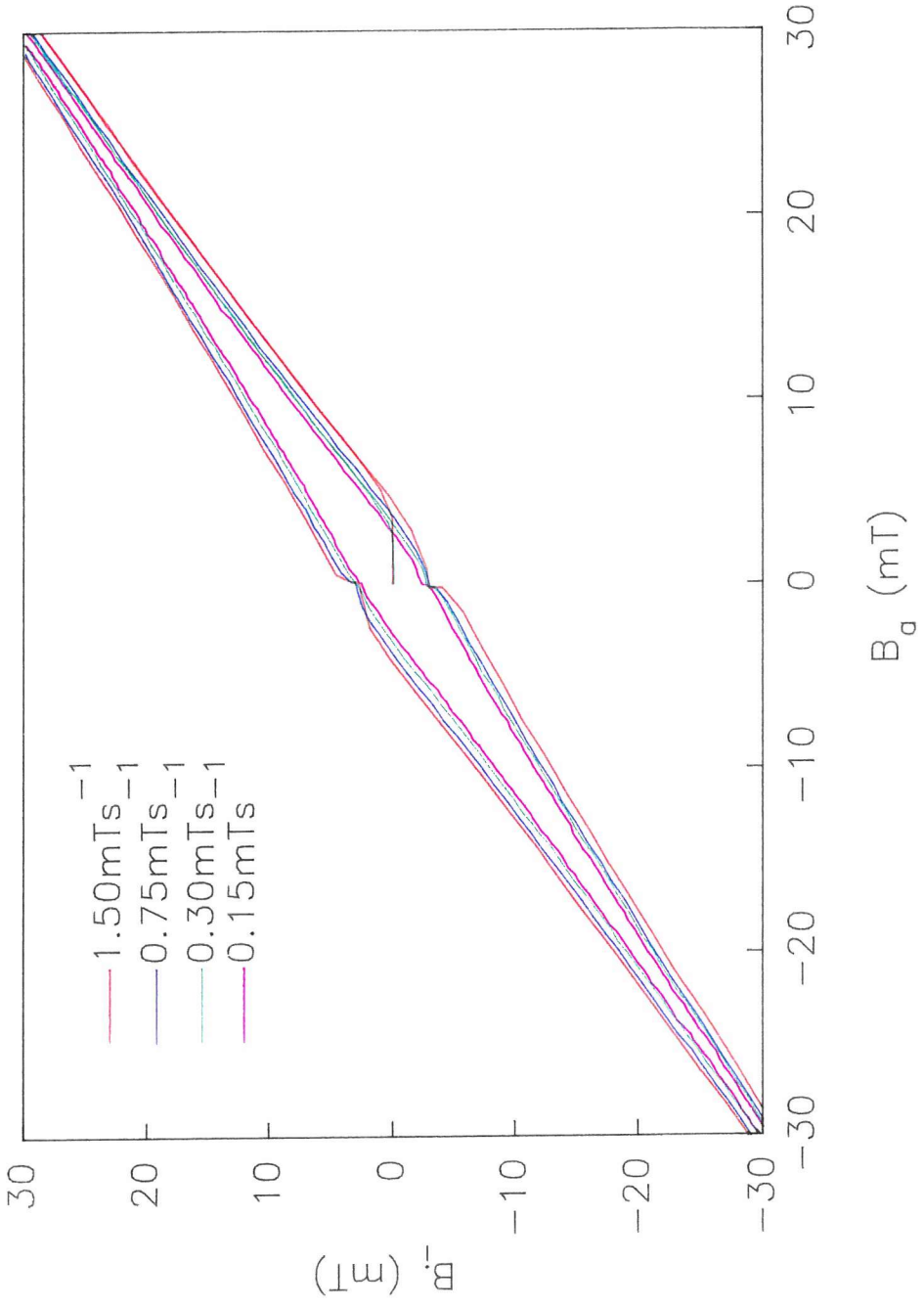

Figure 5.14 Shielding curve of BSCCO #2 at 77K for various applied field sweep rates.

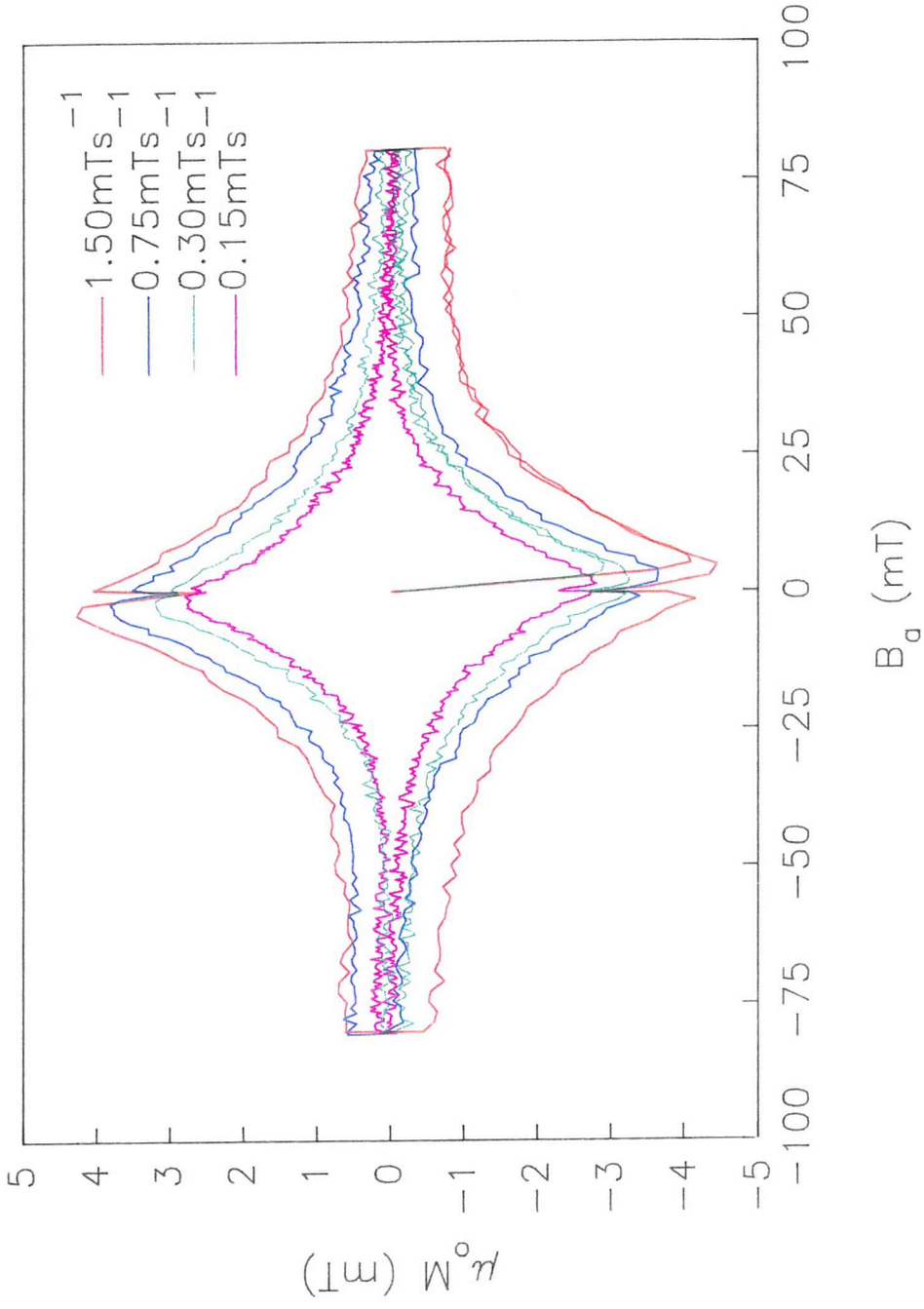

Figure 5.15 Magnetisation loops for BSCCO #2 at 77K and various applied field sweep rates.

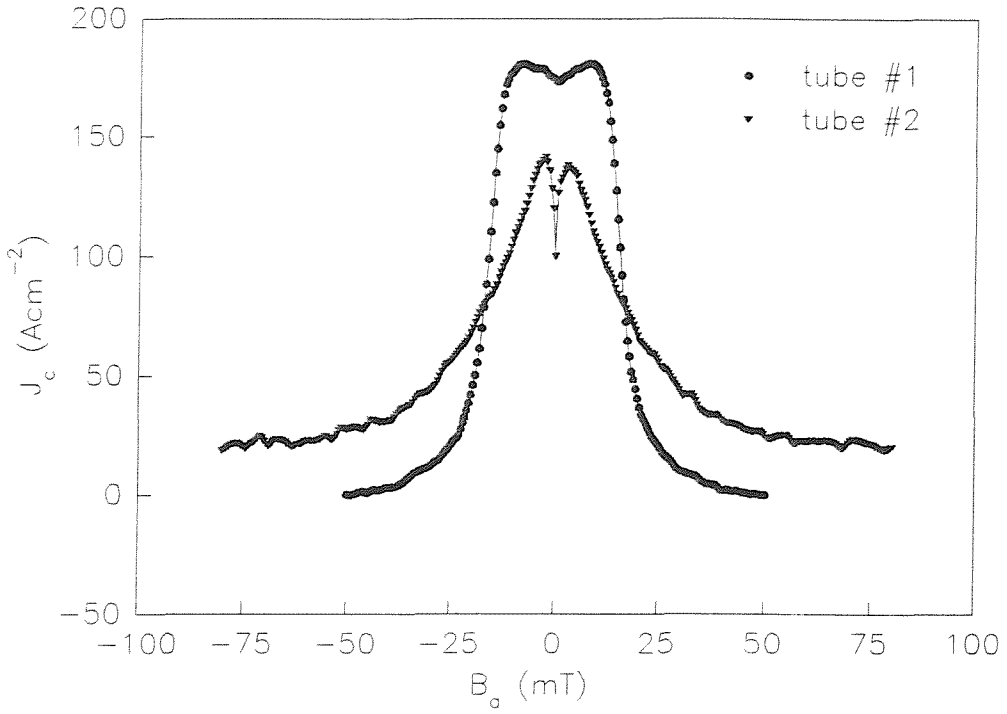

Figure 5.16 Field dependence of critical current for BSCCO tubes at 77K, 1.5mTs^{-1}.

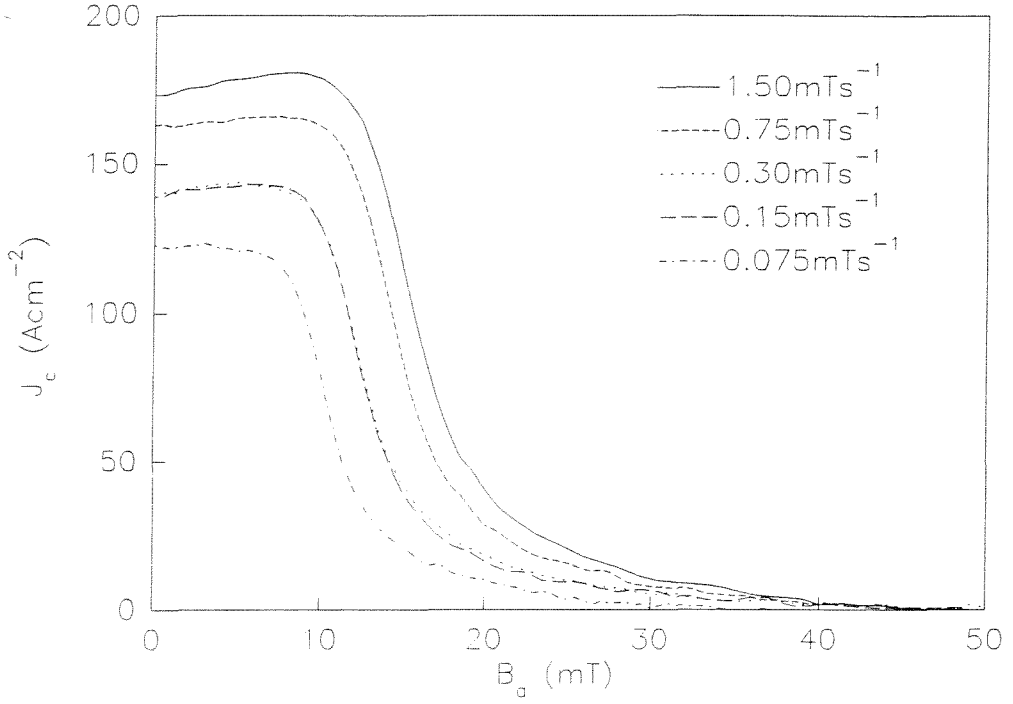

Figure 5.17 Field dependence of critical current for BSCCO #1 at 77K and various applied field sweep rates.

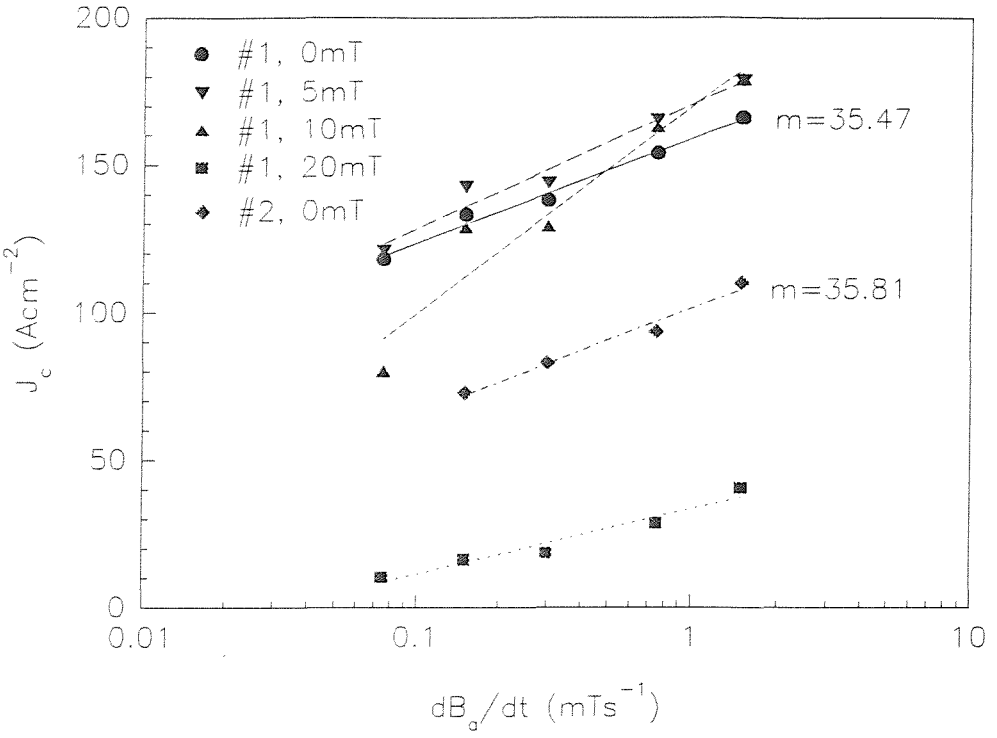

Figure 5.18 Critical current dependence on applied field sweep rate for BSCCO tubes.

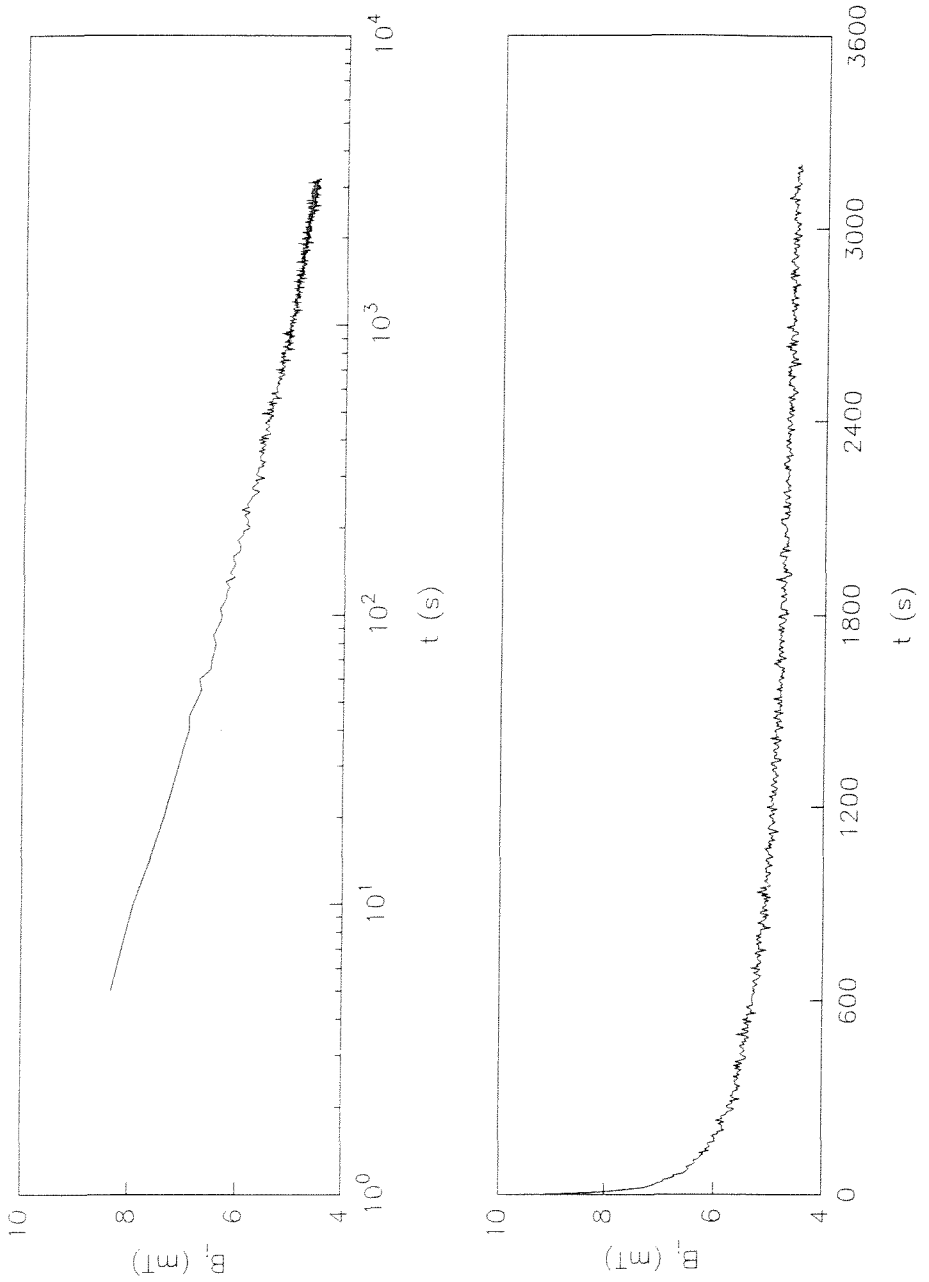

Figure 5.19 Relaxation of trapped field in zero-field-cooled BSCCO #1.

6 Experimental results, 2.2-4.5K.

6.1 YBCO tube.

6.1.1 Low-field measurements.

Measurements on the YBCO tube at low temperatures were initially performed at 4.2K with the sample immersed in liquid helium. A double glass cryostat was used for this, mounted axially in the copper-wound solenoid with the tube in the region of maximum field. The shielding curve and resulting magnetisation loop for a sweep rate of 1.5mTs^{-1} (0.09Tmin^{-1}) are shown in Figures 6.1 and 6.2 respectively. The shielding curve gives $B_{sh} \simeq 17\text{mT}$, $B_{tr} \simeq 17.3\text{mT}$ and $J_c = 783\text{Acm}^{-2}$. In contrast to the 77K results, the difference between B_{sh} and B_{tr} is almost negligibly small given that the B_a intervals were quite large, making it difficult to find B_{sh} exactly. The magnetisation curve and the J_c field-dependence found from it (Figure 6.3) show that, similarly to the 77K curves, the critical current initially falls off very quickly with applied field, although not by the order of magnitude seen at 77K. However, at 4.2K the decrease in $J_c(B)$ at higher fields is much less; the width of the magnetisation loop is almost constant, and there is no indication that the upper critical field of the intergranular network is being approached. No flux jumping occurs at these low fields, as one would expect from the predictions in 2.4.1.

6.1.2 Measurements to 3T.

Since a persistent superconducting current seemed to extend to much higher fields than the copper solenoid could provide, the YBCO tube was mounted in the 3T

superconducting magnet (4.3.2) and cooled to 4.5K. Thermal contact was maintained by a helium exchange gas at 1Torr throughout the experiments. It is not clear why the magnet and sample (at the same temperature) did not quite cool to 4.2K. Measurements errors were considered and subsequently ruled out, and there were no obvious heat leaks since all the instrumentation wires were thermally dumped on entering the sample space. The magnet cooled down to this temperature consistently, to within less than ± 0.02K, and readings at 2.2K were always accurate, so the temperature measurement was accepted as accurate (time did not permit further investigation of the cryostat). The cryostat was always left overnight once filled with LHe before any measurements were made to ensure thermal equilibrium.

The shielding and magnetisation curves to ± 3T at 4.5K are shown in Figures 6.4 and 6.5 respectively, for a sweep rate of 0.31Tmin^{-1}. It is immediately obvious that the hysteresis is much greater than the 4.2K magnetisation, and the magnetisation loop shape is very different. From the shielding curve, $B_{sh} \simeq 0.05$T, $B_{tr} \simeq 0.07$T and $J_c = 2300$Acm^{-2}. The magnetisation curve is quite noisy due to the small B_i-B_a difference, and this makes it difficult to obtain a $J_c(0)$ value from the magnetisation curve, as the J_c field-dependence in Figure 6.6 shows. A value of $J_c(0) \simeq 3500$Acm^{-2} is estimated. The high rate of flux creep at the $B_a = 0$ crossings is clear from the magnetisation loop, and again makes $J_c(0)$ difficult to find accurately. Other features of the magnetisation which require some explanation are the spikes which appear at high fields in both positive and negative, increasing and decreasing, applied field. The most likely source of these is non-linearities in B_a; these could not be seen in a $B_a(t)$ plot, but may be very small since the magnetisation is quite weak. A sharp decrease is seen at around 0.5T in M which might be identified as a flux jump. However, examination of B_i shows no sudden decrease in magnitude, and given the noise present in the measurement such a conclusion cannot be reliably drawn.

The very different shapes and sizes of the magnetisation loops at 4.5K, 0.31Tmin^{-1} and 4.2K, 0.09Tmin^{-1} suggest that, similarly to the BSCCO tubes at 77K, the magnetisation hysteresis is field sweep rate dependent. Further 4.5K measurements were made to ± 1T giving the set of hysteresis loops in Figure 6.7; the ± 1T,

0.31Tmin^{-1} loop fitted as an exact sub-loop of that at 4.5K and the same $\dot{B}_a$. These show that the width of the magnetisation loop does indeed depend on $\dot{B}_a$, an outcome which is surprising at such low temperatures where flux creep would be expected to be extremely low. The loop at 0.062Tmin^{-1}, however, is still much larger and quite different to the 4.2K, 0.09Tmin^{-1} loop. Although it might at first appear that this could be explained in terms of granularity as discussed in 5.1, this does not in fact seem to be the case. If the 4.5K loops were intragranular in origin, we would still expect to see a loop similar to that at 4.2K in the virgin case, up to the upper critical field of the intergranular network, with the magnetisation changing sign and the intragranular component being observed to higher fields. However, the virgin curve at 4.5K (Figure 6.5) proceeds directly to the main hysteresis loop, suggesting that it is still the intergranular component which is being observed. No satisfactory interpretation of these results can be given at present.

The tube was also measured at 2.2K, 0.31Tmin^{-1} (Figure 6.8). The shielded field $B_{sh} \simeq 0.07$T is slightly larger than at 4.5K, giving $J_c = 3225$Acm^{-2}, while $B_{tr} \simeq 0.072$T is very similar to that at 4.5K, and the magnetisation loops are virtually identical. The same irregular features occur as at 4.5K, in almost exactly the same positions. No flux jumping was observed down to this temperature; it may be that, as has been found in other HTS, the flux creep which is evident from the magnetisation loops is acting to stabilise the sample against flux jumping.

6.2 BSCCO tube #1.

6.2.1 Temperature dependence of flux jumping.

Shielding curves of the BSCCO #1 tube were measured in the 3T superconducting magnet. Temperatures below 4.5K were obtained by use of the lambda point fridge

(LPF) which was regulated by a needle valve to give measurements at 3.8, 3.2 and 2.7K. To reach 2.2K, the LHe lambda point, the pressure above the helium was reduced by pumping directly on the LHe space. As it was difficult to control the temperature over long times with the LPF needle valve, the maximum sweep rate of $0.31 T min^{-1}$ was used in examining the flux jumping temperature dependence. The temperature could not be controlled during the time of the experiment because of the magnetic field effect on the SMDT (4.2.2).

The curves obtained are shown in Figures 6.9 to 6.18, and indicate that the sample is quite far from full penetration. Following Chen *et al.*[68], the first flux jump field B_{fj} is found as the difference between the maximum (minimum) field and that at which flux jumping first occurs. This assumes an ideal Bean model. The virgin curve was measured for the 4.5, 3.8 and 2.2K cases (4.5 and 2.2K shown in Figure 6.20, 3.8K is almost indistinguishable from 4.5K); it was found that curves taken immediately after the virgin curve and those following several field excursions showed no difference. Because the whole cryostat had to be heated to above T_c to return the tube to the normal state it was not practical to do this for every measurement, both in terms of time and LHe use. Because of flux jumping across the B_a=0 line B_{tr} could not be measured at this sweep rate. The numerical values found are:

T (K)	B_{fj} (T)	B_{sh} (T)	J_c (Acm^{-2})	First f.j. in virgin curve (T)
4.5	1.73	0.48	7975	1.24
3.8	1.71	0.485	8060	1.14
3.2	1.70	-	-	-
2.7	1.65	-	-	-
2.2	1.56	0.49	8140	1.10

It should be noted that B_{fj} is not synonymous with the field at which flux jumping first occurs in the virgin curve.

The temperature dependence of B_{fj} is shown in Figure 6.19 and indicates a smooth decrease with T. This is as expected at low temperatures. As described in 3.6, it was found that B_{fj} initially increases as T decreases from T_c, reaching a maximum and then decreasing[39]. From the calculations of Wipf[54] and Laquer *et al.*[55], it is expected that the low temperatures here will be well within the decreasing B_{fj} region since $B_{fj}(T)$ peaks around 60 to 70K. Although $B_{fj}(T)$ in Figure 6.19 seems to be approaching a plateau around 5K, the temperature range is really too small to attach much quantitative importance to an analytical form for B_{fj}; in fact in this region the temperature dependence is likely to be almost linear. The numerical B_{fj} values found are somewhat higher than those predicted for HTS at low temperatures[59][69] but are on a par with some experimentally observed at 5K in melt-processed YBCO[68], albeit at lower $\dot{B}_a$. Conclusive comparisons are difficult to make because of the variability of HTS materials. It may be observed that the first flux jumps at this high sweep rate are close to the maximum field at which they would be observable for the field excursion in these loops, given the $B_i=B_a$ region. This is not ideal, and higher field excursions would be useful.

Although adiabatic theory can be used to predict B_{fj}, this requires a knowledge of the specific heat of the superconductor and its temperature dependence, which is not clearly agreed upon despite extensive studies (Junod[102] and references therein); the predictions for HTS are usually based on some approximation of $C(T)$. While this may be reasonable for a generic HTS material, it cannot be as easily applied to a specific real one. This theme will be returned to in 6.2.3. The general form of the flux jumping equation,

$$B_{fj} = [3\mu_o \gamma C \frac{J_c}{dJ_c/dT}]^{\frac{1}{2}} \qquad (6.1)$$

does not assume the $J_c(T)$ dependence and may therefore be more useful in considering experimental data where dJ_c/dT is available. These all point to the need for further good HTS data over a wide temperature range. The major limitation of the adiabatic theory is of course that $\dot{B}_a$ is not taken into account, and the qualitative empirical forms outlined in 3.6 are resorted to. Although the theory developed by

Yamafuji *et al.*[49] does account for $\dot{B}_a$, detailed knowledge of other parameters such as heat transfer are also required.

The symmetry in the shielding and magnetisation loops is clear in the Figures, although sometimes a large jump is "mirrored" by two smaller jumps in the other half of the magnetisation. A common feature is that large jumps may be preceded by small ones. All the flux jumps are incomplete. LTS measurements have shown that the number of jumps in the magnetisation loop tends to increase with decreasing temperature, and that the jump spacing decreases with T, increasing again at low temperatures. Here it is found that the total number decreases with temperature: from 31 in M^+ at 4.5K to 19 at 2.2K. Consideration of the number, spacing and magnitude of flux jumps at the temperatures above points out some very interesting effects. A close examination of these may help to clarify the flux jumping process in HTS. Plotting the size of the flux jump, ΔM^{fj}, against the applied field at which the jump occurs, B_a^{fj}, shows quite a marked behaviour at $B_a^{fj} < -1.2$T and $> +1.2$T, as seen in Figures 6.21 and 6.22, and might be thought of as showing three regions of flux jumping grouped by jump size. This is in contrast to most HTS measurements in which flux jumps around a magnetisation loop are of quite a constant size (at least compared to those here); jumps of decreasing amplitude were observed in virgin curves of LaSrCuO[76] although full penetration was being approached, clearly not the case here.

In the flux trapping region, *i.e.* $|B_a|$ decreasing, three large jumps are observed in M^+ and M^- at all the temperatures. The spacing of these is very similar for the different temperatures, although slightly less for 2.2K. On entering the annihilation region (quadrants 1 and 3) a number of smaller jumps is found which show a general trend of increasing magnitude with decreasing temperature. These cannot be solely identified with vortex annihilation however since the jumps also extend into quadrants 2 and 4. For $B_a^{fj} > +1.2$T and < -1.2T a clear temperature dependence is present in the flux jump size. At 4.5K, the jump amplitude decreases exponentially; this portion of the magnetisation looks similar to an underdamped simple harmonic oscillator. With decreasing temperature the initial size increases and the decrease in amplitude

with B_a^{fj} decreases. At 2.2K the small jumps are of almost constant size. It is also in this region that the number of jumps changes, decreasing with temperature. The field spacing of the jumps is quite uniform for $T \leq 3.8$K, and increases with decreasing temperature. The observation of these small flux jumps is a novel feature not reported elsewhere. In all cases flux jumping seems to continue to ± 3T, so that higher field measurements would be useful to see whether an exponential decay in ΔM^{fj} is seen at progressively higher fields for decreasing temperature. The origin of the flux jump structure described above will be considered in 6.2.3.

The conclusions here are very much qualitative in nature, mainly due to the limited temperature range over which the measurements were performed. In light of probable applications at 20 to 30K an extended range is highly desirable. The sweep rate dependence of flux jumping is considered in the next section, and shows that the maximum sweep rate, where there are jumps all round the loop even at 4.5K, is not in fact the best to use in examining the effect of temperature, and slower rates would be more enlightening if the sample temperature could be stabilised over the necessary time.

6.2.2 Sweep rate dependence of flux jumping.

The effect of applied field sweep rate on flux jumping in BSCCO #1 at 4.5 and 2.2K is shown by the shielding and magnetisation loops in Figures 6.9, 6.10, 6.17, 6.18 and 6.23 to 6.44. The sweep rates used and the resulting B_{fj} (calculated as described in 6.2.1) at either temperature were as follows:

$\dot{B}_a$ (Tmin^{-1})	B_{ff} (T), 4.5K	B_{ff} (T), 2.2K
0.31	1.75	1.56
0.256	1.83	1.65
0.225	1.88	1.73
0.17	2.15	1.72
0.144	2.98	1.764
0.124	3.19	1.76

At 0.093Tmin^{-1} no flux jumping is present at 4.5K (Figures 6.33 and 6.34), so that this may be taken as the equilibrium curve. Because of the long time required at this rate a 2.2K measurement was not done. The trapped field B_{tr} can be found from this loop and compared to the virgin curve value of B_{sh} found at 0.31Tmin^{-1}; a comparison of the loop sizes shows that the magnetisation width is independent of sweep rate. A $B_{tr} \simeq 1.0$T was found, almost twice the value of $B_{sh} \simeq 0.48$T reported in the previous section, but equal to the $B_a(B_i=0)$ value found here. It was noted in 5.2.1 that if additional flux trapping in the grains was the reason for the enhanced B_{tr} over the virgin curve B_{sh}, the $B_a(B_i=0)$ value would be larger than B_{sh}[25]. This is indeed the case here, so granular effects may be appropriately considered. A $J_c(0) \simeq 17200$Acm^{-2} is found from the magnetisation, and the decrease in fields up to 1T is very small, as shown in Figure 6.45 (67 and 77K $J_c(B_a)$ are shown for comparison). This low critical current field-dependence is typical of BSCCO at low temperatures up to much higher fields than 1T (although the maximum $B_a = \pm 3$T, the critical current cannot be found in the $B_i \simeq$ constant region on the returning B_a). Once more, an extension to significantly larger applied fields would be very useful. Since these tubes are now available "off the shelf" at a reasonable price (£100-£200) it would be feasible and worthwhile to perform these measurements on a cut tube to obtain direct information on the granular magnetisation.

The relationship between B_{jj} and $\dot{B}_a$ was described in 3.6; that derived by Watson[40] gives

$$B_{jj} \propto \log \dot{B}_a \tag{6.2}$$

over most of the sweep rate range, and

$$\log B_{jj} \propto \frac{1}{\dot{B}_a} \tag{6.3}$$

at low sweep rates. These can be compared with the $B_{jj}(\dot{B}_a)$ results found here. Figure 6.46 shows each on linear axes, and B_{jj} decreases with increasing $\dot{B}_a$, the decrease being much more marked for 4.5K. The 2.2 and 4.5K points begin to converge for 0.225Tmin^{-1} and above, suggesting a transition to the same dependency. The $B_{jj}(T)$ values at 0.31Tmin^{-1} lie between the 2.2 and 4.5K points, and thus suggest that points for temperatures between these also lie between the respective lines at lower sweep rates, as one would expect. The relationship at low $\dot{B}_a$ is considered by plotting $\log B_{jj}$ against $1/\dot{B}_a$ as in Figure 6.47. This dependency may be good for all points at 2.2K, and the lowest rates at 4.5K, but is clearly not held for the whole 4.5K range. The more general dependence of (6.2) is shown in the linear plot of Figure 6.46, and can certainly be said to hold for $\dot{B}_a \geq 0.225\text{Tmin}^{-1}$ at either temperature. As stated in 3.6, the value of $\dot{B}_a$ at which the relationship deviates from (6.3) increases with temperature. While there is a clear break in the dependence at 4.5K, there is not sufficient data to be conclusive as to the nature of the change, although qualitative agreement with established LTS relations is found.

Considering the form of the magnetisation loops one can see a similar exponential decay of small jumps in the shielding regions at 0.256 and 0.225Tmin^{-1} at 4.5K to that at 0.31Tmin^{-1}. At the lower sweep rates the jumps extend to lower B_a, and by 0.17Tmin^{-1} this structure is no longer apparent. All of the loops show symmetry in M^+, M^- and were found to be highly reproducible around subsequent field excursions. The total number of jumps decreases with sweep rate as one would expect from the empirical results of 3.6. Both the large and small flux jumps can be seen to "grow" with increasing $\dot{B}_a$. At 2.2K the same behaviour is seen, but is less obvious. Flux

jumping clearly extends to sweep rates well below $0.124 \mathrm{Tmin}^{-1}$, where at 4.5K jumping ceases between 0.124 and $0.093 \mathrm{Tmin}^{-1}$: this concurs with Watson's finding[40] that there is a temperature for given $\dot{B}_a$ above which flux jumping does not occur. The number of jumps in each quadrant of the magnetisation was found to obey the general rule of Q1=Q3, Q2=Q4=Q1-1 after the initial magnetisation curve[39]. Although symmetry gives Q1=Q3 and Q2=Q4 for most cases, the Q2=Q1-1 formula is not observed. This departure is due to the small jumps in the shielding region described above.

6.2.3 Possible origins of novel flux jumping observations.

The flux jumping behaviour seen in the shielding regions of the magnetisation loops at the temperatures and field sweep rates described above requires some explanation as it does not correspond to any of the empirically derived flux jumping relations in LTS. Since it has been established in the previous section that granular effects are apparently present, one might reasonably look to these as a possible source of unconventional behaviour, as has been so widely observed in weak-linked HTS materials. Since the fall-off in $J_c(B)$ is very small, in may be concluded that intergranular currents will be dominant over the field range here. One can also take into consideration the virgin curves shown in Figures 6.20, 6.23 and 6.24; as noted in 6.2.1, the first flux jump field in the virgin curve is lower than that found from the full magnetisation loop at the given T, $\dot{B}_a$. A full critical state has clearly been established prior to the first jump in the virgin curve.

Since the unusual small jumps are all in the shielding area, and correspond directly to those in the virgin shielding curve, it is reasonable to suppose that these occur solely in the intergranular region. If, after a field excursion to the maximum applied field, flux is trapped in the grains as well as by the intergranular persistent current, jumps in the trapping part of the curve could be due to a combination of the two components. The "middle" group of jumps described in 6.2.1, partly existing in the

annihilation region, might then represent a transition to the purely intergranular flux jumping which follows. Since $B_{fj} \propto J_c/(\mathrm{d}J_c/\mathrm{d}T)$, there is likely to be a higher field at which flux jumps begin in an intragranular-only sample than for a weak-linked network of grains. Although there will be some difference in specific heat between the two, this is less influential. If a flux jump occurs in an intragranular area, it is reasonable to expect that this might trigger a concurrent jump in the intergranular area. This is clearly a very tentative explanation, and experimental evidence of flux jumping in the intragranular regions only (with a cut tube) would be needed before advancing any further.

To explain the decay features of the small jumps seen at different temperatures in 6.2.1, one may consider the influence of flux pinning. It has been shown in HTS that flux creep stabilises against flux jumping for stepwise increments in B_a[68][76]; it has not been demonstrated for continuous sweep rates, although the inverse of the sweep rate frequency is analogous to the measurement interval between discrete applied field steps. The flux jump magnitude was seen in 6.2.1 to decrease exponentially with increasing applied field at a given temperature, and to increase with decreasing T. As B_a increases, pinning centres in the superconductor become weaker, allowing flux to move smoothly through the material. Thus at lower B_a flux may be constrained to move by jumping rather than smooth creep. In the same way at lower T, stronger pinning centres disallow stabilising flux creep and make flux jumping more likely. Again this is a cautious conclusion which requires more data at higher B_a and wider T to draw upon.

6.2.4 Temperature spikes due to flux jumps.

In order to observe the temperature rise due to the heating associated with flux jumping, the SMDT was fixed directly onto the inner tube wall of BSCCO #1, and the temperature logged with B_a and B_i during the applied field ramp. From such measurements it should be possible to obtain an estimate of the specific heat of the

BSCCO material. Measurements were taken at T_o=4.5K and sweep rates of 0.124 and 0.31Tmin^{-1}. A one-to-one correspondence of temperature spikes and flux jumps could be observed for all the jumps in a loop. These are similar to those observed in LTS by Neuringer & Shapira[47].

It should first be possible to find a theoretical value for the specific heat from the adiabatic flux jump equation,

$$B_{fj} = [3\mu_o \gamma C(T_c - T_o)]^{\frac{1}{2}} \qquad (6.4)$$

Although the adiabatic theory does not account for the applied field sweep rate, one might reasonably suggest that the theoretical B_{fj} will be that at which flux jumping first appears in the sample taking the overall conditions, *i.e.* at the lowest sweep rate. As noted in 6.2.2, flux jumping ceased between 0.124 and 0.093Tmin^{-1}; data at 0.124Tmin^{-1} will thus be used. Using this hypothesis, values of T_c=90K (this value is used since the quoted T_c=89-91K), T_o=4.5K and B_{fj}=2.942T (from this measurement) can be inserted into (6.4), giving a volumetric specific heat:

$$\gamma C = 0.027 \text{JK}^{-1}\text{cm}^{-3}$$

The difference between B_{fj} above and that found at the same sweep rate in 6.2.2 can be attributed to experimental conditions; although measurements at a given rate were reproducible around more than one loop for immediately following excursions, there may be enough temperature variation, *etc.* between different cool-downs to give some small scatter in the numerical values as above.

Figures 6.48 and 6.49 show the rises in temperature as voltage spikes in the SMDT output at 0.31Tmin^{-1}; these give an even clearer indication of flux jumping than B_i. The magnetic field effect on the diode is evident, and this made calibration of the voltage too difficult to do for so many closely spaced jumps. Because the diode is influenced not only by the applied field, but also by the local field at the inner tube wall, a simple calibration could not be done. The field effect is in the form of a temperature offset[90]. The same measurement performed at 0.124Tmin^{-1} gave the

spikes shown in Figures 6.50 and 6.51. The calibrated temperature rise was found by assuming that the temperature before the flux jump is T_o=4.5K, and that the sample returns to this temperature upon completion of the flux jump and re-joining the equilibrium magnetisation line. Thus the magnetic field-dependent offset could be found either side of the jump, and, since B_i is constant for some time after the jump and the change in B_a is small, a calibration could be applied working from either side of the jump to give the real temperature rises shown in Figures 6.52 and 6.53. These show the following changes in B_i and final temperatures T_F:

B_a(T)	ΔB_i (T)	T_F (K)
0.058	0.459	12.22
-0.777	0.181	9.43
-1.136	0.037	5.83
0.049	0.457	12.93
1.068	0.132	6.84

The specific heat of the tube is estimated as follows. It is well known that the stored magnetic energy density in an infinitely long solenoid generating a field B is given by

$$u_B = \frac{B^2}{2\mu_o} \tag{6.5}$$

Since the 3T superconducting magnet coil is somewhat longer than the tube, we can approximate it as being infinite. Considering the stored magnetic energy, we have to include both the tube itself and the enclosed volume. To do this, the magnetic field in the inner volume is simply B_i, and assuming a Bean model $B(r)$ the field in the tube wall is taken as the average field across it,

$$\bar{B} = \frac{B_a + B_i}{2} \tag{6.6}$$

(see Figure 6.54). To find the stored energy U_B before and after a flux jump, (6.5) is applied in each region with the appropriate volume. If adiabaticity is assumed, all of the change in stored energy will go into raising the temperature of the tube. The specific heat can then be found:

$$C_v = \frac{dq}{dT} \simeq \frac{\Delta U_B}{\Delta T} \tag{6.7}$$

The values of γC thus found are in the range of 0.014 to 0.041$K^{-1}cm^{-3}$, very close to the adiabatic theory prediction. The mean value is:

γC = 0.0276$JK^{-1}cm^{-3}$
st. dev. = 0.0101
var. = 0.0001

This is practically identical to the theoretical estimate.

The above result seems good given the approximations and experimental errors involved. Because the temperature spike increases over a short time, the true value of T_F may not in fact be observed, and those above may be underestimates. However, since two flux jumps of similar magnitude gave similar T_F, it appears that the measurement is very close to being correct; the flux jump with the highest T_F=12.93K gave γC=0.026$JK^{-1}cm^{-3}$, the closest to the theoretical value, which suggests that this is very near to the real T_F. In both the 0.124 and 0.31$Tmin^{-1}$ measurements the temperature spikes are in proportion to the flux jump size (Figures 6.48 to 6.51). If T_F was seriously underestimated in the data, one would expect to see some out-of-proportion spikes since the point during the temperature rise at which the measurement is made is essentially random. End effects in the tube are not accounted for in applying (6.5), and U_B is therefore likely to be slightly overestimated since the internal field profile will not be flat over the length of the tube. If data starting from the virgin state was used, U_B could be found from the equivalence between the hysteretically stored energy and the work done:

$$U_B = \int_0^{H_j} M dH \tag{6.8}$$

However, although all the energy is dissipated in a complete flux jump, *i.e.* $T_F=T_c$, the amount lost in a partial jump would still have to be estimated. This method has to be used for solid samples (disks, rods, *etc.*); the tubular geometry allows $\bar{B}$ to be found easily from measurements. The simple calculation used here gives sufficiently good results. Other sources of error are B_a for the start and finish of the flux jump and B_i for the start of the jump; these are likely to be insignificant. The specific heat also has a field-dependence[102] which is not well documented. This could explain some of the scatter in the γC values above, although there seemed no clear relationship to either B_a or $\bar{B}$.

Three other features of the above are worth noting. First, because the volume of the whole tube was used in calculating U_B and hence the specific heat, the agreement between measurement and theory would imply that the flux jumps occur across the whole volume of the tube, at least for the larger jumps, and are not localised in the tube wall. Also, examining the number of points in the temperature spike shows that flux jumping occurs over a much longer time than conventionally expected. The flux jump duration in LTS is on the order of milliseconds to tens of milliseconds. Here the measurement interval was approximately 1s, and the jump can be seen to take between one and two seconds to complete. This is extremely slow. The subsequent decrease in temperature back to T_o is noticeably slower. Thirdly, from the agreement of the theoretical and experimental values, the adiabatic assumptions in using (6.4) and in taking $\Delta q=\Delta U_B$ in (6.7) seem justified, as does the calculation of B_{fj} from the magnetisation loops used (*i.e.* as the difference between the maximum or minimum field excursion and the field of the first jump).

Clearly the measurement of temperature rise could be improved upon by faster data logging in the flux jump region. Obtaining $B_i(t)$ during a jump could also be of use in determining the velocity of the flux front.

Comparison of this specific heat value to other experimental data is not easy because of the differing samples and conditions for which such data is given. Junod[102] gives minimum values of $C/T \sim 11 \text{mJK}^{-2}\text{mol}^{-1}$ for BSCCO 2212. There is some uncertainty as to the specific heat temperature dependence at low temperatures; a number of authors have found that there is no linear term for the low temperature $C(T)$[102][103]. Taking $\gamma = 6.0 \text{gcm}^{-3}$ the specific heat value derived above gives $C/T \simeq 0.889 \text{JK}^{-2}\text{mol}^{-1}$, somewhat larger than other values. If the linear $C(T)$ term can indeed be neglected, a $C = \beta T^3$ relationship gives γC and B_{fj} from (6.4) as:

$$\gamma C(2.2\text{K}) = 0.0032 \text{JK}^{-1}\text{cm}^{-3}$$
$$B_{fj}(2.2\text{K}) = 1.03\text{T}$$

This is a rather gross simplification because, irrespective of the linear term, there are several others in $C(T)$ which may need to be included, and the temperature dependence is far from simple. With the above values of specific heat, the adiabatically stable thickness, a_{fj}, can be found. Estimating $J_c(2.2\text{K}) \simeq 17660 \text{Acm}^{-2}$ from the linear $J_c(T)$ dependence used in 3.4 to derive the from of (6.4), and $J_c(4.5\text{K}) = 17200 \text{Acm}^{-2}$ (the magnetisation value) we find:

$$a_{fj}(4.5\text{K}) = 1.36\text{mm}$$
$$a_{fj}(2.2\text{K}) = 0.46\text{mm}$$

values which compares well with HTS predictions (2.4.1). This may explain why no flux jumping was observed in the YBCO tube down to 2.2K at 0.31Tmin^{-1}, in addition to the evidence of flux creep, as the wall thickness of 1.75mm may be close to or below a_{fj} for that material.

The preceding results indicate a size which is technologically useful: while multifilamentary wires are likely to be used to provide parallel current paths to overcome poorly-linked regions in one conductor, these values of a_{fj} means that flux

jumping is not likely to be a problem with such HTS wires having filaments with dimensions on the order of a millimetre to tenths of millimetres.

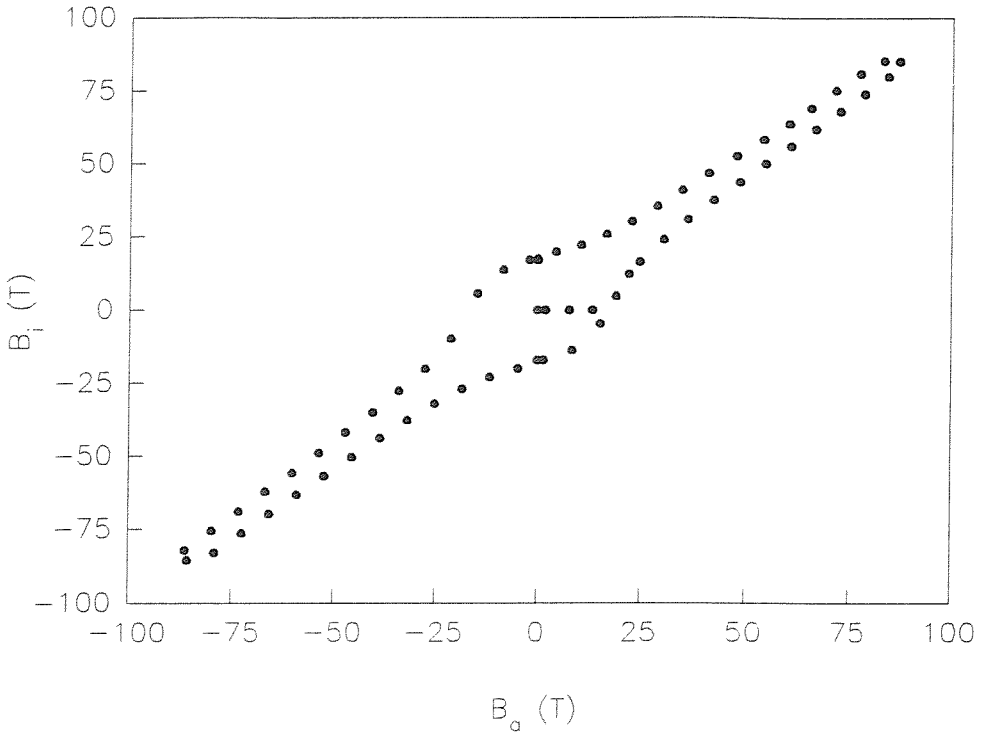

Figure 6.1 Shielding curve of YBCO tube at 4.2K, 1.5mTs^{-1}.

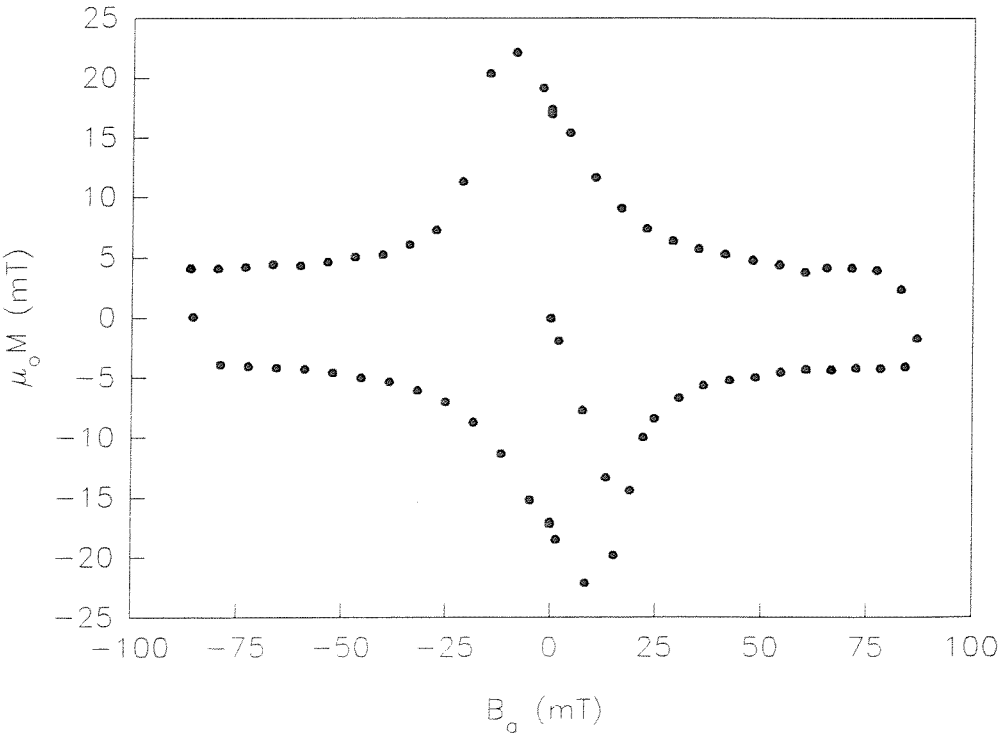

Figure 6.2 Magnetisation loop of YBCO tube at 4.2K, 1.5mTs^{-1}.

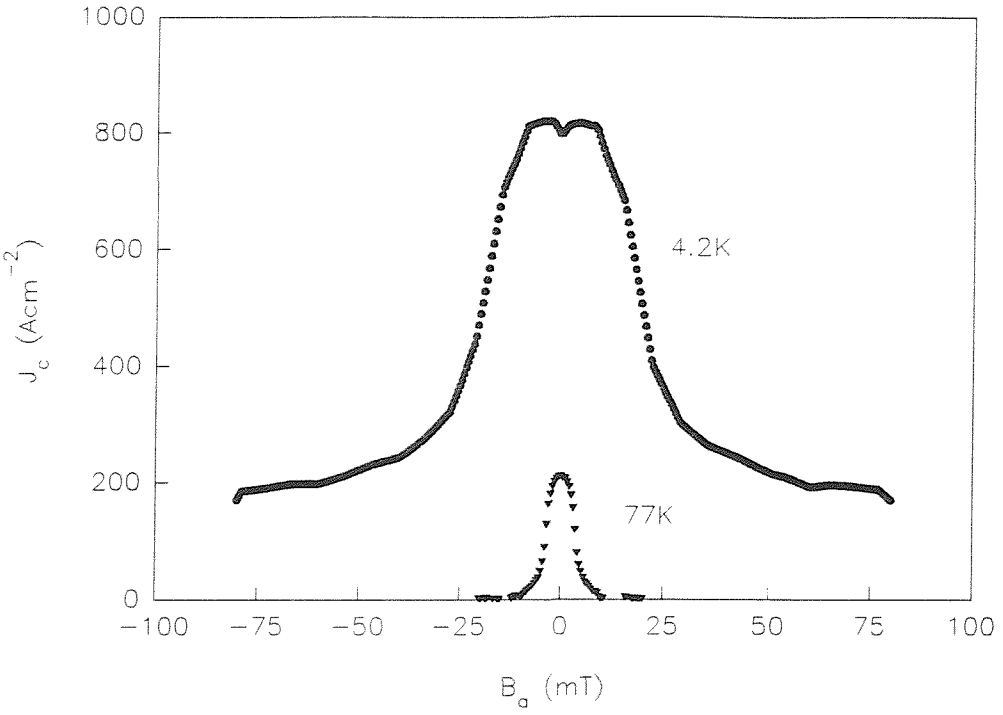

Figure 6.3 Field dependence of critical current for YBCO tube at 4.2K; 77K shown for comparison.

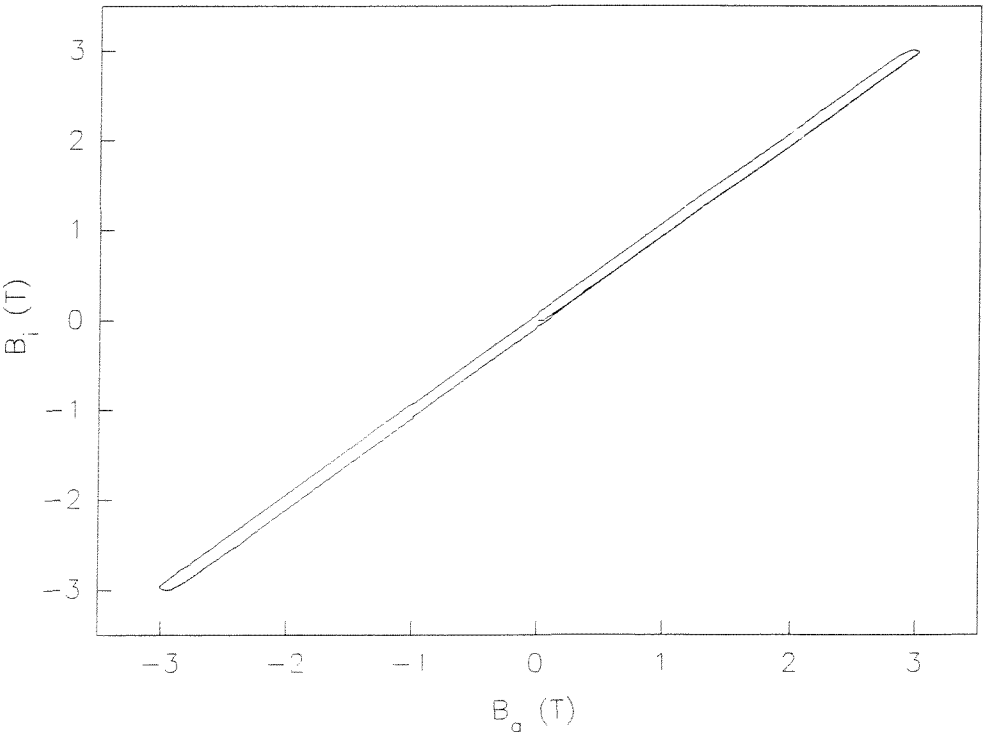

Figure 6.4 Shielding curve of YBCO tube to $\pm$3T at 4.5K, 0.31Tmin^{-1}.

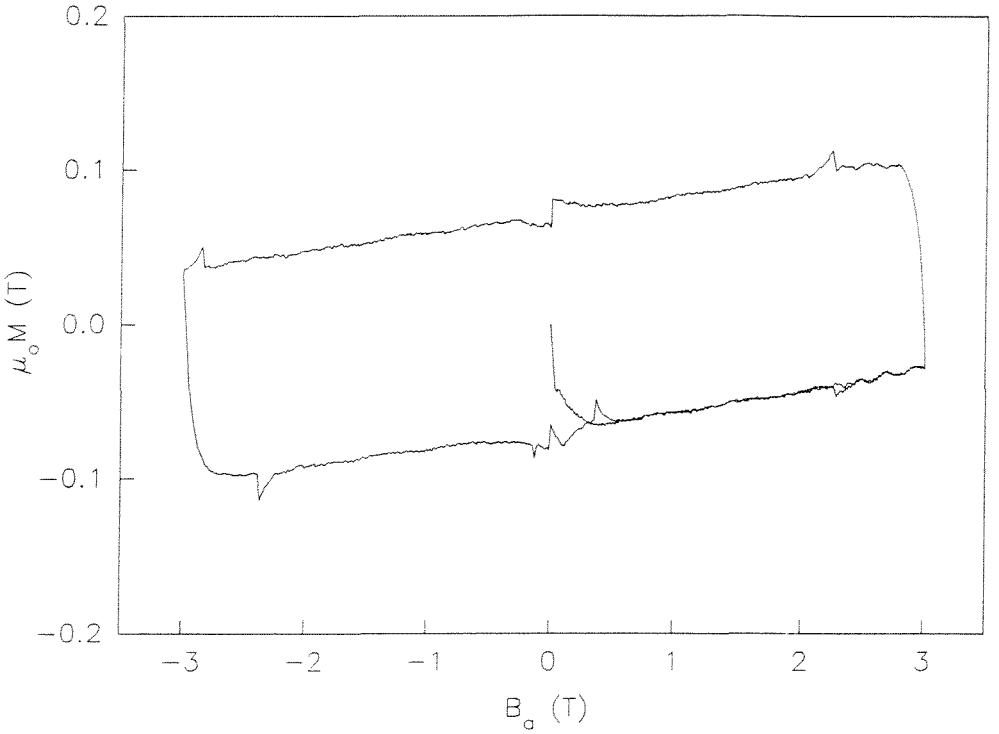

Figure 6.5 Magnetisation loop of YBCO tube to ±3T at 4.5K, 0.31Tmin^{-1}.

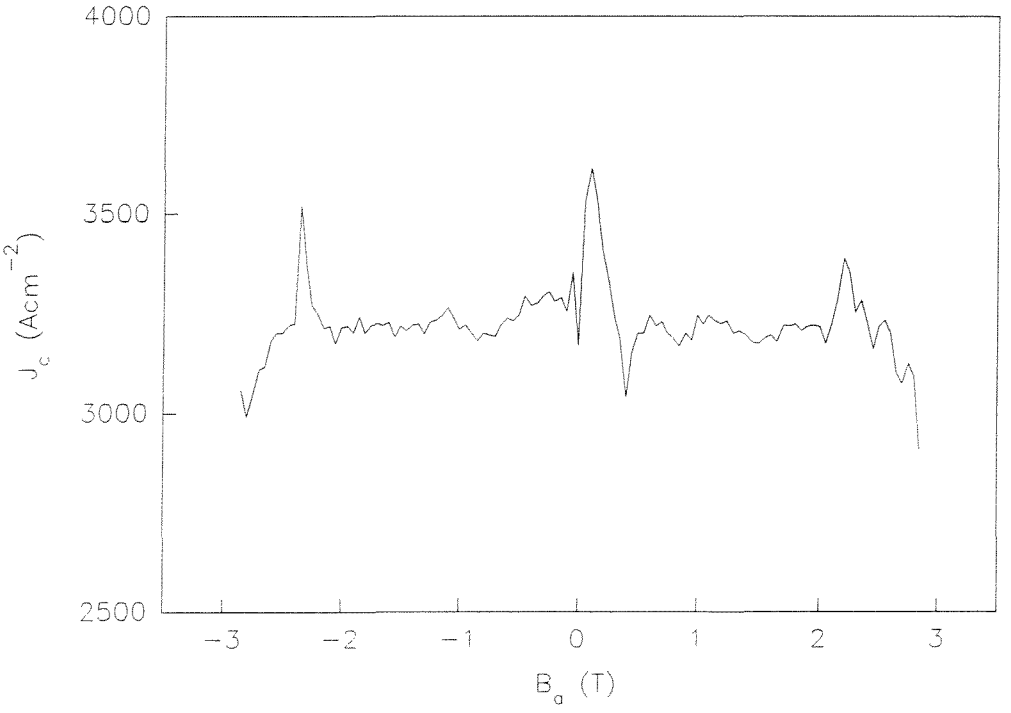

Figure 6.6 Field dependence of critical current for YBCO tube at 4.5K, 0.31Tmin^{-1}.

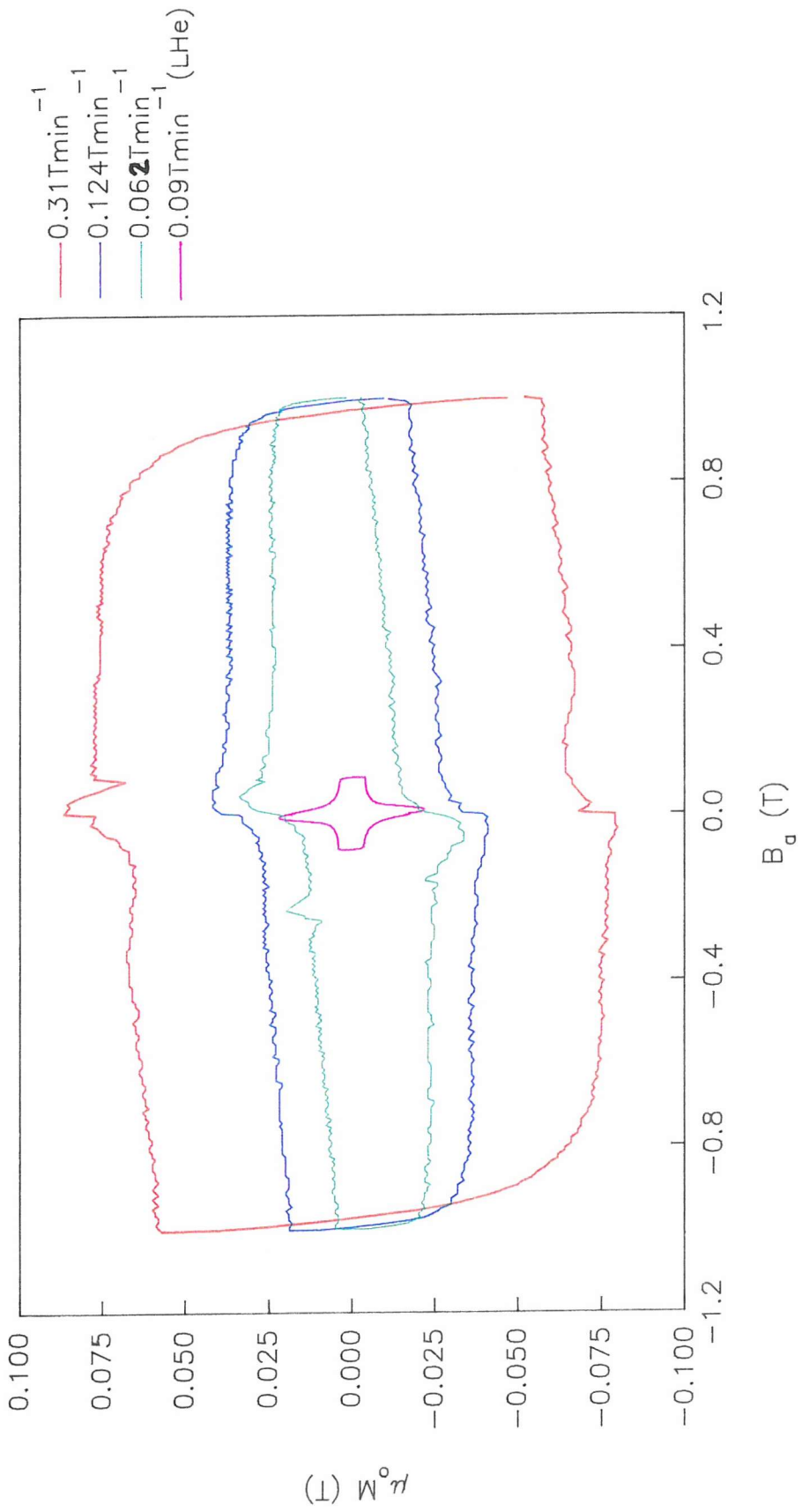

Figure 6.7 Magnetisation loop of YBCO tube at 4.5K and various applied field sweep rates.

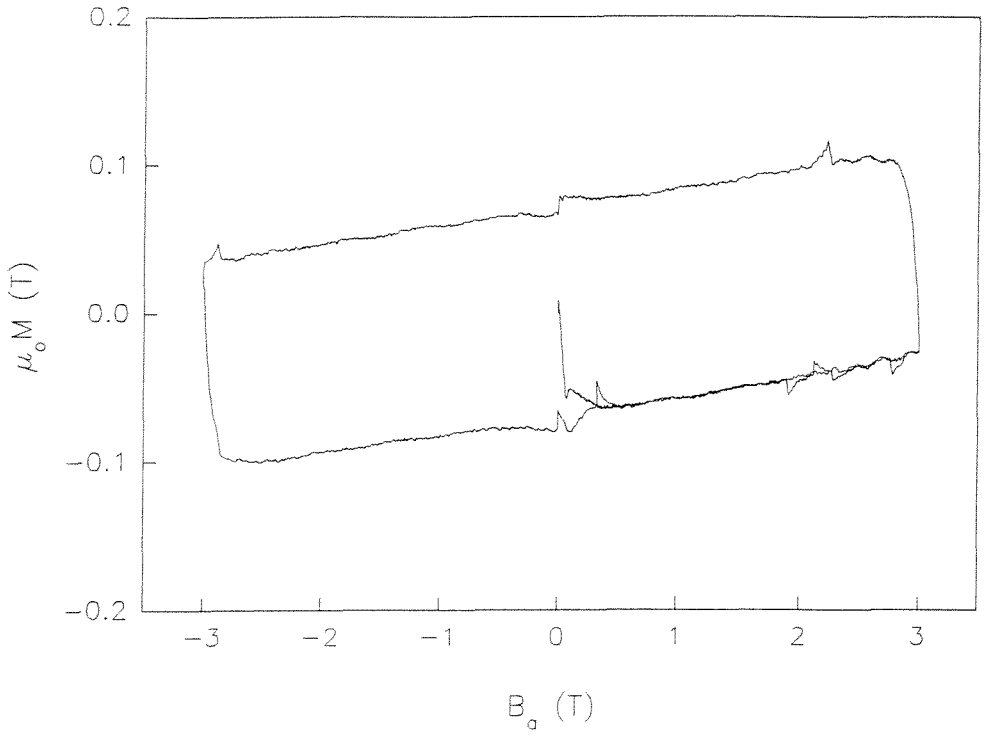

Figure 6.8 Magnetisation loop of YBCO tube to $\pm$3T at 2.2K, 0.31Tmin^{-1}.

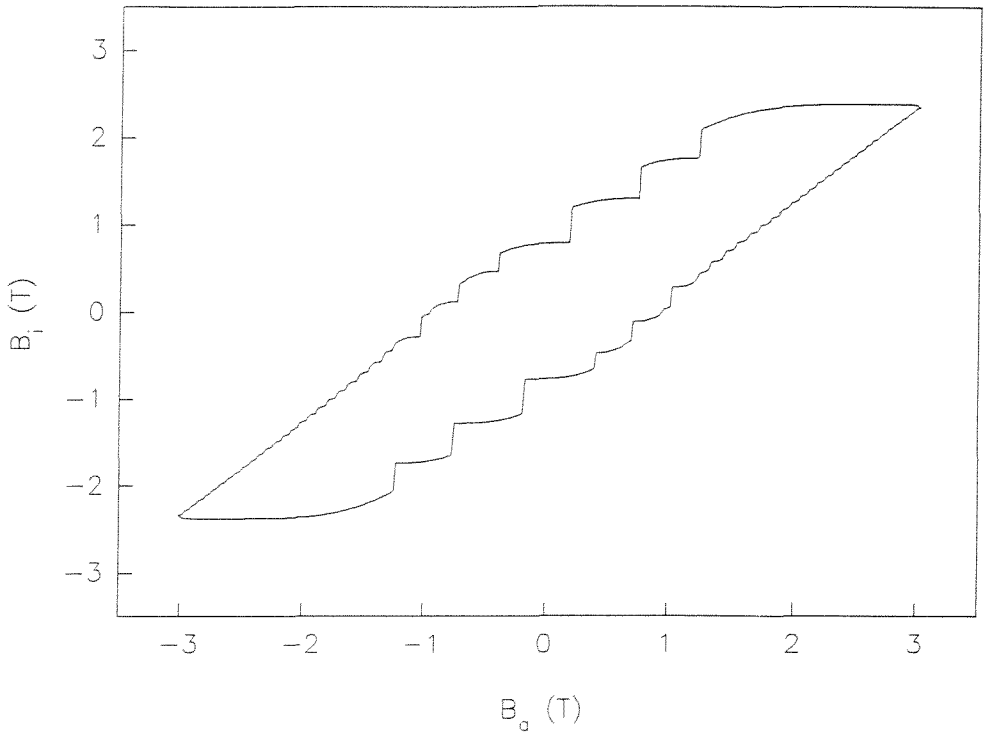

Figure 6.9 Shielding curve of BSCCO #1 at 4.5K, 0.31Tmin^{-1}.

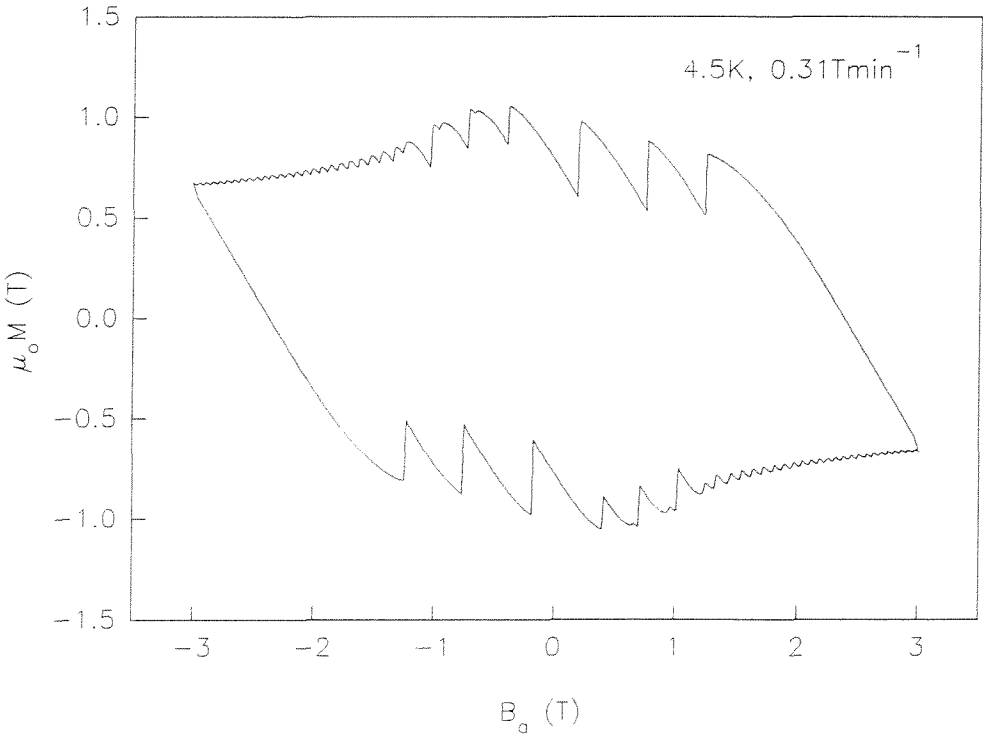

Figure 6.10 Magnetisation loop of BSCCO #1 at 4.5K, 0.31Tmin^{-1}.

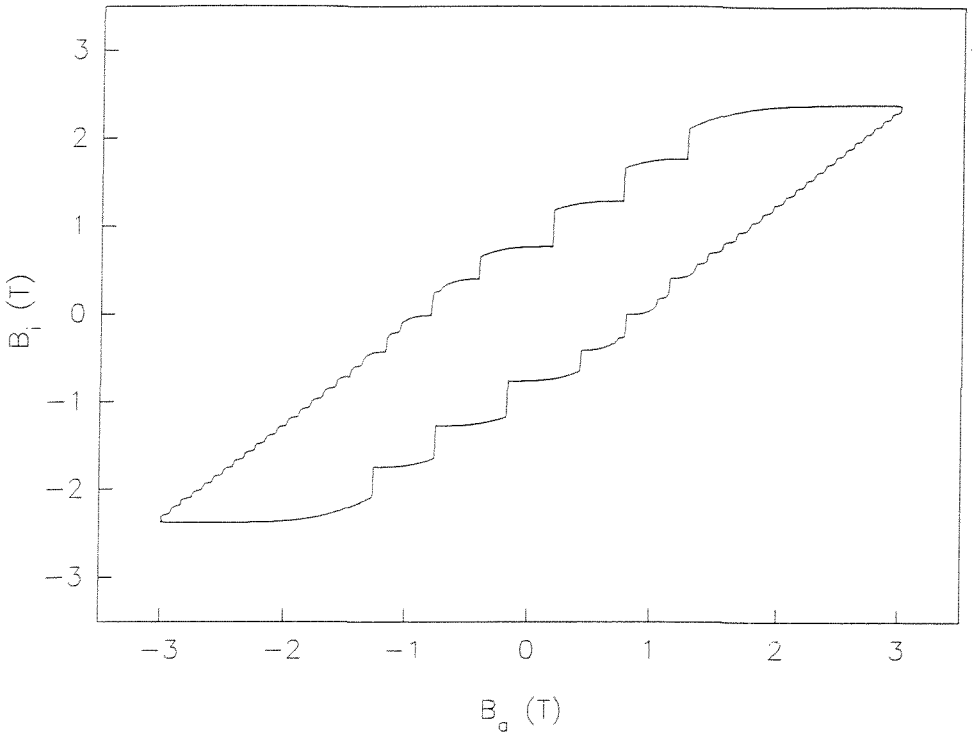

Figure 6.11 Shielding curve of BSCCO #1 at 3.8K, 0.31Tmin^{-1}.

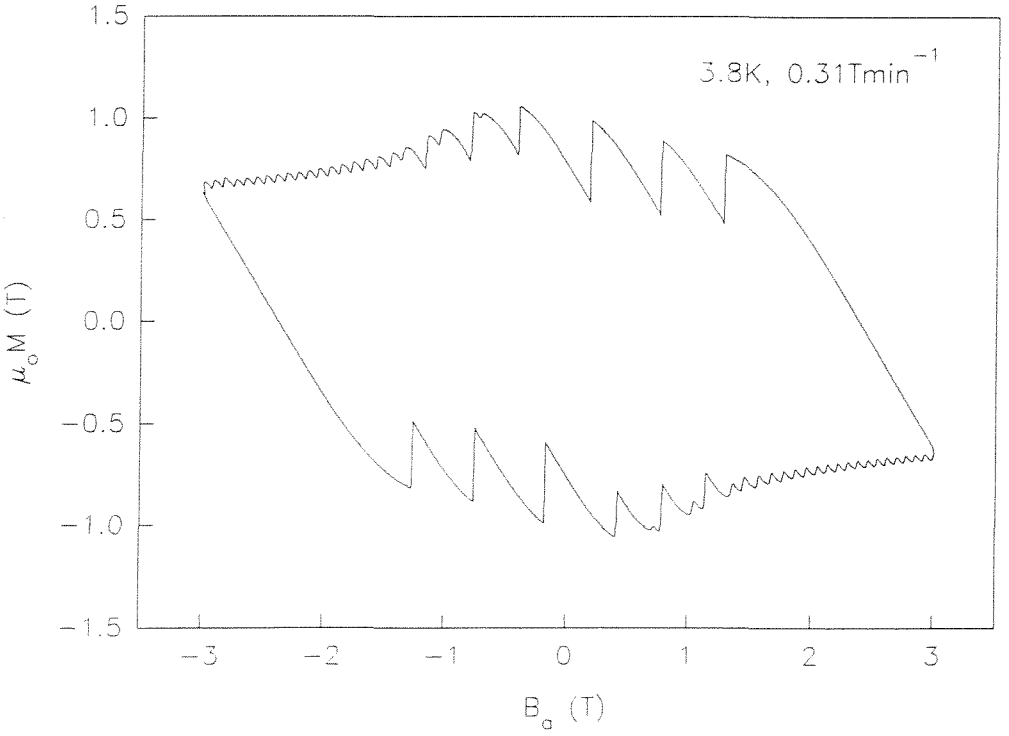

Figure 6.12 Magnetisation loop of BSCCO #1 at 3.8K, .31Tmin^{-1}.

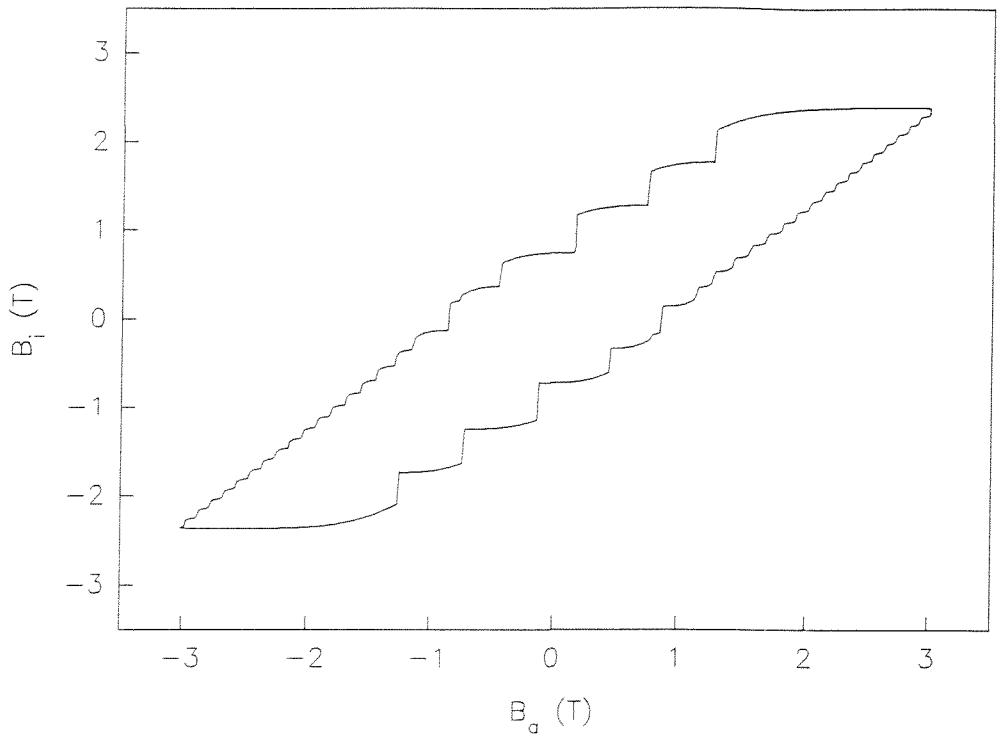

Figure 6.13 Shielding curve of BSCCO #1 at 3.2K, 0.31Tmin^{-1}.

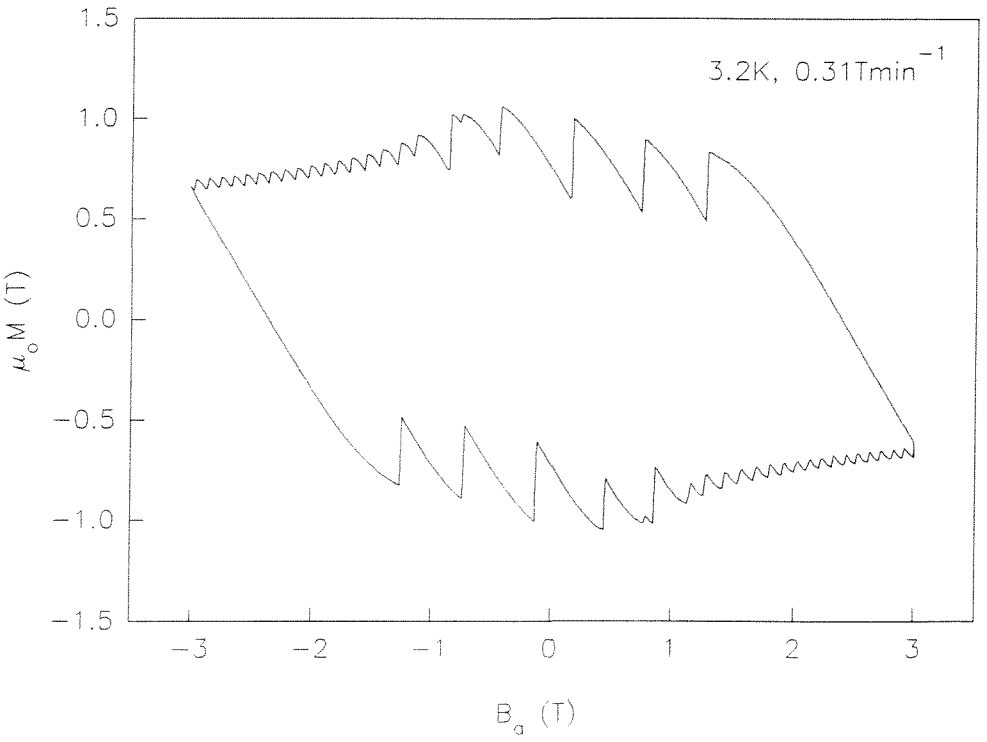

Figure 6.14 Magnetisation loop of BSCCO #1 at 3.2K, 0.31Tmin^{-1}.

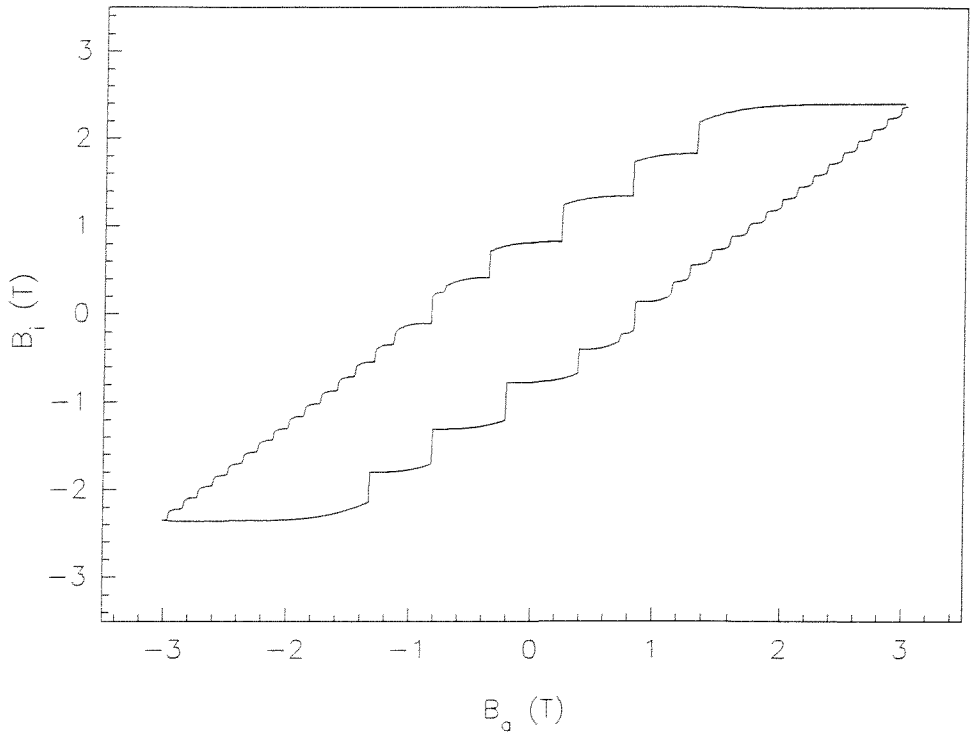

Figure 6.15 Shielding curve of BSCCO #1 at 2.7K, 0.31Tmin^{-1}.

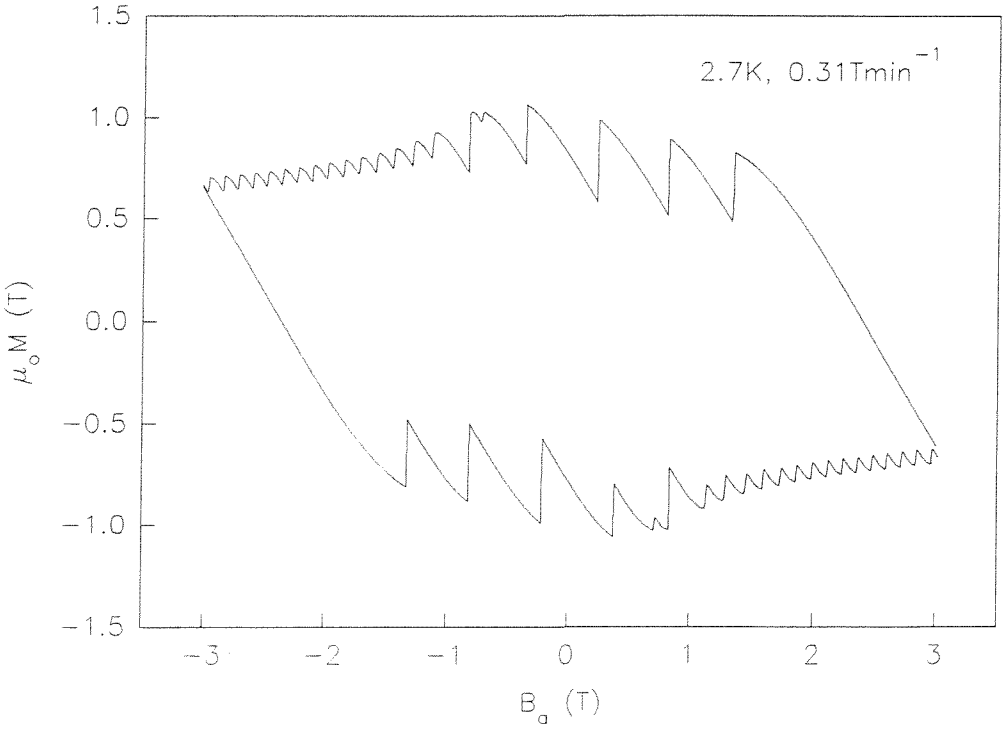

Figure 6.16 Magnetisation loop of BSCCO #1 at 2.7K, 0.31Tmin^{-1}.

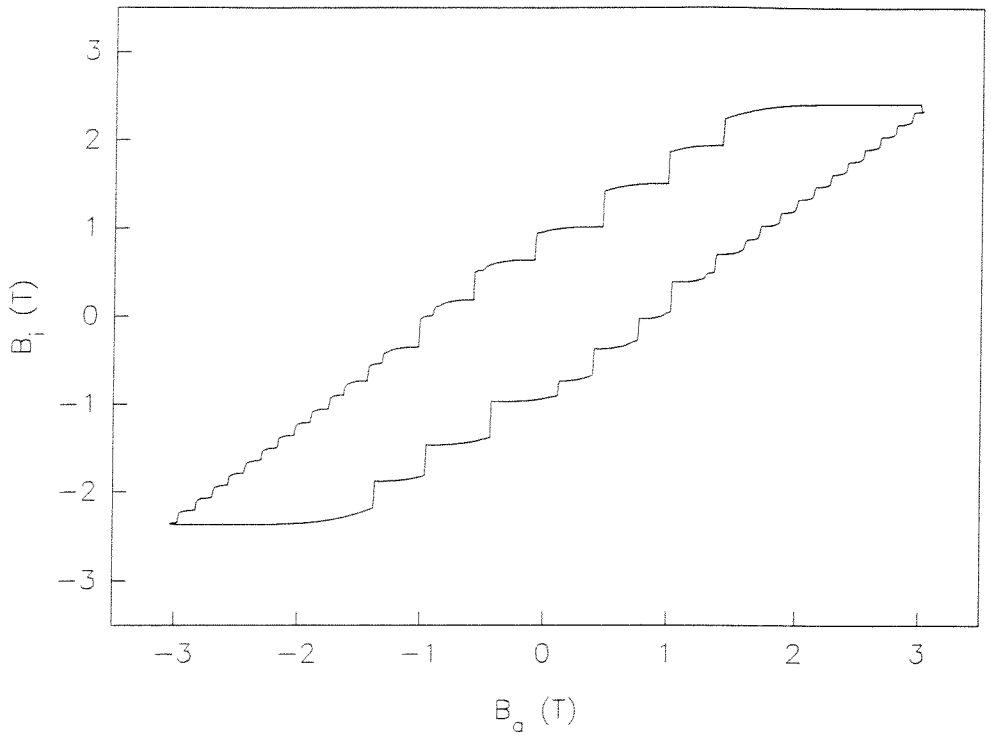

Figure 6.17 Shielding curve of BSCCO #1 at 2.2K, 0.31Tmin^{-1}.

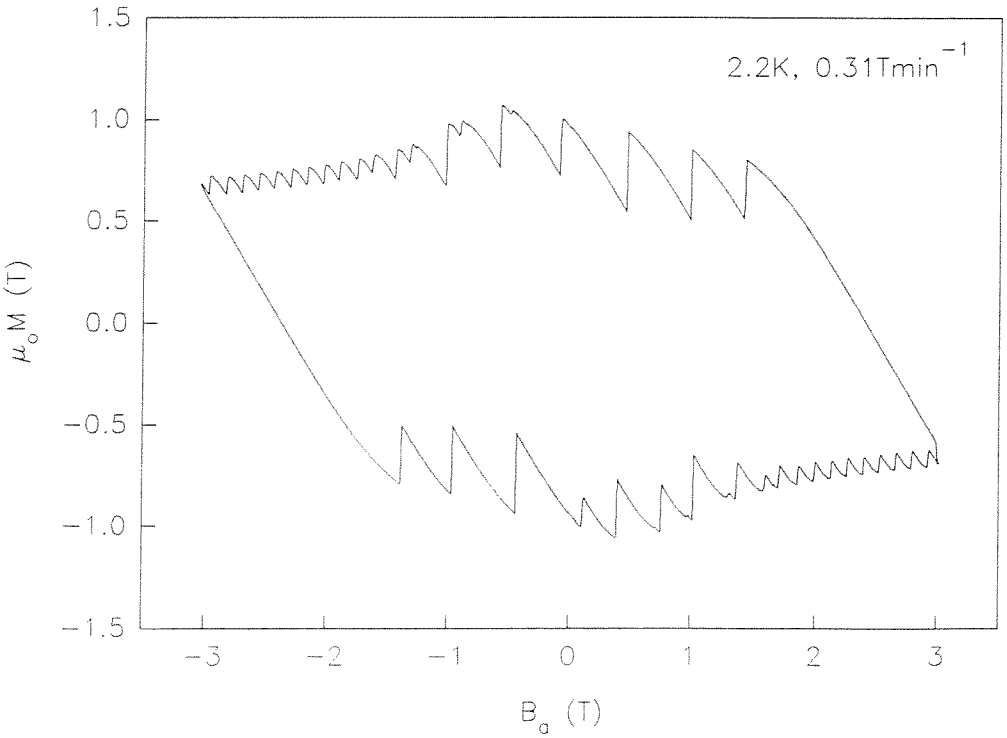

Figure 6.18 Magnetisation loop of BSCCO #1 at 2.2K, 0.31Tmin^{-1}.

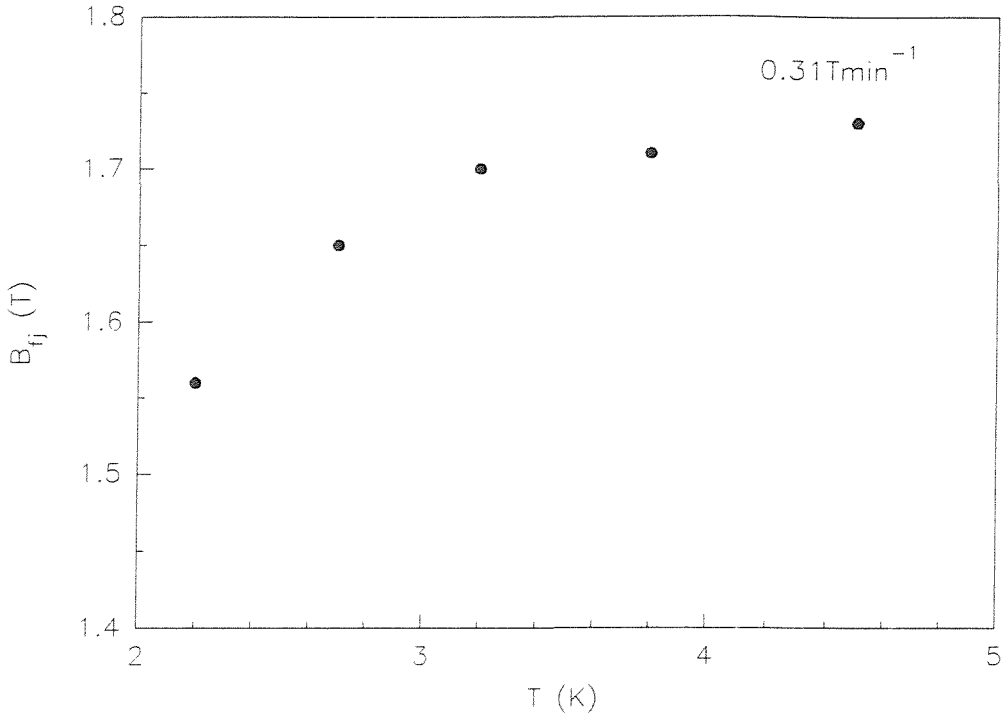

Figure 6.19 Temperature dependence of B_{fj} for BSCCO #1 at 0.31Tmin^{-1}.

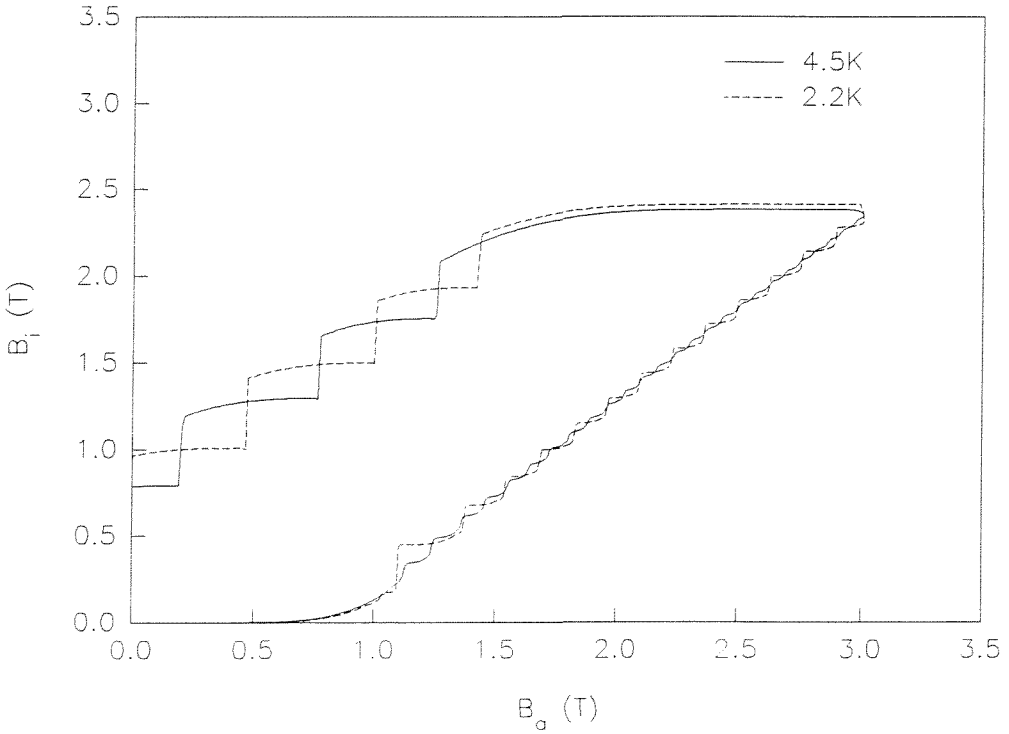

Figure 6.20 Virgin shielding curves of BSCCO #1 at 4.5 and 2.2K, 0.31Tmin^{-1}.

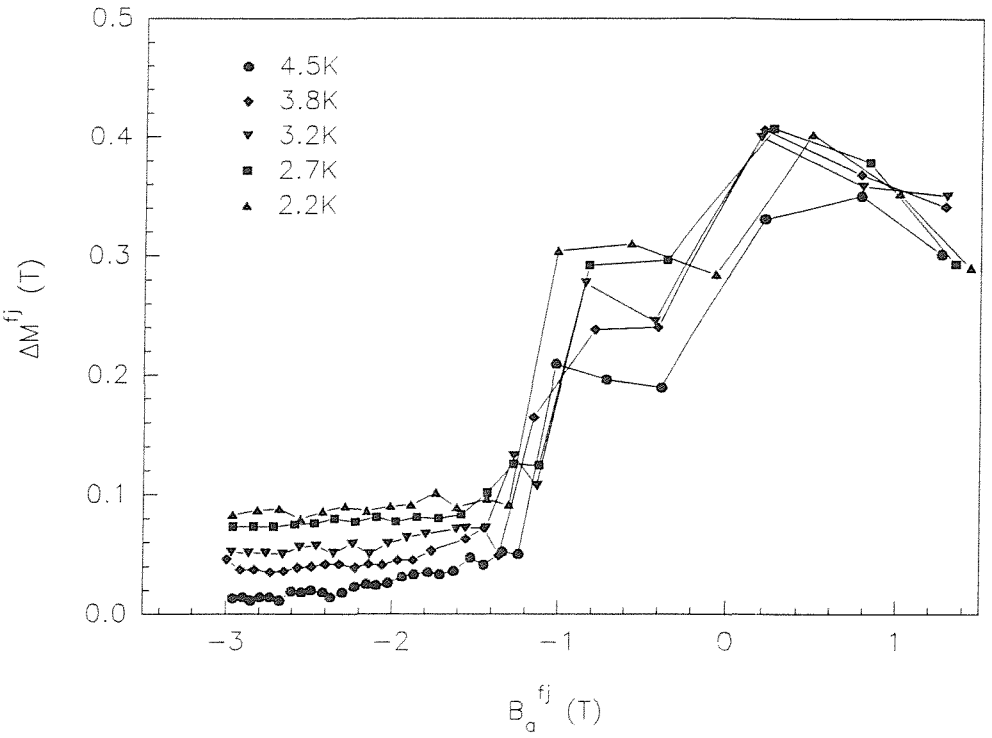

Figure 6.21 Flux jump size in M^+ *versus* applied field at which jump occurs.

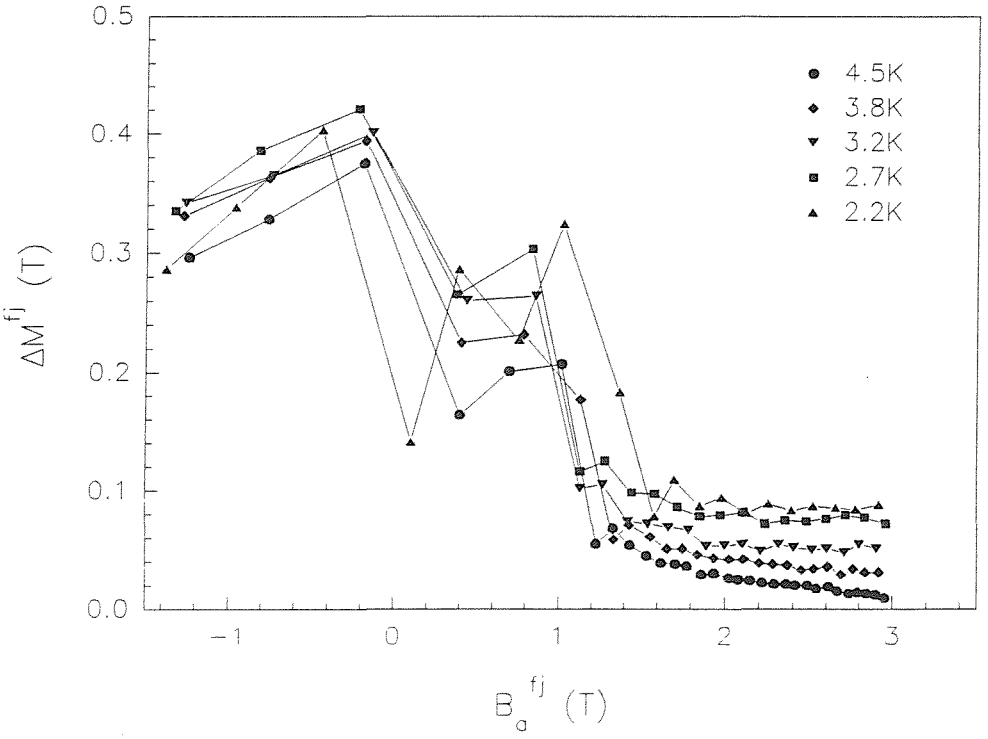

Figure 6.22 Flux jump size in M^- *versus* applied field at which jump occurs.

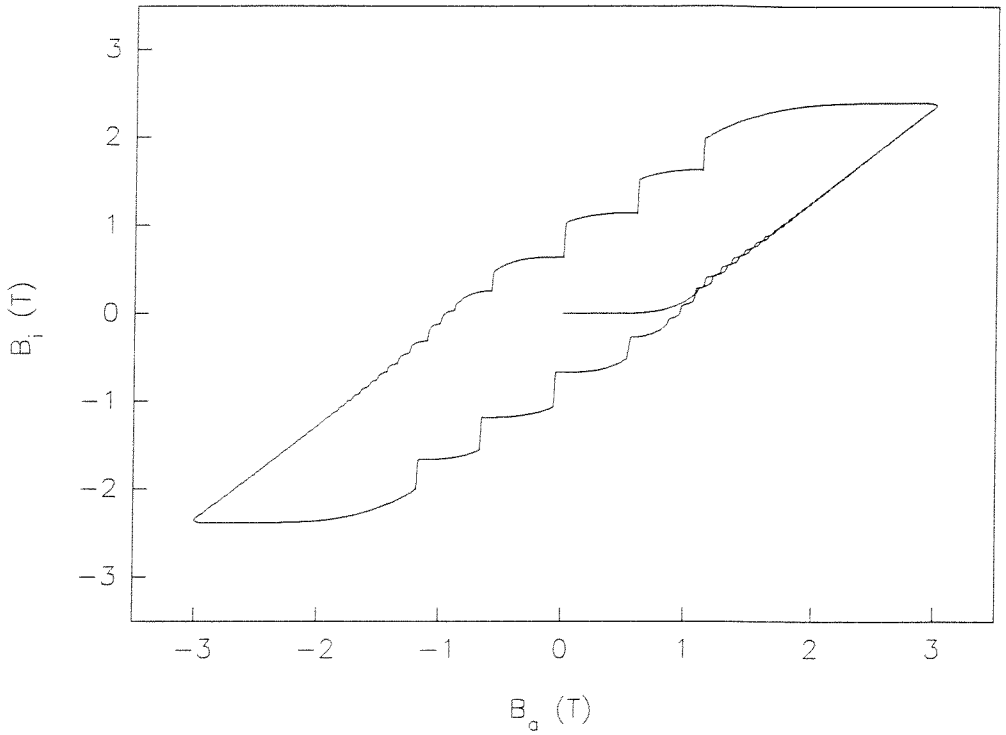

Figure 6.23 Shielding curve of BSCCO #1 at 4.5K, 0.256Tmin^{-1}.

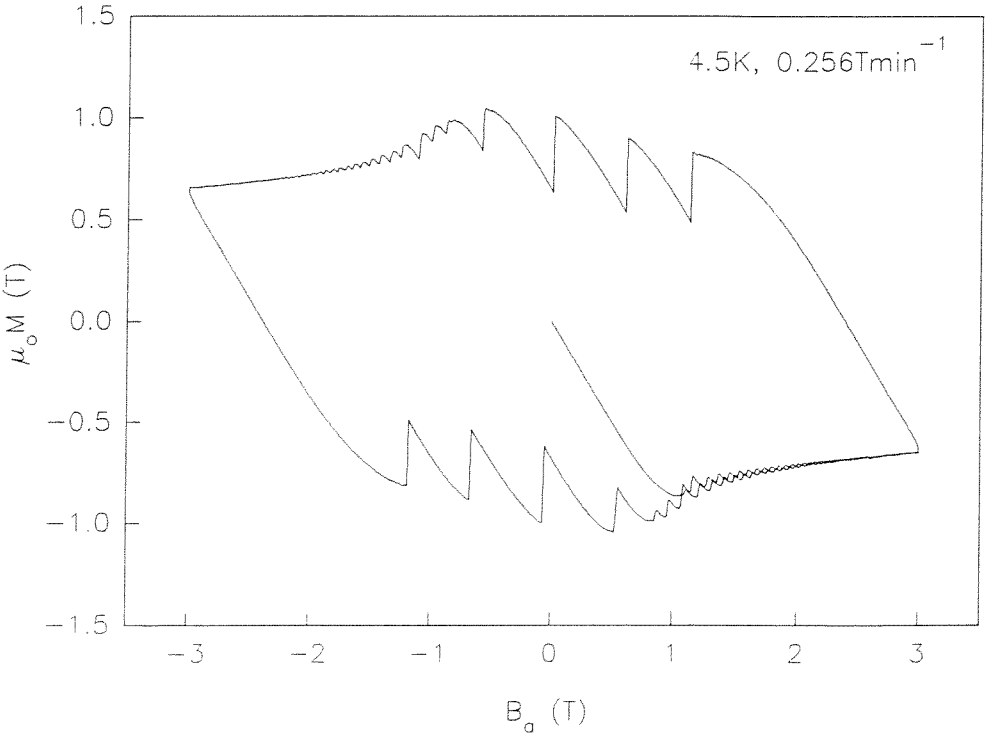

Figure 6.24 Magnetisation loop of BSCCO #1 at 4.5K, 0.256Tmin^{-1}.

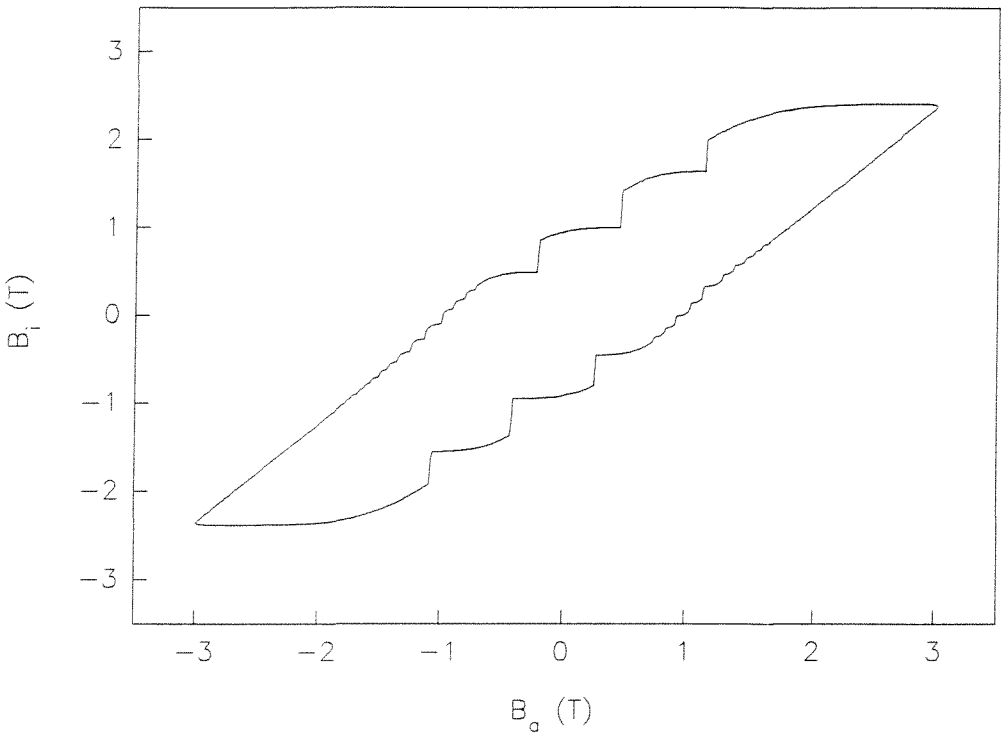

Figure 6.25 Shielding curve of BSCCO #1 at 4.5K, 0.225Tmin^{-1}.

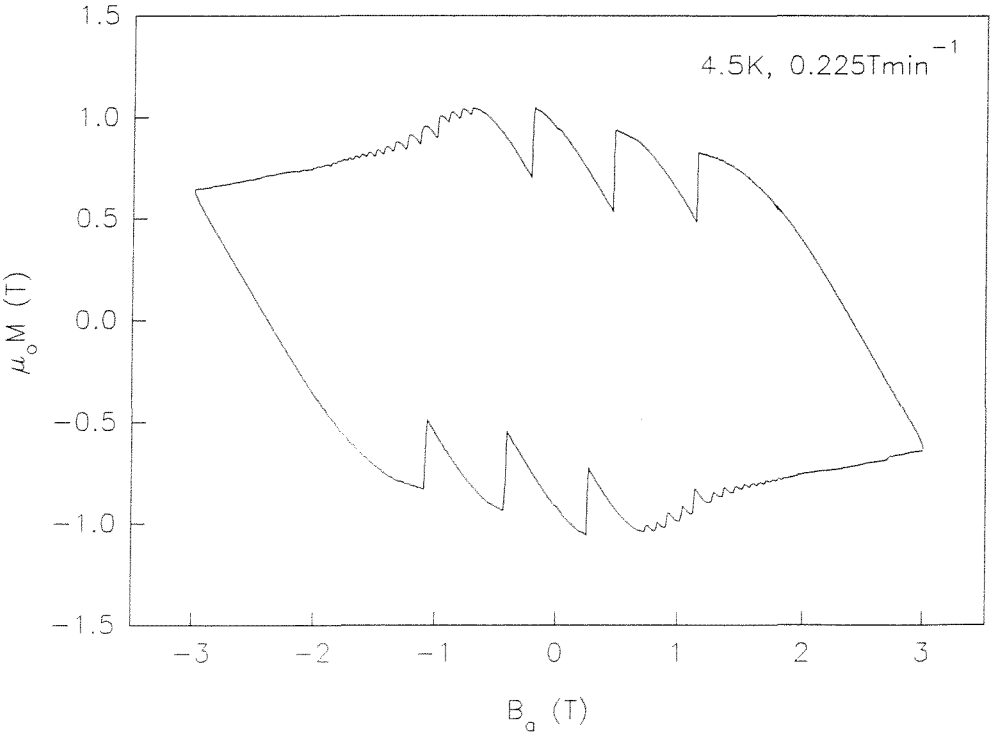

Figure 6.26 Magnetisation loop of BSCCO #1 at 4.5K, 0.225Tmin^{-1}.

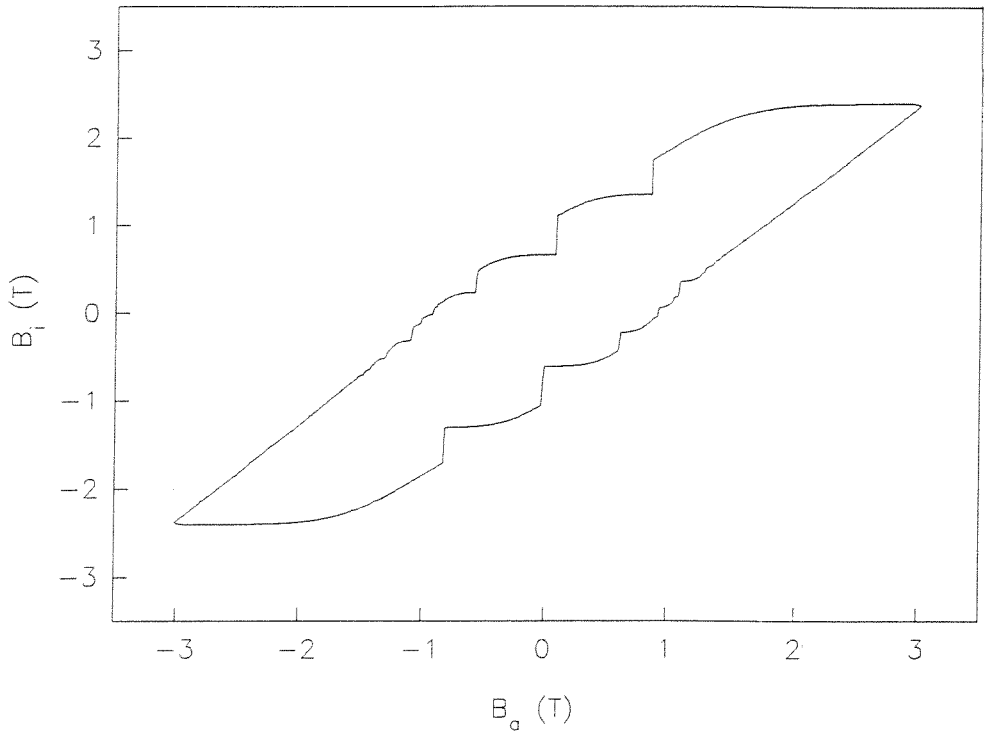

Figure 6.27 Shielding curve of BSCCO #1 at 4.5K, 0.17Tmin^{-1}.

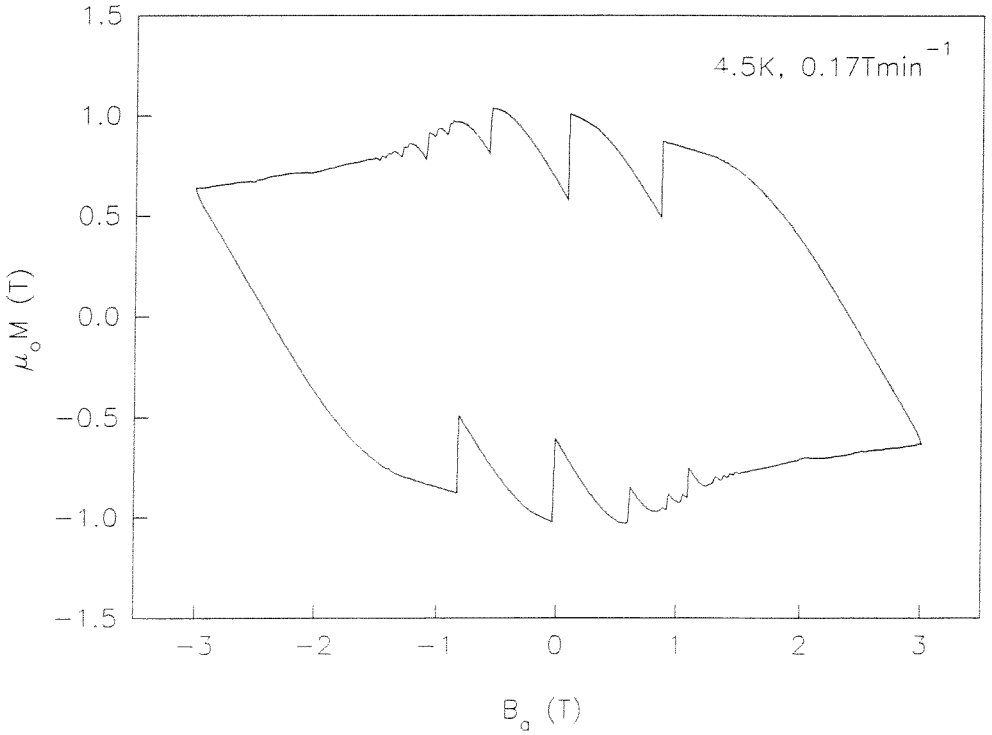

Figure 6.28 Magnetisation loop of BSCCO #1 at 4.5K, 0.17Tmin^{-1}.

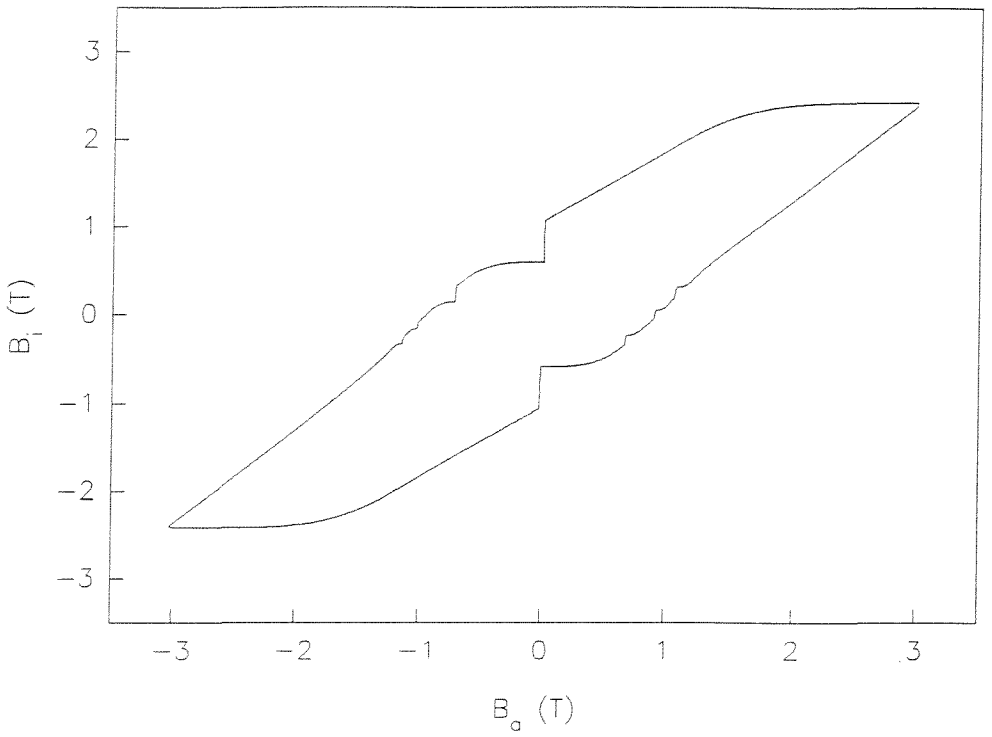

Figure 6.29 Shielding curve of BSCCO #1 at 4.5K, 0.144Tmin^{-1}.

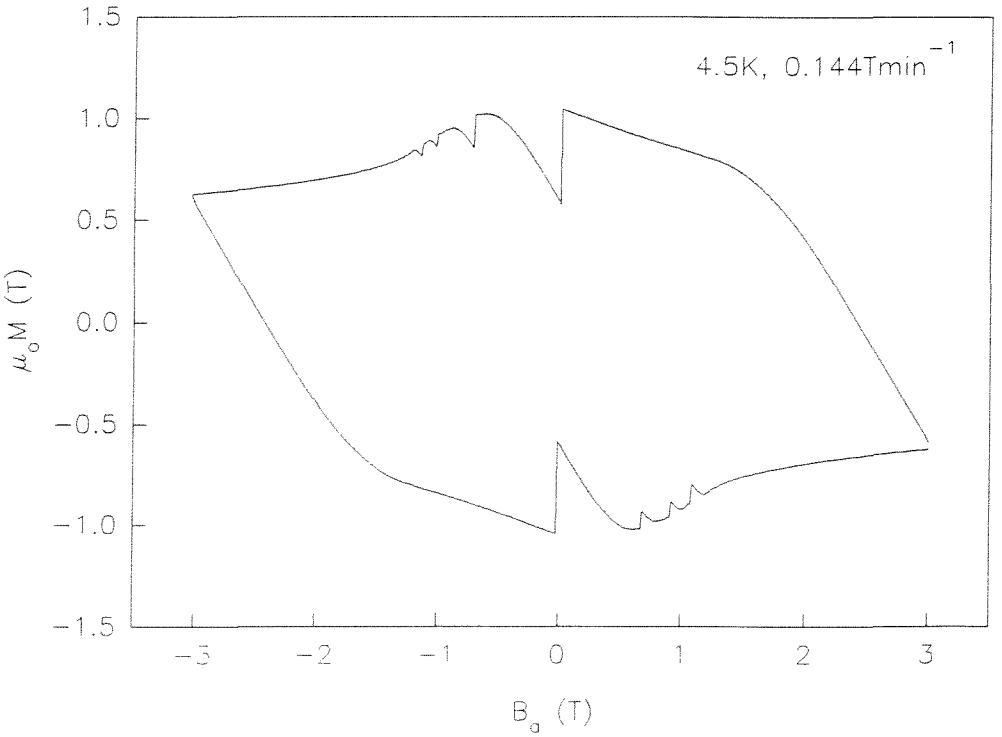

Figure 6.30 Magnetisation loop of BSCCO #1 at 4.5K, 0.144Tmin^{-1}.

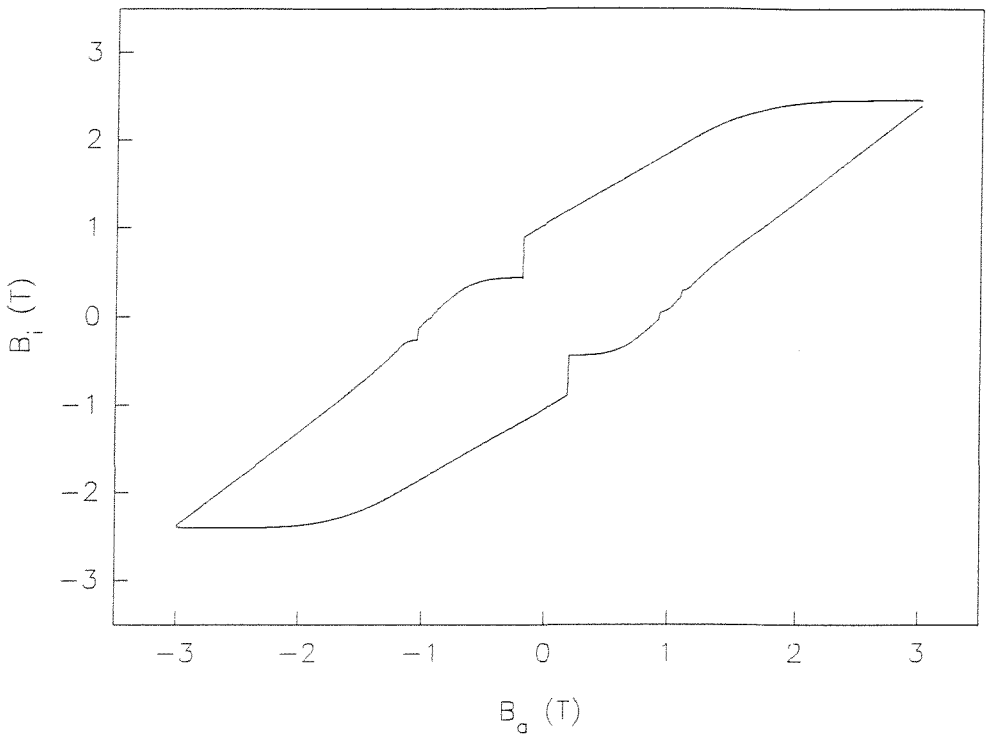

Figure 6.31 Shielding curve of BSCCO #1 at 4.5K, 0.124Tmin^{-1}.

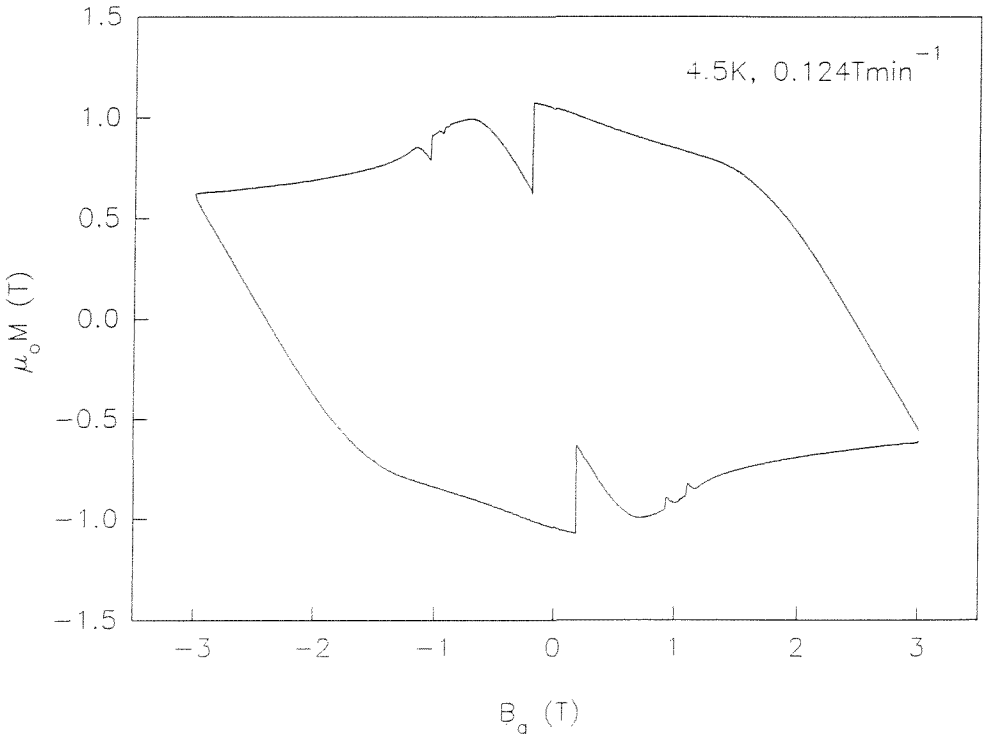

Figure 6.32 Magnetisation loop of BSCCO #1 at 4.5K, 0.124Tmin^{-1}.

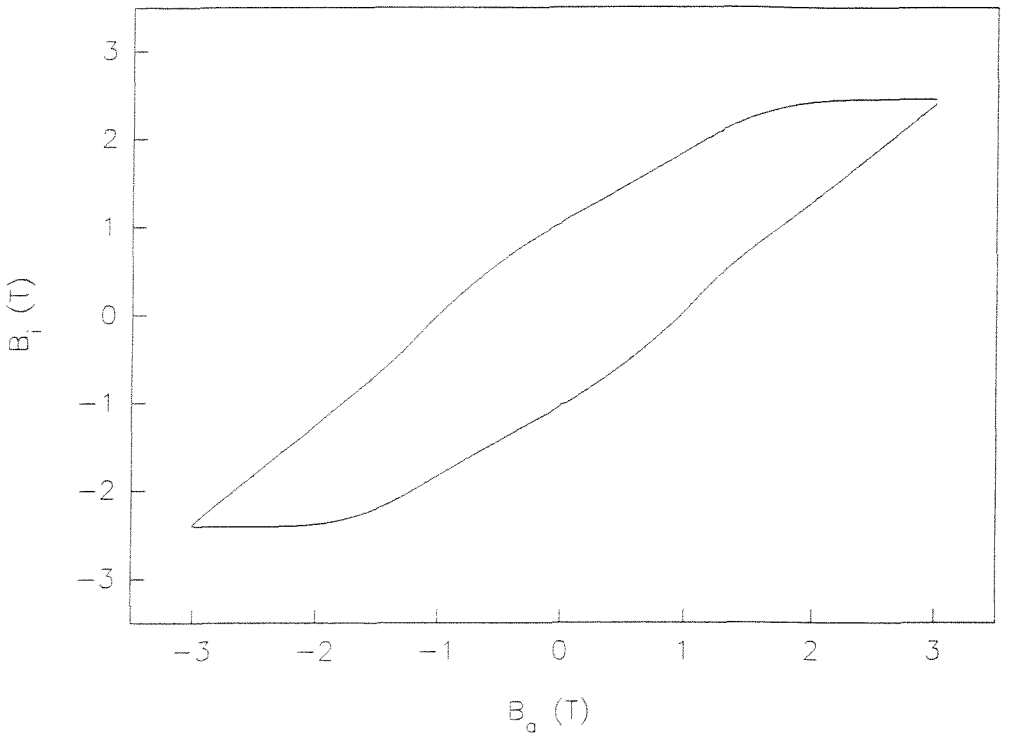

Figure 6.33 Shielding curve of BSCCO #1 at 4.5K, 0.093Tmin^{-1}.

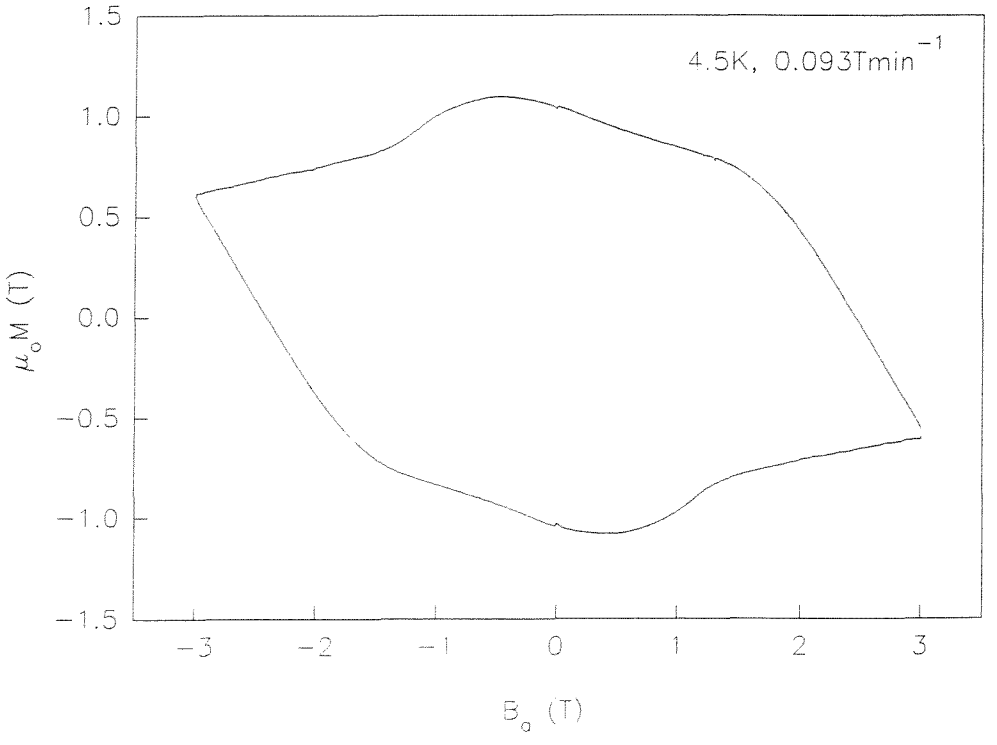

Figure 6.34 Magnetisation loop of BSCCO #1 at 4.5K, 0.093Tmin^{-1}.

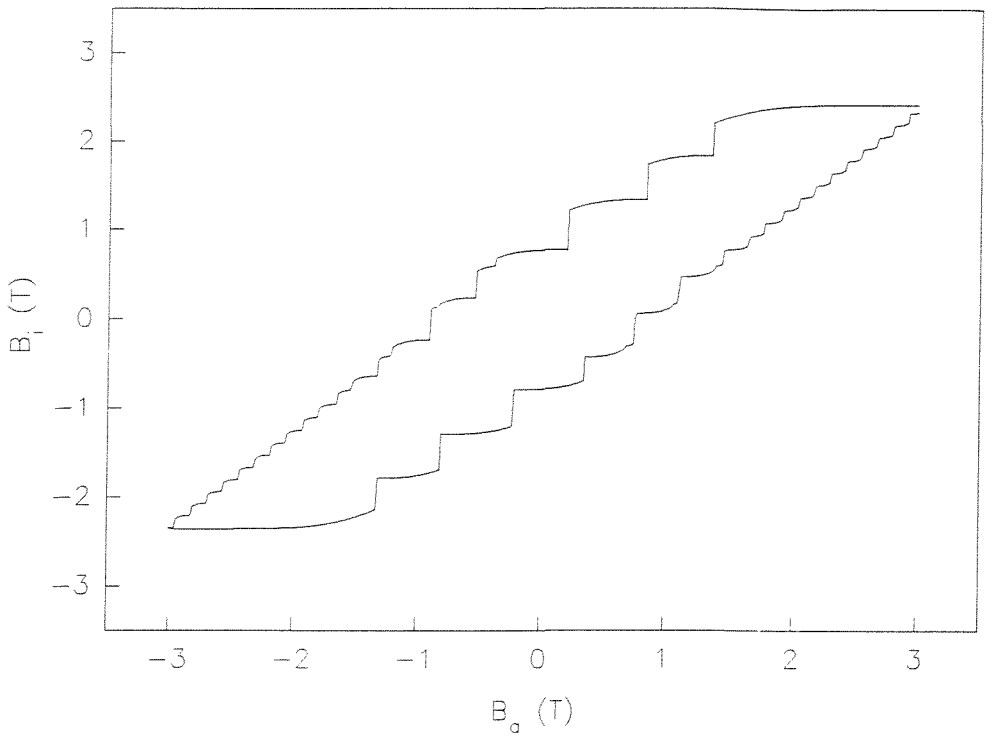

Figure 6.35 Shielding curve of BSCCO #1 at 2.2K, 0.256Tmin^{-1}.

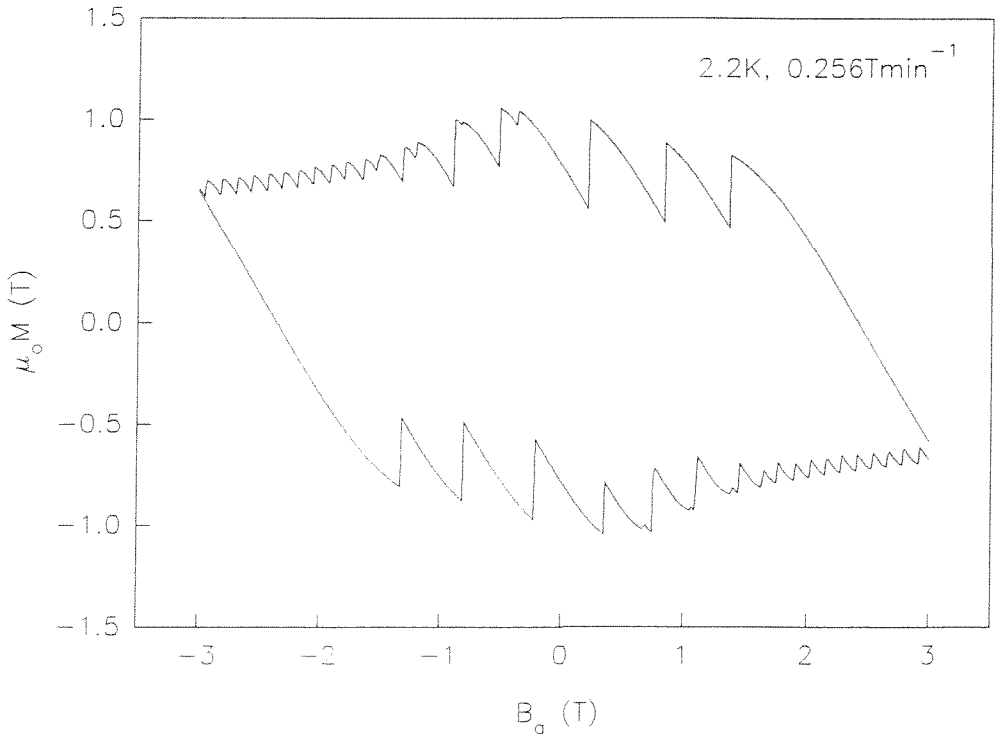

Figure 6.36 Magnetisation loop of BSCCO #1 at 2.2K, 0.256Tmin^{-1}.

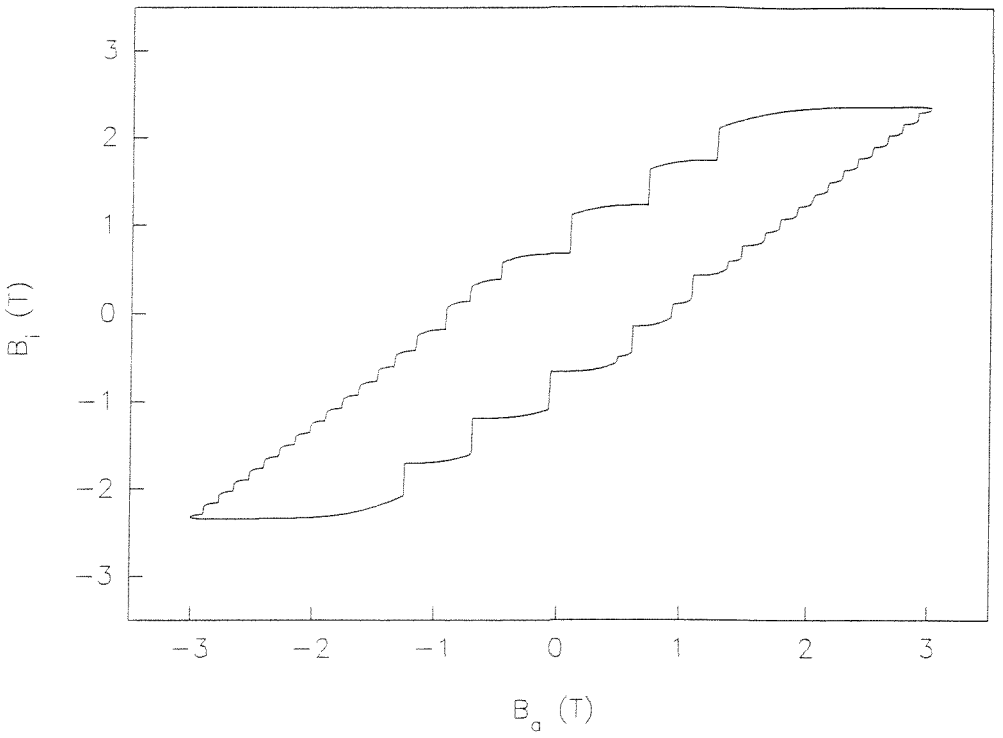

Figure 6.37 Shielding curve of BSCCO #1 at 2.2K, 0.225Tmin^{-1}.

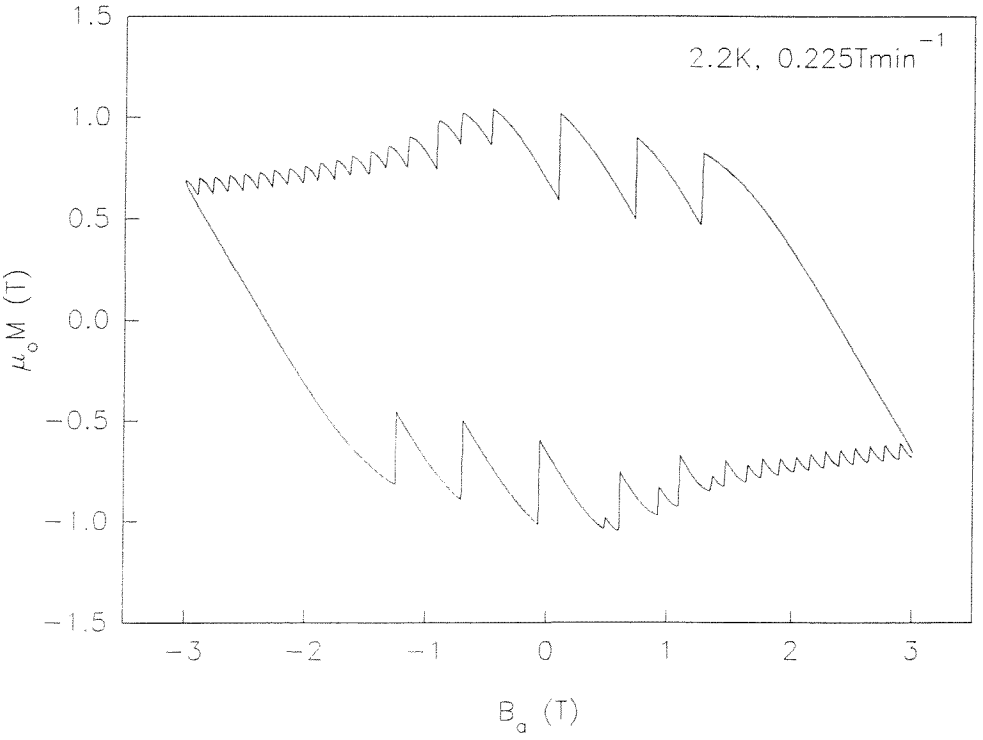

Figure 6.38 Magnetisation loop of BSCCO #1 at 2.2K, 0.225Tmin^{-1}.

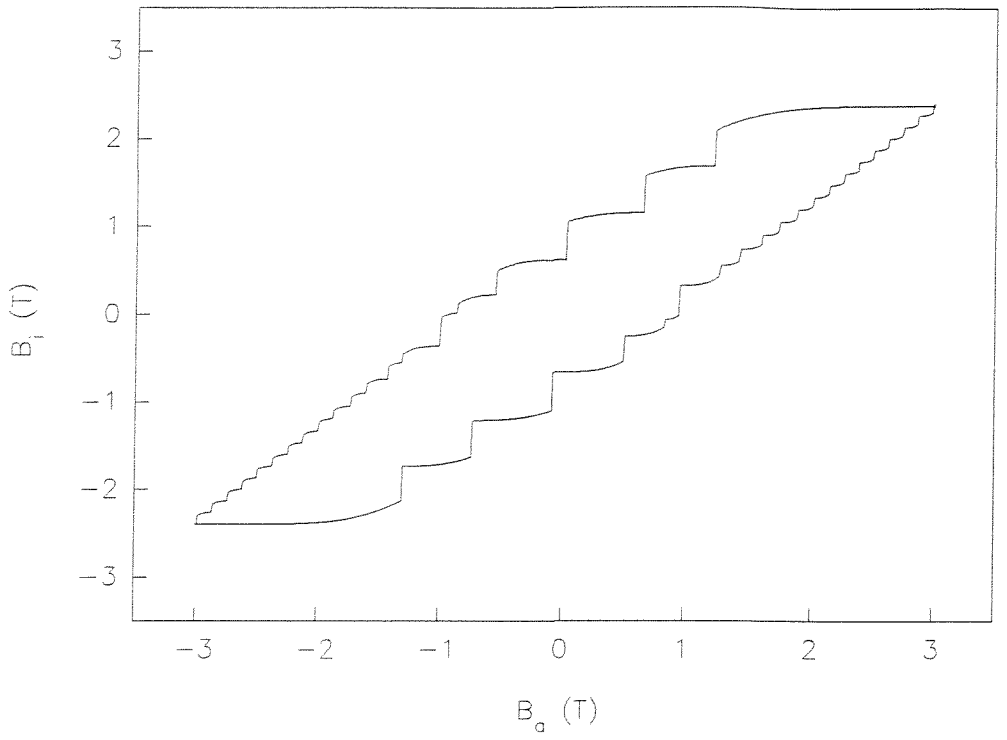

Figure 6.39 Shielding curve of BSCCO #1 at 2.2K, 0.17Tmin^{-1}.

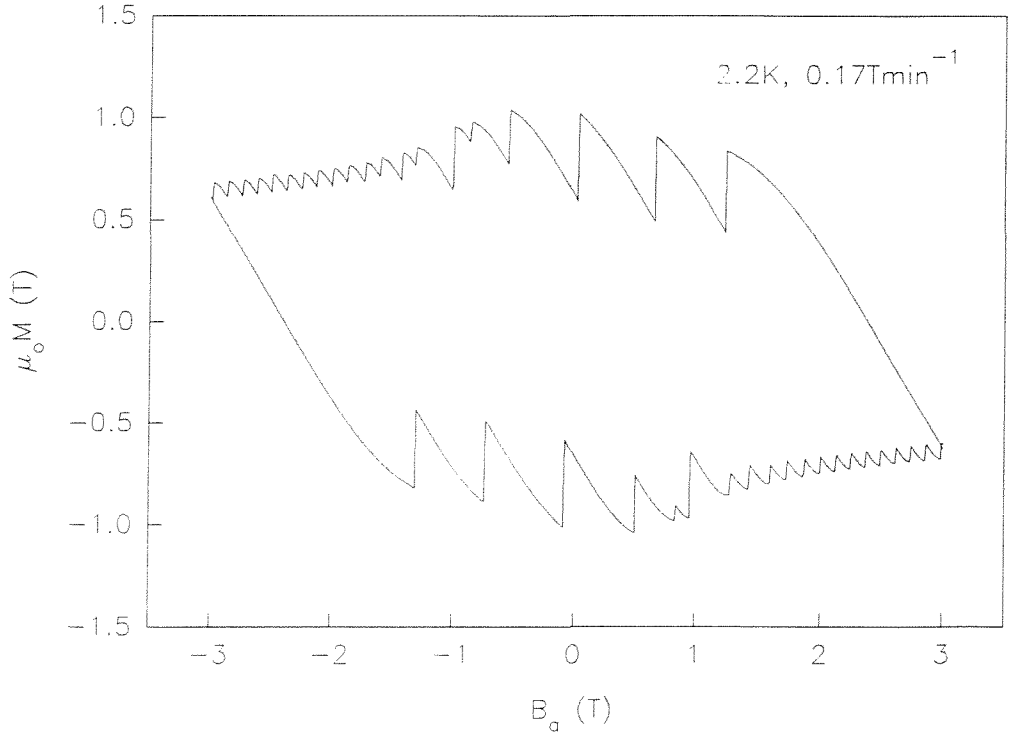

Figure 6.40 Magnetisation loop of BSCCO #1 at 2.2K, 0.17Tmin^{-1}.

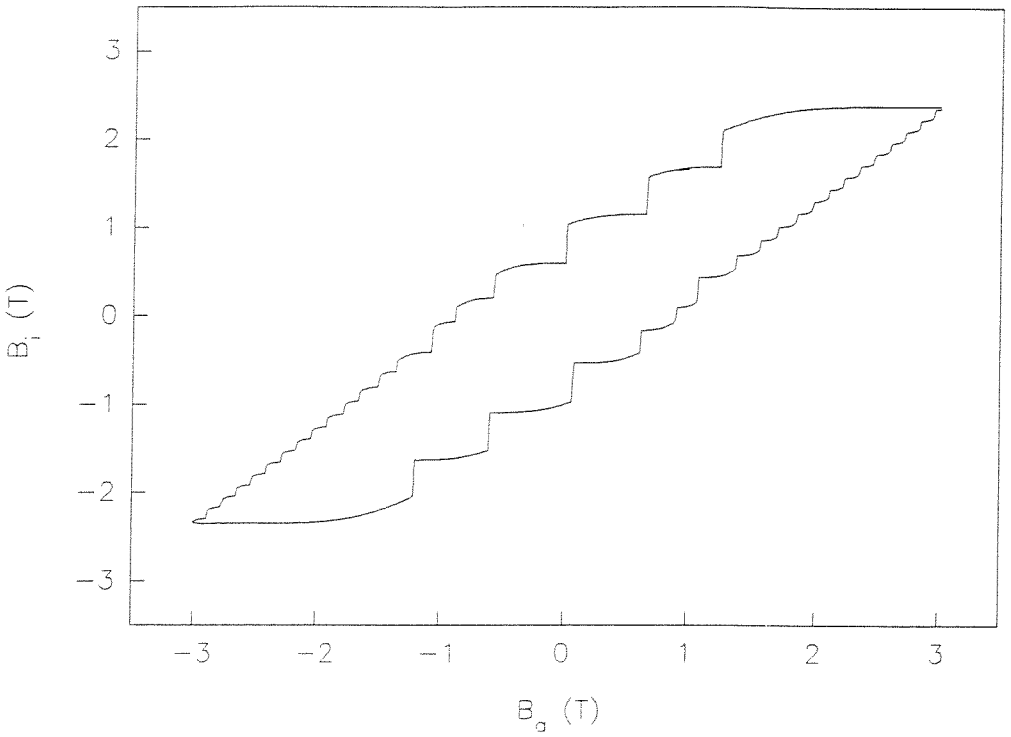

Figure 6.41 Shielding curve of BSCCO #1 at 2.2K, 0.144Tmin^{-1}.

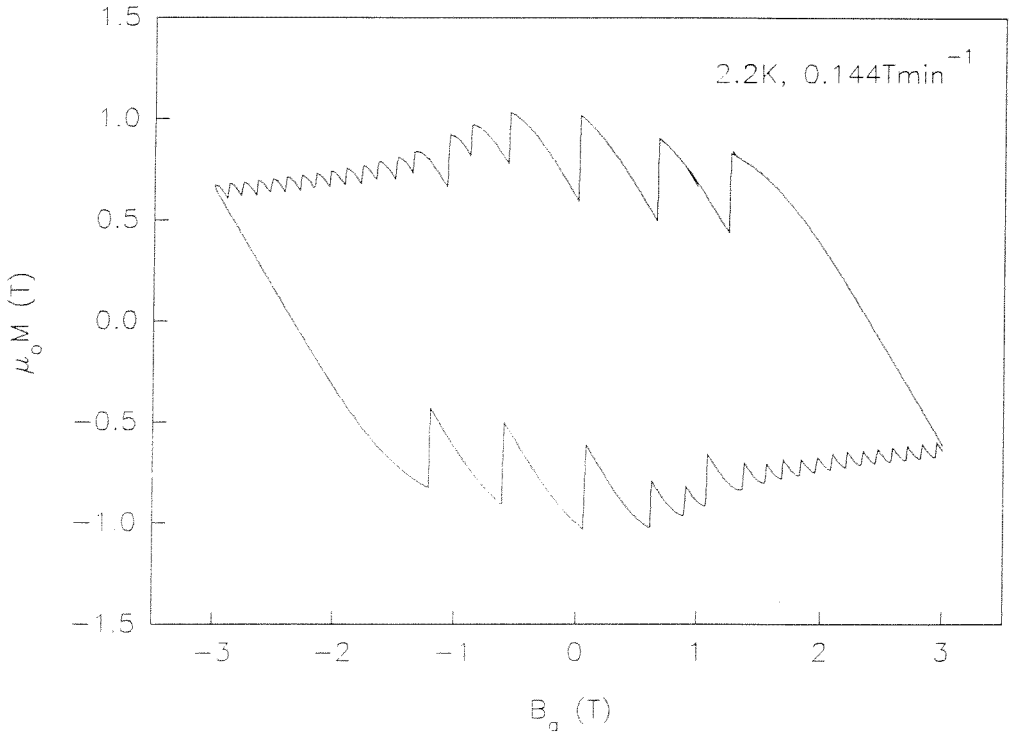

Figure 6.42 Magnetisation loop of BSCCO #1 at 2.2K, 0.144Tmin^{-1}.

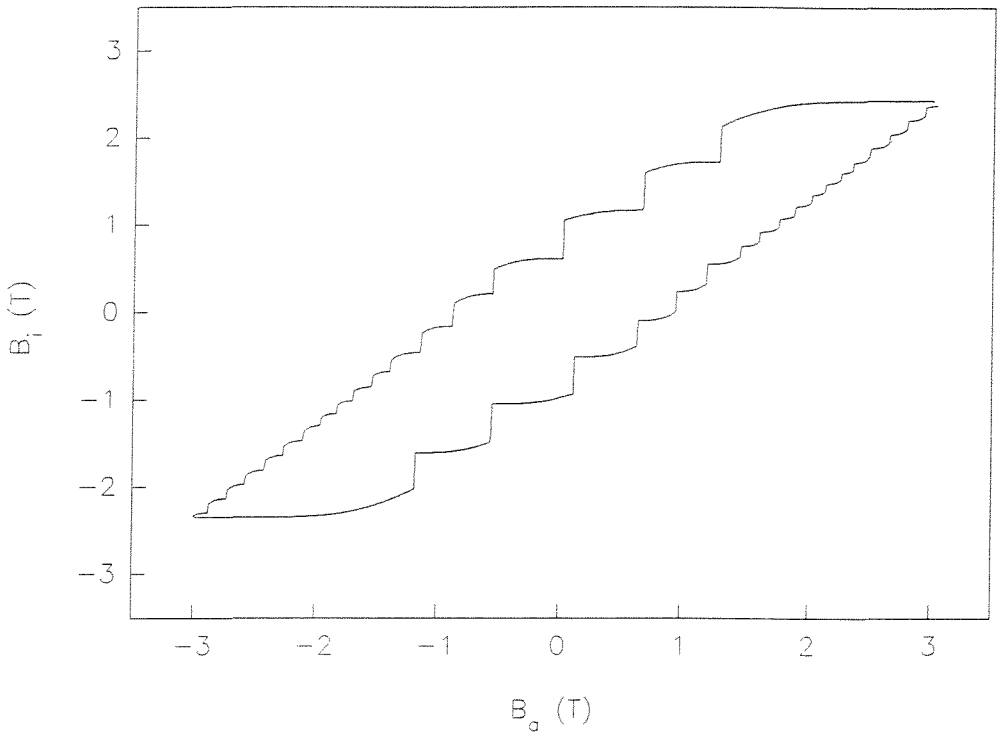

Figure 6.43 Shielding curve of BSCCO #1 at 2.2K, 0.124Tmin^{-1}.

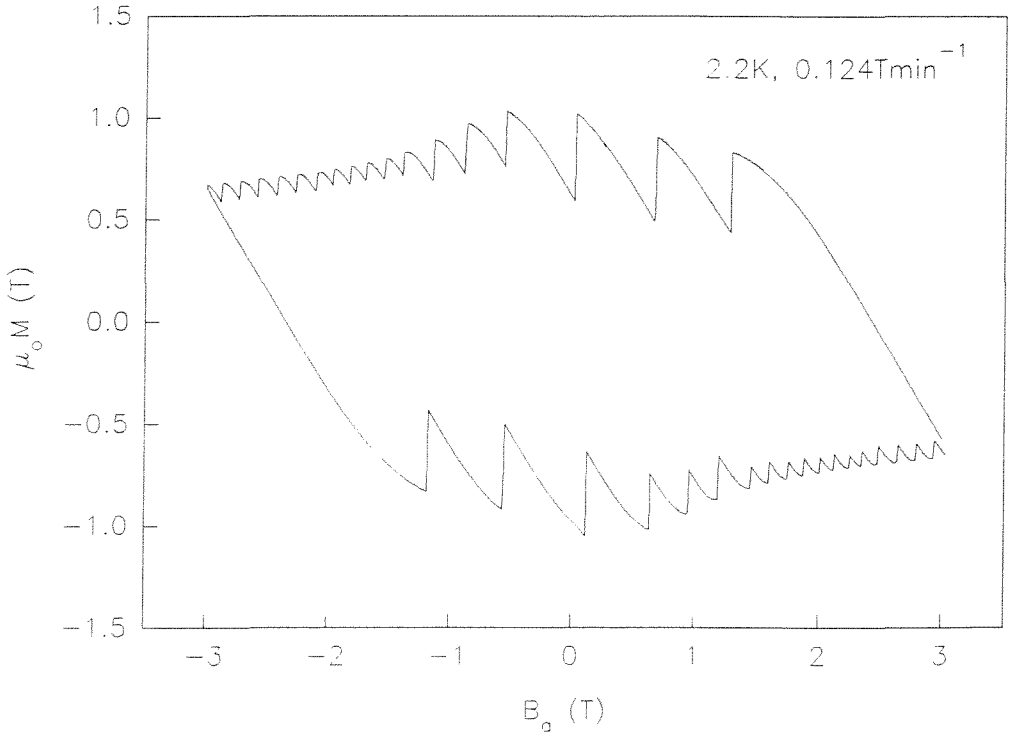

Figure 6.44 Magnetisation loop of BSCCO #1 at 2.2K, 0.124Tmin^{-1}.

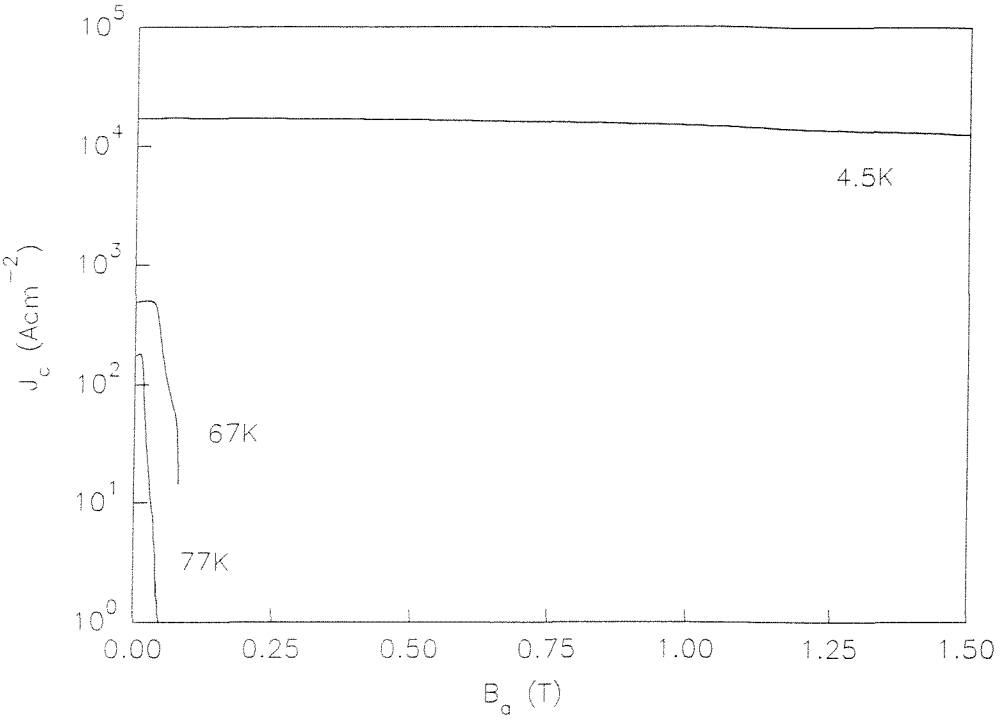

Figure 6.45 Applied field dependence of critical current for BSCCO #1 at 4.5, 67 and 77K.

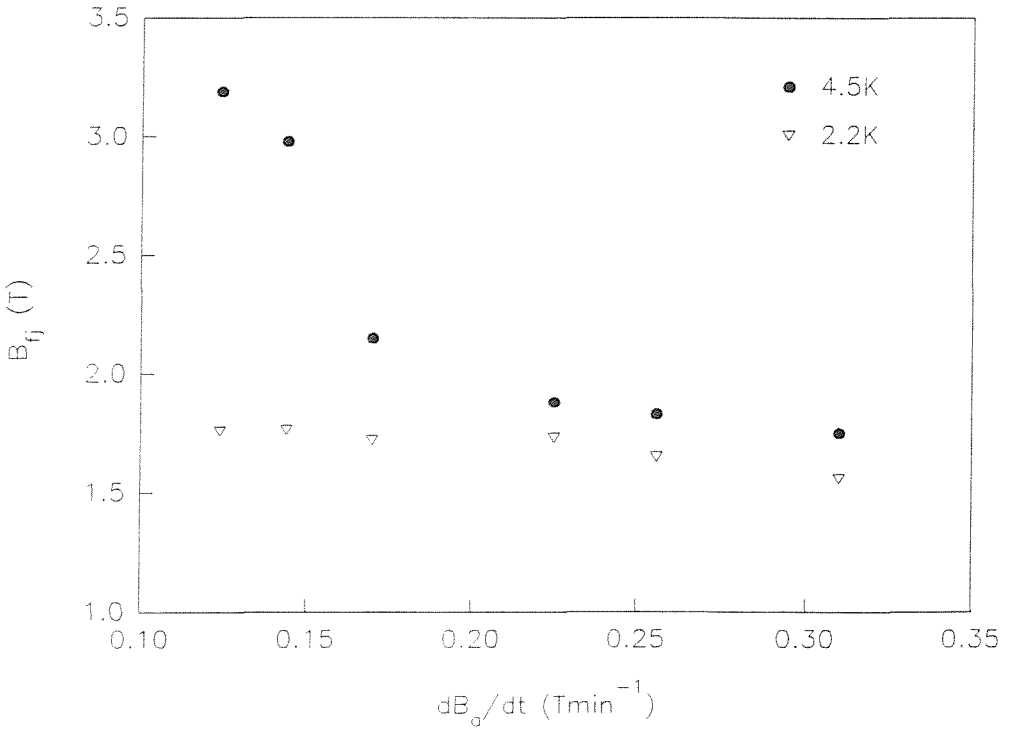

Figure 6.46 Sweep rate dependence of flux jump field at 2.2 and 4.5K.

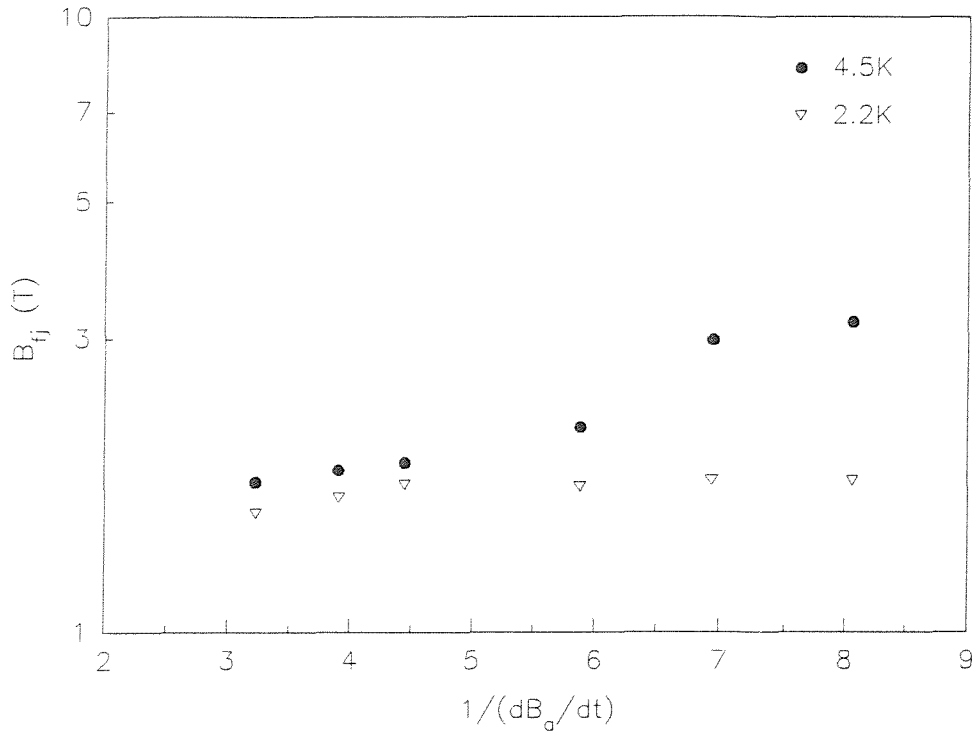

Figure 6.47 log B_{fj} dependence on $1/\dot{B}_a$ at 2.2 and 4.5K.

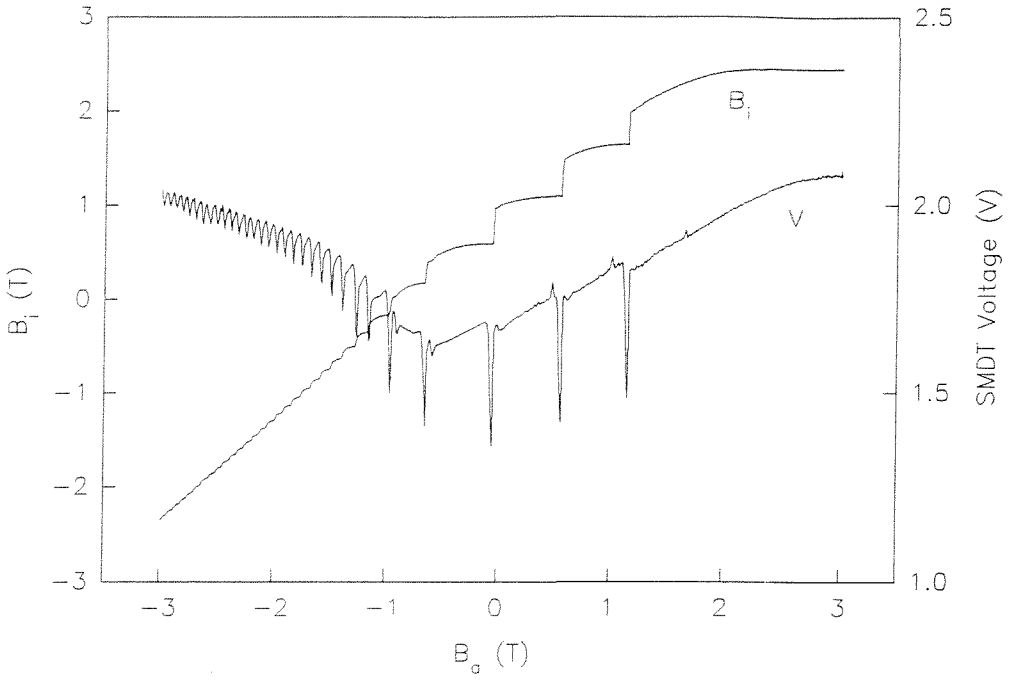

Figure 6.48 Temperature spikes due to flux jumps at 4.5K, 0.31Tmin^{-1}.

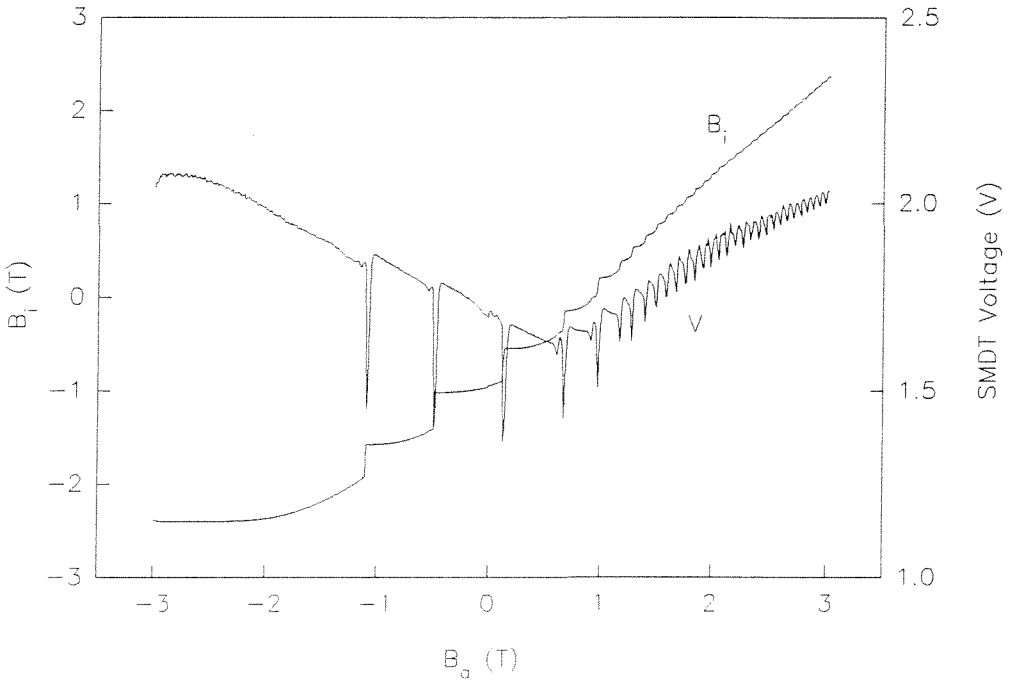

Figure 6.49 Temperature spikes due to flux jumps at 4.5K, 0.31Tmin^{-1}.

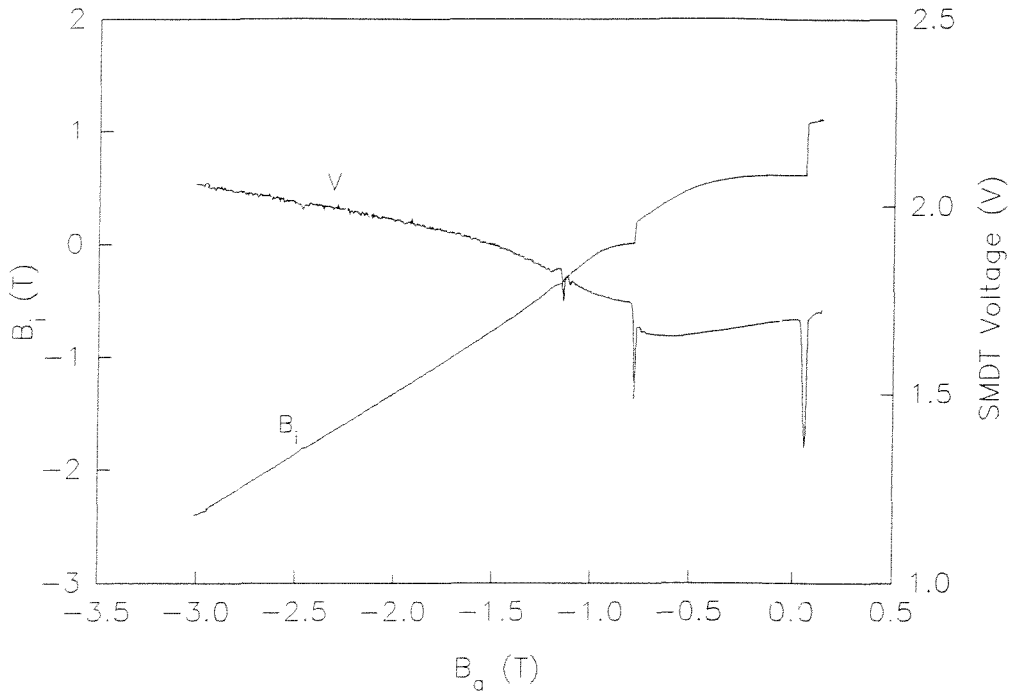

Figure 6.50 Temperature spikes due to flux jumps at 4.5K, 0.124Tmin^{-1}.

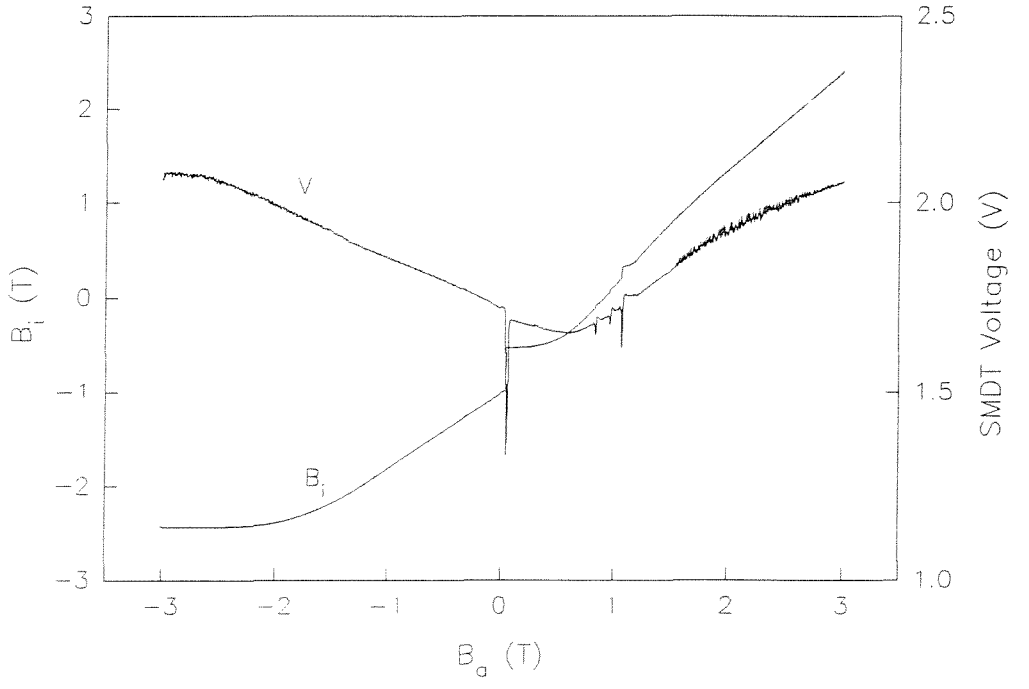

Figure 6.51 Temperature spikes due to flux jumps at 4.5K, 0.124Tmin^{-1}.

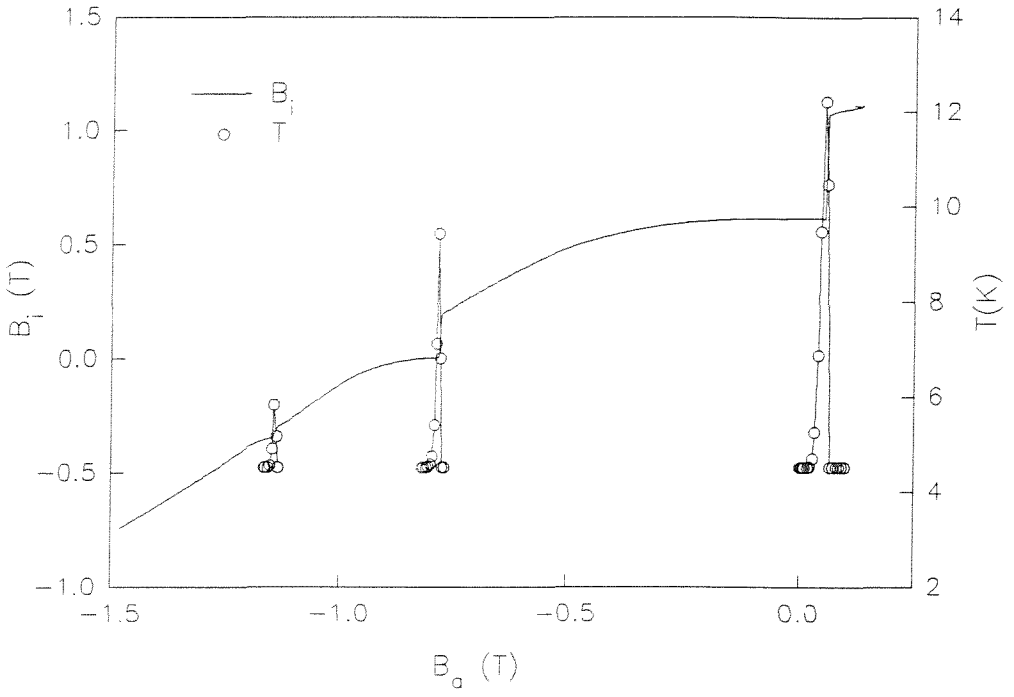

Figure 6.52 Calibrated temperature rises due to flux jumps at 4.5K, $0.124 T min^{-1}$.

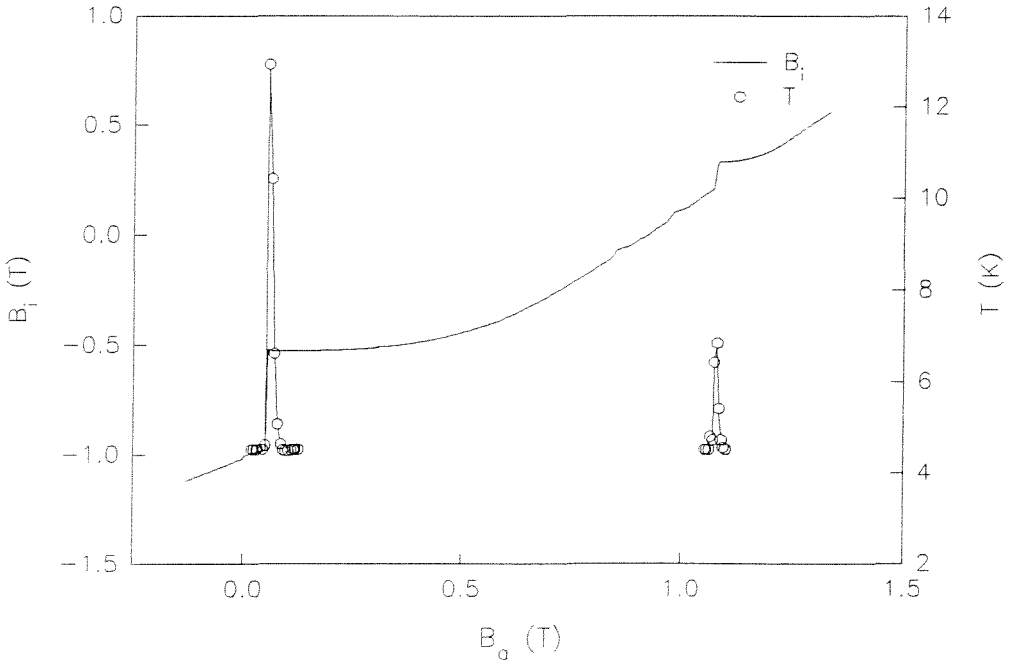

Figure 6.53 Calibrated temperature rises due to flux jumps at 4.5K, $0.124 T min^{-1}$.

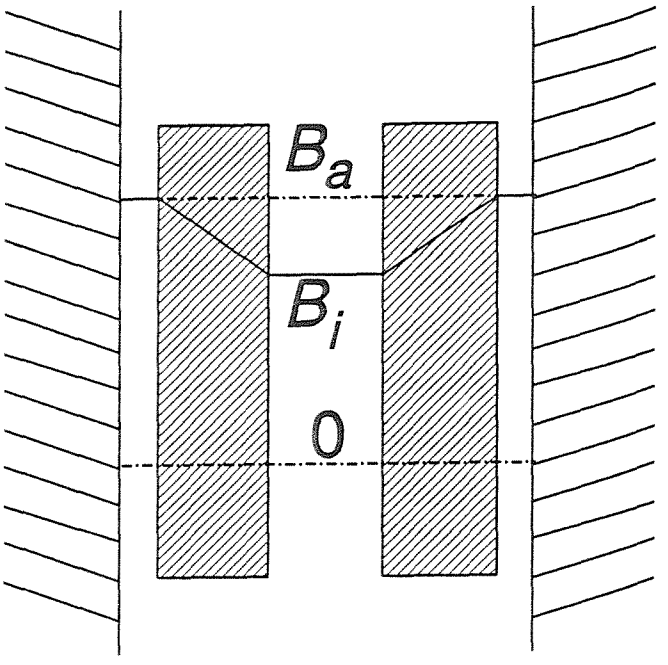

Figure 6.54 Magnetic flux profile used to calculate stored energy in tube.

7 Conclusions.

7.1 Shielding and magnetisation.

The shielding measurements performed on the HTS tubes at and around 77K show the low critical current densities of 100 to 200Acm^{-2} which are typical of these materials. The applied field dependence shows a fast decrease in J_c in small fields as is usual at these high temperatures; both J_c and its field-dependence increased rapidly as the temperature was lowered even moderately, to around 63K. Flux creep rates are high in both the YBCO and BSCCO tubes, and are manifested as a sweep rate dependent magnetisation in BSCCO. These factors repeat the well-known limitations on HTS applications at 77K. Improvements may be made on the sintered YBCO performance by melt-processing methods, but BSCCO still seems unlikely to be to be useful for large-current applications at liquid nitrogen temperatures. The granular nature of the YBCO sample is believed to be responsible for the enhancement of flux trapping over shielding, and the larger J_c which is found from the magnetisation loop width compared to that from the virgin shielding field.

At liquid helium temperature the improvement in critical current for YBCO is small, $J_c \simeq 780$Acm^{-2}, and a rather surprising sweep-rate dependent magnetisation was found at 4.5K in fields up to $\pm$3T. Although the granular structure may be the source of some of the unusual characteristics at low temperatures, no clear explanation could be given without further experimental work. The J_c of BSCCO was much more improved at low temperatures. A large difference between the shielding field B_{sh} and the trapped field B_{tr} appears at low temperatures, giving a magnetisation $J_c \simeq 17200$Acm^{-2}, twice that found from B_{sh}. This again seems to indicate that granular effects are involved. The $J_c(B)$ dependence is very small up to 1T, and appears to extend to much higher fields before decreasing significantly; this is as expected for

BSCCO at low temperatures and shows the most promise for high-current or high-field applications of any of the HTS materials.

Although the issue of the inter- and intra-granular components was not resolved for these samples, it would be a simple task to do so if time were available. By cutting an axial slot in the tube wall the intergranular current path can be broken and the intragranular magnetisation detected by the same method as used here.

7.2 Flux jumping properties.

No flux jumping was observed in the YBCO tube, possibly because the wall thickness was below the adiabatically stable limit, or because the flux creep creating a field sweep rate dependent magnetisation stabilised the sample against flux jumping.

Flux jumping was clearly observed in the BSCCO #1 tube between 2.2 and 4.5K at various sweep rates. The flux jump field B_{fj} increases with both increasing temperature and decreasing sweep rate. At 4.5K no jumping was observed below approximately 0.124Tmin^{-1}; although the field sweep rate dependence of B_{fj} apparently follows the conventional empirical relationship of $B_{fj} \propto \log \dot{B}_a$ at sweep rates equal to and above 0.225Tmin^{-1}, the dependence at lower rates is not entirely clear. No analytical temperature dependence can be given because of the limited range. Both the field sweep rate and temperature ranges need to be extended to obtain firm quantitative relationships.

The granular effects evidenced by the flux trapping and critical current properties may well create unusual flux jumping behaviour not seen in previous studies on small or single crystal samples. Such effects have been invoked here to provide a possible explanation of the flux jump structure observed in the shielding regions of the magnetisation, where exponentially decaying jumps were present at all the

temperatures considered and at the higher sweep rate values used. Further experimental data on the intragranular state is required to be conclusive.

Despite the tentative nature of some of the interpretation of the results, a number of important numerical parameters for flux jumping in BSCCO have been found:

- For the lowest sweep rate at which flux jumping occurs, 0.124Tmin^{-1}, $B_{fj}=2.9$ to 3.2T at 4.5K from the two measurements taken. This is rather higher than most HTS predictions but comparable to some other experimental values.

- For $B_{fj}=2.942\text{T}$ at 4.5K, a volumetric specific heat $\gamma C=0.027\text{JK}^{-1}\text{cm}^{-3}$ is found from the adiabatic flux jump equation. This is in very good agreement with a mean value $\gamma C=0.0276\pm0.0101\text{JK}^{-1}\text{cm}^{-3}$ found from a direct measurement of the temperature rise and energy dissipation in flux jumps at 0.124Tmin^{-1} and 4.5K. The adiabatic approximations thus seem justified.

- The above value of specific heat gives the adiabatically stable thickness $a_{fj}\simeq 1.36\text{mm}$ at 4.5K.

- For a simple T^3-only specific heat temperature dependence, the value at 4.5K implies $\gamma C=0.0032\text{JK}^{-1}\text{cm}^{-3}$, $B_{fj}=1.03\text{T}$ and $a_{fj}=0.46\text{mm}$ at 2.2K.

The above suggests that flux jump instabilities can be easily eliminated in BSCCO at low temperatures by controlling the conductor size, without having to resort to the extremely small diameters of LTS. At liquid nitrogen temperatures flux jumping does not appear to be a serious issue at all in moderate magnetic fields should efficient HTS conductors be developed which can operate that region. Measurements performed on a bulk sample have given parameters which may be considered when designing a solid form of HTS device such as a flux tube, flux pump or quasi-permanent magnet. The experimental results confirm the theoretical flux jumping predictions for HTS in being encouraging for the application of these materials in high-field and high-current situations.

Appendix 1 An investigation into glass-ceramic HTS.

A1.1 Introduction.

A1.1.1 Glass-ceramics in the Bi(Pb)-Sr-Ca-Cu-O system.

Glass-ceramic materials are formed by the controlled re-crystallisation of glasses. They have a highly dense, fine-grained structure, and applications range from cookware to missile nose cones. The advantage of these materials lies in their strength and machinability, neither of which are usually associated with ceramics. The discovery of superconductivity in the Bi-Sr-Ca-Cu-O system[3] suggested that it may be possible to make glass-ceramics out of these compounds.

Although none of the cations in the HTS compounds are glass-formers as defined in the original treatise on glass formation by Zachariasen[104], Bi_2O_3 is a conditional glass former[105], *i.e.* it can form a glass in the company of certain other compounds. Bi-Pb glasses were previously made by Dumbaugh[106][107]. These make the possibility of glass formation and subsequent re-crystallisation in the superconducting Bi-Sr-Ca-Cu-O system promising. The successful production of such glass-ceramics was first reported by Komatsu *et al.* (1988)[8]. All three superconducting phases (2201, 2212 and 2223) have been observed in glass-ceramic BSCCO. It was quickly found in sintered ceramics that Pb addition was beneficial in the 2212 phase, and really essential for growth of the 2223 phase. Very large amounts of Bi and Pb can be accommodated in silicate glasses (*e.g.* up to 90%wt. Pb), and the ease of glass formation in such compounds is related to the electronic structure of Pb^{2+}, suggesting that the Pb content might aid glass formation in a Bi(Pb)-Sr-Ca-Cu-O material. Studies have shown that a 20% substitution of Pb for

Bi is the most effective[108][109]; the Pb substitutes in a 1:1 ratio onto the Bi sites. It is not universally agreed whether or not Pb does indeed aid glass formation. Although glass-ceramic processing for YBCO with added B_2O_3 or P_2O_5 (both well-known glass-formers) has been attempted[110] it is not possible to obtain an amorphous pure-YBCO glass[8].

The technological advantages of a glass-ceramic HTS are two-fold: first, a machineable material would enable bulk shapes to be worked on after heat treatment, which is not possible with the brittle ceramic HTS. A second advantage is the possibility of being able to produce glass-ceramic HTS fibres. This is done by drawing fine glass fibres from a glass pre-form, and subsequently heat treating them to obtain the superconducting phase[9][111][112]. Such a method of manufacturing HTS wires is attractive because it is a simple process, and uses existing technology similar to that for optic fibres. However, to draw fibres from a glass melt requires good glass formation, a suitably high viscosity and a large working range (the temperature range available for drawing). Ca, and possibly Sr, are "network modifiers" which tend to reduce the viscosity the glass; one of the main problems in obtaining Bi(Pb)-Sr-Ca-Cu-O fibres is the very low viscosity of the molten glass. Only very low critical current densities have been reported: $22Acm^{-2}$ at 30K[111] to approximately $40Acm^{-2}$ at 60K[112], with T_c lower than the bulk material. Bulk J_c's of up to $1800Acm^{-2}$ have been reported[113], and densities of almost 100% of theoretical can be obtained (although in mixed phases)[114].

The main problem of glass-ceramic production is that of isolating the desired phase. The 2212 phase is much easier to obtain than 2223 which requires annealing at very well-controlled temperatures (to within a few °C) for long times. However, 2223 is the most attractive phase from an applications standpoint due to its high T_c of around 110K. The process of glass formation in these materials has to be understood to achieve a useful viscosity and working range. Determination of the 2223 phase nucleation and growth mechanisms are of the highest importance if HTS glass-ceramics are to be successful.

A1.1.2 Characterisation of glass-ceramics.

The thermal properties of glass-ceramics are mainly characterised by three temperatures: the glass transition temperature T_g, one or more (depending on the number of phases) crystallisation temperatures T_x and the melting point T_m. These can be found from differential thermal analysis (DTA). This technique measures the temperature of a sample compared to an inert standard (usually burnt alumina) in a heating ramp, and thus measures the exotherms and endotherms at various temperatures which can be associated with the above characteristic points. T_g is defined as the temperature below which the material is strictly a glass, and above which it is a super-cooled liquid[105]; it shows in DTA curves as a slight hump or change of gradient. The accurate identification of T_g from DTA data is often difficult and requires experience to do well. The "working range" of a glass is the difference between T_x and T_g. The crystallisation of different phases shows up as exothermal peaks in DTA as the material moves to a lower free energy state, while partial melting occurs as endotherms. The associated technique of thermogravimetric (TG) analysis measures the mass of the sample, indicating oxygen uptake, *etc.*

DTA can be used in conjunction with X-ray diffraction (XRD) data to identify the various phases with their respective T_x. This is usually done by using XRD on a sample quenched from a given temperature to preserve its state at that point. In the case of superconducting materials, T_c measurements by resistance or susceptibility can also be used to identify the phases.

A1.1.3 Research aims.

The intention of this study was to examine the formation of the Bi(Pb)-Sr-Ca-Cu-O 2223 glass-ceramic, aiming to identify the phase growth process, with the hope of understanding the 2223 nucleation. XRD and DTA of the materials was carried out at the Pilkington Technology Centre, Lathom.

A1.2 Glass formation.

Although the Bi(Pb)-Sr-Ca-Cu-O 2223 system forms a glass easily on rapid cooling, there has been repeated evidence of crystalline CaO in the glass. To make glass preforms suitable for drawing into fibres, it is important to have a completely amorphous glass. An excess Bi content was shown by Komatsu *et al.* (1990)[115] to aid crystallite-free glass formation. Since the ability to form a glass is fundamental to further investigation, this was selected as an experimental starting point.

Bi_2O_3, PbO, $SrCO_3$, $CaCO_3$ and CuO of $\geq 99.99\%$ purity were mixed and ground in an agate mortar in stoichiometric ratios to give $Bi_{1.6+y}Pb_{0.4}Sr_2Ca_2Cu_3O_{10}$ with $y=0.0$, 0.4, 0.9, and 1.4. The precursor powders were melted in alumina crucibles for 30 minutes at 1150°C in air, and then quenched between copper plates. The resulting glassy material was in the form of plates 0.4 to 1.2mm thick, with a lustrous grey-black colour. These were powdered for XRD analysis, using a percussion mortar since the glasses were extremely hard.

The powder XRD patterns are shown in Figure A1.1. A small CaO peak can be seen in the XRD pattern for $y=0.0$; no crystalline material was detected for higher Bi contents, and the XRD graphs show the broad amorphous curve associated with a glass. X-ray fluorescence (XRF) was used to detect any impurities since it is known that the BSCCO compounds are very susceptible to poisoning, and showed that all the samples contained 2 to 3% Al, approximately equivalent to a formula ratio of 0.9. This indicates that alumina crucibles are not suitable for use with these materials, and that platinum ones are necessary. More importantly, Al_2O_3 is a well-known glass-former, and may screen any effects of varying the Bi content. It is not clear whether this level of Al contamination would affect the superconductivity or phase formation; in fact Al has been added to BSCCO compounds to aid glass formation without expecting to significantly alter the superconducting properties[116][117] (many additives have been used for various reasons, *e.g.* Sn, Sb, Pt, and even Te). Al also

increases the viscosity of the molten glass which may make it a good additive for fibre production. However, an uncontrolled Al content has to be avoided.

The DTA of two powdered $y=0.0$ samples at 10°Cmin^{-1} showed $T_g \simeq 330$°C, two crystallisation peaks of $T_{x1} \simeq 475$°C and $T_{x2} \simeq 525$°C, and a range of partial melting endotherms from 715°C to 950°C (Figure A1.2). This T_g value is slightly lower than most reported which are generally in the range of 340-390°C, with some higher, 400-450°C. This could be because the estimate of the position in the DTA curve is too low; as noted above, it is not always easy to identify T_g accurately. The very sharp T_x peaks indicate rapid crystallisation.

The above compositions were repeated using platinum crucibles with precursor powders that had been previously decomposed overnight at 800°C. The XRD patterns showed the CaO and some $CaCO_3$ crystalline content more clearly for $y=0.0$. DTA on the powdered $y=0.0$ sample gave T_g very similar to the above, but with T_{x1} and T_{x2} slightly lower at 428°C and 512°C respectively; a solid sample gave the same T_g but higher T_{x1}, T_{x2} of 442°C and 555°C. The onset of partial melting in both cases was practically the same as above. TG analysis showed a large weight gain up to the crystallisation peaks in the powdered sample, which one may associate with oxygen uptake; the solid sample showed only a small weight gain, around the partial melting endotherms. It is not clear how much influence the Al poisoning in the first set of samples had, although the clearer crystalline peaks in the second $y=0.0$ XRD point to its glass-forming enhancement. The difference in T_{x1},T_{x2} between the solid and powdered samples suggests a surface nucleation mechanism since one would not expect any difference where bulk nucleation dominates; this finding is similar to that of Tatsumisago *et al.* (1989)[118] for similar BSCCO glasses.

A1.3 Superconducting phase formation and heat treatment.

The kinetics of phase growth in the BSCCO system are very complicated, and can be strongly affected by small changes in composition, temperature, *etc.* The three main phases of 2201, 2212 and 2223 seem to grow successively from each other at increasing time and temperature in the heat treatment. The 2223 phase forms in a very small temperature-time region, and often co-exists with 2212; obtaining phase-pure 2223 is very difficult. Crystallisation of a given phase is determined by both the nucleation rate and the crystal growth rate[119]. In the BSCCO system the following process seems to occur[120] (the exact temperatures vary between references). The 2201 phase forms first above around 450°C, with phases of Cu_2O, CaO and possibly Ca_2CuO_3 and $CaPbO_3$. Above about 620°C 2212 starts to grow at the expense of 2201, which practically disappears at 840°C. 2223 begins to form after about 60 hours annealing at near this temperature from an intergrowth of 2212 and other phases. Pb substitution for Bi decreases the time required for 2223 formation[109] and therefore seems to play a role in crystal growth or nucleation; the exact nature of this role will be important to determine. Formation of phase-pure 2223 requires very close temperature control. Most authors have reported heat treatment temperatures between 845 and 850°C: even a difference of a few degrees can affect the end phases.

A1.3.1 Experimental results.

To investigate the heat treatment process, the second batch of glasses prepared in A1.2 were annealed in air in a tube furnace at 844°C and 850°C for 24 and 120 hours. The as-quenched glassy plates were put on platinum gauze on an alumina slide to prevent contamination, and the temperature ramped up over approximately 40 minutes; on completion of the heat treatment the samples were allowed to slowly cool

to room temperature. The furnace temperature was calibrated using Al and Ag wire to find set points at their melting temperatures (660.37°C and 961.93°C respectively).

The a.c. susceptibility of the 844°C/120h sample with $y=0.0$ is shown in Figure A1.3. The double transition of a two-phase sample is observed, indicating the presence of 2212 with T_c=78-81K and 2223 with T_c=102-109K. The onset of the upper transition is very much slower than the lower one, showing the poor quality of the 2223 phase. The sharp 2212 transition implies relatively good quality. Because the measurement is uncalibrated, the superconducting volume fraction of the whole cannot be estimated; 2223 makes up approximately 35% of the superconducting volume from the susceptibility curve. The data is taken in zero applied d.c. field with an a.c. field of 0.3mT at 11Hz, with increasing temperature. It is therefore the flux expulsion that is measured, a more reliable verification of bulk superconductivity than the shielding fraction. The curve is very noisy due to the small volume of the sample, and possibly a small superconducting volume. Because the susceptometer was not routinely available for use this measurement could not be performed on other samples, a major limitation to analysis.

The samples were powdered for XRD analysis to remove any crystal orientation which might distort the peak heights. The XRD patterns (Cu-Kα radiation) are shown in Figures A1.4 to A1.7. Because the standard JCPDS data files for the different Bi(Pb)-Sr-Ca-Cu-O phases were not available, exact determination of all the phases present is difficult. The 2212 and 2223 phases can be identified by their characteristic (002) peaks at 2θ=5.8° and 4.7° respectively[121]. Other clear peaks are at 33° for the 2212 (020) and (200) planes, and at 24° for 2223. For 844°C/24h and 850°C/24h (Figures A1.4 and A1.5) the patterns are identical; the (002) peaks at approximately 5.8° are clear and the sample is almost completely 2212. This is as expected for the short annealing time before the 2223 has begun to grow. No impurity phases were detected by the computer matching program. At the longer annealing times of 120h the 2223 phase has grown as evidenced by the 4.7° peaks in Figures A1.6 and A1.7, with 2212 also present. The relative fractions of the two main phases can be estimated from the (002) peak heights, showing that the 850°C/120h sample is predominantly

2212 with 2223, while the 844°C/120h sample contains a larger fraction of 2223 with 2212 as witnessed by the much stronger 4.7° and 24° peaks. These results agree with the two-phase results of the a.c. susceptibility measurement on the 844°C/120h sample, although the relative fractions are different.

The above indicates that a heat treatment temperature of close to 844°C is the optimum for formation of the 2223 phase in the glass-ceramic, with long processing times requires for the transformation of 2212 to 2223. Samples with increased Bi content, $y=0.4$ and 0.9, were also annealed at 850°C for 120h. The XRD patterns in Figures A1.8 and A1.9 show that these contain 2212 only with no 2223. Thus a Bi-rich composition apparently impedes 2223 formation. The production of a 2212 glass-ceramic is evidently much easier than the 2223, and may prove to be the only form in which a single-phase material can be routinely obtained.

A1.3.2 High temperature XRD.

In order to further clarify the phase formation mechanism, a high temperature XRD technique was attempted. Most XRD analysis of phase formation is performed by quenching the material from a series of time and temperature points and examining the development of the phases with respect to these[109][120]. However, the cooling process may change the structure of the material, giving misleading conclusions as to the intermediate phases. Some high temperature XRD has been done with small samples on a Pt heater[122]. The system at Pilkington's Technology Centre uses a Philips diffractometer with a small tube furnace which has windows through which an angle of 55° can be scanned; this was the first commercial high temperature XRD apparatus in the UK. A powdered sample is held in a Ti plate in the furnace, which is then evacuated to prevent oxidation of the heating elements.

This procedure was used on 2223 glass samples from the batches described previously. A computer controlled program was set to take scans at various

temperatures in the heating schedule from 400°C to 850°C, with two scans 20 minutes apart at each temperature. Although devitrification of the glass could be observed at 400°C, no phase identification was possible for any of the XRD patterns obtained. The reasons for this are unclear; although heating in a vacuum may be expected to affect phase formation, identification of the phases present should still be achieved. This negative result for the 2223 glass-ceramic was also found by others using an identical system[123] although very good results were obtained with 2212[124].

A1.4 Conclusions.

The following points may be drawn from the above investigation of 2223 glass-ceramics:

- The 2223 material forms a glass easily upon rapid quenching from the melt. An excess Bi content aids glass formation, but impedes the growth of the desired 2223 phase. Al may be a better additive to improve glass formation and increase viscosity if fibres are to be drawn.

- The optimum temperature for heat treatment to obtain the 2223 phase is close to 844°C.

- While the 2212 phase forms within 24h at the correct temperature, the 2223 phase formation requires very much longer processing times. Although 2223 was obtained for 120h heat treatments, no single-phase samples were achieved.

In order to pursue such an investigation further, constant access to XRD and other measurement facilities are essential, and a number of furnaces are required to perform

parallel processing in view of the long times involved, where here a single one was used and use of XRD *etc.* with Pilkington was necessarily limited.

The nucleation mechanism for 2223 continues as the most important feature to be determined. The samples considered here were solid glass plates as quenched; the heat treatment of powdered glasses may improve nucleation, as well as making the production of shaped components easier. It may be possible to nucleate the phase by "seeding" a powdered glass with phase-pure 2223 as this is a common method with other glass-ceramics. The roles of the various cations and their respective ratios also remain to be clarified. The precise temperature control and long times involved in 2223 formation may make it unlikely to be a commercial success, and 2212 could be reverted to. Nevertheless, from the limited results presented here, the feasibility of a glass-ceramic processing route for HTS has been demonstrated.

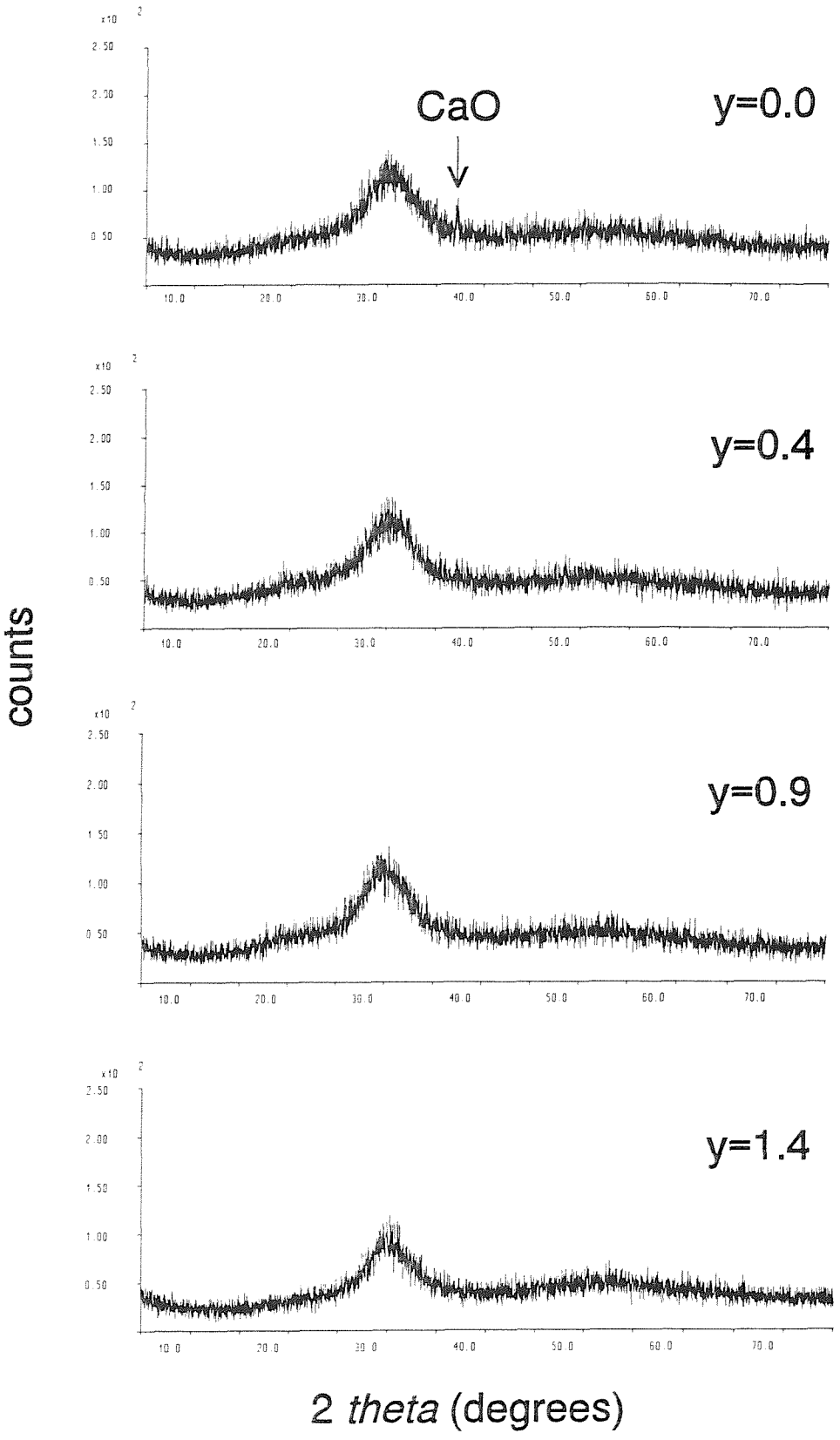

Figure A1.1 XRD patterns of Bi(Pb)-Sr-Ca-Cu-O 2223 glass for varying Bi content.

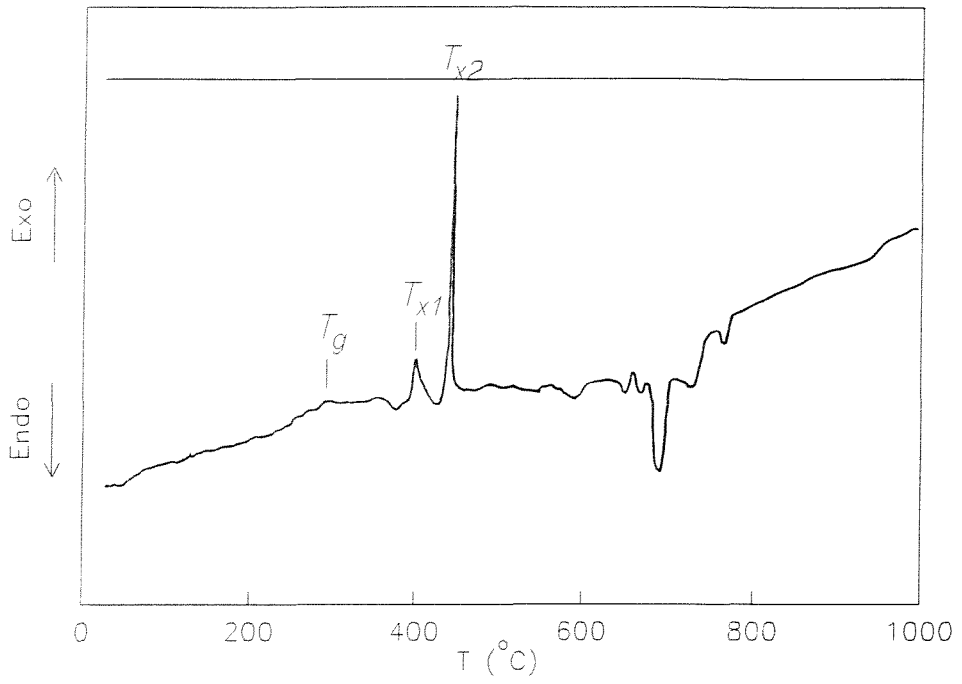

Figure A1.2 DTA at 10°Cmin^{-1} of Bi(Pb)-Sr-Ca-Cu-O 2223 glass with y=0.0.

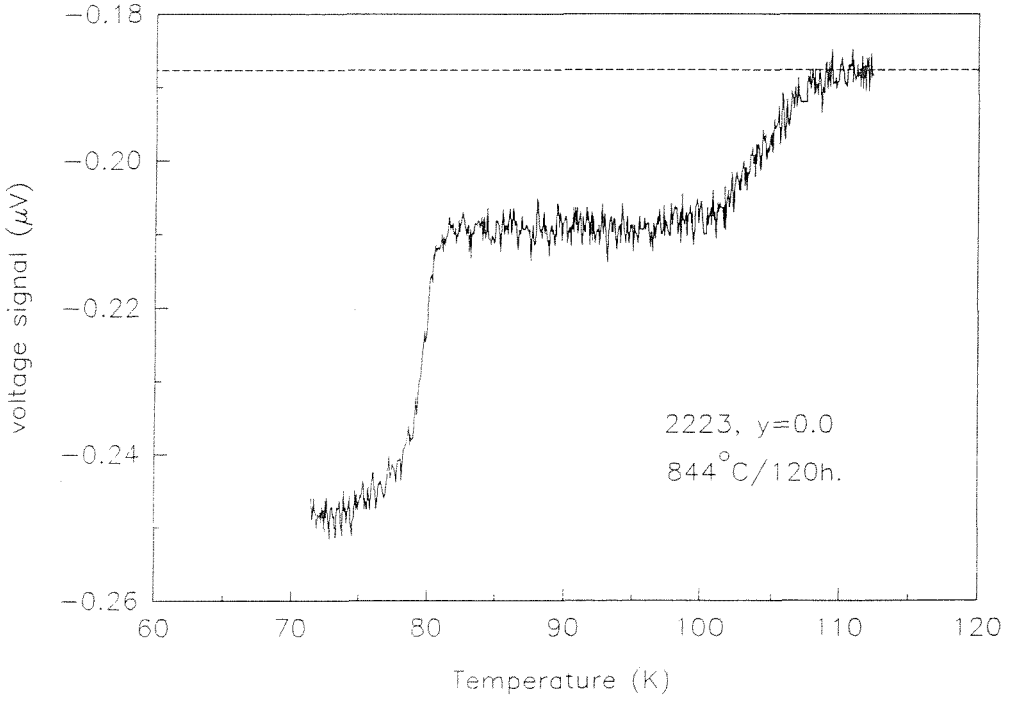

Figure A1.3 a.c. susceptibility of glass-ceramic with $Bi_{1.6}Pb_{0.4}Sr_2Ca_2Cu_3O_{10}$ stoichiometry heat treated at 844°C/120h.

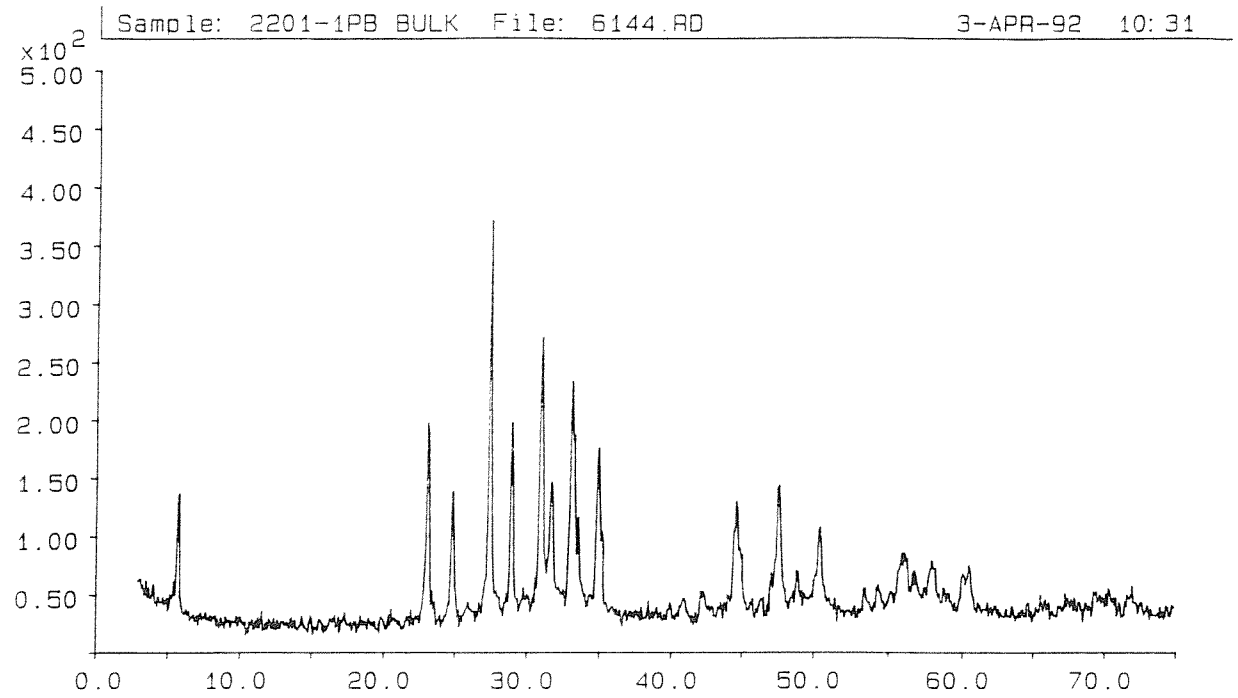

Figure A1.4 XRD pattern of Bi(Pb)-Sr-Ca-Cu-O 2223 glass-ceramic annealed at 844°C for 24h.

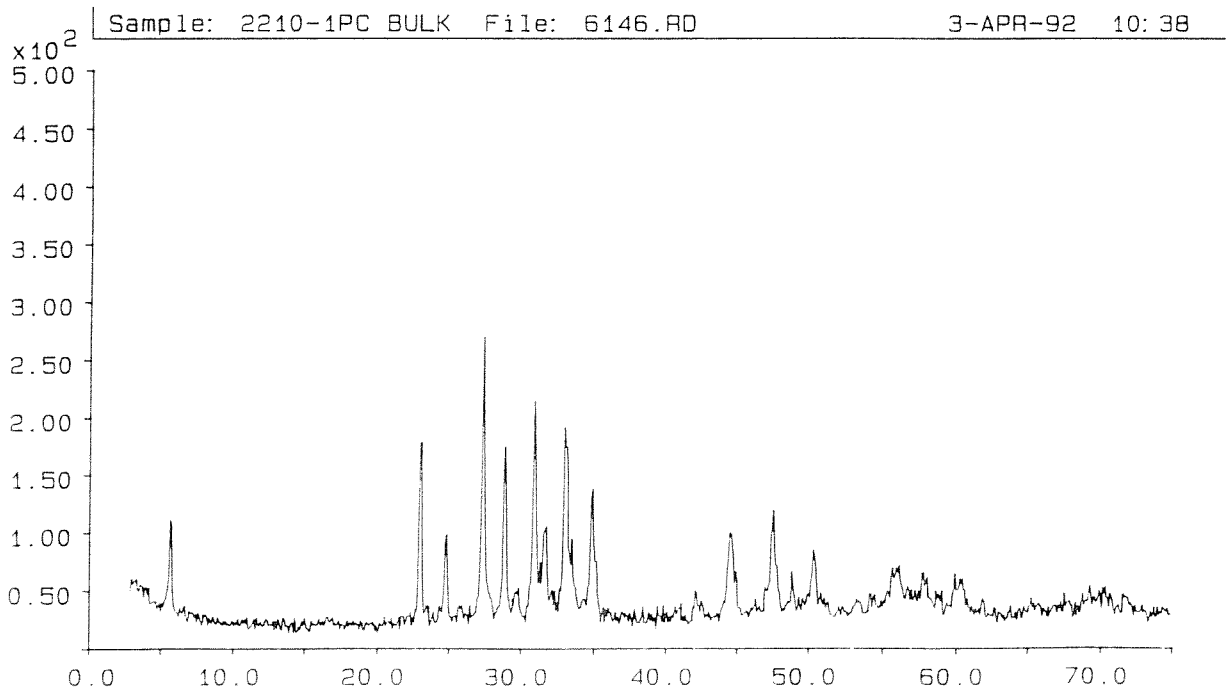

Figure A1.5 XRD pattern of Bi(Pb)-Sr-Ca-Cu-O 2223 glass-ceramic annealed at 850°C for 24h.

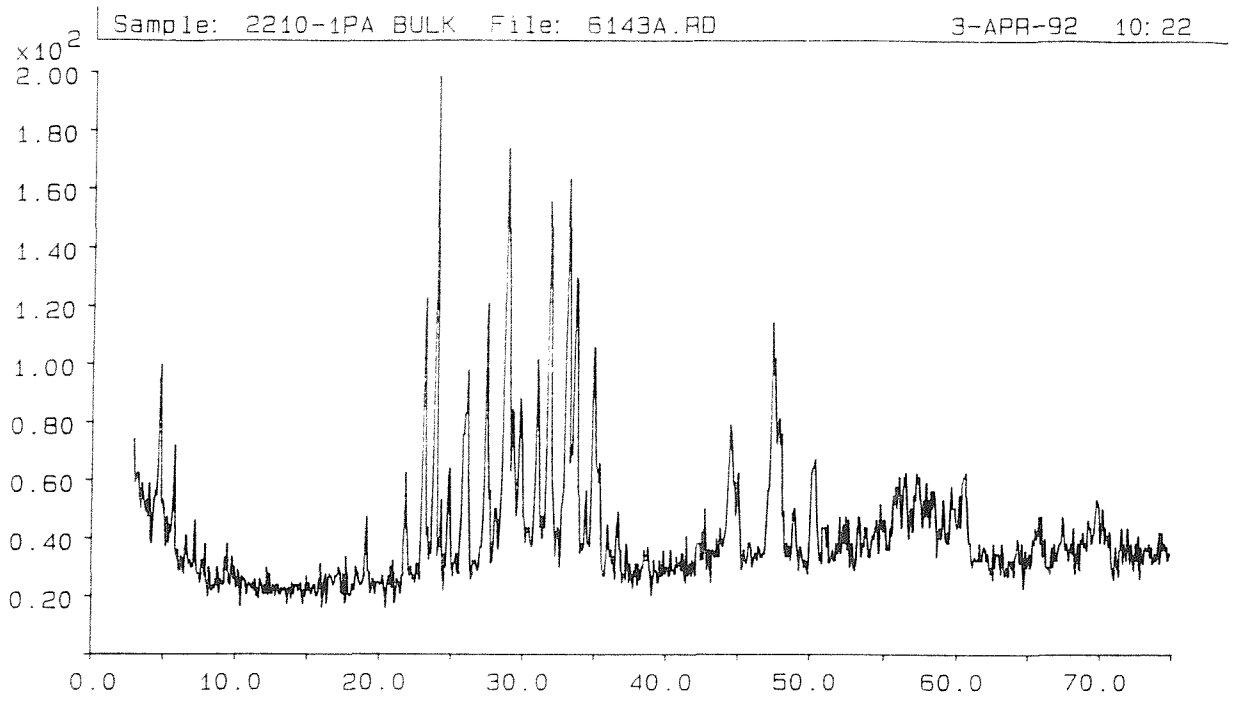

Figure A1.6 XRD pattern of Bi(Pb)-Sr-Ca-Cu-O 2223 glass-ceramic annealed at 844°C for 120h.

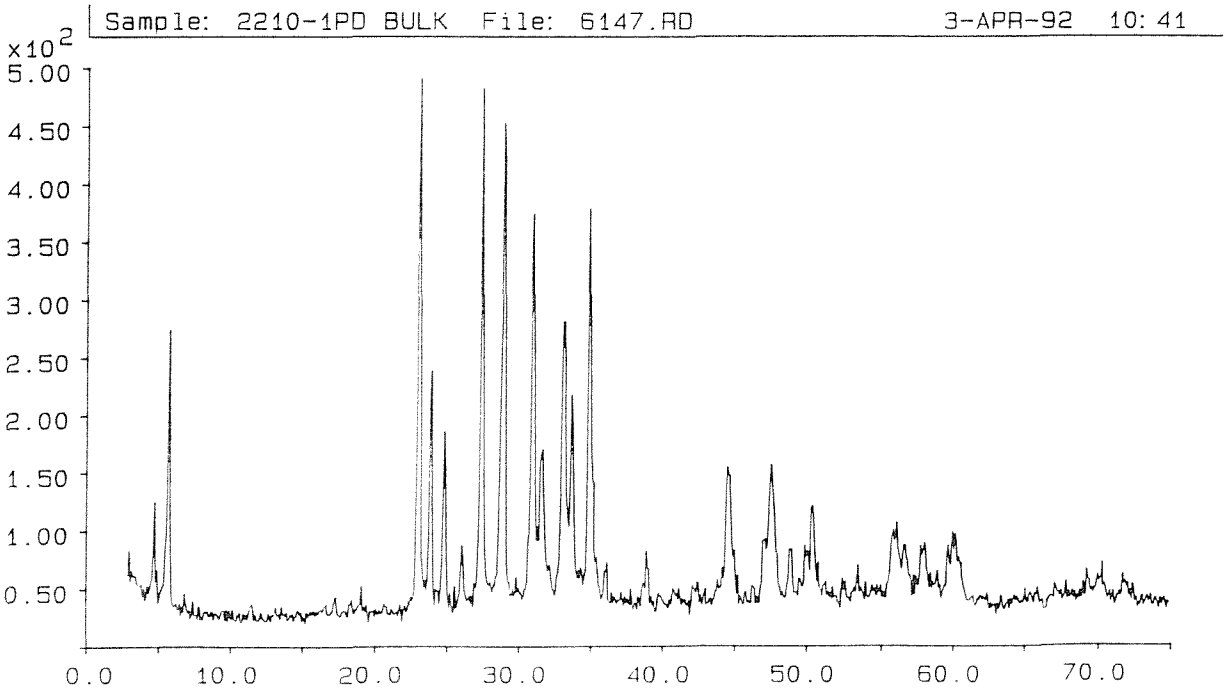

Figure A1.7 XRD pattern of Bi(Pb)-Sr-Ca-Cu-O 2223 glass-ceramic annealed at 850°C for 120h.

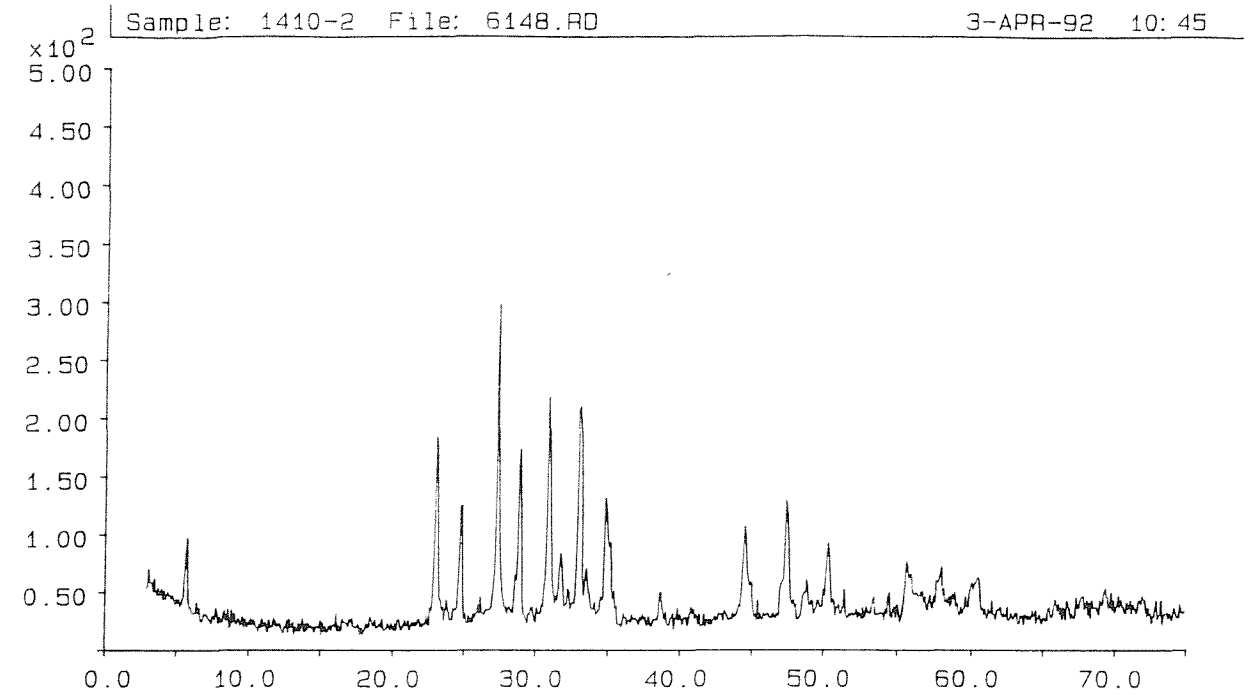

Figure A1.8 XRD pattern of Bi(Pb)-Sr-Ca-Cu-O glass-ceramic with y=0.4 annealed at 850°C for 120h.

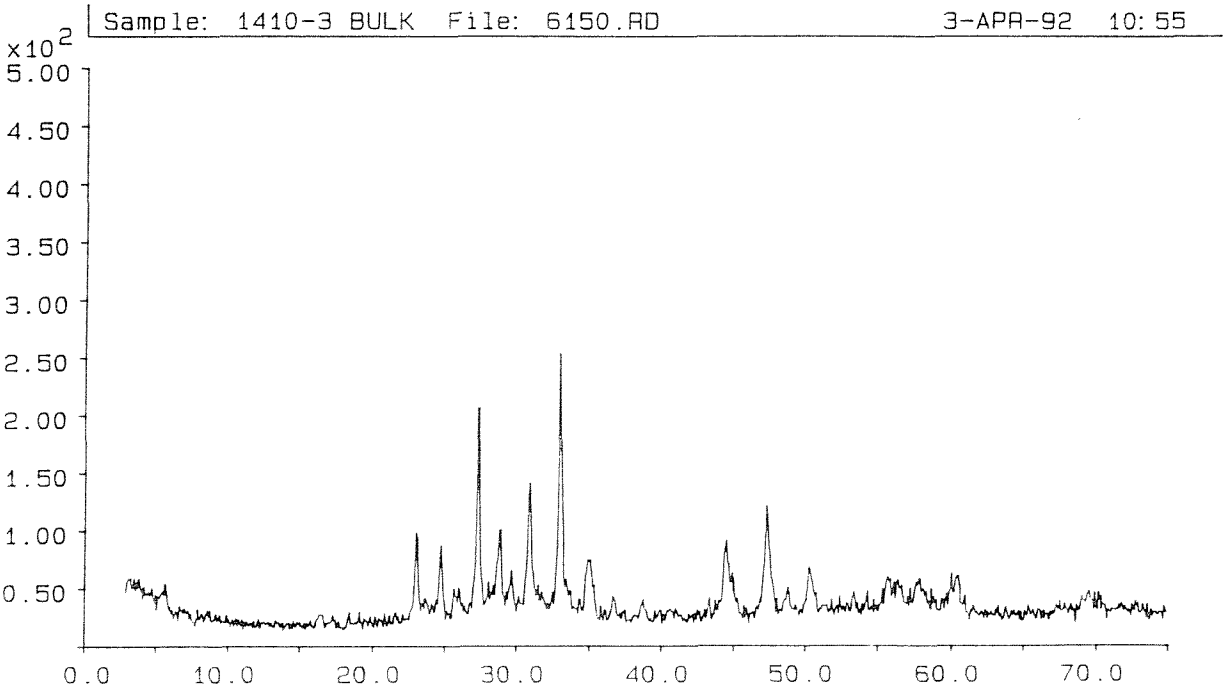

Figure A1.9 XRD pattern of Bi(Pb)-Sr-Ca-Cu-O glass-ceramic with y=0.9 annealed at 850°C for 120h.

Appendix 2 Papers published in the course of this work.

"Flux jumping in high temperature superconducting flux tubes", J.W. Burgoyne & J.H.P. Watson.

Oral presentation at the 6th Annual Conference on Superconductivity and Applications, Buffalo, NY, USA, 15-17 September 1992.

Also presented as a poster at the 4th International Conference on Superconductivity: Materials, Physics and Applications (ICMAS-92), Paris, France, 21-22 October 1992.

FLUX JUMPING IN HIGH TEMPERATURE SUPERCONDUCTING FLUX TUBES.

J. W. Burgoyne & J. H. P. Watson
The Institute of Cryogenics, University of Southampton,
Highfield, Southampton SO9 5NH, U.K.

ABSTRACT

Flux jumping in the intergranular shielding curves and magnetisation hysteresis of a $Bi_2Sr_2CaCu_2O_{8+x}$ flux tube has been studied at temperatures close to 4.2K and at various applied field sweep rates. Large incomplete flux jumps are observed, increasing in number with field sweep rate. For higher sweep rates, large jumps are followed by a number of exponentially decaying small jumps which are explained in terms of the granular nature of the superconductor. The results are compared to conventional flux jumping theory and predictions for high temperature superconductors.

INTRODUCTION

Flux jumping is a well known phenomenon in high field type II superconductors, and has been extensively characterised for conventional low-T_c materials. Adiabatic theories[1,2] allow predictions of flux jumping, and hence stabilisation against it, and empirical dependencies for dH/dt and T have been found[3,4,5]. The usual solution of finely-divided filamentary superconducting wire may not be practicable with high temperature superconductors (HTS), and it is therefore important to know the limitations placed upon such bulk materials by flux jumping.

It has been predicted that HTS are immune to flux jumping below 5 to 9T at 77K[6,7,8]; at 4.2K the flux jump field is predicted to fall to around 0.4T[8] and flux jumping must be considered in light of the possible high-field applications of Bi-based HTS at low temperatures. Flux jumps have been observed in single crystal[9,10,11,12] and melt-textured[13,14,15,16] cuprate oxides in small samples. The use of a flux tube allows the straightforward measurement of bulk intergranular properties on a small-device scale; the use of flux tubes to produce high fields has been suggested by Watson[17].

EXPERIMENTAL

The flux tube used in these experiments is of melt-textured $Bi_2Sr_2CaCu_2O_{8+x}$ (x=0.15 to 0.20) with T_c=89 to 91K, supplied by Hoechst AG, with dimensions 15mm i.d. x 25mm o.d. x 50mm. Measurements were carried out in an Oxford Instruments exchange gas cryostat with a 3T superconducting magnet. The cryostat temperature may be lowered to 2.2K by a lambda point fridge. The magnet is

conduction-cooled, and the sample sits in a He exchange gas at ~ 1 torr (Figure 1): heat transfer conditions are known to affect flux jumping, so this situation may be more prone to flux jumping than in liquid helium. Measurements to higher field in liquid helium are proceeding. The applied field B_a is measured from the magnet current, and the field in the enclosed tube volume B_i by a cryogenic Hall probe (F.W. Bell BHA-921); the sample temperature is measured by an SMDT silicon diode thermometer (Institute of Cryogenics). The magnetic field was swept at rates between 0.062 and 0.31Tmin^{-1}, the upper limit being set by the magnet specification, applied axially to the tube bore. The tube magnetisation is obtained as $\mu_o M = B_i - B_a$ and is quoted in Tesla to emphasise this fact.

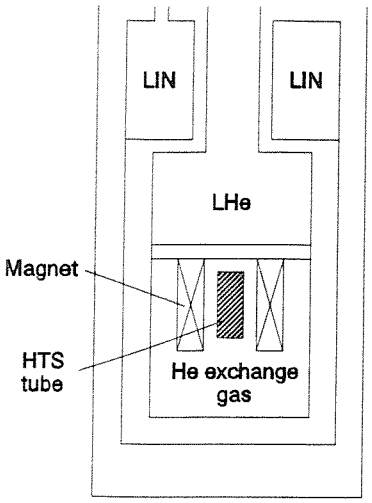

Figure 1: 3 Tesla magnet and cryostat.

RESULTS AND DISCUSSION

The flux tube shielding curve was measured at 4.5K and applied field sweep rates of 0.093, 0.124, 0.17, 0.225 and 0.31Tmin^{-1}. The virgin curve at 0.31Tmin^{-1} is shown in Figure 2. The critical current density may be derived from

$$J_c = \frac{B_{sh}}{\mu_o w} \qquad (1)$$

where B_{sh} is the maximum shielded field and w the tube wall thickness. In the virgin shielding region the intergranular current component only is measured and thus for B_{sh}=0.48T an intergranular, or transport, J_c(0T, 4.5K) = 7640Acm^{-2} is obtained. Previous measurements at 77K indicate J_c(0, 77) = 160Acm^{-2}.

The penetration of flux into the tube in a series of flux jumps starting at 1.24T is clearly seen; the average field which the tube sees at this point is $B^* = (B_i+B_a)/2 \simeq 0.82$T. The flux jump size decreases exponentially with increasing applied field. The magnetisation

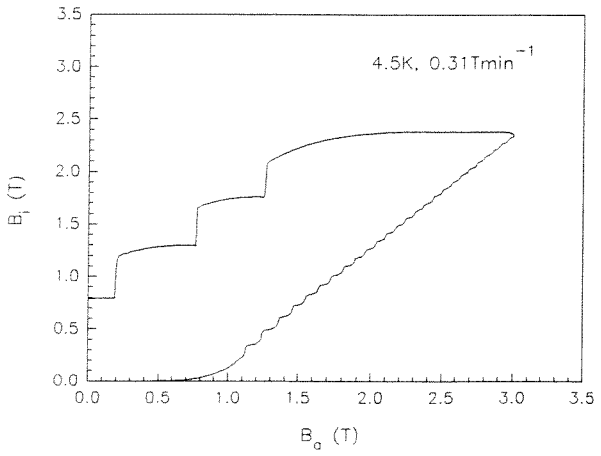

Figure 2: Virgin shielding curve at 4.2K.

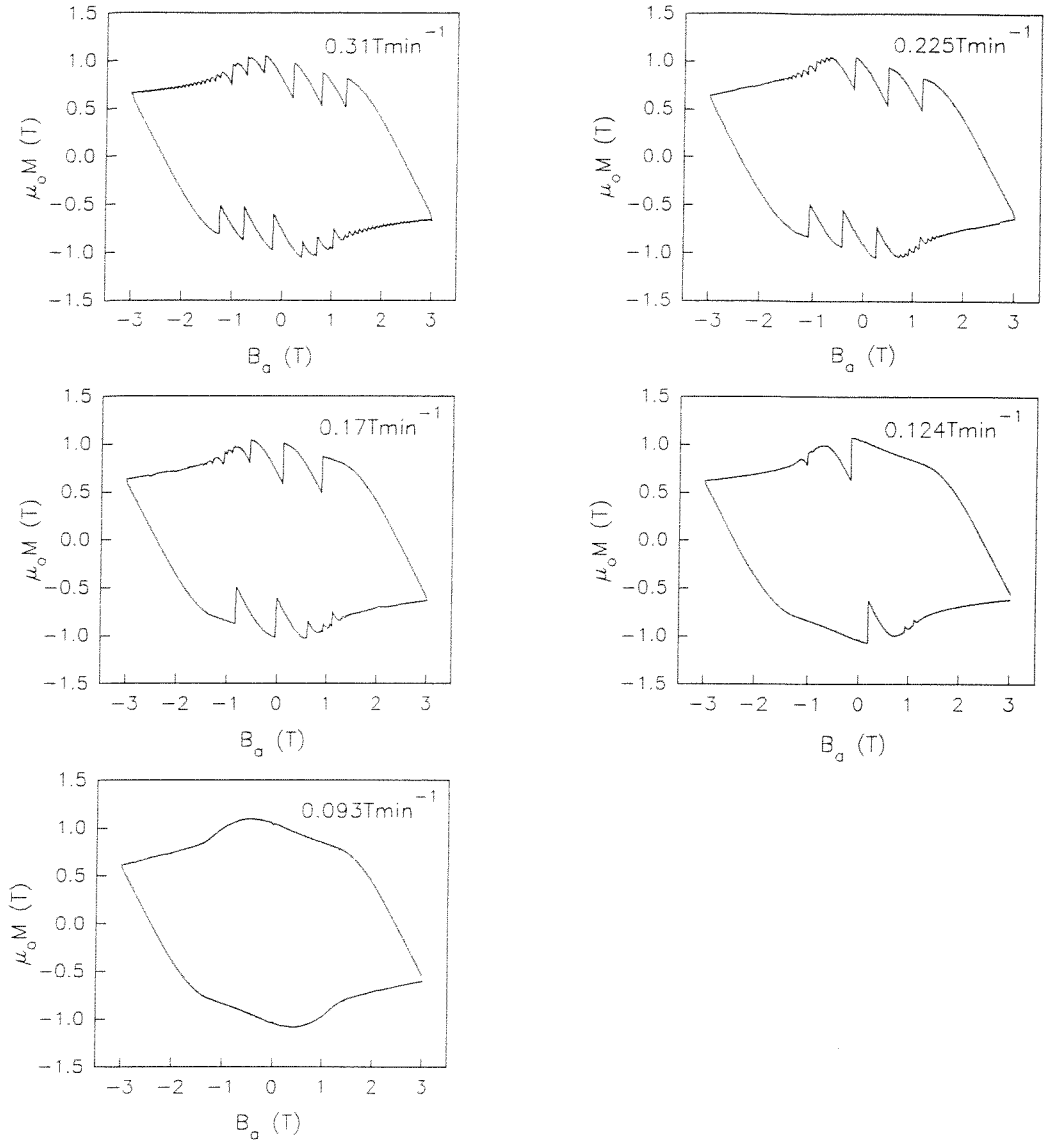

Figure 3: Magnetisation loops at 4.5K and various applied field sweep rates.

curves at 4.5K (Figure 3) show an increase of flux jumping with sweep rate $\dot{B}_a$. The width of the magnetisation loop is effectively constant for all $\dot{B}_a$. Other measurements indicate that the position and size of flux jumps for given T, $\dot{B}_a$ are closely reproducible around subsequent loops. The flux jumps may be described as "major" and "minor" jumps, the minor jumps being particularly noticeable at 0.225 and 0.31Tmin^{-1}. These two regions will be discussed in turn.

The number of major jumps around the hysteresis loop clearly increases with $\dot{B}_a$ as observed in conventional superconductors. It is expected that the number of jumps in the first quadrant *Q1* ($+B_a$, $-M$) will equal the number in the third

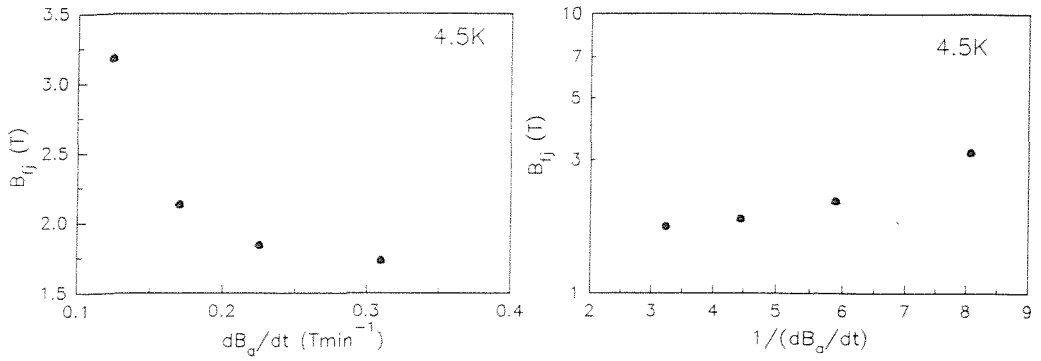

Figure 4: Applied field sweep rate dependence of flux jump field B_{fj}.

quadrant *Q3*, and that $Q2 = Q4 = Q1 - 1$[4]. This empirical rule is only partially observed, for 0.124, 0.225 and possibly 0.17Tmin^{-1}.

Considering still only the major jumps, the flux jump field B_{fj}, may be found from the magnetisation as the field from the maximal B_a at which flux jumping first occurs[15] (this assumes an ideal Bean model). Thus we find B_{fj} = 1.73, 1.84, 2.13, 3.18T for 0.31, 0.225, 0.17, 0.124Tmin^{-1} respectively; the dependence of B_{fj} on $\dot{B}_a$ is shown in Figure 4. At low sweep rates $\dot{B}_a$ one expects[5]

$$\log B_{fj} \propto \frac{1}{\dot{B}_a} \tag{2}$$

and for the behaviour to deviate from this at higher $\dot{B}_a$. Figure 4 suggests that this may be the case for the above measurements, although a wider range of $\dot{B}_a$ is really required.

Figure 5 shows part of the shielding curve at 0.093Tmin^{-1}, which may be taken as the equilibrium curve, together with the virgin curve at 0.31Tmin^{-1}. Since the hysteresis loops do not change significantly with sweep rate, the two may be directly compared to show a large enhancement of flux trapping over shielding such that $B_{tr}(B_a=0) \simeq 1.0$T compared with B_{sh} = 0.48T. This effect has previously been observed in $YBa_2Cu_3O_{7-x}$ tubes[18,19] and explained in terms of the granular nature of HTS. It is well known that these materials

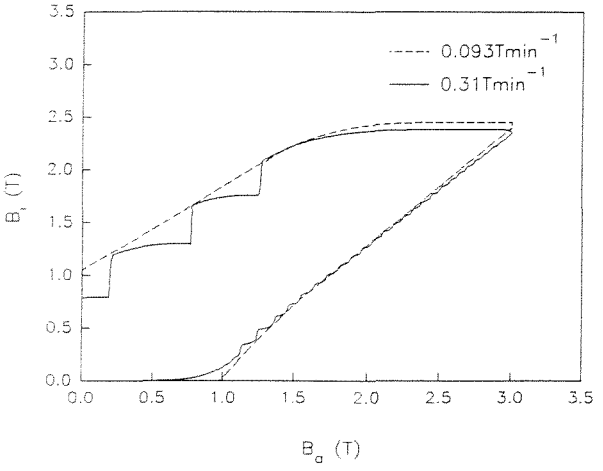

Figure 5: Shielding curves at 0.093Tmin^{-1} (equilibrium curve) and 0.31Tmin^{-1}.

have inter- and intra-granular components to many of their properties, and these may be quite clearly seen in a tubular geometry. At low fields the grains are totally shielded and flux enters only into the intergranular network; at higher fields the grains will be penetrated and hence trap flux, producing the above enhancement of B_{tr} compared to the ideal Bean model where $B_{tr} = B_{sh}$. Calculating J_c from the magnetisation loop yields J_c("total") = 16500Acm^{-2}.

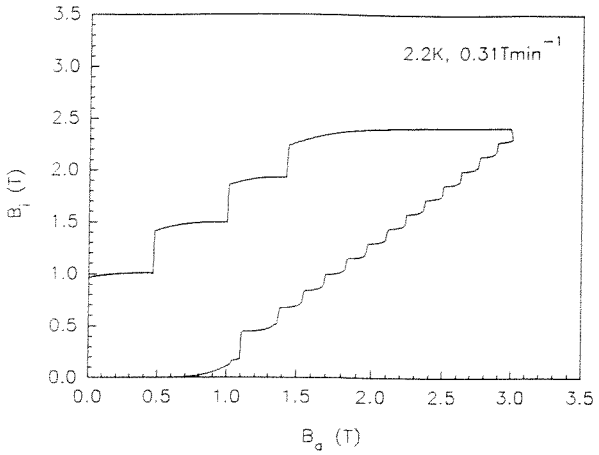

Figure 6: Virgin shielding curve at 2.2K and 0.31Tmin^{-1}.

The virgin shielding curve at 2.2K and 0.31Tmin^{-1} is shown in Figure 6 from which values of B_{sh} = 0.49T and $J_c(0, 2.2)$ = 7800Acm^{-2} are derived. Flux jumps are observed in a similar way to 4.5K, but here the jumps are of an almost constant size after the first flux jump at 1.1T, lower than at 4.5K. The subsequent jumps are also very uniformly spaced. Full magnetisation loops at 3.2K and 2.2K are given in Figure 7 and flux jump fields are found to be 1.70T and 1.56T respectively. The decrease of B_{fj} is as expected at low T (Figure 8); B_{fj} initially increases with decreasing T from T_c, reaches a maximum, and decreases again.

The minor jumps which are observed in the 0.31Tmin^{-1} hysteresis curves show a marked effect with decreasing T. At 4.5K the size of the jumps, ΔM^{fj}, decreases exponentially with the field at which they occur, B_a^{fj}. The decay is less for 3.2K, and at 2.2K the minor jumps are of almost constant size. At the same time, the number of minor jumps decreases with T. This is illustrated in Figure 9 where although there is little pattern to the major jumps, the decreasing decay of minor jumps is clear.

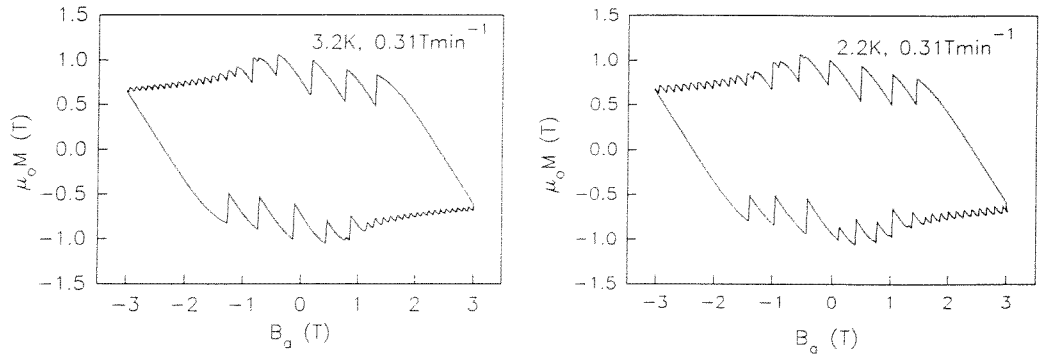

Figure 7: Magnetisation hysteresis curves at 3.2K and 2.2K, 0.31Tmin^{-1}.

To explain the disparity between the flux jump field for the major jumps and that at which flux jumps are first observed in the 4.5K and 2.2K virgin curves, we suggest that granular effects may again be invoked. The flux jumping in the virgin curves (Figures 2, 6) corresponds to the minor jumps in the hysteresis loops which may therefore be identified with the intergranular region. The exponential decay of ΔM^{fj} is not altogether surprising since flux jumping is a thermal process, and a mechanism similar to the exponential flux line hopping of Anderson's flux creep theory[20] may be operating. As the temperature is lowered flux pinning becomes stronger, thus reducing the exponential decay, eventually tending to a constant value at the lowest temperatures. The major jumps would then be associated with bulk inter- plus intra-granular properties.

Adiabatic flux jumping theory[2] gives

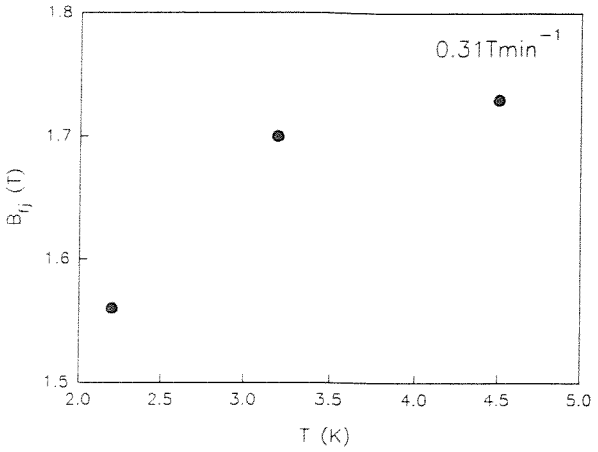

Figure 8: Temperature dependence of flux jump field B_{fj} at 0.31Tmin^{-1}.

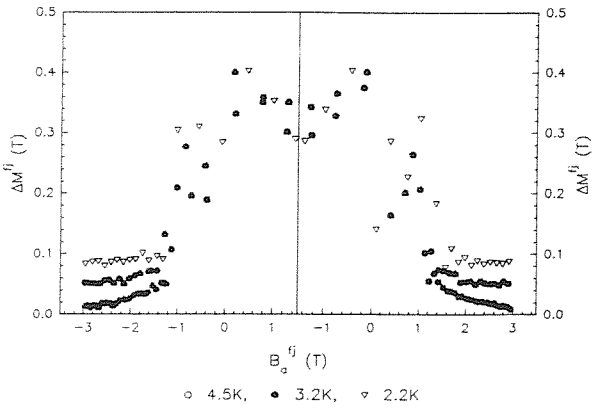

Figure 9: Size of flux jumps at 2.2K, 3.2K and 4.5K *vs.* applied field at which jumps occur.

$$B_{fj} = [3\mu_o C \frac{J_c}{\partial J_c/\partial T}]^{\frac{1}{2}} \qquad (3)$$

where C is the specific heat. The ratio of J_c to $\partial J_c/\partial T$ enters into (3) and may explain the different flux jumping behaviours. The specific heat should be practically the same for inter- and intra-granular regions, while it is known that J_c and $\partial J_c/\partial T$ are widely different. Thus unconventional flux jumping behaviour may be expected. Further work is progressing to form a more quantitative basis for these hypotheses.

CONCLUSIONS

In summary, flux jumping has been examined in an HTS flux tube with respect to applied field sweep rate and temperature dependencies. Flux jumping behaviour is found to be in agreement with the empirical relations previously observed in conventional superconductors, but novel effects are observed which are attributed to the granular nature of HTS. Two regions of flux jumping behaviour seem to be operating, the inter- and intra-granular. Flux jump fields are found to be higher than those predicted for HTS.

ACKNOWLEDGEMENTS

The authors wish to acknowledge the help of Mr I.D. Mears and Mr M.P. Webb of the Institute of Cryogenics, financial assistance from SERC, The Institute of Physics and Pilkington plc, Hoechst AG for supplying the HTS tube and British Aerospace plc for lending the 3T magnet. We would like to acknowledge the use of the SERC funded Chemical Databank Service at Daresbury, U.K. for part of the work described in this paper.

REFERENCES

1. Wipf, Phys. Rev. 161, 404 (1967).
2. Swartz & Bean, J. Appl. Phys. 39, 1991 (1968).
3. Wipf & Lubell, Phys. Lett. 16, 103 (1965).
4. Watson, J. Appl. Phys. 37, 516 (1966).
5. Watson, J. Appl. Phys. 38, 3813 (1967).
6. Laquer et al., IEEE Trans. Mag. 25, 1516 (1989).
7. Collings, Proc. MRS Intl. Mtg. on Advanced Materials, Tokyo, Japan, 1988 (MRS, 1989), 155.
8. Collings, Procs. ISS 1989, Advances in Superconductivity 2 (Springer, Tokyo, 1990), 327.
9. Levet et al., Nature 331, 307 (1988).
10. Tholence et al., Solid State Commun. 65, 1131 (1988).
11. Guillot et al., Phys. Lett. A 127, 363 (1988).
12. Guillot et al., Physica C 162, 361 (1989).
13. Hsu et al., Solid State Commun. 75, 799 (1990).
14. Chen et al., Appl. Phys. Lett. 56, 2675 (1990).
15. Chen et al., Physica C 173, 227 (1991).
16. Watanabe et al., Jpn. J. Appl. Phys. 30, L1638 (1991).
17. Watson, Proc. ICEC12, Southampton, U.K., 1988 (Butterworths, 1988), 988.
18. Willis et al., IEEE Trans. Mag. 25, 2502 (1989).
19. Burgoyne, MSc. Thesis, University of Southampton, U.K. (1990).
20. Anderson, Phys. Rev. Lett. 9, 309 (1962).

References.

1. M.K. Wu, J.R. Ashburn, C.J. Torng, P.H. Hor, R.L.Meng, L. Gao, Z.J. Huang, Y.Q. Wang & C.W. Chu, Phys. Rev. Lett. **58**, 908 (1987)
2. R.J. Cava, B. Batlogg, R.B. van Dover, D.W. Murphy, S. Sunshine, T. Seigrist, J.P. Remeika, E.A. Rietman, S. Zahurak & G.P. Espinosa, Phys. Rev. Lett. **58**, 1676 (1987)
3. H. Maeda, Y Tanaka, M. Fukoutomi & T. Asano, Jpn. J. Appl. Phys. **27**, L209 (1988)
4. Z.Z. Sheng & A.M. Hermann, Nature **332**, 138 (1988)
5. D. Caplin, Nature **335**, 204 (1988)
6. J.C. Phillips, *Physics of High-T_c Superconductors* (Academic Press, London, 1989)
7. S. Jin & J.E. Graebner, Mat. Sci. Eng. **B7**, 243 (1991)
8. T. Komatsu, R. Sato, K, Imai, K. Matusita & T. Yamashita, Jpn. J. Appl. Phys. **27**, L550 (1988)
9. M. Onishi, T. Kohgo, Y. Chigusa, M. Kyoto & M. Watanabe, Jpn. J. Appl. Phys. **28**, L2204 (1989)
10. C.H. Rosner, M.S. Walker, P. Haldar & L.R. Motowidlo, Cryogenics **32**, 940 (1992)
11. Y. Iwasa, 6th Ann. Conf. on Supercond. & Appl., 15-17 Sept. 1992, Buffalo, NY, USA (pre-print)
12. D.W. Hazelton, P. Haldar, M.S. Walker, J.G. Hoehn, J.A. Rice & W.S. Uzbanski, *ibid.*
13. T.L. Francavilla & D.U. Gubser, *ibid.* (pre-print)
14. K.G. Herd & E.T. Laskaris, *ibid.*
15. J.H.P. Watson, Proc. ICEC 12, 12-15 July 1988, Southampton, UK (Butterworths, Guildford, UK, 1988), 988
16. A.F. Hildebrant, D.D. Elleman, F.C. Whitmore & R. Simpkins, J. Appl. Phys. **33**, 2375 (1962)
17. P.S. Swartz & C.H. Rosner, J. Appl. Phys. **33**, 2292 (1962)

18. F.J. Eberhardt, A.D. Hibbs & A.M. Campbell, IEEE Trans. Mag. **25**, 2146 (1989)
19. E. Tjukanov, R.W. Cline, R. Krahn, M. Hayden, M.W. Reynolds, W.N. Hardy, J.F. Carolan & R.C. Thompson, Phys. Rev. B **36**, 7244 (1987)
20. J.O. Willis, M.E. McHenry, M.P. Maley & H. Sheinberg, IEEE Trans. Mag. **25**, 2502 (1989)
21. J.W. Purpura & T.R. Clem, IEEE Trans. Mag. **25**, 2506 (1989)
22. O.G. Symko, W.J. Yeh, D.J. Zheng & S. Kulkarni, J. Appl. Phys. **65**, 2142 (1989)
23. J. Wang, J. Li, W. Yang & L. Zhou, IEEE Trans. Mag. **27**, 1029 (1991)
24. M.R. Cimberle, C. Ferdeghini, G.L. Nicchiotti, M. Putti, A.S. Siri, C. Rizzuto, C.A. Costa, M. Ferretti, C.L. Olcese, F.C. Matacotta & E. Olzi, Supercond. Sci. Technol. **1**, 30 (1988)
25. J.R. Cave, M. Mautref, C. Agnoux, A. Leriche & A. Février, Cryogenics **29**, 341 (1989)
26. J.W. Burgoyne, *Magnetisation measurements of a high temperature superconducting flux tube*, MSc. Thesis, University of Southampton, 1990
27. Y.B. Kim, C.F. Hempstead & A.R. Strnad, Phys. Rev. **129**, 528 (1963)
28. D. Saint-James, E.J. Thomas & G. Sarma, *Type II Superconductivity* (Pergamon, Oxford, 1969)
29. J.E. Evetts, A.M. Campbell & D. Dew-Hughes, Phil.Mag. **10**, 339 (1964)
30. M.N. Wilson, *Superconducting Magnets* (Oxford, 1983)
31. P.S. Swartz & C.P. Bean, J. Appl. Phys. **39**, 4991 (1968)
32. J.E. Kunzler, Rev. Mod. Phys. **33**, 501 (1961)
33. C.P. Bean, Phys. Rev. Lett. **8**, 250 (1962)
34. Y.B. Kim, C.F. Hempstead & A.R. Strnad, Phys. Rev. Lett. **9**, 306 (1962)
35. H.J. Goldsmid & J.M. Corsan, Phys. Lett. **12**, 39 (1964)
36. J.M. Corsan, Phys. Lett. **12**, 85 (1964)
37. F. Lange, Cryogenics **5**, 143 (1965)
38. S.L. Wipf & M.S. Lubell, Phys. Lett. **16**, 103 (1965)
39. J.H.P. Watson, J. Appl. Phys. **37**, 516 (1966)
40. J.H.P. Watson, J. Appl. Phys. **38**, 3813 (1967)

41. P.O. Carden, Aust. J. Phys. **18**, 257 (1965)
42. P.F. Smith, A.H. Spurway & J.D. Lewin, Brit. J. Appl. Phys. **16**, 947 (1965)
43. N. Morton, Cryogenics 8, 79 (1968)
44. B.B. Goodman & M. Wertheimer, Phys. Lett. **18**, 236 (1965)
45. R. Hancox, Phys, Lett. 16, 208 (1965)
46. P.S. Swartz & C.P. Bean, Bull. Am. Phys. Soc. **10**, 359 (1965)
47. L.J. Neuringer & Y. Shapira, Phys. Rev. **148**, 231 (1966)
48. S.L. Wipf, Phys. Rev. **161**, 404 (1967)
49. K. Yamafuji, M. Takeo, J. Chikaba, N. Yano & F. Irie, J. Phys. Soc. Jpn. **26**, 315 (1969)
50. M.N. Wilson, C.R. Walters, J.D. Lewin & P.F. Smith, J. Phys. D: Appl. Phys. **3**, 1517 (1970)
51. T. Akachi, T. Ogasawara & K. Yasukochi, Jpn. J. Appl. Phys. **20**, 1559 (1981)
52. R.G. Mints & A.L. Rakhmanov, Rev. Mod. Phys. **53**, 551 (1981)
53. Y. Iwasa, IEEE Trans. Mag. 24, 1211 (1988)
54. S.L. Wipf, Proc. ICEC 12, 12-15 July 1988, Southampton, UK (Butterworths, Guildford, UK, 1988), 931
55. H.L. Laquer, F.J. Edeskuty, W.H. Hassenzahl & S.L. Wipf, IEEE Trans. Mag. **25**, 1516 (1989)
56. S.L. Wipf & H.L. Laquer, IEEE Trans. Mag. **25**, 1877 (1989)
57. E.W. Collings, Cryogenics **28**, 724 (1988)
58. E.W. Collings, MRS Intl. Mtg. on Adv. Mats., Tokyo, 1988, **Vol. 6** (Materials Research Society, 1989), 155
59. E.W. Collings, *Advances in Superconductivity II: Proc. ISS'89* (Springer, Tokyo, 1990), 327
60. T. Ogasawara, Cryogenics 29, 2 (1989)
61. S.L. Wipf, Cryogenics 31, 936 (1991)
62. J.C. Levet, M. Potel, P. Gougeon, H. Noel, M. Guillot & J.L. Tholence, Nature **331**, 307 (1988)
63. J.L. Tholence, H. Noel, J.C. Levet, M. Potel & P. Gougeon, Solid State Commun. 35, 1131 (1988)

64. M. Guillot, M. Potel, P. Gougeon, H. Noel, J.C. Levet, G. Chouteau & J.L. Tholence, Phys. Lett. A **127**, 363 (1988)
65. K. Chen, S.W. Hsu, T.L. Chen, S.D. Lan, W.H. Lee & P.T. Wu, Appl. Phys. Lett. **56**, 2675 (1990)
66. S.W. Hsu, K. Chen & W.H. Lee, Solid State Commun. **75**, 799 (1990)
67. L.P. Wang, K. Chen, C.L. Lin & J.J. Chu, J. Appl. Phys. **70**, 7492 (1991)
68. K. Chen, Y.C. Chen, S.W. Lu, W.H. Lee & P.T. Wu, Physica C **173**, 227 (1991)
69. K. Watanabe, N. Kobayashi, S. Awaji, G. Kido, S. Nimori, K. Kimura, K. Sawano & Y. Muto, Jpn. J. Appl. Phys. **30**, L1638 (1991)
70. K. Watanabe, S. Awaji, G. Kido, N. Kobayashi, Y. Muto, K. Kimura & K. Sawano, Supercond. Sci. Technol. **5**, S228 (1992)
71. K. Watanabe, S. Awaji, N. Kobayashi, S. Nimori, G. Kido, K. Kimura & M. Hashimoto, Cryogenics 32, 959 (1992)
72. T. Takizawa, M. Kosaka, K. Kanbara, M. Morita & K. Sawano, Jpn. J. Appl. Phys. **30**, L1790 (1990)
73. M. Guillot, J.L. Tholence, O. Laborde, M. Potel, P. Gougeon, H. Noel & J.C. Levet, Physica C 162-164, 361 (1989)
74. K. Kadowaki & T. Mochiku, Physica C **195**, 127 (1992)
75. A. Gerber, J.N. Li, Z. Tarnawski, J.J.M. Franse & A.A. Menovsky, "Magnetic instabilities in high temperature superconductors under quickly varying magnetic fields" (1992, pre-print)
76. M.E. McHenry, H.S. Lessure, M.P. Maley, J.Y. Coulter, I. Tanaka & H. Kojima, Physica C 190, 403 (1992)
77. J.L. Tholence, H. Noel, J.C. Levet, M. Potel, P. Gougeon, G. Chouteau & M. Guillot, Physica C 153-155, 1479 (1988)
78. O. Durmeyer, J.P. Kappler, A. Derory, M. Drillon & J.J. Capponi, Solid State Commun. 74, 621 (1990)
79. A.G. Swanson, J.S. Brooks, H. Anzai, N. Konoshita, M. Tokumoto & K. Murata, Solid State Commun. 73, 353 (1990)
80. Cao Xiaowen & Huang Sunli, Solid State Commun. **70**, 1115 (1989)
81. C.P. Bean, Rev. Mod. Phys. 36, 31 (1964)

82. P.W. Anderson, Phys. Rev. Lett. **9**, 309 (1962)

83. T.T.M. Palstra, B. Batlogg, R.B. van Dover, L.F. Schneemeyer & J.V. Waszczak, Phys. Rev. B **41**, 6621 (1990)

84. C. Ebner & D. Stroud, Phys. Rev. B **31**, 165 (1985)

85. Y. Yeshurun & A.P. Malozemoff, Phys. Rev. Lett. **60**, 2202 (1988)

86. D.J. Bishop, P.L. Gammel & D.A. Huse, Sci. Amer., Feb. 1993, 24

87. P.S. Swartz & C.P. Bean, Technical Report No. AFML-TR-65-431, Air Force Materials Laboratory, Air Force Systems Command, Wright-Patterson Air Force Base, Ohio (1966)

88. N. McN. Alford, Solid State Science Group, ICI Advanced Ceramics (personal communication)

89. Hoechst AG, *Materials for Superconducting echnology*, 1991 edition

90. A.S. Bahaj, R.M. Igra & R.G. Scurlock, Proc. ICEC 12, 12-15 July 1988, Southampton, UK (Butterworths, Guildford, UK, 1988), 384

91. P. Leiderer & R. Feile, Z. Phys. B **70**, 141 (1988)

92. T. Puig, L.M. Martinez, M.T. Aurell, A. Sanchez, D.-X. Chen & J.S. Muñoz, *Physics and Materials Science of High Temperature Superconductors*, ed. Kossowsky *et al.*, (Kluwer Academic Publishers, 1990), 467

93. E.M. Gyorgy, G.S. Grader, D.W. Johnson, L.C. Feldman, D.W. Murphy, W.W. Rhodes, R.E. Howard, P.M. Mankiewich & W.J. Skocpol, Appl. Phys. Lett. **52**, 328 (1988)

94. A.P. Malozemoff, *Physical Properties of High Temperature Superconductors I*, ed. Ginsberg (World Scientific, Singapore, 1989), 71

95. H.G. Schnack, R. Griessen, J.G. Lensink, C.J. van der Beek & P.H. Kes, Physica **197**, 337 (1992)

96. W.J. Yeh, L. Chen, F. Xu, B. Bi & P. Yang, Phys. Rev. B **36**, 2414 (1987)

97. M.A.K. Mohamed, W.A. Miner, J. Jung, J.P. Franck & S.B. Woods, Phys. Rev. B **37**, 5834 (1988)

98. M. Polák, W. Windte, W. Schauer, J. Reiner, A. Gurevich & H. Wuhl, Physica C **174**, 14 (1991)

99. C. Keller, H. Küpfer, R. Meier-Hirmer, U. Wiech, V. Selvamanickam & K. Salama, Cryogenics 30, 410 (1990)

100. Y. Ren, P.A.J. de Groot, F. Gencer & J.S. Abell, Supercond. Sci. Technol. **3**, 349 (1990)
101. L. Půst, Supercond. Sci. Technol. **3**, 598 (1990)
102. A. Junod, *Physical Properties of High Temperature Superconductors II*, ed. Ginsberg (World Scientific, Singapore, 1990), 13
103. M.B. Salamon, *Physical Properties of High Temperature Superconductors I*, ed. Ginsberg (World Scientific, Singapore, 1989), 39
104. W.H. Zachariasen, J. Amer. Chem. Soc. **54**, 3841 (1932)
105. H. Rawson, *Inorganic Glass-Forming Systems* (Academic Press, 1967)
106. W.H. Dumbaugh, Phys. Chem. Glasses **19**, 121 (1978)
107. W.H. Dumbaugh, Phys. Chem. Glasses **27**, 119 (1986)
108. R. Sato, T. Komatsu & K. Matusita, J. Mat. Sci. Lett. **10**, 335 (1991)
109. M. Tatsumisago, S. Tsuboi, N. Toghe & T. Minami, J. Non-Cryst. Solids **124**, 167 (1990)
110. B.J. Chen, M.A. Rodriguez & R.L. Snyder, Superconductivity & Its Applications, Buffalo, NY, USA, 1990, AIP Conference Proceedings 219 (AIP, 1991), 589
111. M. Onishi, T. Kohgo, Y. Chigusa, K. Watanabe & M. Kyoto, Jpn. J. Appl. Phys. **29**, L64 (1990)
112. T. Komatsu, C. Hirose, T. Ohki, R. Sato, K. Matusita & T. Yamashita, Appl. Phys. Lett. **57**, 183 (1990)
113. M. Tatsumisago, S. Tsuboi, N. Toghe & T. Minami, Appl. Phys. Lett. **57**, 2940 (1990)
114. T. Komatsu & K. Matusita, Thermochimica Acta **174**, 131 (1991)
115. T. Komatsu, C. Hirose, R. Sato & K. Matusita, J. Non-Cryst. Solids **126**, 273 (1990)
116. Y. Higashida, H. Yokoyama, K. Michishita, Y. Kubo, H. Yoshida, Y. Abe & H. Hosono, Appl. Phys. Lett. **55**, 1578 (1989)
117. Y. Abe, H. Arakawa, M. Hosoe, Y. Hikichi, J. Iwase, H. Hosono & Y. Kubo, Jpn. J. Appl. Phys. **28**, L1929 (1989)
118. M. Tatsumisago, C.A. Angell, Y. Akamatsu, S. Tsuboi, N. Toghe & T. Minami, Appl. Phys. Lett. **55**, 600 (1989)

119. Z. Strnad, *Glass Ceramic Materials - Glass Science & Technology 8* (Elsevier, 1986), 141

120. W. Wong-Ng, C.K. Chiang, S.W. Freiman, L.P. Cook, N.M. Hwang & M.D. Hill, *Superconductivity and Ceramic Superconductors*, ed. Nair *et al.* (American Ceramic Society, 1990), 115

121. A. Briggs, J. Less-Common Metals **164-165**, 559 (1990)

122. G. Zorn, B. Seebacher, B. Jobst & H. Gobel, Physica C **177**, 494 (1991)

123. S.T. Misture, New York State College of Ceramics at Alfred University (personal communication)

124. S.T. Misture, B.J. Chen, M.A. Rodriguez & R.L. Snyder, 6th Ann. Conf. on Supercond. & Appl., 15-17 Sept. 1992, Buffalo, NY, USA (pre-print)